

DEVELOPMENT AND APPLICATIONS OF HIGH FILL-FACTOR, SMALL FOOTPRINT
MEMS MICROMIRRORS AND MICROMIRROR ARRAYS

By

KEMIAO JIA

A DISSERTATION PRESENTED TO THE GRADUATE SCHOOL
OF THE UNIVERSITY OF FLORIDA IN PARTIAL FULFILLMENT
OF THE REQUIREMENTS FOR THE DEGREE OF
DOCTOR OF PHILOSOPHY

UNIVERSITY OF FLORIDA

2009

© 2009 Kemiao Jia

To my parents, Yongsu Jia and Liping Chang, and my dear loving wife, Ying Zhou for their constant love, care and unwavering support and encouragement

ACKNOWLEDGEMENT

I would first like to thank my advisor, Dr. Huikai Xie, for his continuous support and guidance throughout the past four years. When I first joined Dr. Xie's Biophotonics and Microsystems Laboratory (BML) at the University of Florida in the fall of 2005, MEMS is a relatively new field to me. I am truly indebted for his patience and guidance in introducing me to the field of MEMS. I am grateful for all the insight he has provided for my thesis study. He has been a good mentor who has given me long lasting support in both my academic and personal lives. I have also gained the technical expertise through my interactions with him to become a better microsystem technology engineer.

I would also like to thank my committee members: Dr. Toshikazu Nishida, Dr. Ramakant Srivastava, and Dr. Ho-Bun Chan for their reviews of my work. I have benefitted greatly from my discussions with Dr. Nishida on thermo-mechanical issues. I enjoyed being the teaching assistant for Dr. Srivastava twice for the course of Photonics Laboratory, from which I also learned and strengthened my optics knowledge greatly. I am thankful to Dr. Chan for his encouragement in my thesis writing.

I would like to thank Dr. Hongwei Qu and Dr. Ankur Jain, who have always been the founding pillars of BML, for their help and training at the beginning of my thesis study. I followed Dr. Jain to study the development of CMOS-MEMS micromirrors. Dr. Qu taught me the design and development of CMOS-MEMS accelerometers. Both works became important part of my thesis study. I have benefitted greatly from our professional interactions as well as our personal friendships. They taught me the importance of being organized, responsible and well coordinated in the PhD study. In my personal life, they have also been my good friends. I still remember the many Friday nights we spent together. The laughter we had together were the happiest moment of my bachelor life. Special thanks go to Hongwei's wife, Chen chen and their

two daughters, Wendy and Angela. Their kind care for me has been very heart warming. I also would like to thank Shane Todd for his excellent work before he went to University of California at Santa Barbra, based on which an important part of my thesis study was founded.

I would like to thank my colleagues, Lei Wu, Mingliang Wang, Hongzhi Sun, and Yiping Zhu, who are also my close friends in my personal life. Lei and I met in China even years before we joined the group together. I still remember the countless nights we spent in the lab of Larsen 136 and in the clean room together for our course works and experiments. I enjoyed the numerous discussions and mutual encouragement we had throughout these years. My best wish goes to him and his family as we are going to part our ways after graduation. Mingliang came to BML one semester earlier than I did. As a colleague, his unyielding diligence in his experiment has been most inspiring. His decision and success in switching to another field has been very encouraging. As a friend, his righteous personality, helping heart and constant energy and optimism make him a great company. I enjoyed very much our cooking and swimming together on weekends. Hongzhi is the circuit expert in BML. We have been working on the projects of CMOS-MEMS accelerometers. Although I eventually chose micromirror as my thesis topic, I continued working with him on several academic tape-outs as well as commercial projects for about two years, from which I benefitted greatly on understanding the circuit design aspect of these projects. I thank Dr. Yiping Zhu for his work on the development of PZT-based micromirror devices. Through the daily interactions with Dr. Zhu, I learned the theory and fabrication process of Lead-Zirconium-Titanium-Oxide. His work on the PZT device modeling and fabrication help complete an important part of my dissertation. I wish him continuous happy life and research productivity at the University of California at Berkeley. I also would like to thank my colleague Sagnik Pal for his assistance on electrothermal modeling and device

fabrication. We have been project partners since the summer of 2007 when we first started the project of MEMS-based Dental Optical Coherence Tomography System with Lantis Laser, Inc. Since then we co-published several conference and journal papers. I also want to acknowledge my friends and colleagues Dr. Shuguang Guo, Xuesong Liu, and Zhongyang Guo for their friendship as well as their technical support. I benefitted greatly during my discussions with Shuguang on optics related problems, and with Xuesong and Zhongyang on MEMS inertial sensors. I would also like to thank Andrea Pais, Sean R. Samuelson, Lin Liu, Jingjing Sun, Jiping Li, Anuj Singh for their help and assistance in my experiment.

The BML is part of a bigger microsystem group, the Interdisciplinary Microsystems Group (IMG), at the University of Florida. I am thankful to all IMG members for their support and technical expertise. In particular, I would like to thank Jian Liu, Yawei Li, Naigang Wang, Shuo Cheng, Benjamin Griffin, Erin Patrick, Israel Boniche, Jeremy Sells, Jessica Meloy, Vijay Chandrasekharan, Brandon Bertolucci, Janhavi Agashe, Sheetal Shetye, and Tai-An Chen. Jian and Yawei introduced me to the IMG environment. Naigang Wang and I had a lot of technical discussions, mutual suggestions and helps for each other's experiment. We also became friends and fishing buddies in our personal lives. Thanks to Shuo for teaching me how to use the signal analyzer, and to Ben for helping me with the laser vibrometer. I thank Erin and Israel for their help on flip chip displacement system and the micro-dispenser system. I thank Jeremy and Jessica for their assistance with the wire bonding machine, and Brandon for the help of taking optical images. Special thanks to Erin and Brandon for organizing the sports events such as the Ultimate Frisbee and the rock climbing.

This work would not be completed without the help and support from our external collaborators. I would like to thank Mr. Douglas Hamilton of Lantis Laser, Inc. for his financial

support as well as technical dedication to the project of MEMS-based Dental Optical Coherence (OCT) Tomography System. I was truly impressed by his ability to fully grasp every aspects of the project. Without his effort on the OCT system and probe assembling development, we would not have been demonstrated the prototype product, and our paper would not have been invited to be presented at the Optical MEMS and Nano-photonics conference in 2009. I sincerely hope Lantis Laser's commercial product would be a big success in the field of dentistry. I would also like to thank An-Phong Nguyen for his strong support on the software generation for this project.

The fabrication of the MEMS devices in this work were conducted mostly using the equipments of the former University of Florida Nanofabrication Facility (UFNF), now known as the Nanoscale Research Facility (NRF), for which I would like to thank Alvin Ogdon, Williams Lewis, Ivan Kravchenko, and David Hays for their constant support and maintenance of the facilities. Some of the fabrication was performed at Microfabritech of material science and engineering, for which I would like to thank Dr. Mark Davidson and Dr. Maggie Lambers for their help on the training and operation of the equipments. The scanning electron microscopy (SEM), focused ion beam (FIB) etching and the white light profilometry were performed using the equipments in the Major Analytical Instrument Center (MAIC), for which I want to thank Dr. Luisa Dempere, Dr. Wayne Acree, and Dr. Gerald Bourne for their training and assistance.

I feel eternally grateful for my parents, Yongsu Jia and Liping Chang, for their selfless, endless love for me. I also would like to thank my dear loving wife, Ying Zhou for her constant, unwavering love and support. Her advices helped my research greatly. Her relentless spirit and persistent nature are also great encouragement for me.

This work has been supported by National Science Foundation Biophotonics Program through award number ECCS-0725598, and Lantis Laser, Inc.

TABLE OF CONTENTS

	<u>page</u>
ACKNOWLEDGEMENT	4
LIST OF TABLES.....	11
LIST OF FIGURES	12
ABSTRACT	17
CHAPTER	
1 INTRODUCTION.....	20
1.1 MEMS Micromirrors and Micromirror Arrays.....	20
1.2 MEMS Micromirror Optical Scanners	23
1.3 MEMS Micromirror Arrays	34
1.4 Dissertation Outline	40
2 ELECTROTHERMAL BIMORPH ACTUATION.....	41
2.1 Stress, Strain and Electrothermal Bimorph Actuator.....	41
2.2 Principle of Electrothermal Bimorph Actuation	42
2.3 Physical Characteristics of Cantilevered Bimorphs.....	47
2.3.1 Mechanical Characteristics of a Cantilevered Bimorph Actuator	48
2.3.1.1 Angular responsivity.....	48
2.3.1.2 Bimorph stiffness.....	52
2.3.1.3 Mechanical impact of the resistive heater	53
2.3.2 Thermal Characteristics of a Cantilevered Bimorph Actuator	56
2.3.2.1 Steady-state temperature distribution	57
2.3.2.2 Transient response of the temperature rise.....	62
2.3.2.3 E-T characteristics of a 1-D micromirror.....	63
2.4 Previous Electrothermal Micromirror Designs and Discussion.....	69
2.5 Summary.....	75
3 DEVELOPMENT OF THE FOLDED DUAL S-SHAPED ELECTROTHERMAL BIMORPH ACTUATORS AND ASSOCIATED MICROMIRROR DEVICES	77
3.1 FDS Electrothermal Bimorph Actuator Design Concept	77
3.2 1 st -Generation FDS Micromirror	82
3.3 2 nd -Generation FDS Micromirror: Optimization and Experimental Result	88
3.3.1 Structural Parameters Optimization	88
3.3.2 Fabrication Process Optimization	93
3.3.3 Experimental Result of 2 nd -Generation FDS Micromirror	94
3.3.3.1 Static test result	94
3.3.3.2 Dynamic test result	97

3.3.3.3	Test of device repeatability	99
3.3.3.4	Quality of the mirror surface.....	100
3.4	Summary.....	101
4	DEVELOPMENT OF MICROMIRROR AND MICROMIRROR ARRAY DEVICES WITH ULTRA-HIGH AREA FILL FACTOR.....	103
4.1	Development of the 3 rd -Generation FDS Micromirror Device	103
4.1.1	Design Concept of the 3 rd -Generation FDS Micromirror	103
4.1.2	Fabrication Process of the 3 rd -Generation FDS Micromirror	105
4.1.3	Experimental Result of the 3 rd -Generation FDS Micromirror.....	108
4.2	Development of the HFF MMA Devices	110
4.2.1	Design Concept of the HFF MMA Devices	111
4.2.2	Structural Design of the HFF MMA Devices.....	112
4.2.3	Fabrication and Packaging of the HFF MMA Devices.....	116
4.2.4	Characterization of the HFF MMA Devices	121
4.2.4.1	Mirror plate initial position	121
4.2.4.2	Static piston characterization	122
4.2.4.3	Static rotation characterization	123
4.2.4.4	Frequency responses measurement	124
4.2.4.5	Mirror surface quality measurement.....	126
4.3	Summary.....	126
5	APPLICATIONS OF DEVELOPED MEMS MICROMIRRORS AND MMAS.....	128
5.1	Endoscopic OCT Imaging Application Using 1-D Micromirror	128
5.2	Dental OCT Imaging Application Using the 2 nd -Generation FDS Micromirror	131
5.3	Optical Phased Array Application Using the HFF MMA Devices.....	136
5.4	Summary.....	140
6	DEVELOPMENT OF THE PIEZOELECTRIC FDS MICROMIRROR	141
6.1	Principle of Piezoelectric Bimorph Actuation	141
6.2	FEA Modeling of Single PZT Layer Cantilevered Bimorph Actuator.....	147
6.3	Folded Dual S-Shaped Bimorph Actuator based on Piezoelectric Actuation	151
6.4	Development of Piezoelectric FDS Micromirrors	154
6.4.1	Design of the Piezoelectric FDS Micromirror.....	154
6.4.2	Fabrication of the Piezoelectric FDS Micromirror	156
6.4.3	Characterization of the Piezoelectric FDS Micromirror	159
6.5	Summary.....	162
7	CONCLUSION AND FUTURE PLAN	164
7.1	Research Accomplishment	165
7.2	Future Work	166

LIST OF REFERENCE.....	168
BIOGRAPHICAL SKETCH	182

LIST OF TABLES

<u>Table</u>	<u>page</u>
2-1 Thermal-mechanical properties of commonly used MEMS materials [147-153].	49
2-2 Description of the resistor components in Fig. 2-5	58
2-3 Description of the capacitance components in Fig. 2-7	63
2-4 Structure parameters of the 1-D micromirror	65
2-5 Calculated values of the electrical components for the LEM equivalent circuit	65
3-1 Design parameters summary of 1 st -generation FDS device	84
3-2 Design parameters summary of the 2 nd -generation FDS device	93
4-1 Summary of design parameters of the 3 rd -generation FDS device	107
4-2 Structural parameters of the HFF MMA.....	114
6-1 Coefficients and mechanical properties of some piezoelectric materials [6, 163, 164] ..	146
6-2 Material properties and structural dimensions used in FEM simulation and theoretical calculation	148

LIST OF FIGURES

<u>Figure</u>	<u>page</u>
1-1 Handheld confocal imaging probe reported in [88].	26
1-2 Endoscopic OCT imaging probe reported in [89].	27
1-3 Endoscopic OCT imaging probe reported in [97].	29
1-4 Endoscopic OCT imaging probe reported in [135].	31
1-5 Endoscopic OCT imaging probe reported in [136].	32
1-6 Endoscopic Multi-photon imaging probe reported in [137].	33
1-7 3D schematic and SEM images of the reported MMA device in [72].	36
1-8 MMA device reported in [82].	37
1-9 SEM images of the MMA device reported in [146].	37
1-10 SEM images of the MMA device reported in [61].	38
1-11 SEM images of the MMA device reported in [145].	38
2-1 Structural views of a cantilevered bimorph beam.	43
2-2 Numerical calculation of optimal thickness ratio t_{Al}/t_{SiO_2} .	51
2-3 Cross sectional views of a cantilevered bimorph actuator with embedded Pt heater	54
2-4 Analytical and FEA simulation results of the bimorph ROC under temperature input.	56
2-5 Heat paths of a typical 1-D electrothermal bimorph micromirror	57
2-6 Steady-state LEM equivalent circuit of 1-D micromirror with partitioned bimorph.	60
2-7 Transient response equivalent circuit of 1-D micromirror with partitioned bimorph.	63
2-8 Top and side views of the 1-D micromirror device schematic.	64
2-9 Steady-state simulation results using the LEM equivalent circuit.	66
2-10 Transient simulation results on the bimorph using the LEM equivalent circuit.	67
2-11 Transient simulation results on the mirror plate and the substrate.	68
2-12 Design schematic and device SEM images of typical.	70

2-13	Schematic demonstration of the unstationery and stationery of rotation axis.....	71
2-14	Structure schematic and the SEM images of the 1-D and 2-D LVD micromirror devices.....	72
2-15	Cross sectional view of a 1-D LVD device showing the lateral shift.	73
2-16	Design concept and SEMs of the devices developed by Singh et al.	74
2-17	Design concept and SEMs of the LSF devices developed by Wu et al.	75
3-1	Illustration of the ISC concept.....	78
3-2	Side view of FDS bimorph actuator and FDS micromirror device topology.....	80
3-3	Simulation results of the FDS micromirror by Comsol.	81
3-4	SEM images of 1 st -generation FDS micromirror devices..	83
3-5	Fabrication process flow of 1 st -generation FDS device.....	85
3-6	Static test result of piston mode actuation for 1 st -Generation FDS device.....	86
3-7	Static test result for tip-tilt mode actuation of 1 st -Generation FDS device.....	87
3-8	Various Lissajous patterns generated by varying AC signal frequency ratio and phase difference between the two orthogonal actuator pairs.	87
3-9	Cross sectional view of a realistic S-Shaped half-FDS bimorph actuator.....	89
3-10	FEM simulation result of change in bimorph radii of curvature upon temperature variation.	90
3-11	Beam deflection parameters of half an FDS bimorph actuator	90
3-12	Plot of the normalized tip displacement of a half FDS actuator versus the normalized overlap length.	92
3-13	Cross-sectional view of the process flow.	94
3-14	SEM images of the 2 nd -generation FDS micromirror device showing 480μm initial mirror plate elevation.....	95
3-15	Static measurement result of piston mode actuation for the 2 nd -generation FDS micromirror.....	95
3-16	Static measurement result of rotation mode actuation for the 2 nd -generation FDS micromirror. All actuators had a dc voltage of 4V.	96

3-17	Transient response measurement.	97
3-18	2 nd -generation FDS micromirror frequency response of piston actuation.....	98
3-19	2 nd -generation FDS micromirror frequency response of rotation actuation.	99
3-20	Various Lissajous patterns generated by varying AC signal frequency ratio and phase difference between the two orthogonal actuator pairs.	99
3-21	2 nd -generation FDS micromirror reliability test.	100
3-22	2 nd -generation FDS mirror surface measurement result	101
4-1	Area usage of 2 nd -generation FDS micromirror	103
4-2	Structural demonstration of 2 nd - and 3 rd -generation FDS actuators.....	104
4-3	3D illustration of the 3 rd -generation FDS micromirror.....	105
4-4	Cross-sectional view of the proposed process flow for 3 rd -generation FDS micromirror.....	106
4-5	SEM images of the fabricated 3 rd -generation FDS micromirror.....	108
4-6	Static piston characterization of the 3 rd -generation FDS micromirror.....	108
4-7	Static rotation characterization of the 3 rd -generation FDS micromirror	109
4-8	Surface quality characterization of the 3 rd -generation FDS micromirror.	109
4-9	Portioned view of the proposed HFF MMA based on 3 rd -generation FDS micromirror and its fill-factor estimation.	111
4-10	3D realistic representation of the MMA device.	112
4-11	Static simulation result of an individual MMA pixel following the structural parameters in Table 4-1.	113
4-12	Worst case scenario simulation of the crosstalk between adjacent FDS actuators.	115
4-13	Cross-sectional view of the proposed process flow for HFF MMA.	116
4-14	Surface mounting integration scheme of the HFF MMA devices with IC/PCB driving electronics.	117
4-15	SEM images of the 2×2 HFF MMA devices from the 1 st batch of fabrication.....	117
4-16	SEM images of the 4×4 HFF MMA devices from the 2 nd batch of fabrication.....	118

4-17	Optical images of the 8×8 HFF MMA devices from the 2 nd batch of fabrication.	120
4-18	Optical images of a DIP-packaged surface-mounted 4×4 MMA device.....	120
4-19	Device topological profiles measured by Wyko-Vision optical profilometer.	121
4-20	Characterization of static actuations..	122
4-21	Characterization of static rotation actuation	123
4-22	Frequency response of rotation resonance mode	124
4-23	Piston resonance mode measurement result by Scanning Laser Vibrometer.....	125
4-24	Measurement results of mirror surface quality.....	126
5-1	Schematic of the OCT imaging setup in SUNY-SB and the scan unit by UF.	129
5-2	OCT images of precancerous and cancerous mouse bladder tissue compared with histology results.....	130
5-3	OCT images showing dental microstructures.....	132
5-4	Concept and design schematic of the probe.	133
5-5	Prototype imaging probe developed based on 2 nd -generation FDS micromirror.....	134
5-6	Dental OCT images taken by the 2 nd -generation FDS micromirror.....	135
5-7	OCT imaging system setup.....	135
5-8	Demonstration of the motion capabilities of the mirror pixels.	136
5-9	Theoretical and experimental far-field Fraunhofer diffraction profile of two adjacent sub-apertures.....	138
5-10	Comparative diffraction patterns of single and two adjacent sub-apertures.	139
6-1	Common piezoelectric multi-morph actuator.....	143
6-2	Numerical calculation of the optimal thickness ratio with fixed PZT thickness.	147
6-3	FEM simulation result showing close match to theoretical calculation result using Eq. (6-7).	149
6-4	PZT-SiO ₂ bimorph deflection upon voltage input.	149
6-5	FEM simulations and theoretical calculations of optimal thickness ratio to achieve maximal bimorph deflection. Simulation: $\zeta=1.60$; Calculation: $\zeta=1.55$	150

6-6	S-Shaped tilt-compensating piezoelectric bimorph actuator design. Voltages with reversed polarities are applied to two top electrodes.	152
6-7	Deflection of piezoelectric FDS bimorph actuators.....	153
6-8	FEA simulation result of the piezoelectric FDS micromirror.	154
6-9	Electrical connections of the top electrodes on one FDS bimorph actuator.....	155
6-10	Cross sectional view of the fabrication process of the piezoelectric FDS micromirror. .	157
6-11	SEM images of the fabricated piezoelectric FDS micromirrors.	158
6-12	Static piston characterization of the piezoelectric FDS micromirror.....	159
6-13	Rotation characterization of the piezoelectric FDS micromirror at resonance. Voltages are applied to the “N” electrodes on one FDS actuator.	160
6-14	Lissajous scanning patterns achieved by the piezoelectric FDS micromirror at resonance frequency.....	161
6-15	Surface quality characterization using Wyko optical profiloemeter.....	161

Abstract of Dissertation Presented to the Graduate School
of the University of Florida in Partial Fulfillment of the
Requirements for the Degree of Doctor of Philosophy

DEVELOPMENT AND APPLICATIONS OF HIGH FILL-FACTOR, SMALL FOOTPRINT
MEMS MICROMIRRORS AND MICROMIRROR ARRAYS

By

Kemiao Jia

December 2009

Chair: Huikai Xie

Major: Electrical and Computer Engineering

This dissertation presents the development and applications of high fill factor (HFF), small footprint micromirror and micromirror array (MMA) devices based on microelectromechanical systems (MEMS) technology. The individual micromirror devices developed in this dissertation are motivated by biomedical imaging, especially endoscopic biomedical imaging applications, where the micromirror serves as the lateral scan engine. The MMA devices presented in this dissertation are mainly focused on the application of optical phased arrays (OPAs), where the individual optical apertures in the MMA device are combined to imitate a much larger optical aperture for a wide range of steering state while maintaining the large steering angle and fast steering speed of each individual optical aperture.

Among the various actuation mechanisms of the micromirrors, this dissertation focuses on the electrothermal (E-T) and piezoelectric (P-E) bimorph actuation methods with E-T method being the primary choice of solution and the P-E method being the secondary. A novel bimorph actuator design will be proposed to solve the drawbacks with existing micromirror designs. Based on this bimorph actuator, three generations of E-T micromirror devices and one generation of P-E micromirror devices has been developed, among which the 2nd-generation E-T micromirror has been successfully implemented for a prototype imaging probe ($\Phi=4.2\text{mm}$) for

commercial dental optical coherence tomography application. The 3rd-generation E-T micromirror devices can offer the highest area fill factor (~60%) among the existing micromirror designs. The footprint of the micromirror devices is also among the smallest (1.45mm×1.55mm). Hence they can be applied for further miniaturization of the imaging probe. The P-E micromirror has been developed based on the Sol-gel PZT fabrication method. They also demonstrated considerably large scanning range at resonance frequency. However, the large residual thermal stress of the PZT layer caused undesired deformation of the bimorph actuator and thus limited the device performance. The HFF MMA devices presented in this dissertation are based on the design of the 3rd-generation E-T micromirror. They provide the largest sub optical aperture size ever reported (1.50mm×1.50mm) and thus can achieve a large equivalent optical aperture (*e.g.* 1.4cm×1.4cm) with only a small number (*e.g.* 64) of sub apertures, which simplifies the control electronics dramatically. This has made the MMA device quite suitable for OPA applications.

Unlike traditional HFF micromirror and MMA devices with single-crystal silicon (SCS) supported optical aperture, the fabrication method of the 3rd-generation HFF micromirror and MMA devices is based on a single Silicon-on-Insulator (SOI) wafer without the need for any bonding transfer processes, which simplified the fabrication, enhanced the yield, and reduced the cost. The design of the 3rd-generation micromirror and MMA device also provides surface mounting and flip chip bonding integration capabilities without the need of through wafer vias, which can further reduce the size of the imaging probe or the OPA system. This design, fabrication and packaging method has applied US patent and is currently being processed.

The dissertation consists of seven chapters. Chapter 1 gives a review of micromirror and MMA devices, their applications and the goal of this work. Chapter 2 first discusses the principle and the modeling methods of electrothermal bimorph actuator. Then, the drawbacks with the

existing microirror designs will be summarized followed by the proposal of the novel bimorph actuator design. Chapter 3 presents the development of the 1st-, 2nd- and 3rd-generation of the E-T micromirror devices based on the proposed bimorph actuator. Chapter 4 focuses on the development of the MMA devices. Chapter 5 discusses the current and future application of the developed micromirrors and MMA devices. Chapter 6 presents the development of P-E micromirror device. Finally, Chapter 7 summarizes the work completed and gives the future research plan.

CHAPTER 1 INTRODUCTION

Micro-Electro-Mechanical Systems (MEMS) are among the fastest growing technology areas. With an average annual growth rate of more than 20%, MEMS industry is expected to reach over \$15 billion by the year 2012 [1]. They not only provide better substitute solutions for many conventional technologies, but also have been proven to be key enabling solutions for new applications in consumer products, health care, military, transportation, and telecommunication industries. Medical/Biomedical instrumentation, automotive industry, and consumer products applications will continue dominate the MEMS market in the near future [1-4]. But as they continue to expand, the applications of MEMS technology can be virtually every where.

Micro-Opto-Electro-Mechanical-System (MOEMS), the marriage of MEMS and micro-optics, has received intensive study and development by various research groups around the world. Its advantages in aspects of functionality, cost-effectiveness, reliability and size over conventional optical systems make them irresistible choices of solutions for many optical problems. Despite the telecom meltdown at the beginning of this century, many of the technologies not only have survived and been successfully commercialized, but also most of the key ideas and technologies are now making a steady and firm comeback. As one of the most important parts of MOEMS research and the one that actually initiated the development of MOEMS, the research of micromirrors has achieved some of the most successful MOEMS devices [3-6].

1.1 MEMS Micromirrors and Micromirror Arrays

By the manners of use, micromirrors can be categorized into two groups: Binary or on/off micromirrors, and analog micromirrors. With the development of the digitized world, the binary micromirrors have seen the most progress and commercialization. They are the key enabling

devices in applications such as information display and communication signal control. One outstanding example is the Digital Light Processing (DLP) MOEMS chips developed by Texas Instruments (TI) [7-11]. With TI's early start and large investment, the DLP chips are currently being used in roughly 50% of the world wide market share of the front projection TVs and in many other applications that are well beyond their early use in digital projectors [3, 12-16].

Analog micromirrors have also received great attentions and encouraging successes over the past two decades. With the ability to steer light beam continuously over a certain range, analog micromirrors are more powerful than binary micromirrors in terms of functionalities. The tradeoff is more complicated structures and more difficult to design and fabricate. As individual devices, analog micromirrors have been successfully commercialized by Intermec and Microvision for barcode reading and mobile projection [17-20]. With the recent upsurge of new biomedical imaging techniques, which include Optical Coherence Tomography (OCT) [21-28], Nonlinear Optical Microscopy (NLOM) [29-33] and Confocal Laser Scanning Microscopy (CLSM) [34-40], individual analog micromirrors device also shows great potential in biomedical endoscopic imaging applications.

As a configured array of devices, analog micromirrors arrays (MMA) can be used for spatial light modulation (SLM) in the same way as the TI's DLP, but with much more flexibility [41-43]. Analog micromirror-based optical switching is also among the most promising solutions for future high-port-count DWDM communication networks [44-46]. Imbedding analog MMA in adaptive optics systems for wave-front reconstruction opens even wider application fields including consumer optics, aero space exploring and homeland security [47-52]. In some applications, such as in free-space laser communication system, where

large optical aperture, large scanning range and swift response are desired, analog MMA can work as optical phased arrays (OPAs) and replace the individual micromirror device [52-56].

Despite the various applications of MEMS analog micromirrors and MMAs, their functionalities can be categorized as information display, information control and information collection. MEMS micromirrors in applications where information is collected through them to the people are generally referred to as MEMS micromirror optical scanners. As optical scanners, MEMS micromirrors redirect light in different directions and collect desirable information from the backscattered light over a continuous range. Applications such as laser barcode reading, endoscopic imaging and Laser Detection & Ranging (LADAR) systems all use MEMS micromirror as optical scanners. Most applications only require the optical scanners to have one or two dimensional in-plane rotations, such as laser barcode scanning and endoscopic imaging [17, 32, 39, 57-59]. However, although not required, it is always desirable to have more degrees of freedom (DOF) in such applications. For instance, the primary purpose of endoscopic imaging scanners is for transverse in-plane scanning. But with piston motion capability, it could ease the optical alignment process dramatically and can also leave adjustment room for working distance. In other applications, *e.g.*, MMA scanners for OPA applications, tip-tilt-piston (TTP) actuation capabilities are required to avoid introducing undesirable phase distortions caused by optical path length difference across an OPA [49, 53, 60-62].

The primary objective of this work is to develop a novel MEMS micromirror-based optical scanner for biomedical imaging, especially for endoscopic biomedical imaging applications. Meanwhile, MEMS MMAs based on the presented micromirror design will also be investigated and implemented for OPA applications. This chapter will discuss different types of MEMS micromirror optical scanners, MMAs and give the organization of this dissertation.

1.2 MEMS Micromirror Optical Scanners

Despite the various designs and applications of MEMS micromirror optical scanner, their common characteristic is continuously steering the light beams over certain ranges. With the understanding of this, the design of MEMS micromirror optical scanners must consider the following design aspects:

1. Number of DOF
2. Device footprint
3. Area fill factor
4. Mirror surface quality
5. Range of beam steering
6. Driving voltage
7. Repeatability and reliability
8. Packaging solutions and cost
9. Bandwidth of operation and
10. Power consumption

Different applications address differently on the above listed design aspects. For instance, for the commercial barcode reading application, it does not put high requirement on DOF or aperture size. But as a consumer product for item identification, it does require low power consumption, high repeatability and reliability, and long term performance guarantee.

On the other hand, for endoscopic biomedical imaging applications, it is desired that the optical scanner to have small device footprint for minimum invasiveness, large and flat optical aperture for high image resolution and easy optical alignment, large scanning range for high imaging efficiency, low driving voltage for safety, reliable performances for high image fidelity, and linear angular and translational scanning characteristics for the ease of signal processing and image interpretation. The requirements of small device footprint and large optical aperture require that the micromirror device to have a high area fill factor, *i.e.* a high area ratio of optical aperture size and the device footprint. To achieve the high image resolution, it is required that the micromirror to have ultra flat mirror plate (radius of curvature $> 0.5\text{m}$). Therefore, micromirror

optical scanners based on stressed thin film reflectors are generally not suitable for imaging applications. Other limitations with thin film based micromirrors include small aperture size and small scanning range. Micromirror optical scanners based on Single-crystal Silicon (SCS) or Silicon-on-Insulator (SOI) wafer use bulk silicon as the base of the mirror plate which can provide wider scanning range, larger aperture size and better mirror flatness and therefore are more preferable for imaging applications.

MEMS micromirror optical scanners have been developed using different actuation mechanisms including electrostatic, electromagnetic, piezoelectric and electrothermal. The first micromirror optical scanner ever reported is developed by Kurt. E. Peterson in 1980 based on electrostatic actuation [63]. It utilizes the electrostatic force between the underlying electrodes and the mirror plate to generate the tilt. This design can achieve $\pm 2^\circ$ optical scan angle at resonance and 300V. More recently developed parallel-plate electrostatic micromirrors are able to achieve larger scan angle up to $\pm 8^\circ$ [64-71]. But the pull-in effect still set limitations to the achievable rotation range. A more popular electrostatic actuation method is using comb drive actuation. Compared to parallel-plate actuators, the comb drive actuators can potentially achieve larger force and have less pull-in instability. The larger force can be utilized to reduce the large actuation voltage which is one of the drawbacks of the electrostatic actuation. The most commonly-used structure for comb drive electrostatic actuators to implement 2-DOF rotation is through gimbaled connections [72-77]. Schenk et al. reported a SOI-based staggered vertical comb drive (SVCD) driven 2-D gimbaled micromirror that can achieve $\pm 5.5^\circ$ mechanical scan angle with 16V at resonance frequency [77]. To avoid the extra steps of trench filling and Chemical Mechanical Polishing (CMP) for electrical isolation, Lee et al. reported a double-device-layer SOI-based gimbaled micromirror with SVCD that can generate $\pm 7.5^\circ$ static optical

deflection angle at 130V [76]. To further increase the actuation range and eliminate the actuation instability caused by lithography misalignment, angular vertical comb drive (AVCD) was proposed [78-81]. Patterson et al. reported a SOI-based AVCD driven micromirror using photoresist reflow process to form the initial tilting of the moving combs [79]. The device is able to generate 18° optical scan angle at resonance with 100V driving voltage. Xie et al. reported a Post-CMOS micromirror using stress induced initial tilting of multiple metal-oxide layers on the CMOS chip to realize an AVCD and achieved $\pm 4.7^\circ$ at 20V [78]. Milanovic et al. proposed a new gimbal-less SOI-based micromirror with SVCD and orthogonally positioned mechanical transformers to realize both tip-tilt and piston motion simultaneously [82, 83]. The static optical deflection for both axis are magnified to $\pm 10^\circ$ with $< 150V$ driving voltage. The same device can achieve a piston stroke of $\pm 30\mu m$ at 130V DC as well. Recently, Tsai et al. also reported a gimbal-less micromirror utilizing radial vertical comb drives and achieved $> \pm 2.3^\circ$ mechanical deflection angle at 61V for both axis. But this device is based on SUMMiT-V surface micromachining process [84].

High speed operation and low power consumption have been the two most important advantages of electrostatic micromirror. However, the high driving voltage and relatively small aperture are still the limiting factors for them to be used in *in-vivo* endoscopic imaging applications. In order to achieve considerable scanning range, large area is usually taken by the electrostatic actuators, which inevitably leads to low area fill factor. To overcome this drawback, effort has been made to hide the actuators underneath the mirror plate using wafer transfer techniques, such as anodic bonding and flip chip bonding. But the extra steps make the fabrications rather complicated, expensive and low-yield. Another drawback of electrostatic micromirror for endoscopic imaging applications is that to generate the scanning angle needed,

the device is usually required to operate at resonance frequency. This gives rise to non-linear beam transfer characteristic which brings extra difficulty to signal processing and causes image distortion. Some effort has been made to linearize the transfer characteristic [85-87]. But the problem is not eliminated.

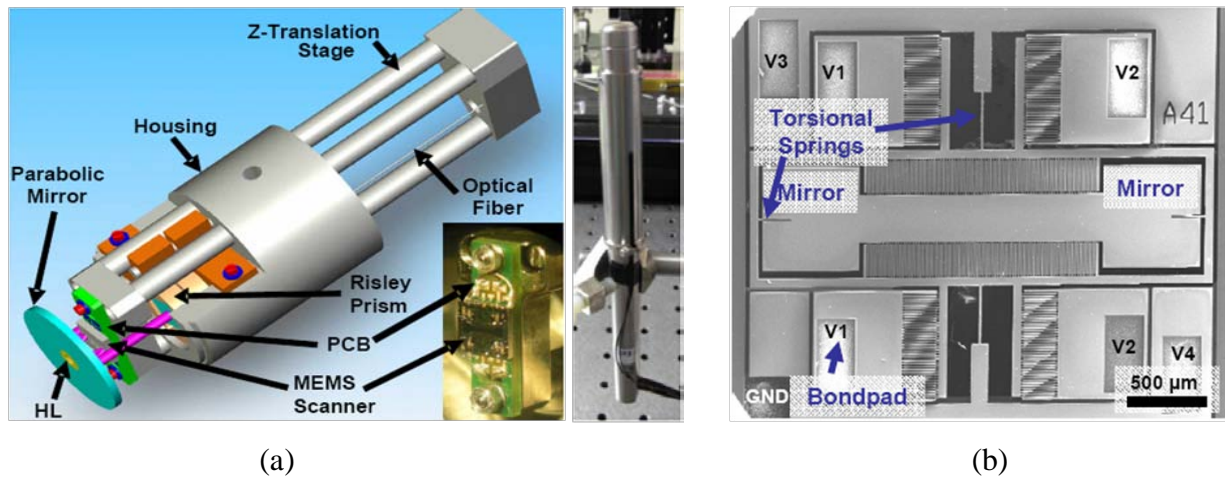


Figure 1-1. Handheld confocal imaging probe reported in [88]. (a) Imaging probe design; (b) Dual-axis electrostatic micromirror.

Imaging catheter designs based on electrostatic micromirrors have been reported. Ra et al. reported a hand held confocal microscope using electrostatic micromirror as the scan engine [39, 88], as shown in Fig. 1-1a. The microscope has a diameter of 10mm and is adapted to skin examination. The micromirror device implemented has a dimension of 3.4mm×2.9mm with a mirror plate of 0.6mm×0.65mm, a fill factor of ~4%, as shown in Fig. 1-1b. The device can provide 5° optical scan angle for both axes at 180V driving signal. Jung and McCormick reported a series of endoscopic OCT imaging probes based on 2-axis electrostatic micromirror device [89, 90]. The smallest probe reported in this series has a diameter of 3.9mm, as shown in Fig. 1-2a. The micromirror device has a dimension of 2.8mm×3.3mm with a circular mirror plate with a diameter of 0.8mm, an area fill factor around ~6.9%. The device can provide 20° optical scan angle for both axes at 100V driving signal. The sizes of the reported probes based on

electrostatic micromirrors are typically limited by the footprint of the micromirror, as shown in Fig. 1-2b. Whereas the minimum device footprint required is eventually decided by the acceptable minimum optical aperture size and the device area fill factor. Another limiting factor of the probe size is the electrical packaging scheme. As shown in Fig. 1-2b, much area is assigned to the copper electrical wires and the bonding wires.

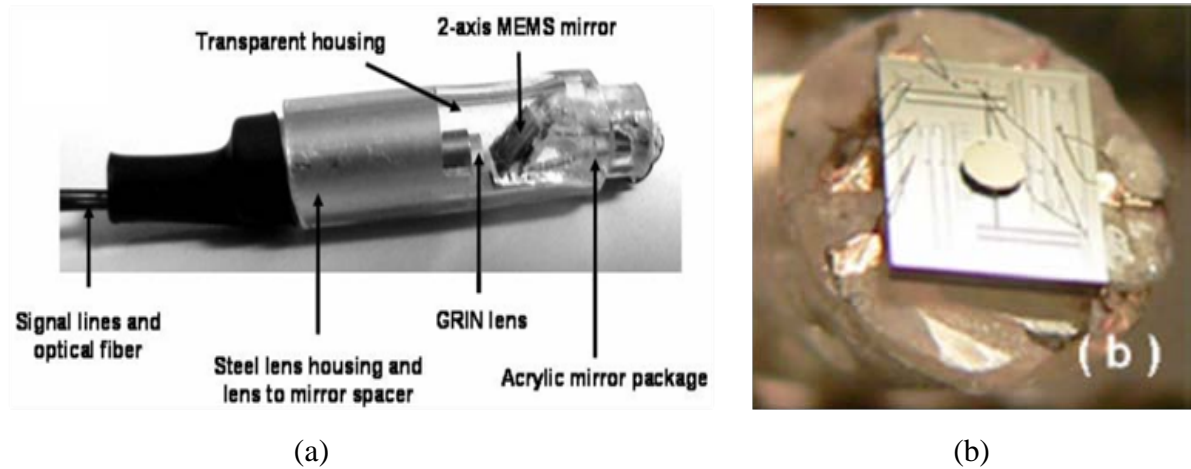


Figure 1-2. Endoscopic OCT imaging probe reported in [89]. (a) Imaging probe design; (b) Electrostatic micromirrors implemented on the probe

Electromagnetic is another popular actuation method. Utilizing the Lorentz Force of current carrier presented in a magnetic field, electromagnetic micromirror controls the motion of the mirror plate by controlling the amplitude and direction of the current [91-96]. The reciprocal characteristic of electromagnetic force can effectively increase the scan range by a factor of 2. Electromagnetic actuators can generate large force with relatively low driving voltage, which allows for large scan range, big aperture size and thick mirror plate. Currently reported electromagnetic micromirror usually employs external magnetic field using permalloy or active electrical coils. Running current conductors are usually embedded in the mirror plate. Ahn et al. reported an electromagnetic micromirror with 2-DOF [93]. The device has a 3.5mm×3.5mm aperture size and can achieve 1.5° of optical deflection angle at 2.2K Hz resonance with 20mA.

To avoid the complex current routing, Yang et al. exploited eddy current to generate the Lorentz Force and achieved 20° resonant optical deflection angle on a $2\text{mm}\times 2\text{mm}$ mirror plate with 9mW power input [92]. Yalcinkaya et al. demonstrated an electromagnetic micromirror with a $1.5\text{mm}\times 1.5\text{mm}$ aperture size [91]. The device performed up to 60° of optical scan angle at resonance with 140mA input. Despite the multiple virtues that electromagnetic micromirror has, including large aperture size, high speed operation and large scan angle, it still suffers from a relatively low area fill factor due to the need of large amount of electric wirings. Electromagnetic mirrors also need external magnet to realize the actuation. Although efforts have been made to replace the external magnet with on-chip coil induced magnetic field, the electromagnetic performance was much inferior compared with external ones. The need for the external magnets greatly complicates the catheter design for endoscopic imaging applications. Fig. 1-3 shows an endoscopic OCT imaging probe developed by Draper lab based on electromagnetic micromirror [97]. The probe has an outer diameter of 2.8mm and a length of 12mm . The electromagnetic mirror has a dimension of $2.4\text{mm}\times 2.9\text{mm}$ with a $0.6\text{mm}\times 0.8\text{mm}$ mirror plate, a fill factor of 6.9% , as shown in Fig. 1-3b. The device can achieve $\pm 30^\circ$ optical scan angle at 2V driving voltage for both axes. The size of this probe is limited by two factors. The first factor is the footprint of the micromirror device, which is limited by the acceptable optical aperture and the device fill factor. The second factor is the complicated probe design which is caused by the need of the external magnet, as shown in Fig. 1-3a.

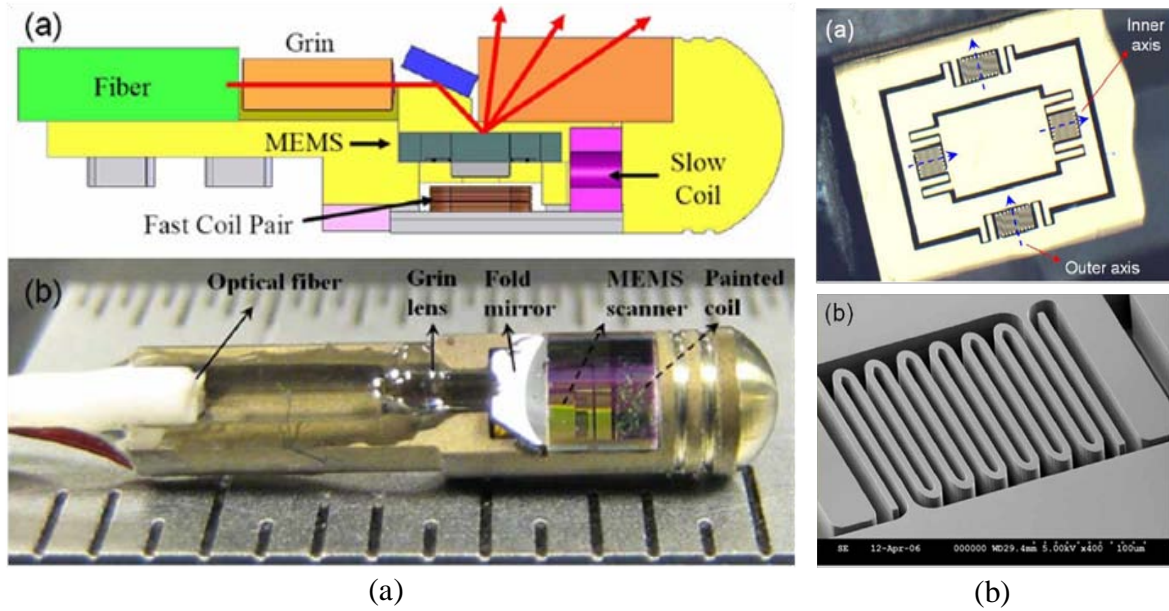


Figure 1-3. Endoscopic OCT imaging probe reported in [97]. (a) Imaging probe design; (b) Dual-axis electromagnetic micromirrors

Piezoelectric micromirror did not start to thrive until the development of thin film piezoelectric materials, such as Lead-Zirconium-Titanium-Oxide (PZT), reaches an applicable state [98-110]. Cantilever PZT structures have been proposed for micromirror actuation, which can realize tip-tilt motion as well as piston at lower voltage input than electrostatic method [111-121]. Kueppers et al. reported a silicon based PZT thin film cantilever prepared by chemical solution deposition (CSD) method [113]. The 390 μm long cantilever showed tip displacement of 20 μm at only 10V DC actuation. Park et al. reported a 1-DOF piezoelectric micromirror with a hinged structure [121]. The PZT film was prepared directly on a stainless steel substrate by aerosol deposition method (ADM). 40 $^\circ$ of optical scan angle has been achieved at resonance with 60V driving signal. A 2-DOF piezoelectric micromirror has been demonstrated by Tani et al. using Arc Discharge Reactive Ion Plate (ADRIP) method [117]. It cascades cantilever PZT morphs in a meandering shape to accumulate angular displacement. The device achieved static mechanical rotation angle of $\pm 8^\circ$ with less than 20V. Fast response, extremely low power

consumption, and large angular displacement make piezoelectric micromirror a favorable choice for endoscopic imaging applications. However, charge leakage, temperature dependence and hysteresis characteristic of the material set additional challenges to use this method for scanning.

Electrothermal micromirror based on electrothermal bimorph actuator is the only type of micromirror that has demonstrated TTP actuation capacities with considerably large operation ranges and area fill factor [122-134]. Although electrothermal micromirror is typically slow and consumes relatively high power, its advantages for endoscopic biomedical imaging applications are also obvious. It has large actuation force which allows the actuations of large, thick mirror plate. It also has the simplest structure design and fabrication process which allows for greater design flexibility and potentially high area fill factor. It allows for thin film and bulk micromachining integration without extra bonding process. It also can be integrated with CMOS easily. These advantages guarantee the performances for the first eight design aspects listed at the beginning of Section 1.2 which make them ideal choice for biomedical imaging applications, especially for endoscopic imaging applications in which operating frequency is not very high and power consumption is not critical. Electrothermal actuators based on various materials have been reported. Ataka et al. reported a bimorph actuator based on dual-layer-polyimide material for micromotion systems [133]. Yang et al. reported a precise tracking positioner based on SiO₂/Doped Silicon bimorph actuator [129]. Singh et al. demonstrated an electrothermal micromirror also based on SiO₂/Doped Silicon bimorph actuator [127]. The device has 0.5mm×0.5mm aperture size and can achieve 16° optical deflection at 1.6V DC and close to 200µm piston stroke at 1V DC. A more favorable electrothermal bimorph material combination is Al/SiO₂. Bühler et al. first reported a CMOS micromirror based on Al/SiO₂ bimorph actuator [134]. Jain et al. demonstrated both 1-DOF and 2-DOF micromirror with up to ±30°

optical scan angle at less than 15V [123]. Piston stroke of about 0.5mm at 15V was also achieved with this device. The devices reported are based on Post-CMOS MEMS process and use the Al/SiO₂ layer as the bimorph materials with embedded Poly Silicon as the heater material. Wu et al. demonstrated an Al/SiO₂ bimorph based TTP micromirror on SOI wafer [128]. The device has an aperture size of 1mm×1mm aperture size and performed 0.6mm piston stroke at 5.5V and ±30° static optical scan angle at less than 5V.

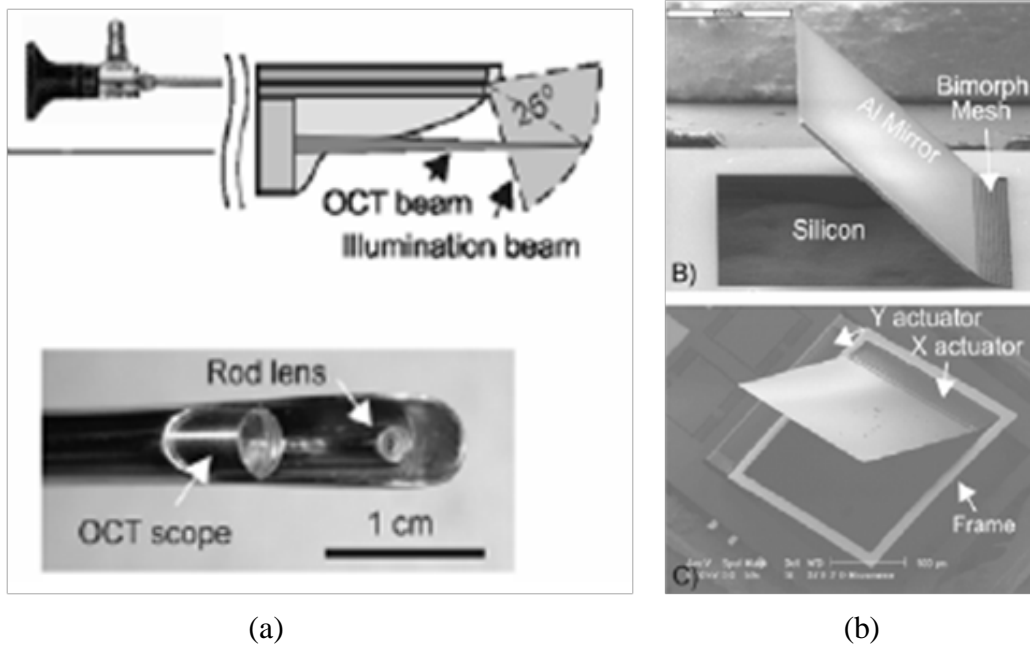


Figure 1-4. Endoscopic OCT imaging probe reported in [135]. (a) Schematic of the imaging probe; (b) Single and dual-axis electrothermal micromirrors

Endoscopic imaging probes based on electrothermal micromirror have been reported. Pan et al. reported an endoscopic OCT image probe using CMOS-MEMS electrothermal micromirror. The probe has an outer diameter of 5.8mm [135], as shown in Fig. 1-4a. The micromirror has a dimension of 2.2mm×2.9mm with a mirror plate of 1mm×1mm, an area fill factor of 16%, as shown in Fig. 1-4b. This device can achieve a typical optical scan range around 40° at 5V for both axes. Xu et al. reported an OCT probe also based on electrothermal

micromirror [136]. The probe has a diameter of about 4mm and a length of 25mm, as shown in Fig. 1-5a. The micromirror device is 1.5mm×1.5mm with a circular mirror plate of 0.5mm in diameter, an area fill factor of around 10%, as shown in Fig. 1-5b. An optical scan range of 40° has been achieved at 1.4V. Morrish et al. reported an endoscopic multi-photon imaging probe, as shown in Fig. 1-6a, with a diameter of 5.0mm [137]. The electrothermal micromirror device implemented in this probe has a dimension of 2.0mm×2.0mm with a mirror plate of 1.0mm×1.0mm, an area fill factor of 25%, as shown in Fig. 1-6b. The device achieved an optical scan angle of 30° for both axes at less than 6V.

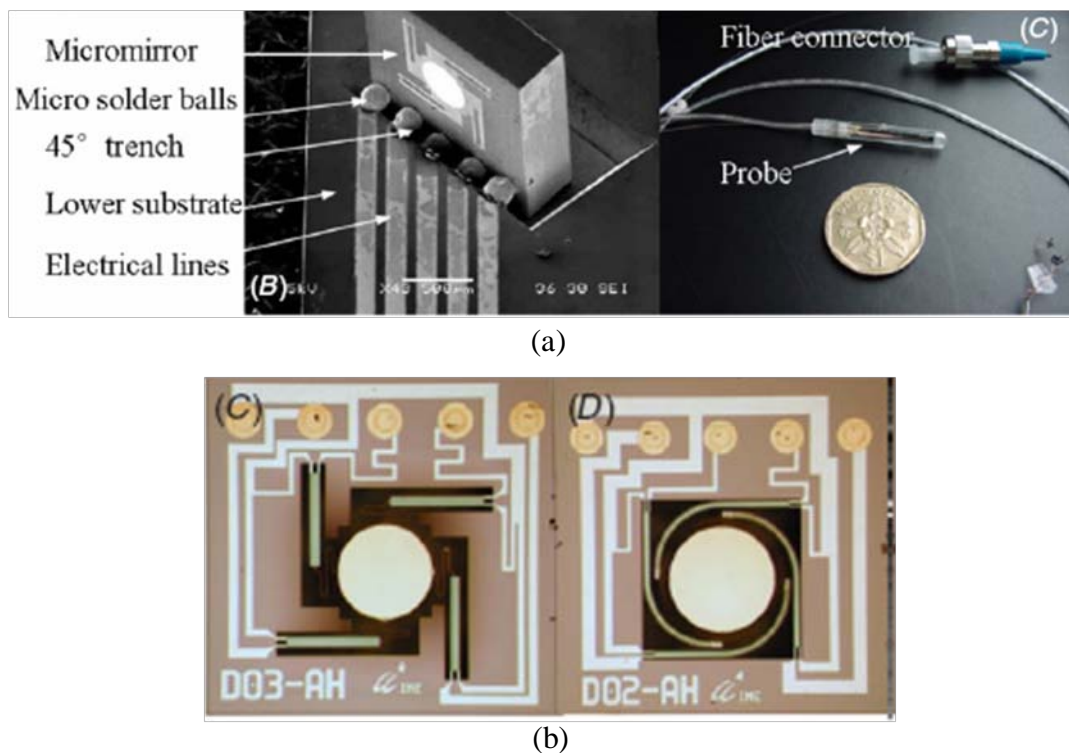


Figure 1-5. Endoscopic OCT imaging probe reported in [136]. (a) Packaging and development of the probe; (b) Dual-axis electrothermal micromirrors.

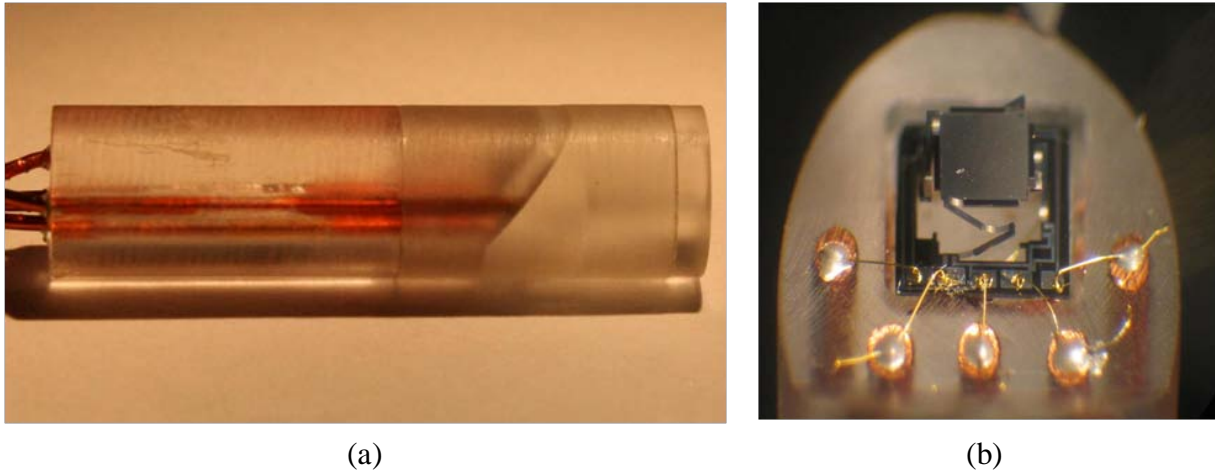


Figure 1-6. Endoscopic Multi-photon imaging probe reported in [137]. (a) Probe after packaging; (b) Dual-axis electrothermal micromirrors inside the probe.

To summarize the above review of the existing types of micromirrors and their applications in biomedical imaging probes, electrostatic micromirrors typically have the lowest area fill factor, the smallest scanning range and the highest driving voltage, and thus are least suitable for the application of endoscopic biomedical imaging. Electromagnetic micromirrors have relatively higher area fill factor, larger scanning range and lower driving voltage. Small probe with a diameter of 2.8mm has been reported in [97] based on electromagnetic micromirror. However, the still low area fill factor and the need for a complex design and integration prohibit further miniaturization and a cost-effective imaging probe. In comparison, electrothermal micromirrors have the highest area fill factor, largest scanning range and the lowest driving voltage, and thus best meet the requirements for endoscopic imaging applications.

However, a few factors still prevent further miniaturization of electrothermal micromirrors based imaging probes. Firstly, the area fill factor, although higher than that of the other actuation mechanisms, still leaves large room for improvement. Secondly, the electrical interconnections inside the probe are occupying a large area as well, as shown in Fig. 1-6b. Therefore, one of the objectives of this work is to develop micromirror devices with ultra-high area fill factor, simple

electrical packaging method such that further miniaturization of the probe can be realized. Due to the advantages summarized above, electrothermal actuation is the primary choice of solution in this dissertation. The design and development of such micromirror devices will be discussed in Chapter 3.

1.3 MEMS Micromirror Arrays

MEMS micromirror arrays (MMAs) are key enabling devices for applications where spatial light modulation and modification is needed such as optical communication network management, digital display, adaptive optics systems, free space laser communication, laser detection and ranging (LADAR) and maskless lithographies [49-53, 55, 60-62, 138-146]. In application such as LADAR and free-space laser communication systems where large, flat combined optical aperture, large steering angle, and fast response time are desired, it is necessary to divide the large aperture of the scanner to an array of individually addressable scanners with smaller aperture size, *i.e.*, an optical phased array (OPA), to reduce the inertia that need to be actuated and hence boost the response time [52, 53, 55, 60-62] as well as the achievable steering angle. Conventional OPAs are based on liquid crystals [142-144]. But they generally have small aperture size, small scan range, phase distortion and material dispersion problems, which can be effectively solved by MEMS MMAs.

MEMS MMAs can be implemented for OPA applications via a variable blaze approach [56], for which some requirements must be met. First of all, due to the need of ultra-high power laser in many OPA applications, the MMA device must provide high reflectivity to prevent the device from being drastically heated up, which demands the MMA device to have a high area fill factor. It is also important to have HFF in order to achieve high SNR and a compact system design. Secondly, the combined optical aperture must be large enough to maintain the laser beam coherent in a long distance. Thirdly, the individual mirror element in a MMA device

must be uniform in optical and mechanical characteristic to avoid phase discontinuity across the entire optical aperture. Other preferable characteristics of MMA device for OPA application includes large scan angle for large number of steering states and large individual mirror elements, or sub-apertures. Large sub-aperture will help achieve the required combined optical aperture with minimum number of elements, which will simplify the driving electronics and ease the control the uniformity among sub-apertures.

So far, HFF MMA device have been developed based on electrostatic and electrothermal actuation mechanisms. Both actuation methods achieve HFF by hiding the actuator underneath the mirror plate. Electrostatic MMA devices are either based on thin film micromachining technology or bulk silicon micromachining technology. With the advanced development of thin film micromachining technologies such as Sandia's SUMMiT-V and MEMSCAP's MUMPs, thin film based MMAs can easily implement hidden actuators and achieve ultra-high fill factor. Krishnamoorthy et al. reported a 1×4 MMA device based on MUMPs process. The device achieved less than 1° of deflection angle at 25V, $100\mu\text{m} \times 200\mu\text{m}$ sub-aperture size. The area fill factor is unspecified. Tsai and Wu reported a 1×10 HFF MMA device with TTP scan capability based on SUMMiT-V process. The device achieves an area fill factor of 98%, $\pm 13.4^\circ$ optical scan angle at 75V, and a sub-aperture size of $196\mu\text{m} \times 196\mu\text{m}$. Since the mirror plate of SUMMiT-V and MUMPs MMA is usually based on stressed thin film, the size of the mirror plate, or the sub-aperture size is limited in order to maintain acceptable radius of curvature. The achievable scan range in thin film based MMA is also structurally limited.

Bulk silicon based electrostatic MMAs do not have the above limitations. However, in order to hide the actuators under the SCS-supported mirror plate, additional wafer transfer steps are needed which greatly complicate the fabrication process, making it low yield and expensive.

Jung et al. reported a 5×5 electrostatic MMA based on SOI bulk micromachining [72]. Each mirror is 360μm×360μm in size and can tip tilt 1.8°, piston 70nm at 180V, as shown in Fig. 1-7. The fill factor of the MMA region is 99%. This device requires a four-wafer fabrication process with two chemical mechanical polishing (CMP) steps, two anodic bonding steps, and one flip chip bonding step. Milanovic et al. reported a 2×2 MMA with 400μm×400μm sub-aperture size, 90% area fill factor on MMA region, and 15° of optical deflection at 102V [82]. The device is based on a three-wafer fabrication process with one anodic bonding step, one CMP step and one manual pick-and-place step to assemble the mirror plate. The device before and after mirror plate assembling is shown in Fig. 1-8a and Fig. 1-8b, respectively. Recently, Kim et al. reported an 8×8 MMA with 340μm×340μm sub-aperture size and an area fill factor of 84% at the MMA region, as shown in Fig. 1-9 [146]. Each mirror is capable of less than 5° optical deflection at 60V. The device fabrication requires totally three wafers, two anodic bonding and CMP steps.

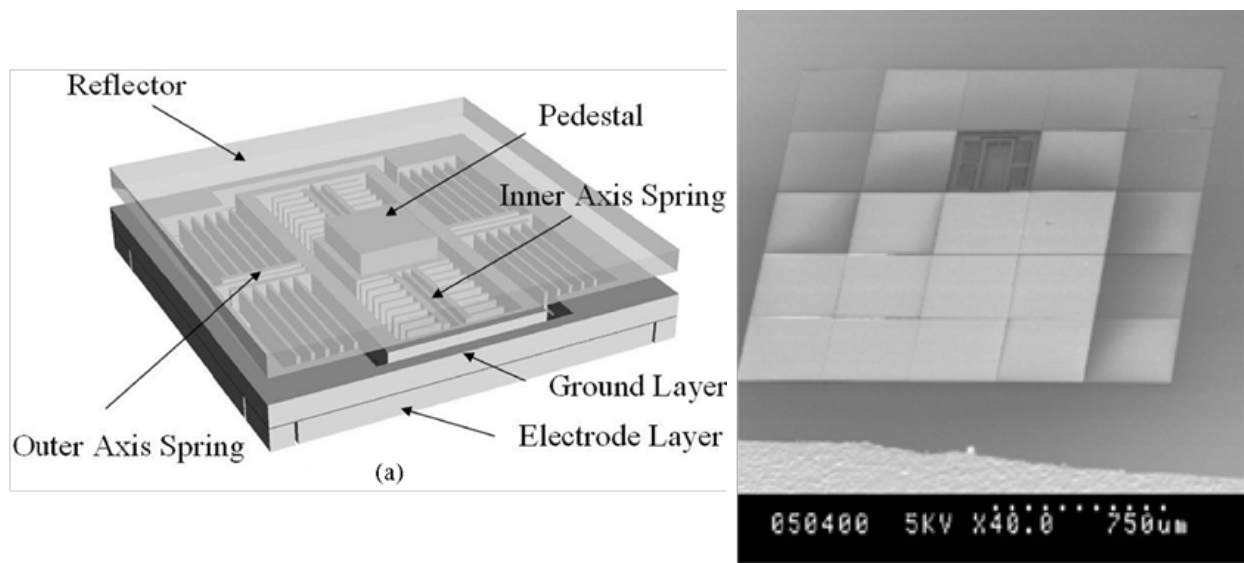


Figure 1-7. 3D schematic and SEM images of the reported MMA device in [72].

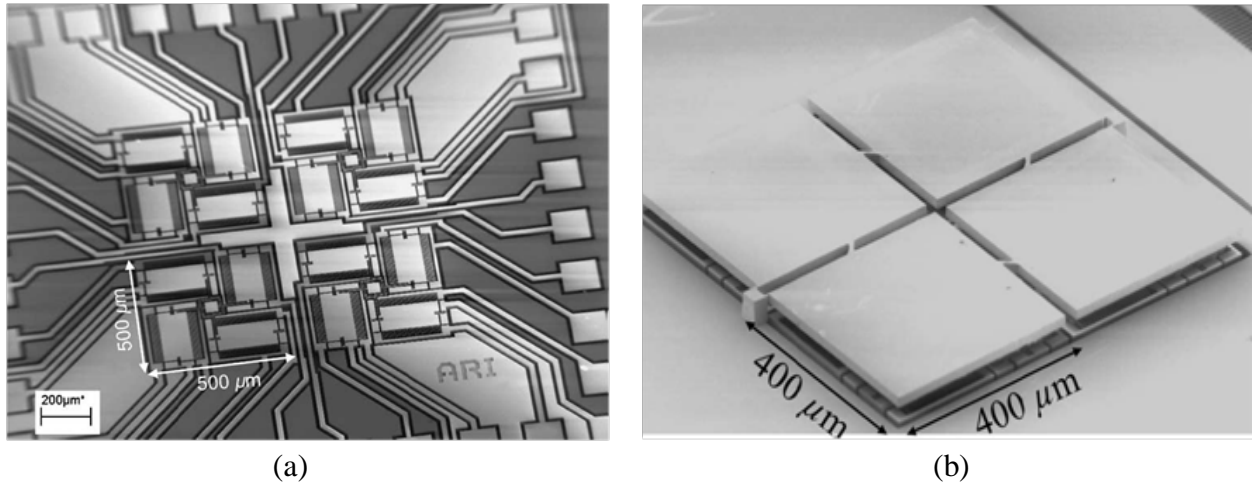


Figure 1-8. MMA device reported in [82]. (a) Before mirror plate assembling; (b) After mirror plate assembling

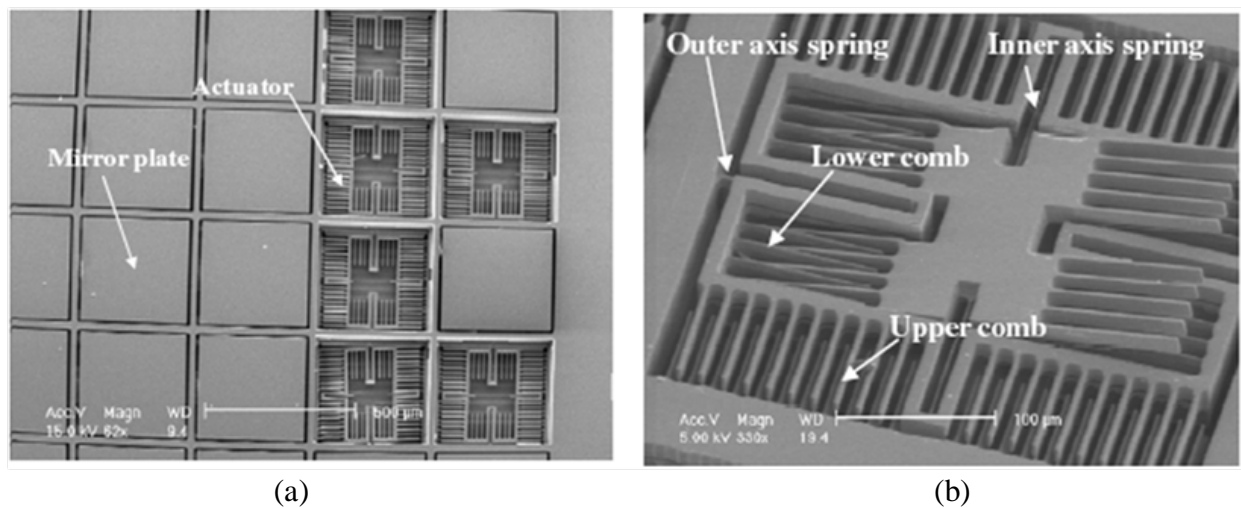


Figure 1-9. SEM images of the MMA device reported in [146] (a) MMA device top view; (b) Actuator underneath

Electrothermal MMAs have also been reported. Wu et al. demonstrated a 4×4 electrothermal bimorph actuated MMA based on SOI wafer [61]. Each sub-aperture is 0.5mm×0.5mm in size and can achieve $\pm 30^\circ$ optical deflection and 215μm piston stroke all at less than 5V. This device is based on a single SOI wafer fabrication process. Because this design did not implement hidden actuators, the area fill factor on the MMA region is less than 50%, as shown in Fig. 1-10. Gilgunn et al. recently presented a 3×3 SOI-CMOS-MEMS electrothermal

MMA with bimorph actuators [145]. The device, shown in Fig. 1-11, achieved an area fill factor of 95% with sub-aperture size of 1mm×1mm. It can perform 1-D rotation up to 90° with < 3V actuation signal. The fabrication process of this design requires one CMOS-MEMS actuator chip and one SOI wafer for fabricating the mirror plate. The two parts are integrated together using a flip-chip bonding process.

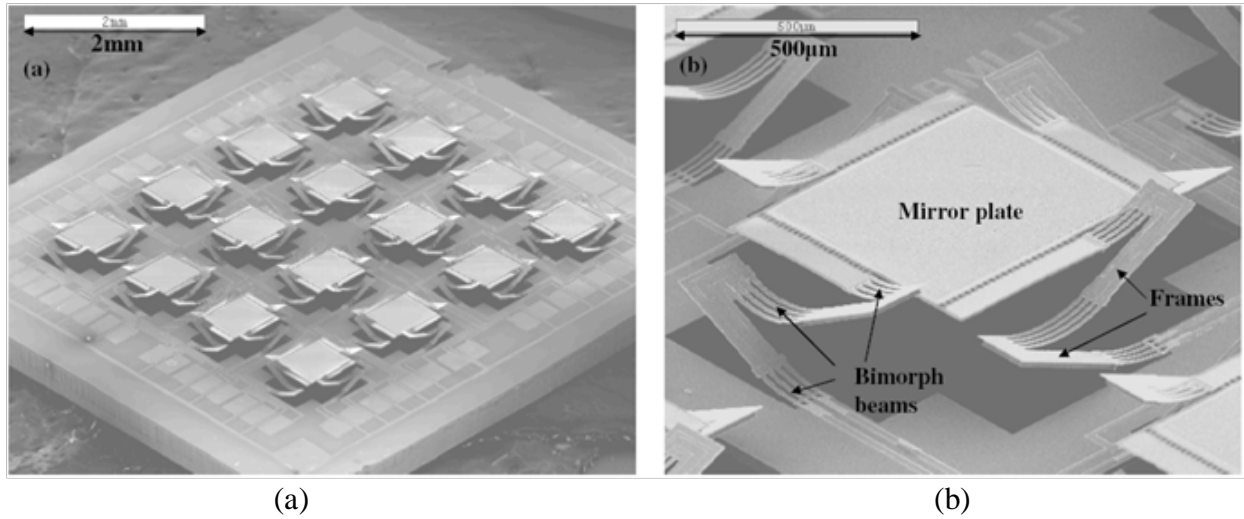


Figure 1-10. SEM images of the MMA device reported in [61] (a) MMA device; (b) One sub-aperture.

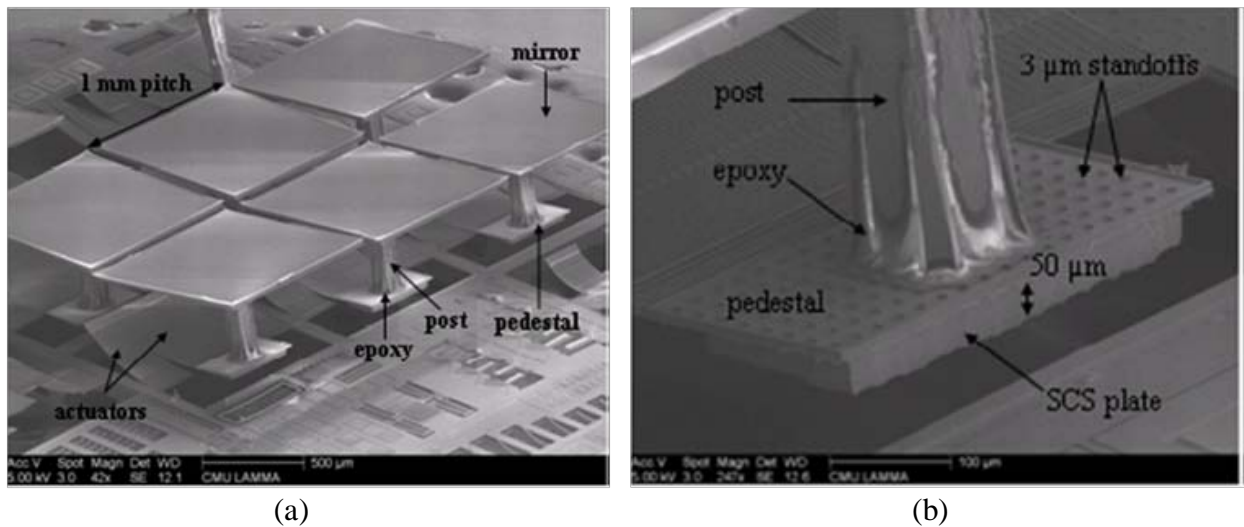


Figure 1-11. SEM images of the MMA device reported in [145] (a) Top view of the MMA device after integration; (b) Zoom-in image of the flip-chip gluing point on the actuator.

To summarize the above review on the current development of MMA devices, for electrostatic MMAs, thin-film based devices still suffers from limited mirror surface quality, limited sub-aperture size, and small steering angle. In order to achieve a considerably large combined optical aperture with good surface quality, thin film-based MMAs usually need to limit the sub-aperture size to $< 100\mu\text{m}$ and combine a large number of sub-apertures. This will require stringent control of process variations and complex electronics to drive the large number of sub-apertures. On the other hand, electrostatic MMAs with bulk single-crystal silicon (SCS) supported mirror plates can achieve large sub-apertures, but require either multiple bonding/polishing processes or manual assembling process which makes the fabrication of the device rather expensive yet low-yield. More over, both thin film and bulk SCS-based MMAs suffer from small steering angle.

For eletrothermal MMAs, large aperture size and scanning range are still favorable virtues. Yet Wu's design still suffers from a low area fill factor in order to be implemented for OPA applications. For Gilgunn's device, although it provided an interesting fabrication method, but it still need a flip-chip bonding step to transfer the mirror plate to the actuators and the design itself suffers from un-stationary rotation axis which will cause conflict between neighboring elements during actuation.

Currently, no simple and scalable solutions have been proposed to resolve MMAs with high fill factor, SCS-supported large sub-apertures and TTP actuation capabilities for neither electrostatic nor electrothermal actuation methods. This leads to the other objective of this work. In this dissertation, one such solution based on electrothermal bimorph actuation method will be presented. Detailed discussion of this solution and the experimental result achieved so far will be presented in Chapter 4.

1.4 Dissertation Outline

The organization of this dissertation is as follows. There are seven chapters in this dissertation. Chapter 1 gives an introduction and motivation of this work, including background introduction and comprehensive literature reviews of MEMS micromirrors and MMAs. Chapter 2 will first present in detail the principle of electrothermal bimorph actuation. Then, the finite element analysis (FEA) and lumped element method (LEM) modeling modalities will be introduced and applied to analyze the characteristics of a cantilevered bimorph actuated 1-D micromirror. These two modeling methods will be frequently used in later chapters. Finally, previous designs of electrothermal micromirrors will be reviewed. In Chapter 3, a novel Folded Dual S-shaped (FDS) electrothermal actuator design concept will be presented to solve the existing problems of the electrothermal micromirror design, followed by the experimental results of the 1st- and 2nd-generation of the FDS devices. In Chapter 4, a novel design and fabrication method will be implemented for the 3rd-generation FDS micromirror and MMA device to achieve ultra-high area fill factor. Chapter 5 will focus on the application efforts based on the developed micromirror and MMA devices. Chapter 6 will discuss the operation principle of piezoelectric bimorph actuation and the development of the micromirror devices based on piezoelectric actuation. Based on Sol-gel PZT fabrication method, a piezoelectric version of the FDS micromirror will be discussed. The design, fabrication as well as the experimental result achieved so far for the piezoelectric micromirror will be presented and discussed. Finally, Chapter 7 will give the summary of this work and future plan.

CHAPTER 2 ELECTROTHERMAL BIMORPH ACTUATION

As an introduction to electrothermal actuation and a basis for the followed content of this dissertation, this chapter will discuss the theory and operation principle of electrothermal bimorph actuators. Some modeling modalities will be included later in this chapter. A detailed discussion of some earlier electrothermal micromirror designs will be presented at the end of this chapter.

2.1 Stress, Strain and Electrothermal Bimorph Actuator

A uniformly formed single layer thin film by itself, without any boundary constrains, is free of stress because of its natural pursuit of lowest potential energy. But when the thin film is grown, deposited or bonded to a substrate or any other thin films, stress arises from the contacting surface [147, 148]. This type of stress is called growth stress, or intrinsic stress, which is strongly dependent on the materials involved, process temperature and environment conditions. The presence of the intrinsic stress implies that if the thin film is freed from constrains set by the substrate or the neighboring layer, it would change its in-plane dimensions or it would change its radius of curvature.

Stress induced after the thin film growth, deposition or bonding is referred to as extrinsic stress which can arise from changes in the physical environment of the thin film including temperature, force, material phase, etc. Applying extrinsic stress to the thin film would also change its dimensions or the radius of curvature. The electrothermal bimorph actuation method can be then described as: To use the growth or intrinsic stress to determine the initial rest position of the object of interest, and use Joule heating to generate thermally induced extrinsic stress and realize the actuation.

In terms of physical behavior, stress can be categorized into two types. For stress that results in a positive strain, *i.e.*, the thin film has a tendency to contract, it is called tensile stress. While for stress that causes a negative strain, *i.e.*, the thin film has a tendency to expand, it is called compressive stress. In the following discussion and analysis, we will follow the convention such that tensile stress and its strain will have a sign of positive, while compressive stress and its strain will have a sign of negative.

Before the principle of electrothermal bimorph actuation is discussed, some assumptions concerning the structure and deformation of the bimorph are invoked and are presented as follows:

1. The films deform within the elastic limit for all materials involved;
2. The elastic properties of the materials involved are temperature invariant;
3. Localized edge effects around the boarder of the films are ignored.

2.2 Principle of Electrothermal Bimorph Actuation

An electrothermal bimorph structure consists of a stack of two layers of thin-film materials with different coefficients of thermal expansion (CTEs). The simplest bimorph actuator is a single cantilevered bimorph beam, shown in Fig. 2-1. The cantilevered bimorph beams can be intelligently connected together to form more complicated bimorph actuators. But the basic principle of electrothermal bimorph actuation can be drawn from this basic building block.

As the thin films in a bimorph undergo internal or external changes, *e.g.*, thermal expansion, phase transformation or other physical effects, the strain generated in each thin film is different if the two thin films are freed of the constrain imposed by each other. This difference in their strain development is referred to as the strain incompatibility or strain mismatch within the bimorph when it is considered as a unity [148]. This strain mismatch is also subjected to both intrinsic and extrinsic factors, which can be written as:

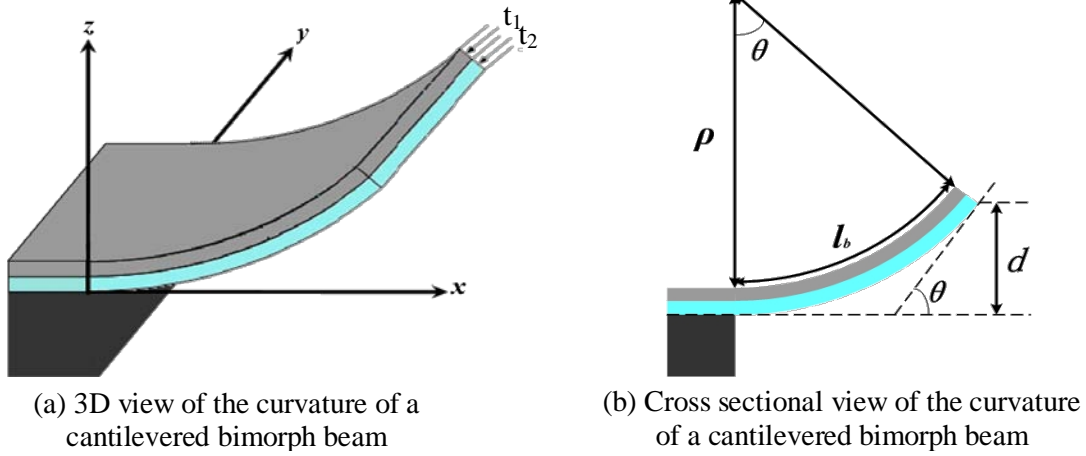


Figure 2-1. Structural views of a cantilevered bimorph beam

$$\Delta \varepsilon = \Delta \varepsilon_{in} + \Delta \varepsilon_{ex} \quad (2-1)$$

in which $\Delta \varepsilon_{in}$ and $\Delta \varepsilon_{ex}$ represent the intrinsic and extrinsic stress induced strain mismatch, respectively. The quantitative study of intrinsic stress has not been developed as well as that of the extrinsic stress. Factors include grain coalescence, vacancy annihilation, impurity incorporation and structure damage due to energetic deposition process all contribute to the development of intrinsic stress. However, we do understand that an important part of the intrinsic stress is thermally induced by the temperature change during and after the growth of the film. While the extrinsic stress, for our analysis interest, is purely caused by Joule heating. Therefore, we can rewrite Eq. (2-1) as:

$$\Delta \varepsilon = \underbrace{\Delta \varepsilon'_{in}}_{\substack{\text{Intrinsic} \\ \text{For initial rest position}}} + \underbrace{\Delta \varepsilon_{th_p}}_{\substack{\text{Extrinsic} \\ \text{For actuation}}} + \underbrace{\Delta \varepsilon_{th_j}}_{\substack{\text{Extrinsic} \\ \text{For actuation}}} = \underbrace{\Delta \varepsilon'_{in}}_{\text{Not well understood}} + \underbrace{\Delta \varepsilon_{th_p} + \Delta \varepsilon_{th_j}}_{\text{Thermally induced}} \quad (2-2)$$

where $\Delta \varepsilon_{th_p}$ represents the strain mismatch induced by temperature change during and after growth process of the film, while $\Delta \varepsilon_{th_j}$ represents the strain mismatch induced by Joule heating.

Since $\Delta\varepsilon_{th_p}$ and $\Delta\varepsilon_{th_j}$ are both thermally induced, we can temporarily set aside the difference in terms by assuming $\Delta\varepsilon_{th}$ as the strain mismatch between the two thin film layers. Given the structure parameters of the bimorph beam, the inverse of radius of curvature caused by $\Delta\varepsilon_{th}$ has been readily derived as [149, 150]:

$$\frac{1}{\rho_{th}} = \frac{\beta_b}{t_1 + t_2} \Delta\varepsilon_{th} \quad (2-3)$$

where ρ_{th} is the beam radius of curvature, t_1 and t_2 are the thickness of the top and bottom layers respectively. β_b is called the curvature coefficient of the bimorph combination, which is given by:

$$\beta_b = 6 \frac{(1 + \frac{t_1}{t_2})^2}{\frac{E'_1}{E'_2} \cdot \frac{t_1^3}{t_2^3} + 4 \frac{t_1^2}{t_2^2} + 6 \frac{t_1}{t_2} + 4 + \left(\frac{E'_1}{E'_2}\right)^{-1} \cdot \left(\frac{t_1}{t_2}\right)^{-1}} \quad (2-4)$$

where E'_1 and E'_2 are the biaxial elastic modulus for each material and is determined by the elastic modulus and Poisson ratio, as Eq. (2-5):

$$E'_i = \frac{E_i}{1 - \nu_i} \quad i = 1, 2 \quad (2-5)$$

When the top layer is much thinner than the bottom layer, *i.e.*, the case when a thin film is deposited on a bulk substrate, plugging Eq. (2-4) into Eq. (2-3) with the assumption of $\frac{t_1}{t_2} \rightarrow 0$ renders [147]:

$$\frac{1}{\rho_{th}} = 6 \frac{E'_1 t_1}{E'_2 t_2^2} \Delta\varepsilon_{th} \quad (2-6)$$

which is the well-known *Stoney Formula*, a special case of Eq. (2-3).

With the radius of curvature derived as Eq. (2-3), the tangential angle at the tip of the bimorph beam θ_{th} , can be laid out from geometry:

$$\theta_{th} = \frac{l_b}{\rho_{th}} = \frac{\beta_b}{t_1 + t_2} \Delta \varepsilon_{th} l_b \quad (2-7)$$

in which l_b is the length of the bimorph beam.

With θ_{th} derived as such, we can look back to Eq. (2-2) and consider the strain mismatch $\Delta \varepsilon_{th_p}$ and $\Delta \varepsilon_{th_j}$ separately.

Extrinsic thermally induced strain $\Delta \varepsilon_{th_j}$ is introduced by Joule heating only after the two films have been deposited. Therefore, the theoretical value of $\Delta \varepsilon_{th_j}$ is only decided by the temperature change and the difference between the CTEs of the two materials. Assuming the temperature rise after Joule heating is ΔT_j , α_1 and α_2 are the CTEs of the top and bottom material, then the thermal-expansion-induced strain mismatch between the top and bottom layer, $\Delta \varepsilon_{th_j}$, can be expressed as:

$$\Delta \varepsilon_{th_j} = (\alpha_1 - \alpha_2) \Delta T_j \quad (2-8)$$

Inserting Eq. (2-8) into Eq. (2-7) renders the angular actuation capacity due to the Joule heating, as shown in Eq. (2-9):

$$\theta_{th_j} = \frac{l_b}{\rho_{th_j}} = \frac{\beta_b}{t_1 + t_2} \Delta \varepsilon_{th_j} l_b = \frac{\beta_b l_b}{t_1 + t_2} (\alpha_1 - \alpha_2) \Delta T_j \quad (2-9)$$

Eq. (2-9) also implies that if we swap the layer composition bottom to top, the same Joule heating will result in reversed angular actuation with the same magnitude.

An assumption that holds the above analysis true is that the temperature rise due to Joule heating is uniformly distributed along the bimorph beam and results in constant radius of curvature. However, this assumption is in most cases invalid. The radius of curvature varies along the bimorph beam and the bimorph tip tangential tilting angle is actually an accumulation of curvature changing, *i.e.*,

$$\theta_{th_j} = \int_0^{l_b} \frac{dx}{\rho_{th_j}(x)} = \frac{\beta_b l_b}{t_1 + t_2} (\alpha_1 - \alpha_2) \left[\frac{1}{l_b} \int_0^{l_b} \Delta T_j(x) dx \right] = \frac{\beta_b l_b}{t_1 + t_2} (\alpha_1 - \alpha_2) \overline{\Delta T_j} \quad (2-10)$$

in which $\overline{\Delta T_j} = \frac{1}{l_b} \int_0^{l_b} \Delta T_j(x) dx$ is the average temperature rise above the ambient temperature along the bimorph beam. Eq. (2-10) provides the guiding equation for angular actuation of the cantilevered bimorph due to Joule heating. One can have the conclusion that the actuation angle is linearly proportional to the average temperature rise on the bimorph.

The analysis of intrinsic thermally induced strain $\Delta \varepsilon_{th_p}$ is more complicated than that of $\Delta \varepsilon_{th_j}$ since it is developed from accumulative processes. Initially, the bottom layer thin film is grown or deposited on the substrate material at temperature T_2 other than ambient temperature or room temperature T_0 , producing a thermal residual strain on the bottom layer thin film $\varepsilon_{th_p_2}$:

$$\varepsilon_{th_p_2} = -(\alpha_2 - \alpha_s)(T_2 - T_0) = -(\alpha_2 - \alpha_s)\Delta T_2 \quad (2-11)$$

in which α_s is the CTE of the substrate material.

Then, the top layer thin film is grown or deposited on the bottom layer thin film at a different temperature T_1 other than ambient temperature. However, because the substrate dominates the change in dimensions, the thermal strain developed in the top layer thin film is still imposed by the substrate, which is expressed as:

$$\varepsilon_{th_p_1} = -(\alpha_1 - \alpha_s)(T_1 - T_0) = -(\alpha_1 - \alpha_s)\Delta T_1 \quad (2-12)$$

Therefore, as the substrate constrain is removed, the top and bottom layer thin film will develop a strain mismatch equals to the difference between Eq. (2-11) and Eq. (2-12):

$$\Delta \varepsilon_{th_p} = \varepsilon_{th_p_1} - \varepsilon_{th_p_2} = -(\alpha_1 \Delta T_1 - \alpha_2 \Delta T_2) + \alpha_s (\Delta T_1 - \Delta T_2) \quad (2-13)$$

Inserting Eq. (2-13) into Eq. (2-7) renders the initial tilting angle of the bimorph beam, caused by the intrinsic thermally induced strain mismatch:

$$\theta_{th_p} = \frac{l_b}{\rho_{th_p}} = \frac{\beta_b}{t_1 + t_2} \Delta \varepsilon_{th_p} l_b = -\frac{\beta_b l_b}{t_1 + t_2} [(\alpha_1 \Delta T_1 - \alpha_2 \Delta T_2) - \alpha_s (\Delta T_1 - \Delta T_2)] \quad (2-14)$$

Eq. (2-14) also implies that if we swap the layer deposition sequence bottom on top, the bimorph will obtain a reversed initial tilting angle with the same magnitude.

With θ_{th_p} and θ_{th_j} derived as in Eq. (2-14) and Eq. (2-10), the final tilting angle of the bimorph beam θ_{th_final} due to thermal effects can be derived as:

$$\theta_{th_final} = \underbrace{\theta_{th_p}}_{Initial} + \underbrace{\theta_{th_j}}_{Actuation} = \frac{\beta_b l_b}{t_1 + t_2} [(\alpha_1 - \alpha_2) \overline{\Delta T_j} + \alpha_s (\Delta T_1 - \Delta T_2) - (\alpha_1 \Delta T_1 - \alpha_2 \Delta T_2)] \quad (2-15)$$

To be precise, the complete expression of the final tilting angle still needs to take into consideration $\Delta \varepsilon'_{in}$, the not-well-understood factor as appeared in Eq. (2-2). But Eq. (2-15) has adequately explained the bimorph actuation principle in the thermal domain.

2.3 Physical Characteristics of Cantilevered Bimorphs

As explained in Section 2.1, thermal bimorph actuation uses intrinsic stress to determine the initial rest position of the object of interest and use Joule-heating induced extrinsic stress to realize the actuation. Therefore, the physical characteristics of the cantilevered bimorph actuator, both thermal and mechanical, are determined by the dimensions and material selection of the bimorph, and the implementation of the resistive heater. This section is dedicated to discussing the impact of these design parameters on the characteristics of the bimorph actuator. Finite Element Analysis (FEA) modeling and Lumped Element Method (LEM) modeling as the two most frequently used modeling methods will be introduced and applied to the discussion. These two modeling methods will be frequently used in later chapters. The result of this section will provide guidance and support to the actuator design in later chapters.

2.3.1 Mechanical Characteristics of a Cantilevered Bimorph Actuator

2.3.1.1 Angular responsivity

The most direct analytical expression of any rotational actuator design is the angular responsivity of the actuator, *i.e.* the unit rotation angle under certain stimulus input. The angular actuation capacity of the cantilevered bimorph actuator has been derived in Eq. (2-10). The input stimulus in this equation is $\overline{\Delta T_j}$, which is the average temperature rise as a result of the Joule heating. Therefore, the angular responsivity of this actuator S_T upon Joule heating actuation can be obtained by moving $\overline{\Delta T_j}$ to the left side of the equation:

$$S_T = \frac{\theta_{th-j}}{\overline{\Delta T_j}} = \frac{\beta_b l_b}{t_1 + t_2} (\alpha_1 - \alpha_2) \quad (2-16)$$

In order to achieve the desired scan angle with the lowest possible input, or to achieve the largest scan angle with a given input, S_T must be optimized to its maximum. An examination of Eq. (2-16) provides the following information:

1. S_T is proportional to the difference between the two CTEs. $S_T \propto (\alpha_1 - \alpha_2)$;
2. S_T is proportional to the curvature coefficient of the bimorph. $S_T \propto \beta_b$
3. S_T is proportional to the bimorph beam length. $S_T \propto l_b$
4. S_T is inversely proportional to the total film thickness. $S_T \propto (t_1 + t_2)^{-1}$

From item (3) and item (4) listed above, one can see that increasing the bimorph length to thickness ratio, $l_b/(t_1+t_2)$, can enhance S_T significantly. However, the ratio of these two dimensions is also the key parameter for the mechanical characteristics of the bimorph actuator such as beam stiffness and therefore subjected to other constraints.

Item (1) and item (2) provide ways to maximize S_T without sacrificing the mechanical performances. From item (1), we know that by choosing materials with large CTE difference will

increase the responsivity of the actuator. Table 2-1 summarizes the thermal-mechanical properties of commonly used MEMS materials.

Table 2-1. Thermal-Mechanical Properties of Commonly Used MEMS Materials [147-153].

Materials	CTE ($10^{-6}/\text{K}$)	Young's Modulus (GPa)	Poisson Ratio	Thermal Conductivity (W/m·K)
Si	3.0	179	0.27	150.0
SiO ₂	0.4	70	0.17	1.4
Si ₃ N ₄	3.3	310	0.24	30.0
Poly-Si	1.6	160	0.22	-
Al	23.6	70	0.35	237.0
Au	14.5	78	0.44	318.0
Cu	16.9	120	0.34	401.0
Cr	5.0	279	0.21	93.9
Pt	8.9	168	0.38	71.6
Ti	8.6	116	0.32	21.9
Ni	12.8	200	0.31	90.9
SU8	52	4	0.22	0.2
PDMS	310	0.00075	0.5	0.15

From Table 2-1 we find that polymer materials have very large coefficients of thermal expansion. However, they generally have very low Young's modulus and their mechanical properties are highly dependent on temperature, which limit their applications in electrothermal bimorph actuation. Among the other materials listed, the two materials with the largest CTE mismatch are Al and SiO₂, two most commonly used MEMS materials. Therefore, besides the high actuation responsivity it can offer, the Al/SiO₂ combination also provides several other advantages. Both materials can be fabricated by well-developed and cost-effective deposition techniques. Al proves to be a very good reflective material for a wide band of wavelengths and therefore can be used as the coating material for the optical apertures and potentially simplify the fabrication process. One potential drawback of this combination is that both materials have relatively low Young's moduli. But with the other advantages, this drawback can be simply

compensated by structural design. As a result, this combination is selected for the bimorph materials in this dissertation.

From item (2), we know that S_T can also be optimized by maximizing β_b , the curvature coefficient. As described in Eq. (2-4), β_b reflects the impact of the bimorph thickness ratio on the beam radius of curvature. The optimization of β_b has been developed by S. Todd [150]. Assuming constant total thickness (t_1+t_2), the optimal ratio that yields maximum β_b has been calculated to be:

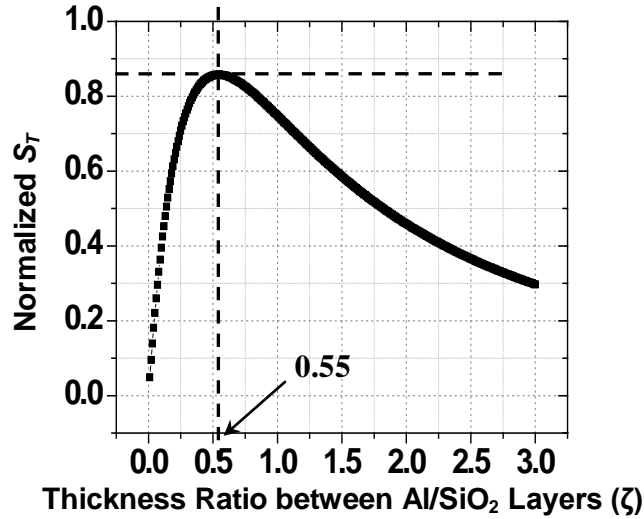
$$\frac{t_1}{t_2} = \sqrt{\frac{E'_2}{E'_1}} \quad (2-17)$$

In this condition, β_b has a maximum value of 1.5 for all material combinations. For Al/SiO₂ combination, the optimal t_{Al}/t_{SiO_2} ratio to achieve maximum S_T is 0.91.

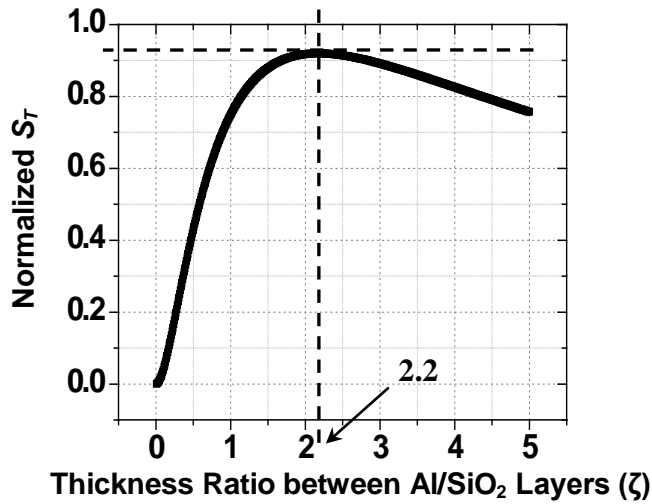
In cases when the bottom thin-film layer maintains a constant thickness with the top layer thickness varying, or the top thin-film layer maintains a constant thickness with bottom layer thickness varying, S. Todd provides a complete, yet complicated analytical result for the former case [150]. Since in this dissertation we have chosen Al/SiO₂ as bimorph materials, we can use numerical methods to find out the optimal ratio for both cases. Notice that when the total thickness of the two layers is not constant, the optimization process needs to take into consideration the (t_1+t_2) factor in the denominator in Eq. (2-17). In the case where we have a fixed thickness for the bottom layer, by substituting ζ for t_1/t_2 and χ for E'_1/E'_2 , we have:

$$\frac{\beta_b}{t_1+t_2} = \frac{\beta_b}{t_2 \left(1 + \frac{t_1}{t_2}\right)} = \frac{1}{t_2} \cdot \frac{6(1+\zeta)}{\chi \cdot \zeta^3 + 4\zeta^2 + 6\zeta + 4 + \chi^{-1} \cdot \zeta^{-1}} \quad (2-18)$$

By arbitrarily setting $E'_1=E'_{Al}$ and $E'_2=E'_{Ox}$, we can plot Eq. (2-16) as a function of ζ . The normalized result of S_T is shown in Fig. 2-2 (a). Similarly, we can have the corresponding plot for the case where the top layer thin film thickness is fixed, as shown in Fig. 2-2 (b).



(a) Case#1: Fixed SiO₂ thickness with varying Al thickness



(b) Case#2: Fixed Al thickness with varying SiO₂ thickness

Figure 2-2. Numerical calculation of optimal thickness ratio t_{Al}/t_{SiO_2} : (a) Fixed SiO₂ thickness with varying Al thickness; (b) Fixed Al thickness with varying SiO₂ thickness

As Fig. 2-2 shows, for fixed SiO₂ thickness, the optimal t_{Al}/t_{SiO_2} ratio to achieve maximum S_T is 0.55, while for fixed Al thickness, the optimal t_{Al}/t_{SiO_2} ratio is 2.2.

The mechanical characteristic of the bimorph actuator is more determined by the total thickness of the bimorph layers rather than the thickness of either layer, therefore in the actual bimorph design we usually choose a fixed total bimorph thickness and use Eq. (2-17) to find the optimal thickness ratio.

2.3.1.2 Bimorph stiffness

An important design aspect of any actuator is the actuator stiffness, or the equivalent spring constant in the working mode. This parameter will eventually determine the actuation capacity of the bimorph actuator, the mechanical bandwidth of the micromirror device, as well as the device resistance to shock-vibration breakdown. For a single cantilevered bimorph actuator, the primary working mode is the out-of-plane rotation mode, for which the spring constant is readily available as:

$$k_{eff} = \frac{E_{eq} \cdot w_b \cdot (t_1 + t_2)^3}{l_b^3} \quad (2-19)$$

in which w_b is the width of the bimorph and E_{eq} is the equivalent Young's modulus of the bimorph actuator, which can be calculated as:

$$E_{eq} = \frac{E_1 t_1 + E_2 t_2}{t_1 + t_2} \quad (2-20)$$

Plugging Eq. (2-25) into Eq. (2-16) renders:

$$S_T = \beta_b \cdot (\alpha_1 - \alpha_2) \cdot \sqrt[3]{\frac{E_{eq} \cdot w_b}{k_{eff}}} \quad (2-21)$$

Eq. (2-21) states that the angular responsivity of the cantilevered bimorph is inversely proportional to the cubic root of the spring constant of the bimorph actuator in the rotation mode, which means that, with a given bimorph width w_b , increasing the stiffness of the bimorph actuator will decrease the responsivity. However, it is also implied in Eq. (2-21) that one way to

increase the bimorph stiffness without sacrificing responsivity is to increase the width of the bimorph w_b . Thus, in performance-specific bimorph actuator design with selected materials, it is possible for designer to try and meet both the responsivity and stiffness specifications by tuning the structure dimensions of the bimorph.

2.3.1.3 Mechanical impact of the resistive heater

In the Section 2.2 we have derived the equations that govern the electrothermal bimorph actuation. Although it is obvious from the discussion that the actuation angle is linearly proportional to the average temperature rise, $\overline{\Delta T_j}$, on the bimorph beam, in practicality this temperature rise needs a physical source. The most effective and straight forward way to implement this physical source is through the Joule heating of an embedded resistor. However, whether or not this resistor would affect the mechanical characteristic of the bimorph actuator, and whether or not this resistor could achieve the temperature rise as expected all raise concerns. Building complete analytical models for the microsystem to solve these concerns is rather challenging and, in most cases, unnecessary. In this section, we will use the FEA modeling method to solve the concern on the mechanical impact of the resistive heater.

Previously reported electrothermal CMOS-MEMS micromirrors use poly-silicon as the heater material. However, it exhibits hysteresis problems and self-annealing effects which limit their applicable scanning ranges [154, 155]. Compared to poly-silicon, platinum (Pt) is a better choice due to its long term mechanical and electrical reliability even at high temperatures. In this dissertation, Pt is chosen as the heater material. As we embed a Pt heater along the bimorph, the bimorph actuator structure changes. Fig. 2-3 shows the cross sectional views of the bimorph with a heater embedded, in which the Pt heater is chosen to have half the width of the bimorph. Analytical calculation of the impact of the Pt heater on the mechanical properties of the actuator

can be rather complicated. In contrast, FEA simulation provides a simple and relatively accurate solution to this issue.

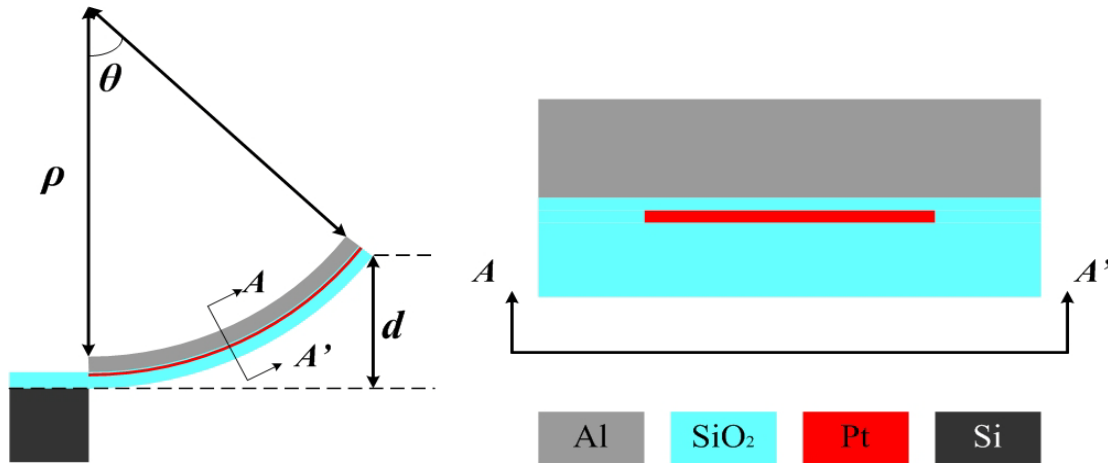


Figure 2-3. Cross sectional views of a cantilevered bimorph actuator with embedded Pt heater

The FEA is a computation method for obtaining approximate solutions to the partial differential equations (PDEs) that govern the microsystem. It divides the microsystem domain into a mesh of discrete subdomains called the finite elements and creates approximate polynomial solutions of the PDEs for each element. Then, the approximate polynomial solutions of each element are pieced together to provide a total solution with an appropriate degree of smoothness over the entire microsystem domain. Using FEA, the deformation characteristics of a cantilevered bimorph with embedded Pt heater can be obtained. Although the absolute result of the FEA simulation is subjected to approximation errors, certain accuracy can still be achieved with appropriate meshing of the structure. Moreover, using the same FEA meshing and simulation procedures on different bimorph structures will provide useful comparative information that is needed to understand the mechanical impact of the embedded Pt heater.

The mechanical characteristics of a cantilevered bimorph can be represented by its change in radius of curvature under certain temperature input. For bimorphs without the Pt embedded heater, the radius of curvature change can be derived from Eq. (2-3) and Eq. (2-10) as:

$$\frac{1}{\rho_{th}} = \frac{\beta_b}{t_1 + t_2} (\alpha_1 - \alpha_2) \overline{\Delta T_j} \quad (2-22)$$

Choosing Al and SiO₂ as the bimorph material, for each temperature input, the radius of curvature (ROC) of the bimorph can be calculated as a function of the total thickness, (t_1+t_2) , as shown in Fig. 2-4a. In this calculation, we assume that the thickness of the bimorph layers is optimized such that $\beta_b=1.5$, as explained in Eq. (2-17). FEA models of bimorphs without the Pt embedded heater are built, meshed and analyzed for the same purpose with the simulation result also shown in Fig. 2-4a, from which one can see that the analytical calculation and the FEA simulation results agree well with each other. Then, the FEA models of the bimorphs with Pt heater embedded were analyzed for their change in the ROC and compared with the FEA simulation results shown in Fig. 2-4a. The discrepancies between the FEA simulation results are extracted as a function of the percentage thickness of the Pt heater with respect to (t_1+t_2) and is plotted in Fig. 2-4b, from which one can see that when the thickness of the Pt heater is within 15% of (t_1+t_2) , the impact of the heater on the mechanical characteristics of the bimorph is still less than 10%. In other words, if we do not consider the impact of the Pt layer, we can still achieve 90% modeling accuracy as long as the thickness of the Pt layer is chosen under 15% of the bimorph thickness (t_1+t_2) .

In this section, we discussed the mechanical characteristics of a cantilevered bimorph actuator including its angular responsivity, mechanical stiffness and the mechanical impact of the embedded resistor. Theoretical calculation and FEA modeling methods were used in the

discussion. So far, all of our previous discussions and derivations use temperature rise $\overline{\Delta T_j}$ as the input, which is provided by the embedded Pt heater. But as mentioned before, whether or not this embedded heater could achieve the temperature rise on the bimorph as expected and how fast can the temperature be stabilized all need verification. The next section will discuss this issue using LEM method.

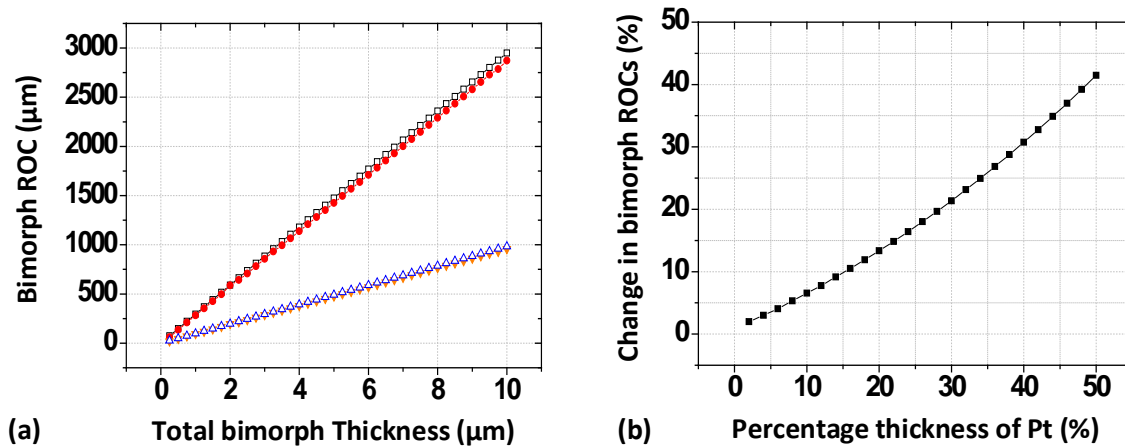


Figure 2-4. Analytical and FEA simulation results of the bimorph ROC under temperature input: (a) Comparison of theoretical calculation and FEA simulation result of bimorph without Pt heater; (b) Impact of the Pt heater on bimorph ROC.

2.3.2 Thermal Characteristics of a Cantilevered Bimorph Actuator

MEMS devices, either sensors or actuators, utilize the energy couplings among different energy domains, such as thermal, mechanical, fluidics and electronics, to realize their functions. LEM in general is a means to resemble such energy couplings for a spatially distributed microsystem using a simplified topology consisting of several discrete elements. Due to the advanced development in the electronics circuit analysis tools such as Cadence Spectre and PSPICE, it is very convenient for MEMS designers to convert the LEM model in other domains into an equivalent LEM model in the electrical domain and analyze, either qualitatively or

quantitatively, the performance of the microsystems. In this section, we will use LEM to study the steady-state temperature distribution and transient thermal response of a bimorph actuator.

2.3.2.1 Steady-state temperature distribution

When analyzing the steady-state temperature distribution on a bimorph actuator, such as the one shown in Fig. 2-3, not only the actuator beam is the target of analysis, but also are the substrate, mirror plate and their connections to the actuator and the ambient environment. Electrical-thermal (E-T) transduction needs to be taken into account since the input stimulus in the actual device is in the electrical domain. Steady-state LEM model of a 1-D micromirror have been developed by S. Todd and H. Xie [150, 156-158]. This method lumps the entire bimorph actuator into a single current source at the point with the highest temperature and split the bimorph into two sections each associated with one end of the bimorph. However, the steady-state temperature distribution along the bimorph was derived from the PDE. In fact, the temperature distribution along the bimorph can be obtained just using LEM method.

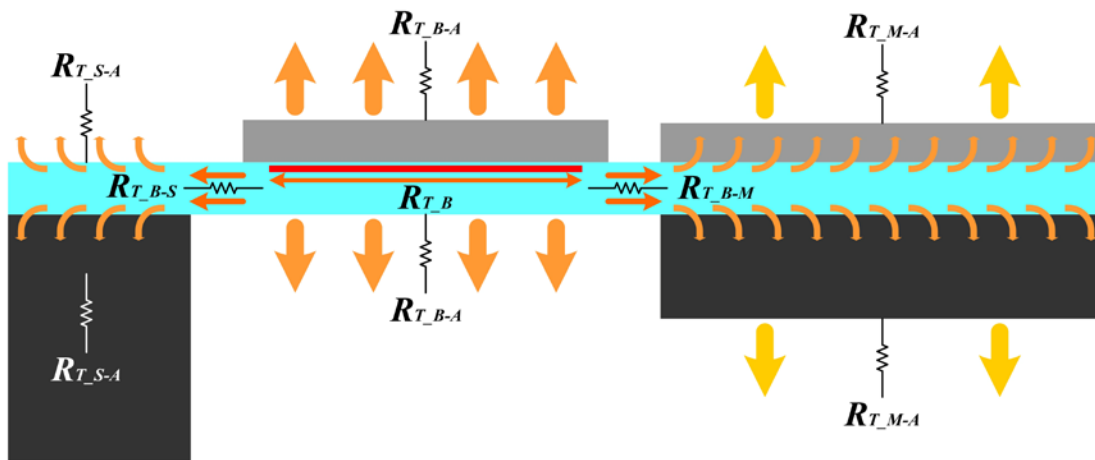


Figure 2-5. Heat paths of a typical 1-D electrothermal bimorph micromirror

The heat paths of a typical 1-D electrothermal bimorph micromirror are illustrated in Fig. 2-5. The resistor components in Fig. 2-5 are described in Table 2-2.

Table 2-2. Description of the resistor components in Fig. 2-5

R_{T_B}	Conduction thermal resistance of the bimorph
$R_{T_{B-A}}$	Convection thermal resistance from the bimorph to the ambient
$R_{T_{B-S}}$	Conduction thermal resistance from the bimorph to the substrate
$R_{T_{S-A}}$	Equivalent thermal resistance from the substrate to the ambient
$R_{T_{B-M}}$	Conduction thermal resistance from the bimorph to the mirror plate
$R_{T_{M-A}}$	Equivalent thermal resistance from the mirror plate to the ambient

In the electrical domain, the effort and flow variables are voltage (Volt) and electrical current (Ampere), respectively. While in the thermal domain, the effort and flow variables are temperature (Kelvin) and heat flow (Watt). This correlation is important for building an E-T LEM model. The heat flow in the thermal domain is generated by the resistive heating of the Pt heater, which has an electrical resistance of:

$$\begin{aligned}
 R_b &= \int_0^{l_b} \frac{\rho_e}{w \cdot t} \left[1 + \gamma_R \Delta T_j(x) \right] dx = R_0 + R_0 \cdot \gamma_R \cdot \frac{1}{l_b} \int_0^{l_b} \Delta T_j(x) dx \\
 &= R_0 \left(1 + \gamma_R \cdot \overline{\Delta T_j} \right)
 \end{aligned} \tag{2-23}$$

in which ρ_e represents the resistivity of Pt at room temperature. w , t represents heater width and thickness respectively. γ_R represents the thermal coefficient of resistivity and R_0 represents the heater resistance at ambient temperature. $\overline{\Delta T_j}$, is the averaged temperature rise along the bimorph. In electrical domain, as a voltage signal V is applied on this resistor, Joule heating takes place and the resistor outputs a thermal heat flux of:

$$P(\overline{\Delta T_j}) = \frac{V^2}{R_b} = \frac{V^2}{R_0} \left[1 + \gamma_R \cdot \overline{\Delta T_j} \right]^{-1} \tag{2-24}$$

It is obvious that if we lump the whole bimorph beam into one element we will not obtain information on temperature distribution. Instead, we can further dissect the bimorph into multiple segments and create equivalent LEM models for each of the segments. Thus, a transmission line of electrical components will be formed, from which the temperature information can be extracted from the nodal voltages of each element. Assuming we divide the bimorph along its axial direction into N segments. Each segment can be represented by a current source of I/N of the total heat flow, a conduction resistance from segment to segment, and a convection resistance to the ambient. The conduction resistance between two adjacent segments is equal to $1/N$ of the total bimorph thermal resistance along the axial direction. On the other hand, the convection resistance from each segment to ambient is N times the convection resistance of the whole bimorph. Fig. 2-6 shows such a steady-state equivalent LEM circuit for a 1-D micromirror actuated by a cantilevered bimorph.

By choosing a large number of N , the steady state temperature distribution on the bimorph beam can be analyzed with very small error. The circuit shown in Fig. 2-6 also provides a simple way of finding the balancing factor used in [150], which is an important parameter of electrothermal bimorph actuator in that it determines the point with the maximum temperature and also the heat flux at both ends of the bimorph. Looking from each current source into the node, the resistances to the left side and to the right side can be calculated if the convection resistances are not considered. Then, from Kirchhoff's Law of Current, we can calculate the heat flux that exits the actuator from the substrate or the left side as:

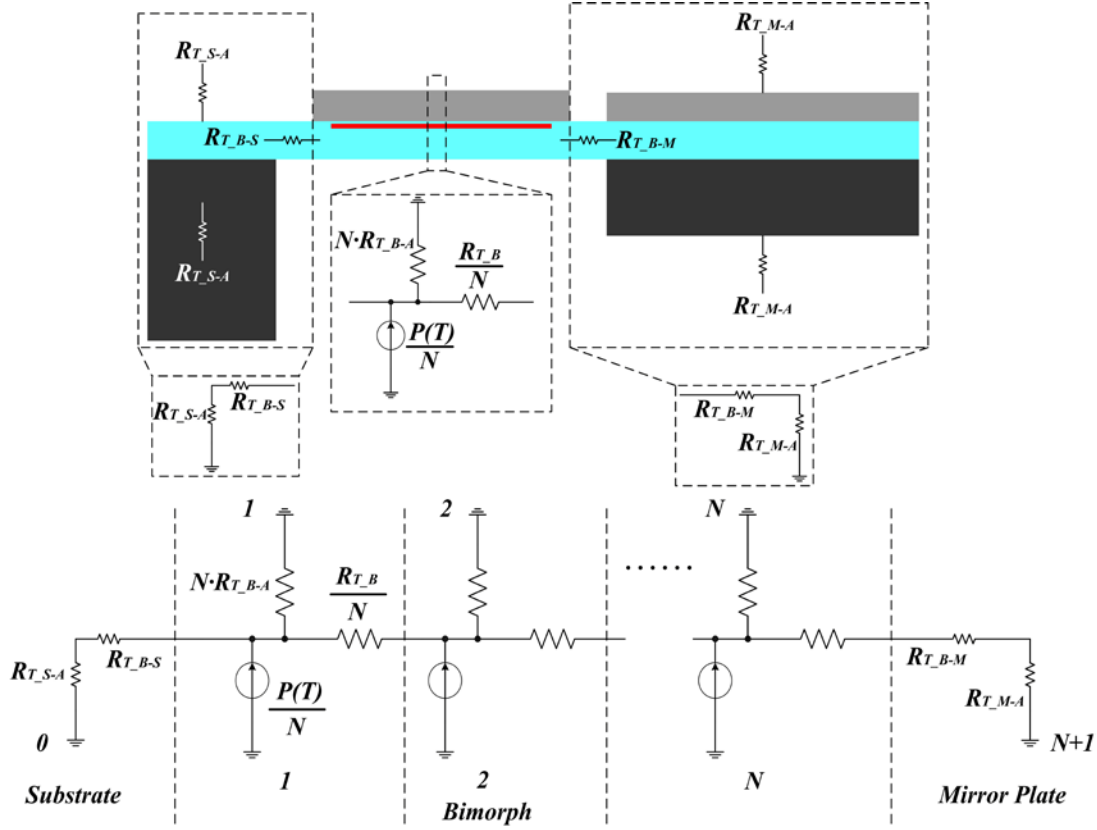


Figure 2-6. Steady-state LEM equivalent circuit of 1-D micromirror with partitioned bimorph

$$\begin{aligned}
 P_{B-S}(\overline{\Delta T_j}) &= \lim_{N \rightarrow \infty} \frac{P(\overline{\Delta T_j})}{N} \sum_{i=0}^{i=N} \left(\frac{\frac{N-i}{N} R_{T_B} + R_{T_{B-M-A}}}{R_{T_B} + R_{T_{B-S-A}} + R_{T_{B-M-A}}} \right) \\
 &= \frac{\frac{1}{2} R_{T_B} + R_{T_{B-M-A}}}{R_{T_B} + R_{T_{B-S-A}} + R_{T_{B-M-A}}} P(\overline{\Delta T_j})
 \end{aligned} \tag{2-25}$$

in which $R_{T_{B-M-A}} = R_{T_{B-M}} + R_{T_{M-A}}$ is the equivalent thermal resistance seen from the right side, or the mirror plate side, of the bimorph to the ambient. Similarly, we can also calculate the heat flux that exits from the mirror plate or the right side as:

$$P_{B-M}(\overline{\Delta T_j}) = \frac{\frac{1}{2} R_{T_B} + R_{T_{B-S-A}}}{R_{T_B} + R_{T_{B-S-A}} + R_{T_{B-M-A}}} P(\overline{\Delta T_j}) \tag{2-26}$$

in which $R_{T_B-S-A} = R_{T_B-S} + R_{T_S-A}$ is the equivalent thermal resistance seen from the left side, or the substrate side, of the bimorph to the ambient. The coefficient on the right side of Eq. (2-25) is the balancing factor:

$$f = \frac{\frac{1}{2}R_{T_B} + R_{T_B-M-A}}{R_{T_B} + R_{T_B-S-A} + R_{T_B-M-A}} \quad (2-27)$$

with which the Eq. (2-25) and Eq. (2-26) can be rewritten as:

$$P_{B-S}(\overline{\Delta T_j}) = f \cdot P(\overline{\Delta T_j}) \quad (2-28)$$

$$P_{B-M}(\overline{\Delta T_j}) = (1-f) \cdot P(\overline{\Delta T_j}) \quad (2-29)$$

The balancing factor f has a value between 0 and 1. Assuming the length of the bimorph is l_b , then Eq. (2-28) and Eq. (2-29) can be interpreted as that the power generated from the first $f \cdot l_b$ part of the heater will all flow to the substrate side and the rest part of the heater, $(1-f) \cdot l_b$ will flow to the mirror plate side. At the point where $x = f \cdot l_b$, the temperature is the highest. It can be concluded from Eq. (2-27)~(2-29) that when $R_{T_B-M-A} = R_{T_B-S-A}$, $f=0.5$ and the power generated by the heater splits equally towards both sides. The maximum temperature is at the middle of the bimorph. Whereas, when either R_{T_B-M-A} or R_{T_B-S-A} is significantly larger than the other resistor components, the heat flux would flow to the side with the smaller thermal resistance and the point with the highest temperature moves to either end of the bimorph.

From Eq. (2-27), Eq. (2-28) and Eq. (2-29), the temperature at both ends of the bimorph can be calculated:

$$\begin{aligned} T_1(\overline{\Delta T_j}) &= f \cdot R_{T_B-S-A} \cdot P(\overline{\Delta T_j}) \\ T_N(\overline{\Delta T_j}) &= (1-f) \cdot R_{T_B-M-A} \cdot P(\overline{\Delta T_j}) \end{aligned} \quad (2-30)$$

A direct interpretation of Eq. (2-30) shows that in order to achieve uniform and even temperature distribution along the bimorph actuator, the thermal resistances looking from either end of the bimorph to the substrate and mirror plate, $R_{T_{B-S-A}}$ and $R_{T_{B-M-A}}$, should be adjusted close to each other and be much larger than the thermal resistance of the bimorph itself R_{T_B} .

The above discussion from Eq. (2-25) to Eq. (2-30) does not consider the convection thermal resistance from the bimorph to the ambient. But following the modeling concept described above, one can build such equivalent circuit considering all factors and perform simulations with Cadence Spectre or PSPICE. The steady-state temperature distribution is directly reflected by the voltage distribution long the segmented bimorph LEM models.

2.3.2.2 Transient response of the temperature rise

In the previous section we have used the distributed LEM modeling to study the steady-state temperature distribution of the cantilevered bimorph. This section will focus on the E-T transient response of the actuator.

In the thermal domain, the mass of the structure stores thermal energy which is analogous to a capacitor in the electrical domain. When analyzing the steady-state thermal characteristic of the bimorph actuator, the mass of the bimorph does not need to be considered. But to analyze the E-T transient response of the actuator, the mass factor must be added to the equivalent electrical LEM circuit in the form of capacitor components.

Fig. 2-7 shows the equivalent transient response circuit of the same 1-D micromirror as shown in Fig. 2-6. A capacitor is added to each bimorph segment equivalent LEM circuit in shunt to represent the mass of that bimorph segment. The descriptions of the added capacitor components are shown in Table 2-3.

Table 2-3. Description of the capacitance components in Fig. 2-7

C_{T_B}	Thermal capacitance of the bimorph segment
C_{T_S}	Thermal capacitance of the substrate
C_{T_M}	Thermal capacitance of the mirror plate

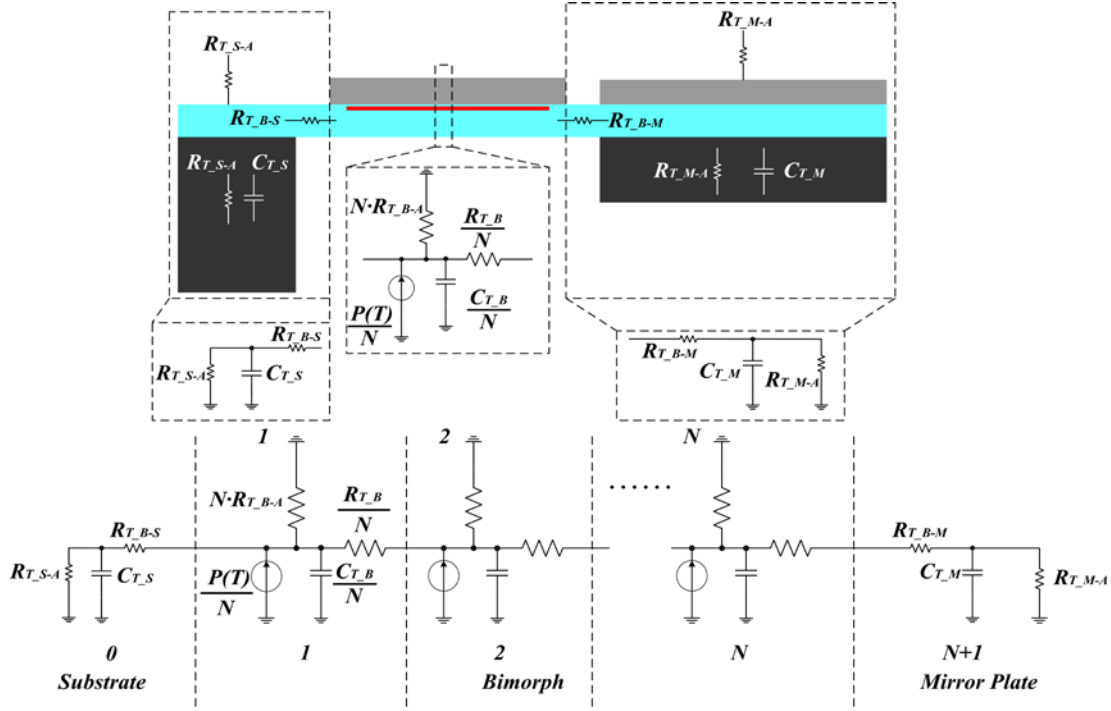


Figure 2-7. Transient response equivalent circuit of 1-D micromirror with partitioned bimorph

With the circuit shown in Fig. 2-7 built, one can study the transient response of the actuator by choosing pulse signal for all the current sources and examining the transient response of the voltages on the node of each bimorph segment.

2.3.2.3 E-T characteristics of a 1-D micromirror

This section will provide a case study of the E-T characteristics of a 1-D micromirror actuated by cantilevered bimorphs using the LEM modeling described in Section 2.3.2.1 and Section 2.3.2.2.

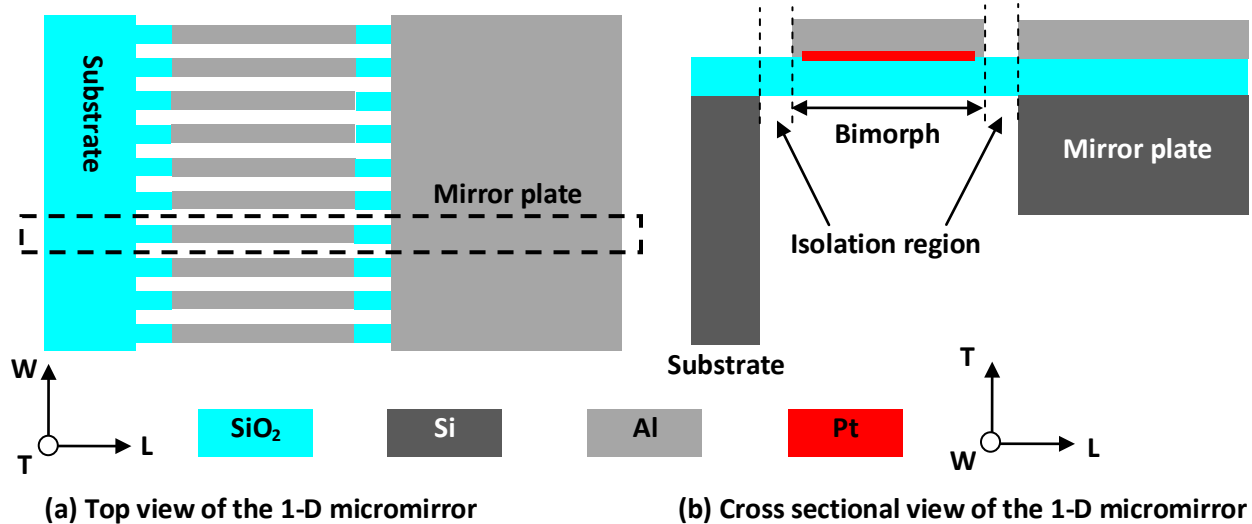


Figure 2-8. Top and side views of the 1-D micromirror device schematic

The cross sectional view and top view of the 1-D micromirror is shown in Fig. 2-8. The structure parameters of the 1-D micromirror are given in Table 2-4. The micromirror is actuated by 10 cantilevered bimorph connected in parallel. For simplicity we only regard the embedded Pt heater as the power source and do not consider its thermal resistance and capacitance into the LEM model. Thermal isolation regions consisting of only SiO_2 are added between the actuator and the mirror plate and the substrate. The width of the isolation is the same as the width of each bimorph. We can take one bimorph actuator and its associated portion of the mirror plate and the substrate as the object of study, as dash circumscribed in Fig. 2-8a. But the E-T characteristics of the 10 bimorph actuators are very similar due to the repeated structure design.

We can choose the segment length of $10\mu\text{m}$ and dissect the bimorph into 12 segments. Based on the parameters given in Table 2-4, the values of the resistance and capacitance components as shown in Fig. 2-7 can be calculated, as shown in Table 2-5. The equivalent thermal resistances from the substrate to the ambient are difficult to calculate due to the lack of boundary conditions. Assuming the bottom surface of the substrate has good thermal contact with a heat sink, this thermal resistance can be estimated to be around $100 \text{ W}\times\text{K}^{-1}$. The thermal

resistance of the isolation region can be calculated based on their dimensions. The convective thermal resistance from the bimorph segment and mirror plate to the ambient can be expressed using the convection coefficient h ($\text{W}\times\text{m}^{-2}\times\text{K}^{-1}$). We choose h to be a variable and will study its impact. The thermal conduction coefficients of Al and SiO_2 used in the calculation are $237\text{W}\times\text{m}^{-1}\times\text{K}^{-1}$ and $1.1\text{W}\times\text{m}^{-1}\times\text{K}^{-1}$ respectively.

Table 2-4. Structure parameters of the 1-D micromirror

Structure Parameters	Value (μm)	Structure Parameters	Value (μm)
Bimorph length	120	Substrate thickness	500
Bimorph width	12	Mirror plate length	400
SiO_2 thickness	1.3	Mirror plate width	192
Al thickness	1.2	Mirror plate thickness	40
Gap between bimorphs	8	Isolation region length	20
Substrate length	200	Isolation region width	12
Substrate width	192	Bimorph segment length	10

Table 2-5. Calculated values of the electrical components for the LEM equivalent circuit

Resistive components	Value ($\text{W}\times\text{K}^{-1}$)	Capacitive components	Value ($\text{J}\times\text{K}^{-1}$)
R_{T_B}/N	3×10^3	C_{T_B}/N	600×10^{-12}
$R_{T_{B-A}}\times N$	$3\times 10^9/h$	C_{T_S}	30×10^{-6}
$R_{T_{B-S}}$	1.2×10^6	C_{T_M}	2.5×10^{-6}
$R_{T_{S-A}}\times N$	1200	Segment number N	12
$R_{T_{B-M}}$	1.2×10^6		
$R_{T_{M-A}}\times N$	$9.6\times 10^7/h$		

First, we assume the Pt embedded heater in each segment provides a dc electrical power of $20\mu\text{W}$, the steady-state temperature distribution along the cantilevered bimorph can be obtained by using Cadence Spectre to simulate the circuit shown in Fig. 2-6 with the component values listed in Table 2-5. Fig. 2-9 shows the simulation result with different values of h . Based on Eq. (2-32), the balancing factor corresponds to each h value is calculated as well.

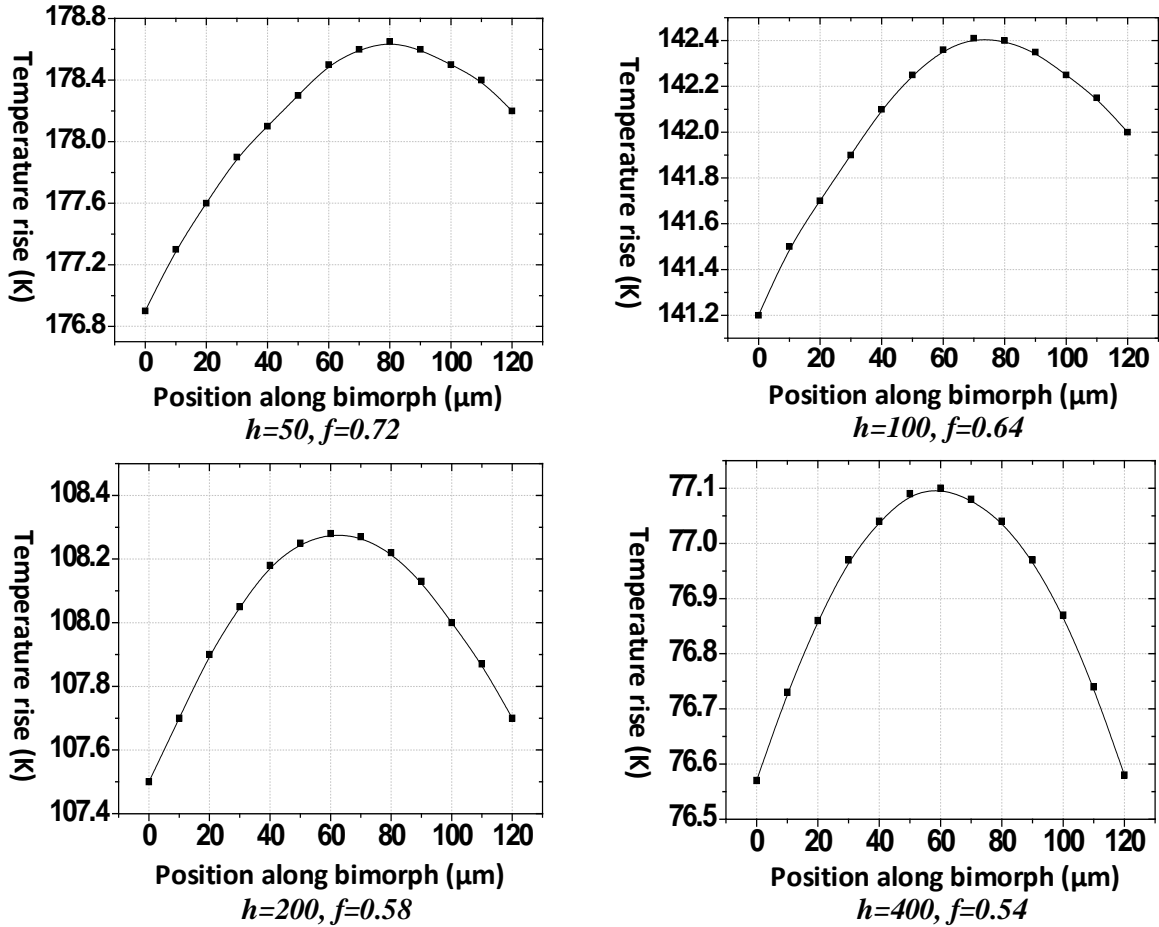


Figure 2-9. Steady-state simulation results using the LEM equivalent circuit.

It is evident from Fig. 2-9 that as the convection coefficient h changes from $50 \text{ W}\times\text{m}^{-2}\times\text{K}^{-1}$ to $400 \text{ W}\times\text{m}^{-2}\times\text{K}^{-1}$, the point with the highest temperature moves toward the center of the bimorph, which closely match with what Eq. (2-32) predicts. At the same time, the average temperature along the bimorph decreases. This is because as h become larger, more power is

passivated into the ambient through the convection. One can also arbitrarily choose the value for the other components listed in Table 2-5, such as the isolation resistances, and obtain the steady-state temperature distribution information by following the same procedure.

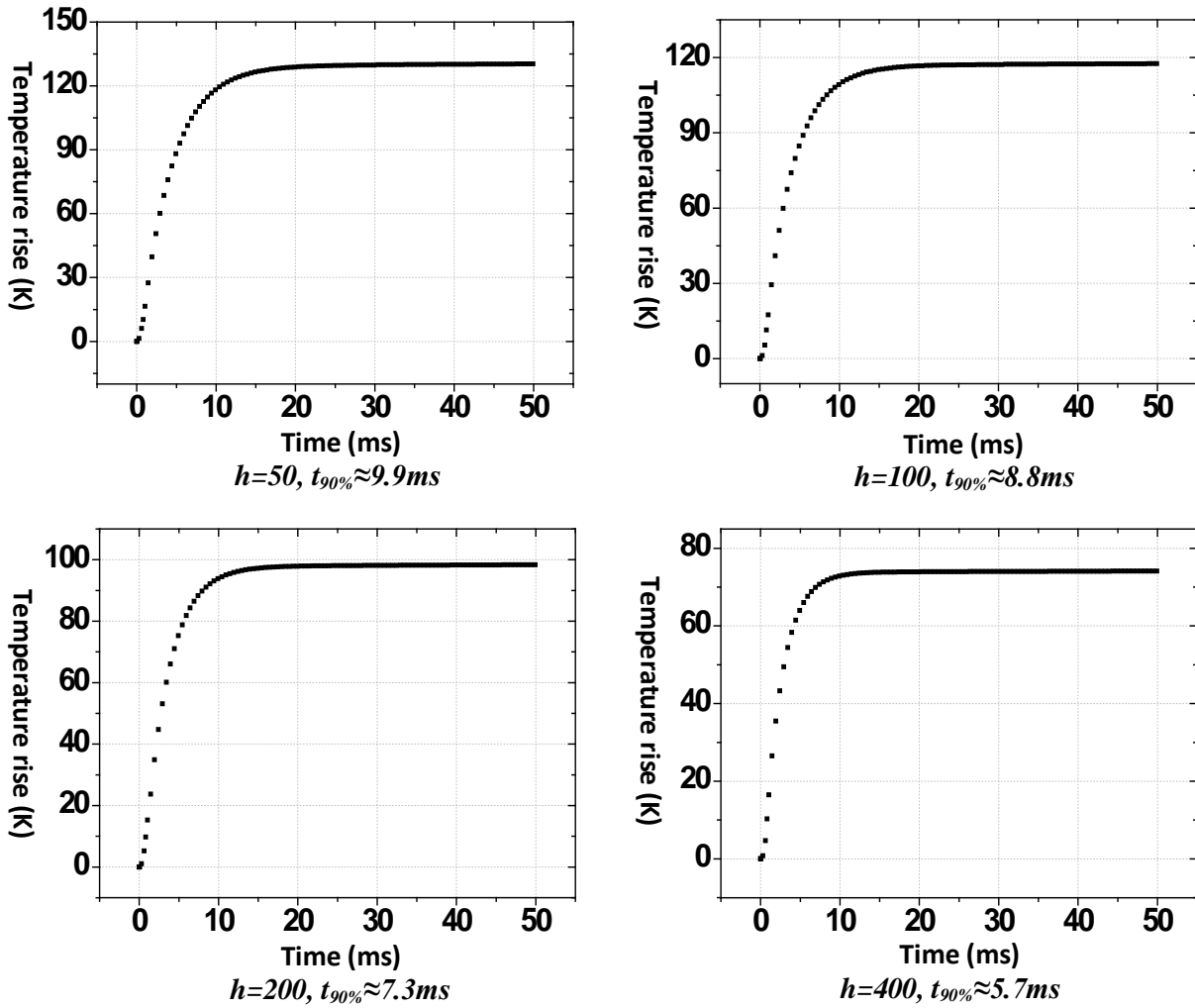


Figure 2-10. Transient simulation results on the bimorph using the LEM equivalent circuit.

Then, the dc current sources in the equivalent circuit are replaced by pulse current sources and a transient simulation is performed also using Cadence Spectre. The simulated transient response of the temperature rise on the bimorph is shown in Fig. 2-10. The 0~90% response time are also estimated from the plots. As shown in Fig. 2-10, as the convection coefficient increases from 50 to 400, the local initial thermal response time on the bimorph decreases from 9.9ms to

5.7ms. This is due to the decrease of the equivalent thermal resistance seen by the capacitance of the bimorph. The reason this response time is called the local initial response time is because the overall response time of this microsystem is decided by the substrate and the mirror plate due to their large thermal capacitance. Fig. 2-11 shows the simulated thermal response on the mirror plate and the substrate when $h=200$. It can be seen from the plots that based on the parameters given in Table 2-5, the thermal response time on the substrate and the mirror plate are 85ms and 2.3s, respectively. The bimorph would first reach a local high temperature within its own response time. Then the temperature will keep changing slowly until the overall steady state is achieved. In this particular case, the overall response time is decided by the mirror plate. Following the same procedures, one can also study the impact of other parameters on the transient response of the bimorph, such as the thermal resistances of the isolation regions.

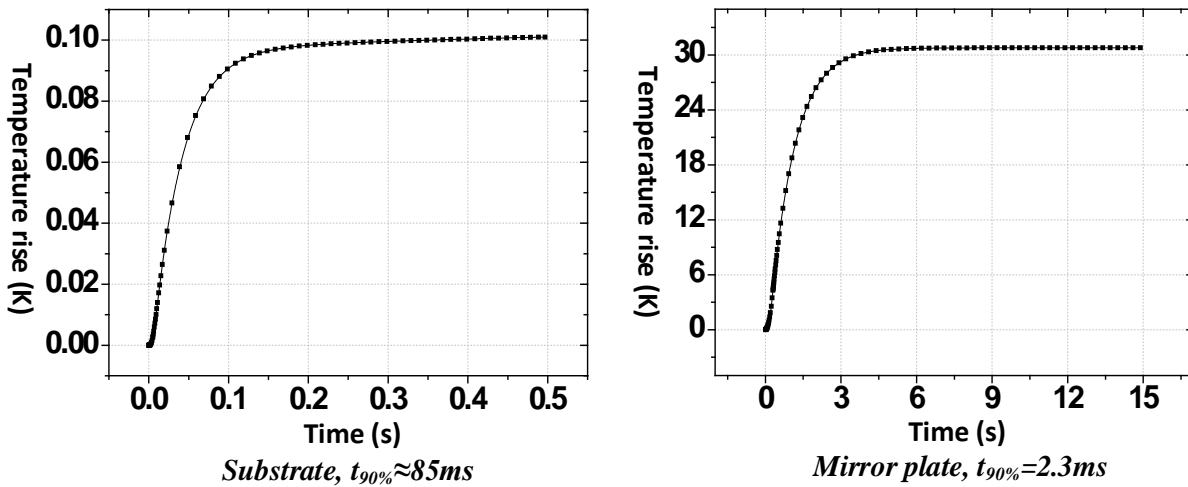


Figure 2-11. Transient simulation results on the mirror plate and the substrate.

It has been shown from the above analysis that, for any given bimorph structure, decided by how much accuracy is expected, one can build such LEM equivalent model by choosing appropriate element size for the modeling procedures. This is in some sense similar to the FEA method we discussed in the previous section. This method is sometimes referred to as the

distributed element method (DEM). It can provide much higher accuracy than the single-element LEM modeling and is much simpler than solving the PDEs. Although Todd's work has resulted in analytical solutions of the cantilevered bimorph PDE under different boundary conditions, it needs to solve the PDE using a case by case scenario and the solutions are different each time a different boundary condition is applied. Moreover, the PDE assumes the structure under analysis is spatially uniform, which is usually not the case in bimorph designs with a certain complexity. In this case, the DEM modeling is easier to implement and provides more flexibility. The above case study provides a description of the capability of DEM modeling. In Chapter 3, we will use the DEM method to build an equivalent circuit model for the proposed bimorph and analyze the E-T steady-state and transient response of the actuator.

2.4 Previous Electrothermal Micromirror Designs and Discussion

Section 2.3 have demonstrated the actuation principles of electrothermal bimorph actuators and introduced modeling modalities for system-level analysis. In this section, we will further discuss electrothermal bimorph based micromirrors with existing design examples. Design concepts and device performances will be presented. Drawbacks and limitations will also be discussed and summarized.

Various electrothermal bimorph based micromirrors have been successfully developed by Xie and Jain [122-126]. These designs use CMOS processes to define Al/SiO₂ bimorph structures and a post-CMOS DRIE process for mirror plate formation and structure release. Fig. 2-12 shows the schematic and SEM images of typical such 1-D and 2-D micromirror designs [125, 126].

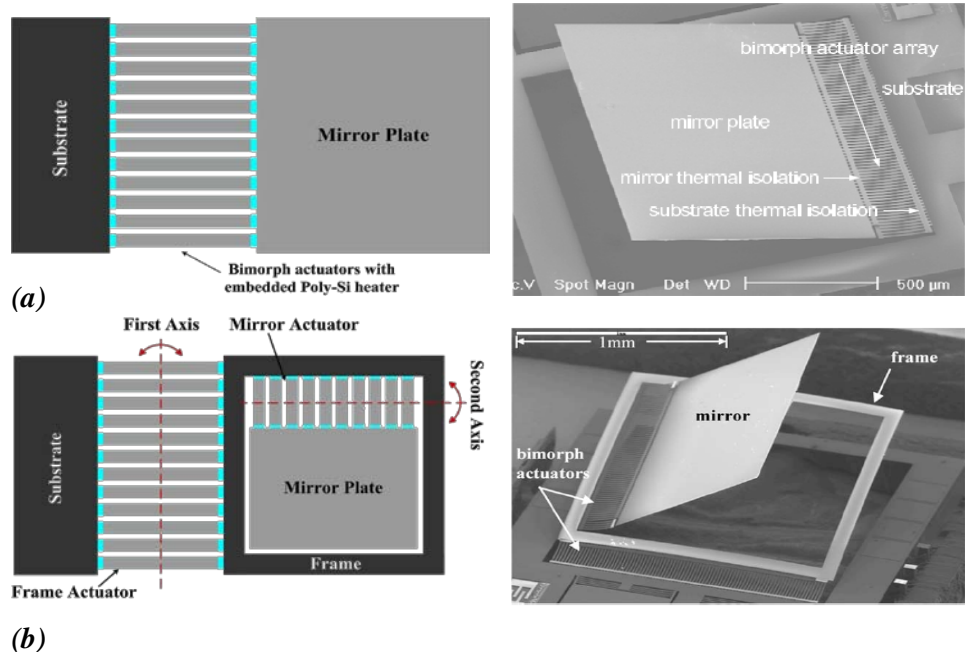


Figure 2-12. Design schematic and device SEM images of typical (a).1-D and (b).2-D electrothermal bimorph actuated micromirrors

As we can see from Fig. 2-12, both designs are based on cantilevered bimorph beams. An array of cantilevered bimorph beams is connected in parallel to increase the actuation capacity. The 1-D micromirror uses one set of bimorphs to generate one dimensional scan while the 2-D micromirror uses two orthogonally positioned bimorph sets for two dimensional scanning. The bimorph set that actuates the mirror plate is gimbaled on a bulk-silicon-based frame that is actuated by the other set of bimorphs anchored to the substrate. Both designs chose Al as the material on the top, as we analyzed earlier in Section 2.3, therefore the mirror plate has initial tilting angles above the substrate/frame level. As a voltage signal is applied to the embedded Poly-Si heater, Joule heating raises the bimorph temperature and the mirror plate is actuated downward. The 1-D micromirror has a resonant frequency of 165Hz and is able to generate mechanical rotation up to 25° at 17V DC [125]. The 2-D micromirror has resonant frequencies of 445Hz and 259Hz for mirror and frame actuators respectively. The device can achieve mechanical rotation of 40° at 15V DC for both axes [126].

Although the scan angles are large for the two devices, there are a few drawbacks that limit their applications. First of all, the rotation axes of the two devices shift dramatically as the mirror plate rotates. Any cantilevered bimorph actuator with a mirror plate connected at the free end will generate rotation axis shifting during rotational scanning. While in many applications such as medical imaging endoscopes, a stationary rotation axis is highly desired for high image quality and fidelity. Fig 2-13a illustrates the cause of this shifting and Fig. 2-13b shows the schematic of a desired mirror plate with a stationary rotation axis.

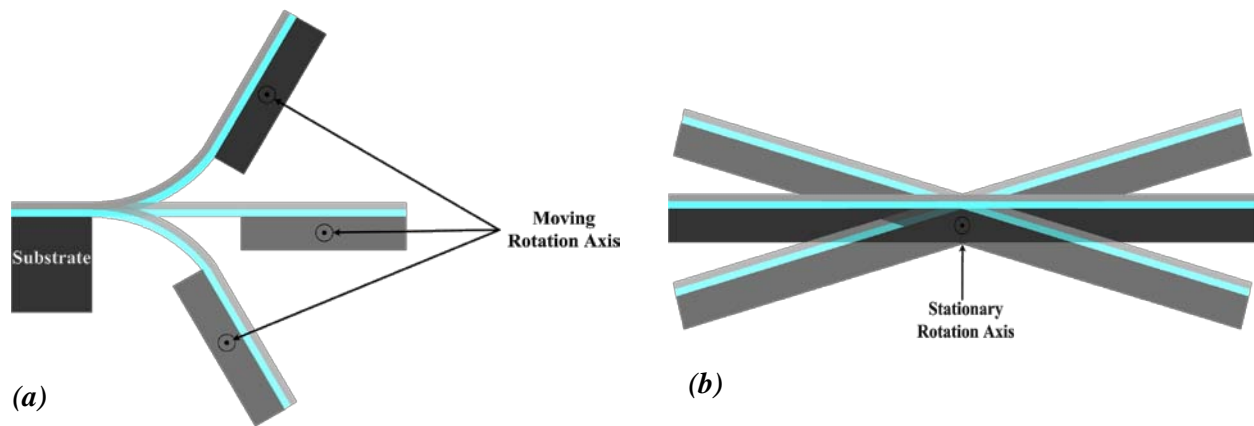


Figure 2-13. (a). Micromirror with shifting rotation axis (Undesired); (b). Micromirror with stationary rotation axis (Desired).

Another drawback of these two designs is the large initial angle which not only complicates the optical design, but also makes the assembling process difficult. The inability of achieving piston motion also limits their applications.

To resolve the above listed drawbacks, large-vertical-displacement (LVD) electrothermal bimorph actuators were proposed in which two sets of bimorphs are positioned in complimentary orientations to compensate the initial tilting. Fig. 2-14a and Fig. 2-14b illustrate the design schematics and SEM images of a 1-D LVD and a 2-D LVD micromirror, respectively [122, 123].

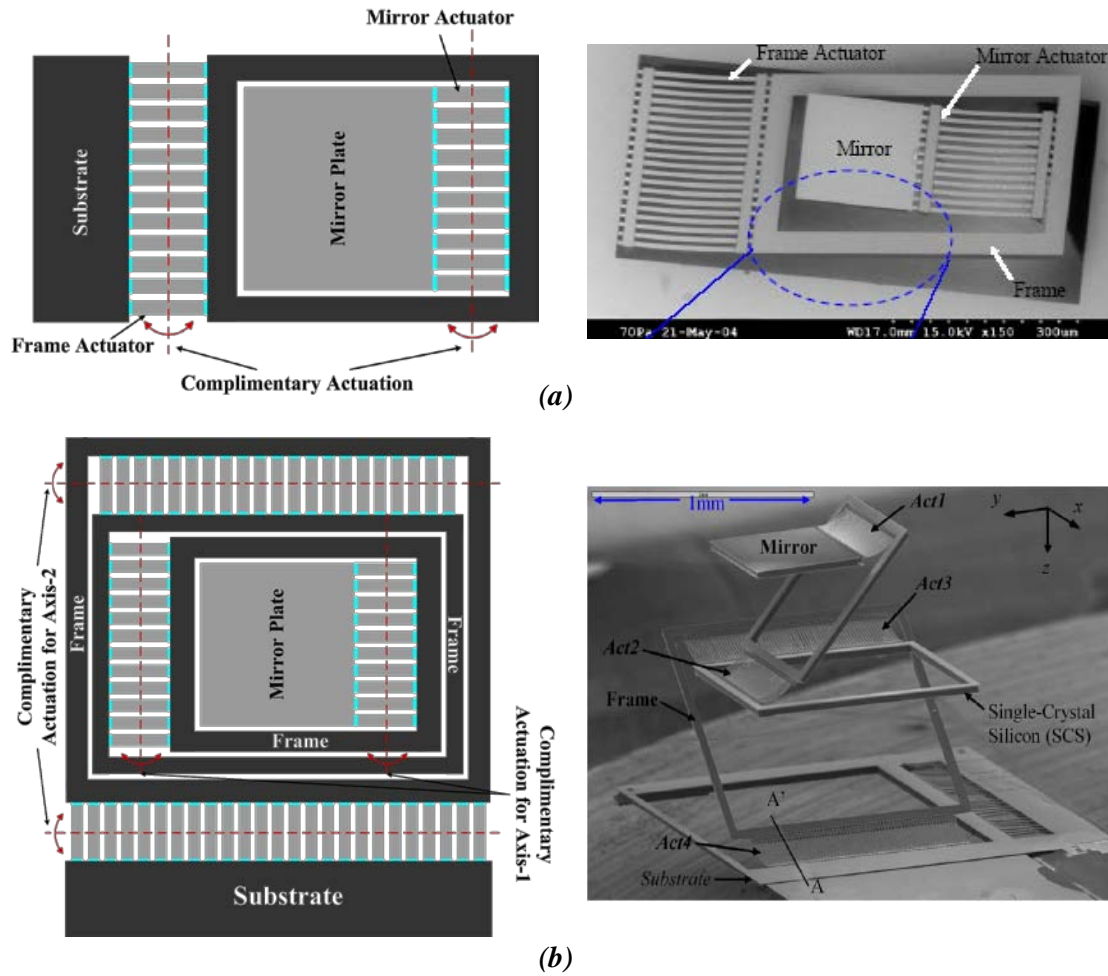


Figure 2-14. (a). Structure schematic and SEM image of 1-D LVD micromirror device; (b). Structure schematic and SEM image of 2-D LVD micromirror device.

In the 1-D LVD device, the complimentary bimorph sets must be designed with the same length so that the initial tilting of the mirror can be compensated by the initial tilting of the frame, resulting in a mirror plate parallel to the substrate. The 2-D LVD device is a cascade of two 1-D LVD devices but with orthogonally oriented bimorph sets to realize 2-D scanning. Both LVD devices have negligible initial tilting of the mirror plate. The 1-D LVD device has achieved over $\pm 15^\circ$ mechanical rotation angle and $200\mu\text{m}$ piston stroke all at less than 6V DC. The resonant frequencies of the mirror and frame actuator are 2.62 kHz and 1.18 kHz, respectively. [122]. The 2-D LVD device has achieved over $\pm 20^\circ$ mechanical rotation angle and

0.5mm piston stroke at less than 15V DC. The resonant frequencies for the four actuators shown in Fig. 2-9(b), (Act1-Act4), are 870Hz, 452Hz, 312Hz, 170Hz, respectively [123].

Compared with the devices shown in Fig. 2-12, the LVD micromirror designs in Fig. 2-14 have resolved the initial mirror plate tilting problem. It also enables vertical piston actuation. However, the rotation axes of LVD devices are still non-stationary. Several other issues of the LVD devices also arise as the structures become more complicated. For instance, the gimbaled structure in the 1-D LVD design has made the area efficiency low. This becomes even worse for 2-D LVD devices. The aperture size of the 2.7mm by 1.9mm 2-D LVD device, shown in Fig. 2-14b, is only 0.5mm by 0.5mm due to this effect. In order to generate tilting-free vertical actuation, the frame and mirror actuators must generate equal but opposite rotation angles. However, the gimbaled LVD structure can not avoid thermal coupling issue which greatly complicates the signal control, especially for dynamic actuation.

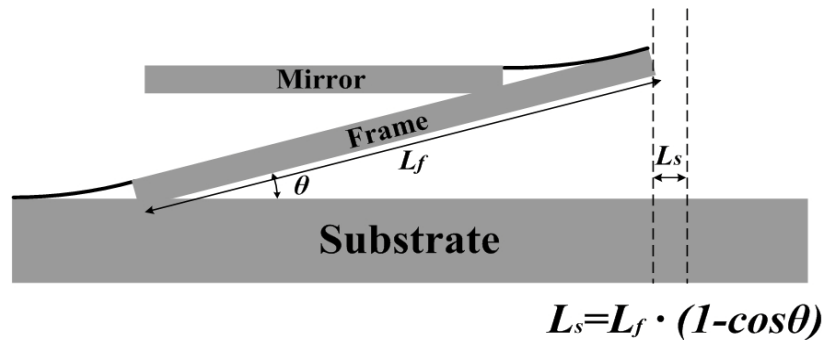


Figure 2-15. Cross sectional view of a 1-D LVD device showing the lateral shift.

The LVD devices also suffer from large lateral shift during piston actuation. The cause of the lateral shift is shown in Fig. 2-15. As it is shown, the lateral shift L_s becomes larger with increased actuation angle θ . Moreover, it causes a fundamental trade-off to LVD designs since larger aperture size requires larger frame length, but larger frame length inevitably leads to larger lateral shift. This drawback significantly reduces the available aperture size when used for

imaging applications where optical alignment is crucial. To solve the remaining problems that LVD devices have, gimbal-less clamped-clamped micromirror designs have been proposed. Singh et al. reported an electrothermal TTP micromirror using Al/Si as the bimorph material pair [127, 159]. The schematic and SEM of this design is shown in Fig. 2-16. The mirror plate is supported by four cantilevered bimorphs and serpentine springs. The device is able to achieve 17° of mechanical deflection and $200\mu\text{m}$ vertical displacement at less than 2V DC.

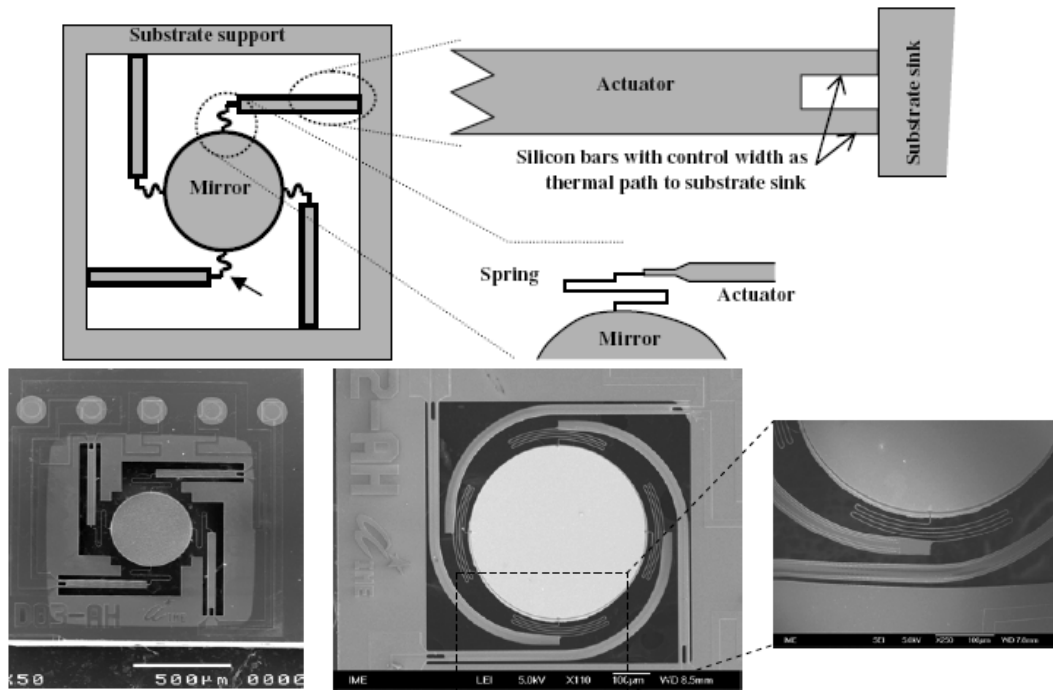


Figure 2-16. Design concept and SEMs of the devices developed by Singh et al.

Although this device can achieve fairly large angular and vertical displacement at low voltage, its simple cantilevered bimorph structure will inevitably generate lateral shift on the tip of the bimorph actuator. This lateral shift is attenuated by the long serpentine silicon spring that connects the actuator to the mirror plate, but it is still conceivable that the rotation-axis shift still exists as the mirror plate is being actuated. The mirror plate will also bear an in-plane spinning mode which is not desirable. This design also suffers from small radius of curvature due to the thin-film based mirror plate. It is questionable whether the overly attenuated silicon spring would

bear a bulk-silicon based mirror plate for dynamic actuation. The resonance frequency of either mode for this device is not provided.

Wu et al. developed a three-segment-bimorph actuator design that can achieve near lateral-shift-free (LSF) large vertical actuation by length control of the segments [61, 128]. The design schematic and SEM of the device is shown in Fig. 2-17.

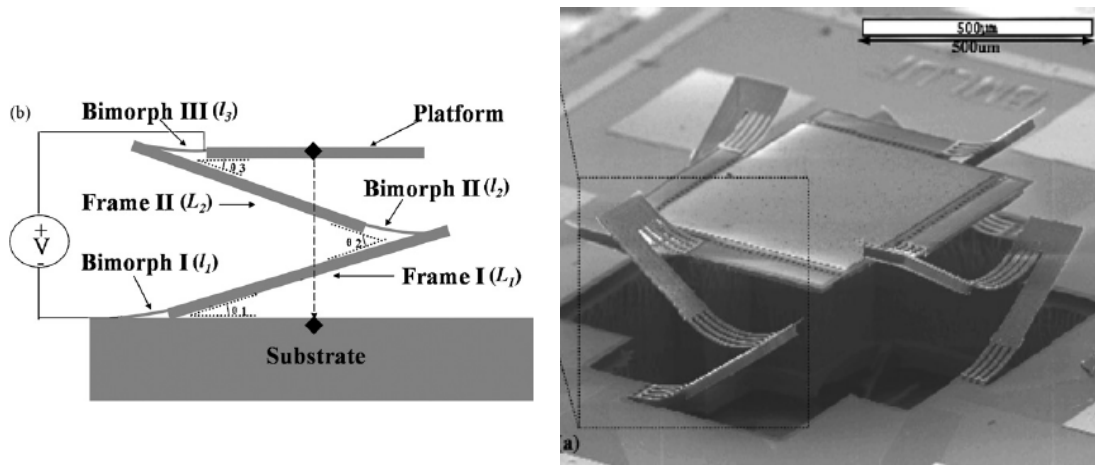


Figure 2-17. Design concept and SEMs of the LSF devices developed by Wu et al.

The LSF design has achieved up to 0.6mm vertical displacement with $\sim 10\mu\text{m}$ lateral shift at less than 5V DC. It also demonstrated a tip-tilt deflection of $\pm 30^\circ$ at 5V DC. However, due to the structural asymmetry, the device suffers from a slightly skewed scan pattern. The rotation-axis shifting, although small, still exists. Area efficiency of the LSF device is not high due to the large area taken by the bimorphs and frames. An aperture size of 0.8mm by 0.8mm has been achieved on a 2.5mm footprint. Lastly, the bulk silicon underneath the long frames also limits the fast response of the LSF device.

2.5 Summary

From the reviews in Chapter 1, we know that in order to be used in applications such as endoscopic imaging and OPAs, it is essential for electrothermal micromirrors to achieve TTP actuation capabilities with large aperture, small footprint, negligible lateral shift and stationary

rotation axis. However, based on the above discussion of the existing designs of electrothermal micromirrors, we have the understanding that although all the designs have their own unique features, there is still a lack of micromirror designs that can meet these requirements all at the same time. It is based on this pursuit that we extended our work to new actuator designs which will be discussed in the next chapter.

CHAPTER 3

DEVELOPMENT OF THE FOLDED DUAL S-SHAPED ELECTROTHERMAL BIMORPH ACTUATORS AND ASSOCIATED MICROMIRROR DEVICES

To resolve the remaining problems as described in Section 2.4, a novel folded dual-S shaped (FDS) electrothermal bimorph actuator is presented in this chapter. The FDS actuator is able to achieve near-zero lateral shift in piston actuation and structurally fixed rotation axis for tip-tilt actuation. To verify the design concept of the FDS actuator, the 1st-generation FDS micromirror has been designed, fabricated, and tested (see Section 3.2). The 2nd-generation FDS micromirror with optimized structure parameters achieved increased operating range. The optimization process and the experimental results of the 2nd-generation FDS micromirror are presented in Section 3.3.

3.1 FDS Electrothermal Bimorph Actuator Design Concept

From the discussion in Section 2.5 we know that the origin of the lateral shift during vertical actuation is the cantilevered bimorph tilting, as shown in Fig. 2-15. Todd et al. proposed an S-Shaped, invert-series-connected (ISC) bimorph actuator based on post-CMOS MEMS process to realize TTP actuation capability [160]. The ISC concept is illustrated in Fig. 3-1. With a single bimorph, shown in Fig. 3-1a, there exists a lateral shift and a tangential tilt angle at the tip of the bimorph. If two bimorphs with inverted layer compositions are connected in series to form an S-shaped beam, as shown in Fig. 3-1b, the tilt angle at the tip of the second bimorph is compensated. However, the lateral shift still remains. If two S-shaped beams are connected in series with the second one folded, as in Fig. 3-1c, both the lateral shift and the tilt angle will be compensated.

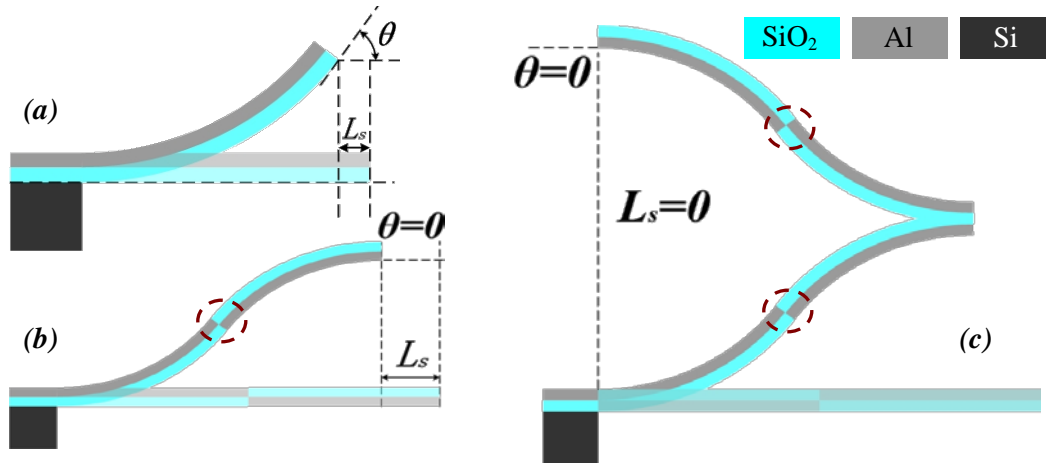


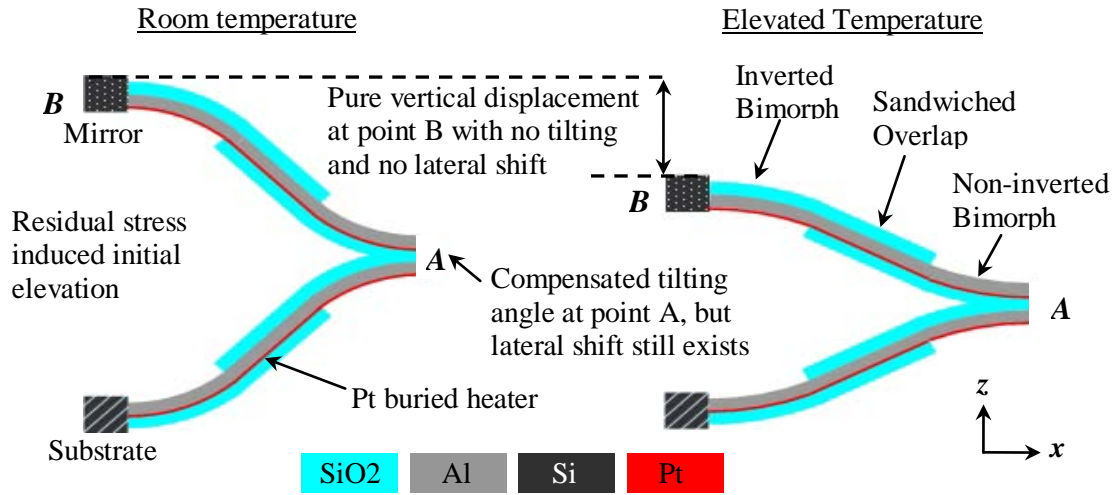
Figure 3-1. ISC concept. (a) Single bimorph with lateral shift and tangential tip tilt. (b) ISC bimorph with zero tip tilt but nonzero lateral shift. (c) Folded ISC bimorphs with zero tip tilt and zero lateral shift.

The device based on this ISC bimorph actuator suffers from the following problems. First, the mechanical robustness of the actuator is compromised by the weak connection between the bimorph segments, as indicated by the circled part in Fig. 3-1. Second, instead of embedding the heater along the bimorph path, the device design has the heater placed at one end of the bimorph actuator, thus resulting in non-uniform temperature distribution and very slow thermal response time. Third, the early ISC design implemented in a foundry CMOS process had pin holes in the SiO₂ layer which resulted in unwanted etch to the poly-Si heater and caused open circuit [160].

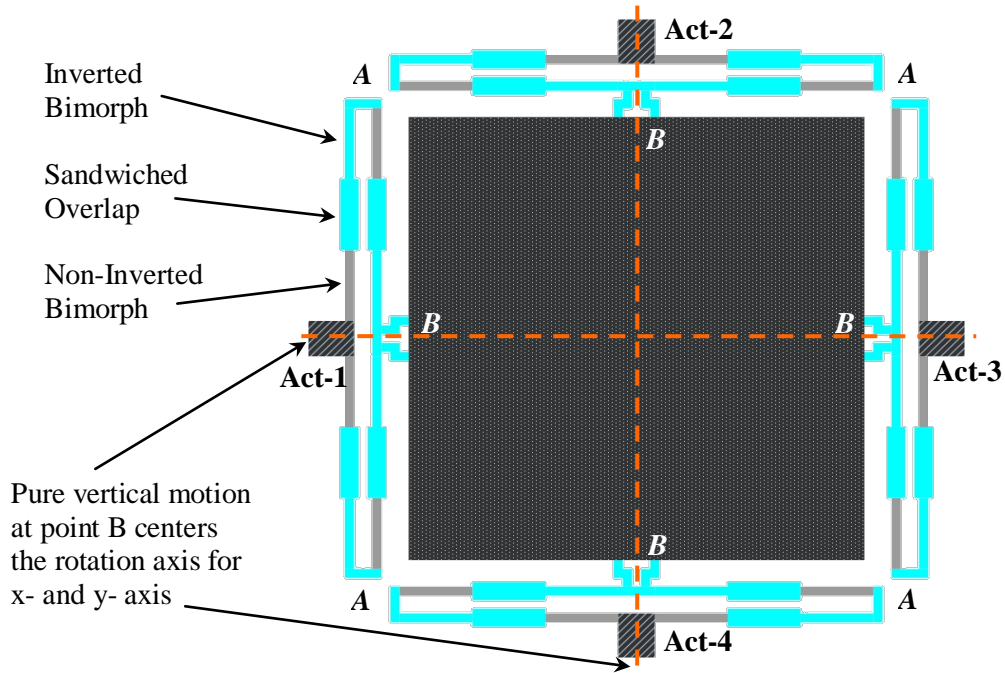
To solve these problems, an improved ISC design, *i.e.*, the FDS actuator design is proposed based on conventional MEMS processes. The side view of a FDS bimorph actuator design is illustrated in Fig. 3-2a. An overlap portion is added at the middle of each S-shaped bimorph beam to increase the mechanical robustness. Pt instead of Poly-Si is employed as the heater material and is embedded along the bimorph. The overlap portion is a sandwiched layer stack which consists of a bottom SiO₂ layer, middle Al layer and top SiO₂ layer. The bottom SiO₂ layer of the overlap portion connects to the bimorph segment that has Al on top and the top SiO₂ layer of the overlap portion connects to the bimorph segment that has SiO₂ on top; while

only a single Al layer goes along the entire FDS bimorph. The width of the overlap is increased to strengthen the connection as well as to increase the stiffness of the actuator. The temperature of the beams can be changed by applying a voltage to the Pt resistors embedded along the bimorph beams. By connecting four pairs of FDS bimorph actuators to the four sides of a square or circular mirror plate, TTP operation can be realized by controlling the voltages applied to the resistors. The top view of a FDS micromirror design is sketched in Fig. 3-2b, where four pairs of FDS actuators are located symmetrically on four sides of a mirror plate. Each pair of FDS actuators is connected to the mirror plate via a pure SiO₂ joint which ensures good thermal isolation between actuators and mirror plate and keep the mirror plate from being heated up and deforms. A Pt heater is embedded between the bottom SiO₂ and Al layer and shares the same path as the Al beam for uniformity. Each pair of FDS actuators shares a single Pt resistor.

When a same voltage is simultaneously applied to all four pairs of actuators the mirror plate moves vertically without any lateral shift. When different voltages are applied to the actuators, the mirror plate performs tip-tilt scanning. As shown in Fig. 3-2a, point B, which connects a bimorph actuator to the mirror plate, moves pure vertically if the bimorph beam is heated evenly. This condition is ensured by the embedded heater along the entire bimorph path. When a same dc bias is applied to all four actuators and a pair of differential ac voltage signals is applied to one pair of opposing actuators, *i.e.*, Act-1 and Act-3, the mirror plate will rotate about the y-axis and the rotation axis is structurally fixed by the other two opposing actuators, *i.e.*, Act-2 and Act-4. Thereby, both piston motion, decoupled from rotation, and tip-tilt scanning with a fixed rotation axis can be obtained.



(a) Side view of FDS bimorph actuator



(b) Top view of a TTP micromirror based on FDS actuator

Figure 3-2. (a) Side view of FDS bimorph actuator. (b) Device topology of the tip-tilt- piston mirror based on FDS with centered rotation axes.

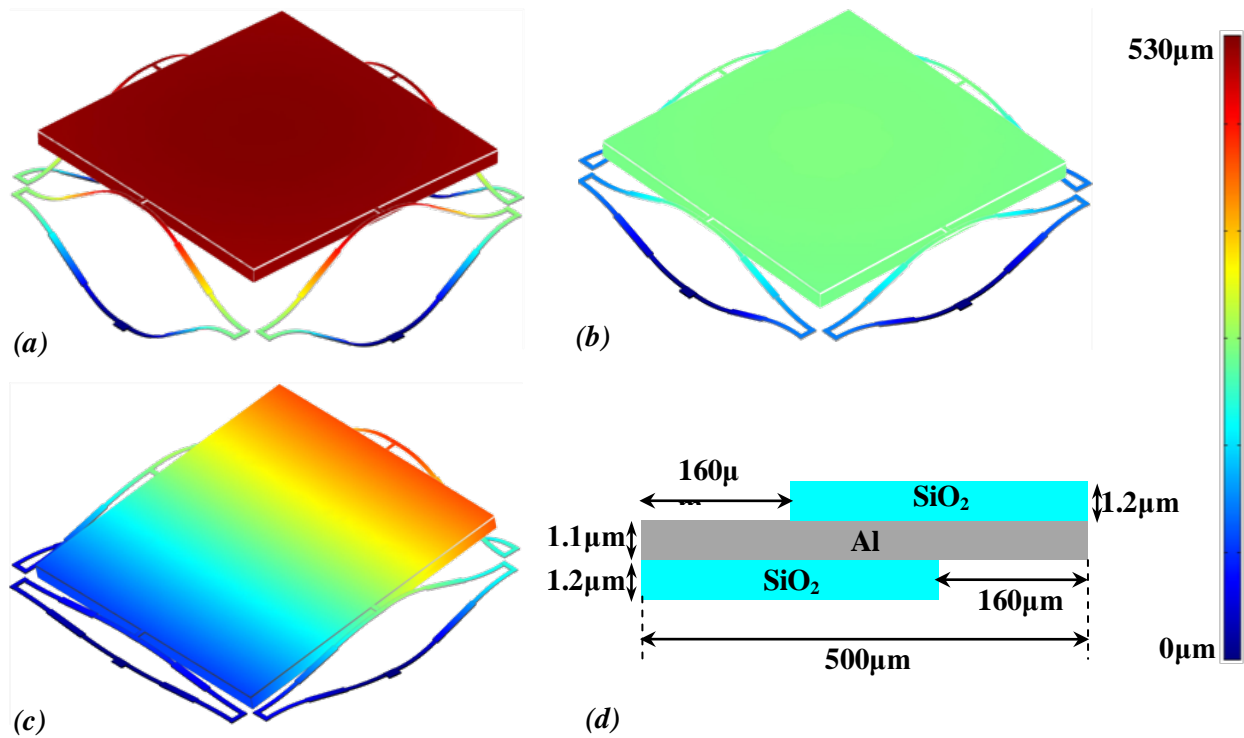


Figure 3-3. Simulation results by Comsol: (a) Initial elevation of the mirror plate due to higher-than-room- temperature thin film deposition temperatures; (b) Downward piston actuation by same temperature rise on all four actuators; (c) Tip/tilt actuation by superimposing differential temperature change on one of the two actuator pairs and maintain constant bias temperature on the other pair. (d) Structural parameters of one S-Shaped bimorph series used in the FEM simulations.

FEM model has been built to demonstrate the tip/tilt and piston thermal actuation of the proposed FDS device. For simplicity and conceptual demonstration, the model shown in Fig. 3-3 does not include the Pt resistor and the thin insulation SiO₂ layer. The mirror plate is 1 mm×1 mm in size with a 40 μm-thick silicon layer as mechanical support. The structural parameters of each S-shaped bimorph series is shown in Fig. 3-3d, and the widths of the bimorphs and the overlap regions are 16 μm and 24 μm, respectively. As shown in Fig. 3-3a, the mirror plate will be elevated out of plane at room temperature (300 K) due to the initial curling of the bimorphs which is caused by the deposition temperatures that are typically much higher than room temperature. For the purpose of understanding the operation principle of this device,

the deposition temperature is assumed at 600 K for all thin film layers. Thus, without actuation, the mirror plate, at 300 K, will be elevated above the substrate level by 528.6 μm upon structure release, as shown in Fig. 3-3a, resembling the initial elevation of the mirror plate shown in Fig. 3-2a. Increasing the temperature on all four actuator pairs will result in a downward piston actuation of the mirror plate. For instance, at 450 K, the mirror plate moves down by 265.3 μm , as shown in Fig. 3-3b. Tip/tilt actuation can be realized by superimposing differential temperature changes to one of the two opposing actuators, while the other two opposing actuators are maintained at a bias temperature. As shown in Fig. 3-3c, a mechanical rotation angle of 12.1° is obtained when all the actuators in one opposing pair are set at 450 K while the actuators of the other pair are set at 300 K and 600 K, respectively. It is also noticed that the weight of the mirror plate causes about 2 μm vertical displacement when the mirror device is placed horizontally. This is equivalent to a small DC offset which is typically negligible compared to the device's piston range of hundreds of microns. The primary resonance mode for the device shown in Fig. 3-3 was found to be the piston mode at 388 Hz. Interestingly, by swapping the top layers with the bottom layers in all bimorphs, the mirror plate can be initially below the substrate. A fabricated device with such a design will be presented in Section 3.2. Piston actuation of this device will cause the mirror plate to move upward.

3.2 1st-Generation FDS Micromirror

Jia et al. demonstrated the first working TTP micromirror design based on FDS actuators. The device showed an initial vertical displacement above the substrate plane and can be actuated downward for 141 μm at 5V DC. Further actuation was not executed for protection of the device. The measured lateral shift during the entire vertical actuation range is only 2 μm . An optical tip-tilt scanning range of $\pm 12^\circ$ was also achieved at less than 5V DC for both axes. A device with the initial mirror plate position below the substrate was also achieved by simply swapping Al/SiO₂

layer arrangement in all bimorph segments. This design helps protect the fragile mirror plate for easy handling and packaging and has a similar piston stroke and tip-tilt scanning angle compared with the device with mirror plate above the substrate plane. The design parameters of the device are summarized in Table 3-1. SEM images of the two devices are shown in Fig. 3-4a and Fig. 3-4b, respectively.

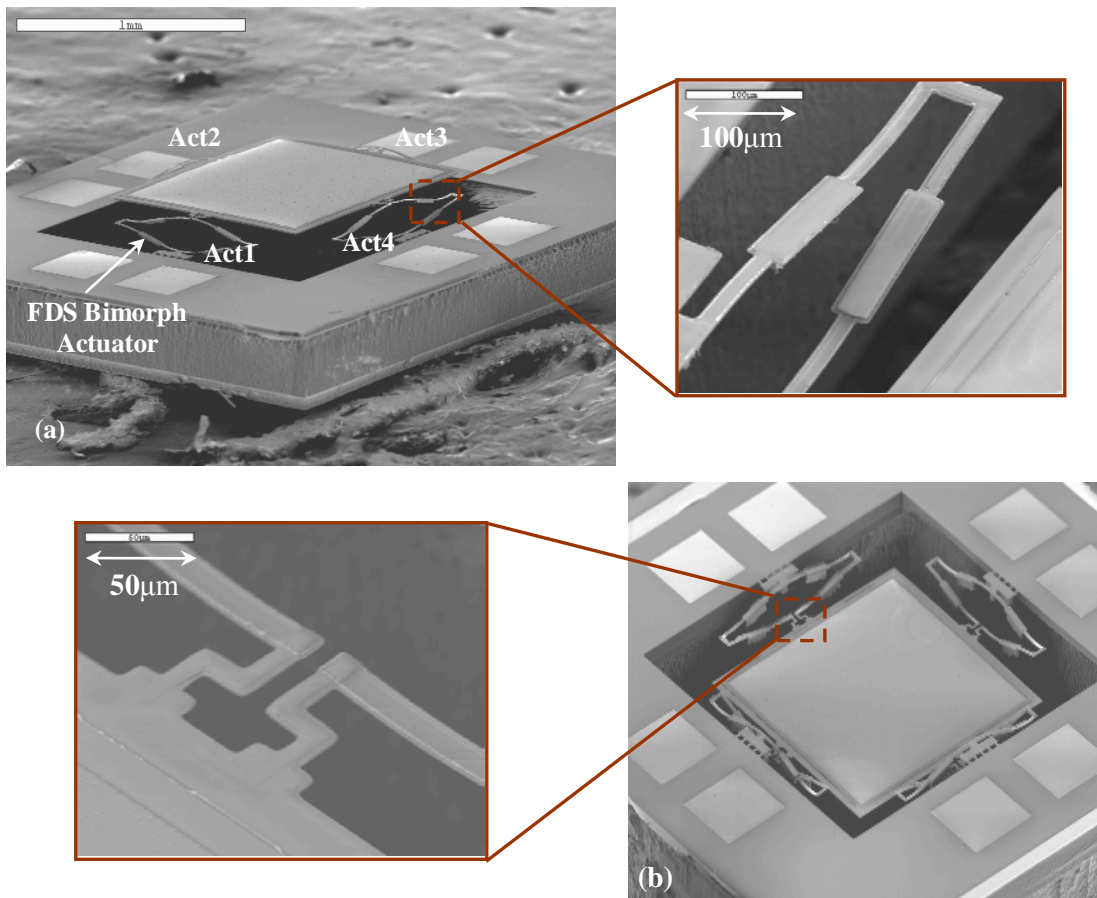


Figure 3-4. SEM images of 1st-generation FDS micromirror devices: (a) device with mirror plate above the substrate plane, and (b) device with mirror plate below the substrate plane.

Table 3-1. Design Parameters Summary of 1st-Generation FDS Device

Structural Parameters	Value
Mirror plate size	1.0mm×1.0mm
Device footprint	2.5mm×2.5mm
Area fill factor	16%
Length of S-shaped bimorph actuator	360μm
Length of NI bimorph segment	120 μm
Length of IV bimorph segment	120 μm
Length of over lap	120 μm
Width of bimorph	12μm
Width of overlap	24μm
Width of Pt heater	6μm
Thickness of bottom oxide	1.2μm
Thickness of Al	1.1μm
Thickness of top oxide	1.2μm
Thickness of Pt heater	0.25μm

The device was fabricated based on a regular silicon wafer. The process flow starts with an oxide deposition and patterning to define the bimorph beams that require oxide at the bottom (Fig. 3-5a). Then a Ti/Pt/Ti lift-off process is performed to form Pt heaters along the bimorphs to reduce thermal response time (Fig. 3-5b). Next, an oxide insulation layer is deposited, followed by an aluminum lift-off process to form the bimorphs and the mirror surface (Fig. 3-5c). Another oxide layer is then deposited and etched to complete the bimorph beams that require oxide on the top (Fig. 3-5d). Finally, a backside silicon etch is performed (Fig. 3-5e), followed by a front-side silicon etch for release (Fig. 3-5f).

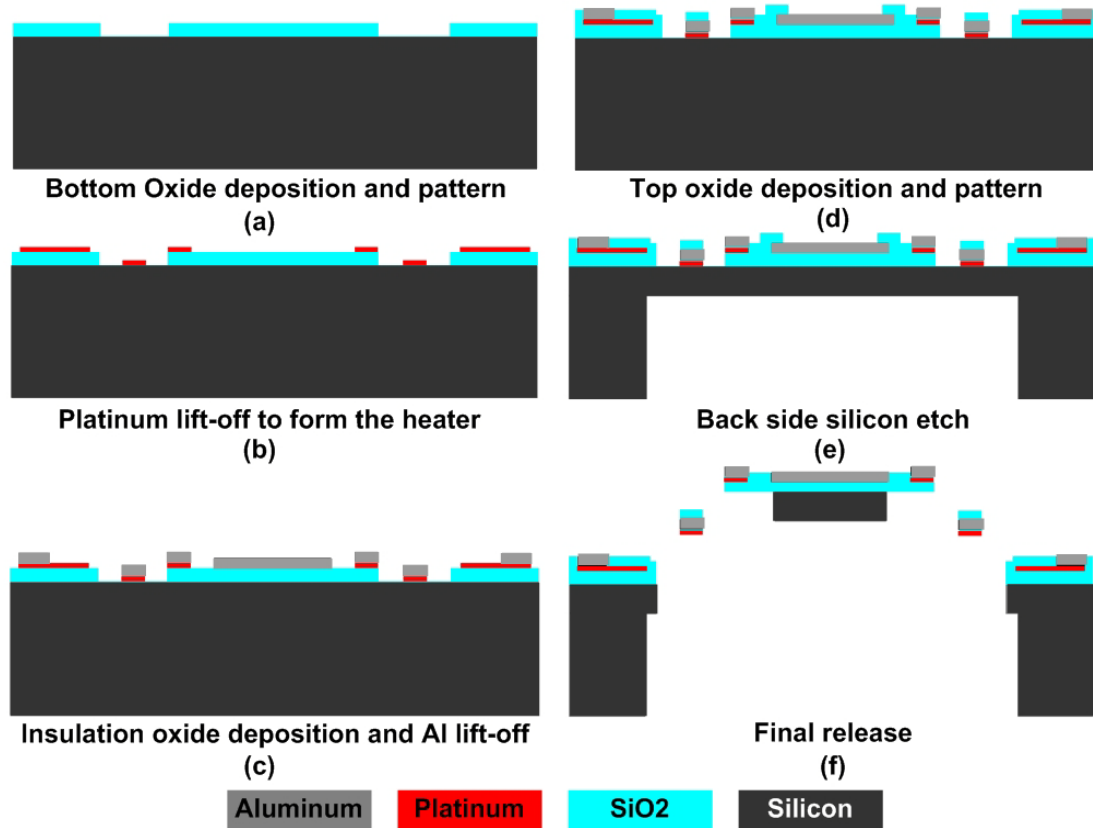


Figure 3-5. Fabrication process flow of 1st-generation FDS device: (a) Bottom oxide pattern. (b) Ti-Pt-Ti heater lift-off. (c) Insulation oxide deposition and Al lift-off. (d) Top oxide pattern. (e) Backside silicon etch. (f) Front side silicon etch through and release.

The mirror surface quality was measured using a Wyko-Vision32 optical profilometer. The measured radius of curvature changes between $\sim 0.15\text{m}$ to $\sim 0.30\text{m}$ from device to device due to non-uniform silicon thickness remaining after the backside silicon etching. The profile of the mirror plate surface was found to be convex which suggested that the main cause of the curvature is the compressively-stressed SiO₂ layer on top of the mirror plate. The problem of the small and varying mirror plate radius of curvature is addressed in the 2nd-generation FDS actuator based devices.

Static piston actuation of the mirror plate is characterized using an Olympus BX51 optical microscope equipped with a Quadra-Chek 200 micro-position recorder which has a reading resolution of $0.5\mu\text{m}$ for all three axes. After each increase of the supply voltage, the image was

refocused and the z-position reading of the mirror plate was recorded. Data points for multiple locations on the mirror plate were taken to verify its piston motion. The mirror plate has an initial tilting angle of approximately 0.2° . The resistances of the four Pt heaters were measured to be $256 \pm 2 \Omega$. The measurement result is shown in Fig. 3-6.

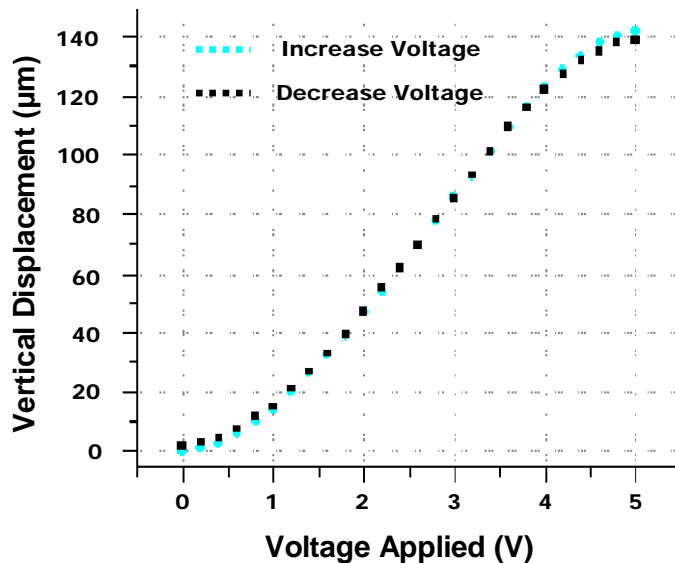


Figure 3-6. Static test result of piston mode actuation for 1st-Generation FDS device

The static rotation measurement was taken by applying a same dc voltage of 2.5V to all four actuators and at the same time superimposing two differentially varying voltages to one opposing actuator pair. A laser beam and a screen were used for this experiment. Fig. 3-7 shows the static measurement result for the rotation actuation. An optical scan angle of $\pm 12^\circ$ was achieved for both x- and y-axis at a pair of 2.5V differential voltages.

The 2-D scanning using this device was demonstrated by simultaneously exciting one or two pairs of actuators shown in Fig. 3-4a. Act1 and Act3, and Act2 and Act4 respectively have the same DC offset and differential AC signals. The frequency and phase of the AC signals were varied in order to generate the Lissajous patterns shown in Fig. 3-8.

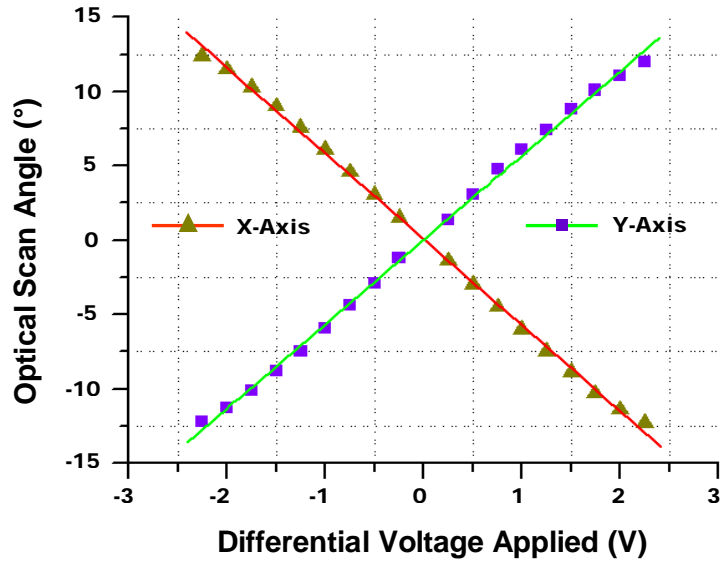


Figure 3-7. Static test result for tip-tilt mode actuation of 1st-Generation FDS device

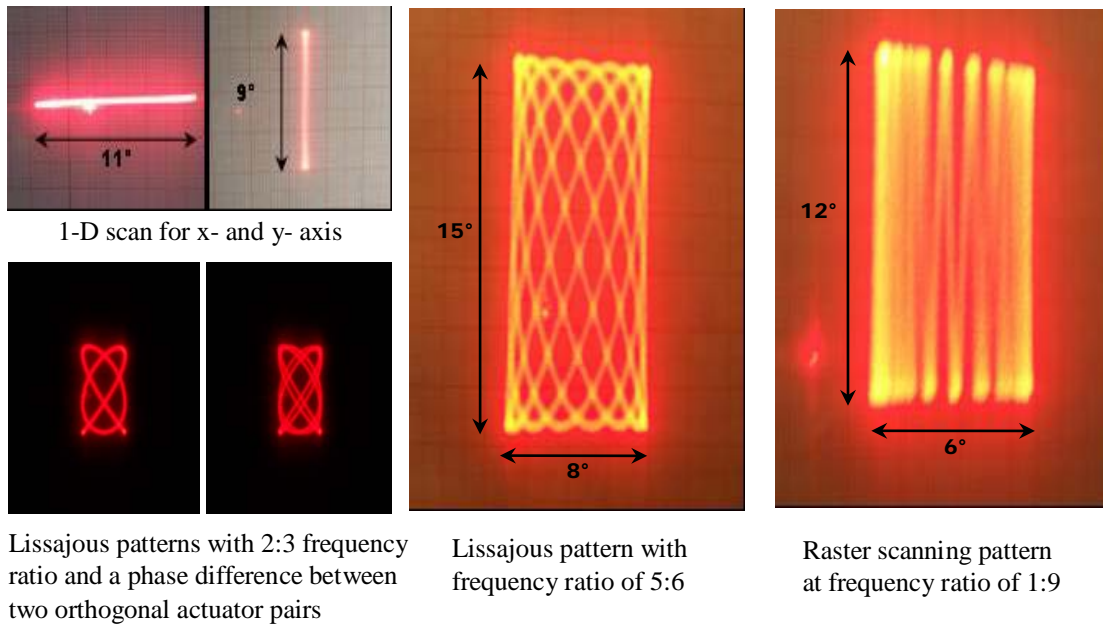


Figure 3-8. Various Lissajous patterns generated by varying AC signal frequency ratio and phase difference between the two orthogonal actuator pairs.

The 1st-generation FDS device has demonstrated successfully the TTP scanning capability. Based on the experimental experience gained from the design and testing of the 1st-generation

FDS device, the 2nd-generation FDS device focuses on solving the observed drawbacks and further improving device performance.

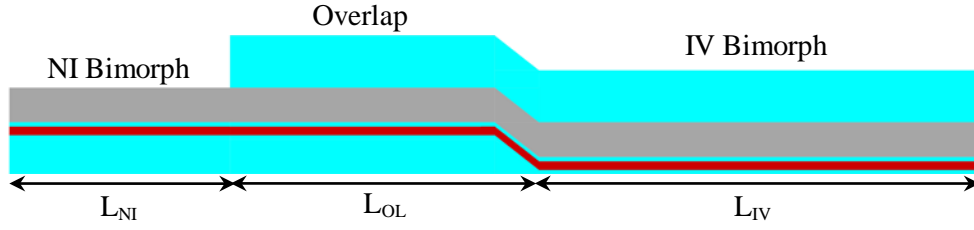
3.3 2nd-Generation FDS Micromirror: Optimization and Experimental Result

From previous section we know that although the 1st-generation FDS device has demonstrated TTP actuation capability successfully; it suffers from several other drawbacks. The non-uniform thickness of the remaining silicon under the mirror plate resulted in varying radius of curvature. The stressed thin film layers caused a convex profile of the top mirror surface and reduced radius of curvature. Moreover, the operation range is small compared with previously reported electrothermal bimorph based micromirrors. The 2nd-generation FDS micromirror is proposed to address these issues. Structural optimization has been conducted to increase the operation range by enhancing the initial displacement of the mirror plate and to relieve the stress level at the actuator-mirror joint, while the radius of curvature problem is addressed by modifying the process flow.

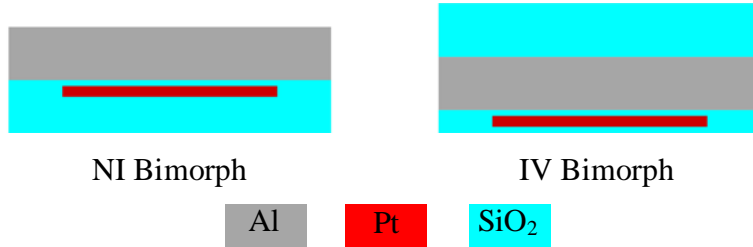
3.3.1 Structural Parameters Optimization

From Fig. 3-2 we know that each FDS actuator consists of a non-inverted (NI) bimorph, an overlap (OL), and an inverted (IV) bimorph. This is due to the fabrication process, as shown in Fig. 3-5, in which a layer of oxide is introduced between Al and Pt for electrical insulation (Fig. 3-5c). This structural asymmetry is further illustrated in Fig. 3-9. In the 1st-generation FDS device the impact of this thin layer was not taken into consideration due to its small thickness. However, it was found that this structural asymmetry will indeed cause significant mismatch between the actuation characteristics of IV and NI bimorphs. Due to the symmetric locations of the FDS actuators around the micromirror, the mirror plate will still be parallel to the substrate surface even with a non-optimal L_{IV}/L_{NI} ratio. But non-optimal length ratios will cause torques acting on the mirror-actuator joints during the actuation, reducing the actuation range and the

device operating stability and reliability. To obtain the optimal length ratio, the changes of the radii of curvature of both IV and NI bimorphs upon the same temperature rise must be found.



(a) Three segments of half an FDS bimorph actuator



(b) Cross sectional view based on realistic NI and IV bimorph

Figure 3-9. Cross sectional view of a realistic S-Shaped half-FDS bimorph actuator

FEM simulations based on the actual layer dimensions of the IV and NI bimorphs have been carried out to obtain the optimal length ratio. Fig. 3-10 shows the simulated inverse of radius of curvature versus temperature change for both IV and NI bimorphs. The ratio of the two plots in Fig. 3-10 gives a constant of ~2.1 which means that under the same temperature change, the radius of curvature of the NI bimorph will change ~2.1 times as much as that for the IV bimorph. From Eq. (2-7) we have:

$$\theta_{NI} = \theta_{IV} \Rightarrow \frac{L_{NI}}{\rho_{NI}} = \frac{L_{IV}}{\rho_{IV}} \Rightarrow \frac{L_{IV}}{L_{NI}} = \frac{\rho_{NI}}{\rho_{IV}} \approx 2.1 \quad (9)$$

from which we can conclude that in order to realize the full tip tilt compensation during the entire actuation range, the length of the IV bimorph must be ~2.1 times of the length of the NI bimorph.

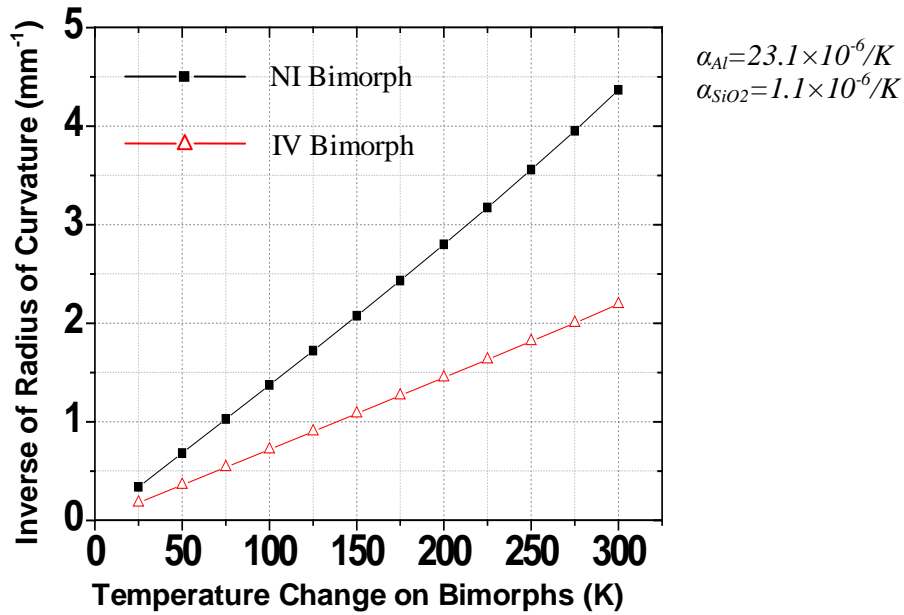


Figure 3-10. FEM simulation result of change in bimorph radii of curvature upon temperature variation.

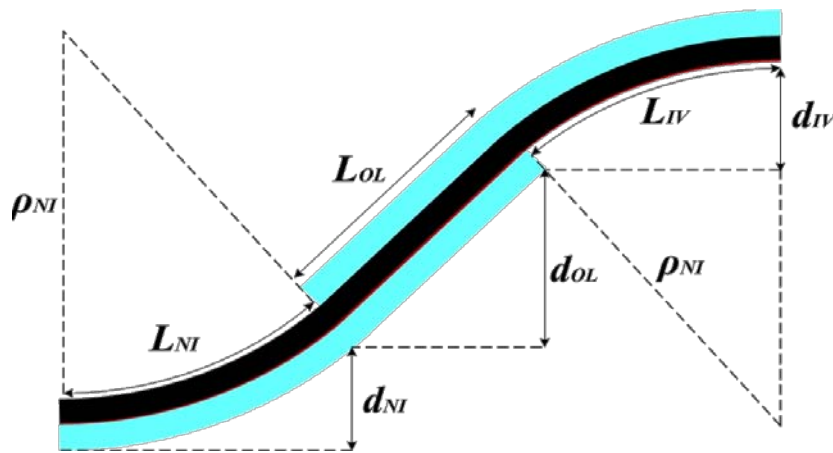


Figure 3-11. Beam deflection parameters of half an FDS bimorph actuator

The side view of an S-shaped half FDS actuator is shown in Fig. 3-11. The tip displacement of a cantilevered bimorph actuator has been readily derived as in Eq. (2-25).

Hence, we can derive the total tip displacement of an S-shaped half FDS actuator using the deflection parameters shown in Fig. 3-11 as:

$$\begin{aligned} d_{FDS} &= d_{NI} + d_{IV} + d_{OL} \\ &= \rho_{NI}(1 - \cos \theta_{NI}) + \rho_{IV}(1 - \cos \theta_{IV}) + L_{OL} \sin \theta_{NI} \end{aligned} \quad (3-2)$$

where ρ_{NI} and ρ_{IV} are the radius of curvature of NI and IV bimorph respectively. L_{OL} is the length of the overlap structure. Under the condition that the tilt at a FDS bimorph tip is fully compensated, *i.e.*, $\theta_{NI} = \theta_{IV} = \theta$, we have:

$$\theta = \frac{L_{NI}}{\rho_{NI}} = \frac{L_{IV}}{\rho_{IV}} \quad (3-3)$$

Plugging Eq. (3-1) into Eq. (3-3) yields:

$$\frac{\rho_{IV}}{\rho_{NI}} = 2.1 \quad (3-4)$$

Plugging Eq. (3-4) into Eq. (3-2), we have:

$$\begin{aligned} d_{FDS} &= \rho_{NI}(1 - \cos \theta) + \rho_{IV}(1 - \cos \theta) + L_{OL} \sin \theta \\ &= \rho_{NI}(1 - \cos \theta) + 2.1 \times \rho_{NI}(1 - \cos \theta) + L_{OL} \sin \theta \\ &= 3.1 \times \rho_{NI}(1 - \cos \theta) + L_{OL} \sin \frac{L_{NI}}{\rho_{NI}} \\ &= 3.1 \times d_{NI} + \eta_{OL} L_b \sin \frac{(1 - \eta_{OL}) L}{3.1 \rho_{NI}} \end{aligned} \quad (3-5)$$

in which η_{OL} is the normalized length of the overlap to the length of one S-shaped actuator, L . The tip displacement of the NI bimorph, d_{NI} , and the radius of curvature of the NI bimorph Based on Eq. (3-5), we can analyze the effects of the overlap length on the initial tip displacement. Normalized d_{FDS} as a function of η_{OL} is plotted in Fig. 3-12, where the Al and oxide deposition temperatures are assumed as 600K and 400K, respectively.

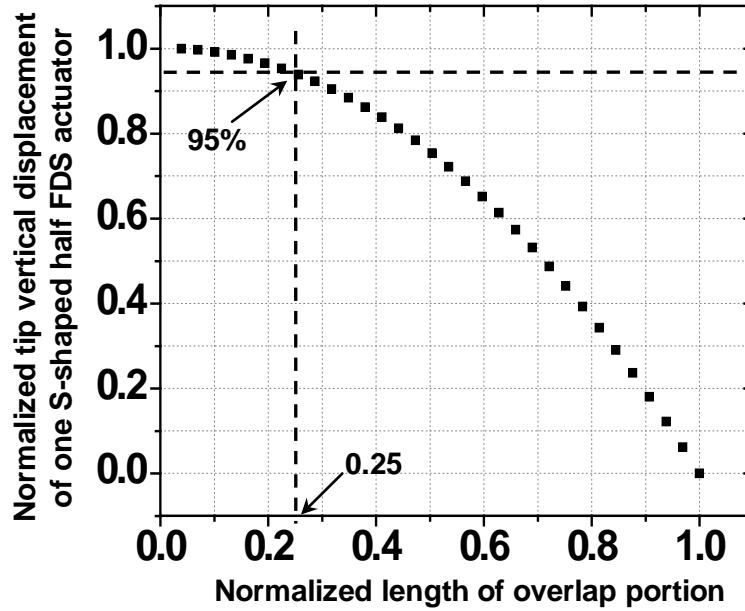


Figure 3-12. Plot of the normalized tip displacement of a half FDS actuator versus the normalized overlap length.

As Fig. 3-12 shows, the vertical displacement of the tip of the S-shaped half-FDS actuator decreases with the normalized length of overlap portion. However, considering the robustness of the actuator, we require the overlap portion to strengthen the connection between the NI and IV bimorphs. From the aspect of the device rigidity, we also need the overlap portion to increase vertical stiffness. Thereby, a reasonable proportion of $\eta_{OL}=0.25$ is chosen to meet the above said requirements while still maintaining approximately 95% of the maximum displacement.

With the overlap occupying 25% of the beam length, L , the normalized lengths of the NI and IV bimorph portions are 24% and 51%, respectively, according to Eq. (3-1).

Following the above optimization result, the structural parameters of the 2nd-generation FDS micromirror is summarized in Table 3-2.

Table 3-2. Design Parameters Summary of the 2nd-Generation FDS Device

Structural Parameters	Value
Mirror plate size	1.08mm×1.08
Device footprint	2.0mm×2.0m
Area fill factor	30%
Length of S-shaped bimorph	500μm
Length of NI bimorph segment	120 μm
Length of IV bimorph segment	250 μm
Length of over lap	130 μm
Width of bimorph	16μm
Width of overlap	32μm
Width of Pt heater	6μm
Thickness of bottom oxide	1.2μm
Thickness of Al	1.1μm
Thickness of top oxide	1.2μm
Thickness of Pt heater	0.25μm

3.3.2 Fabrication Process Optimization

The main cause of the non-uniform silicon thickness under the mirror plate is the non-uniform etching rate across the wafer during backside DRIE silicon etching. Although the wafer was later dissected and processed on die level, it is still difficult and time consuming to etch each die to the same thickness. An effective solution to this issue is to use SOI wafer instead of bare silicon wafer. The device layer of the SOI wafer can be used as mechanical support for the mirror plate, while the buried SiO₂ layer can be used as an etch-stop barrier for the backside silicon etching step. Fig. 3-13 shows the revised process flow for the 2nd-generation FDS micromirror based on SOI wafer. In this fabrication process, the SiO₂ layer on the mirror plate top surface is also removed for the benefit of mirror plate flatness.

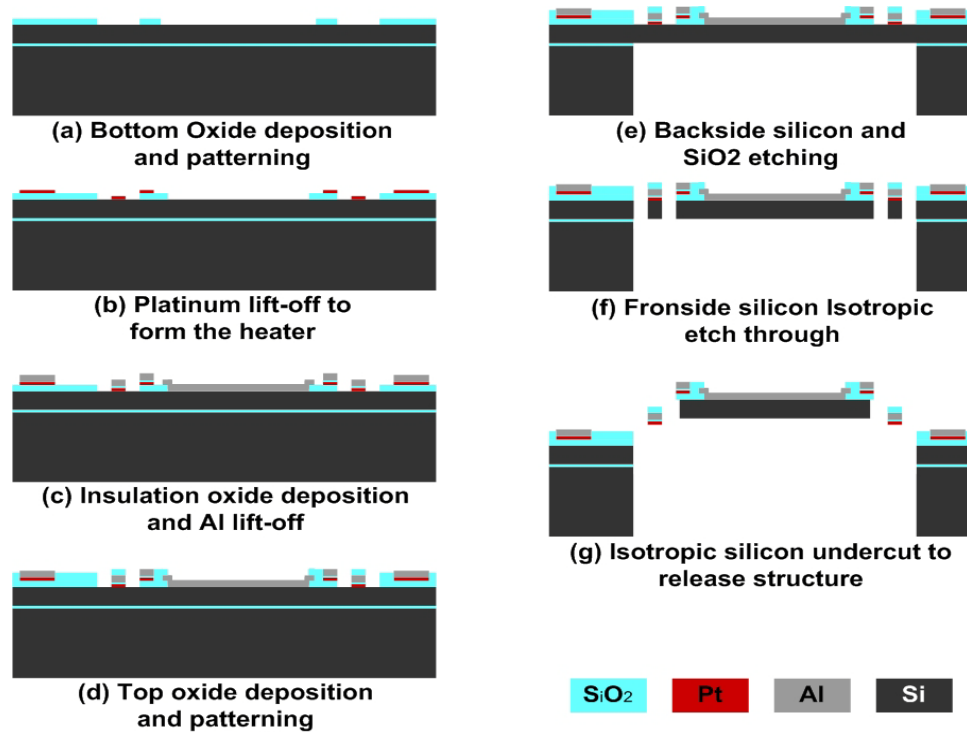


Figure 3-13. Cross-sectional view of the process flow: (a) Bottom oxide patterning. (b) Cr-Pt-Cr heater lift-off. (c) Insulation oxide deposition and Al lift-off. (d) Top oxide patterning. (e) Backside silicon and silicon dioxide etch. (f) Front side silicon etch-through. (g) Release.

3.3.3 Experimental Result of 2nd-Generation FDS Micromirror

3.3.3.1 Static test result

A fabricated 2nd-generation FDS micromirror is shown in Fig. 3-14. The initial elevation of the mirror plate was greatly increased from the 1st-generation FDS device, thereby giving it much larger piston actuation stroke of 480 μ m. Part of the reason for this increase is due to the increase in bimorph length. However, the half FDS bimorph beam length was only increased from 330 μ m to 500 μ m, which can not offer the more than tripled increase for the initial elevation of the mirror plate (1st-generation \sim 141 μ m, 2nd-generation \sim 480 μ m). Therefore, we can conclude that the large increase of the initial elevation is indeed a direct result of the optimization.

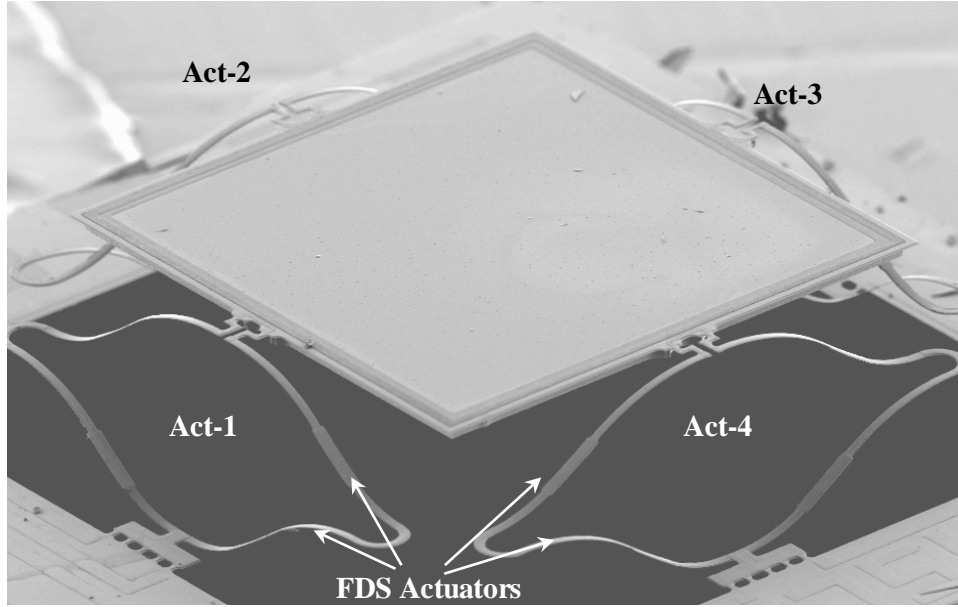


Figure 3-14. SEM images of the 2nd-generation FDS micromirror device showing 480 μ m initial mirror plate elevation

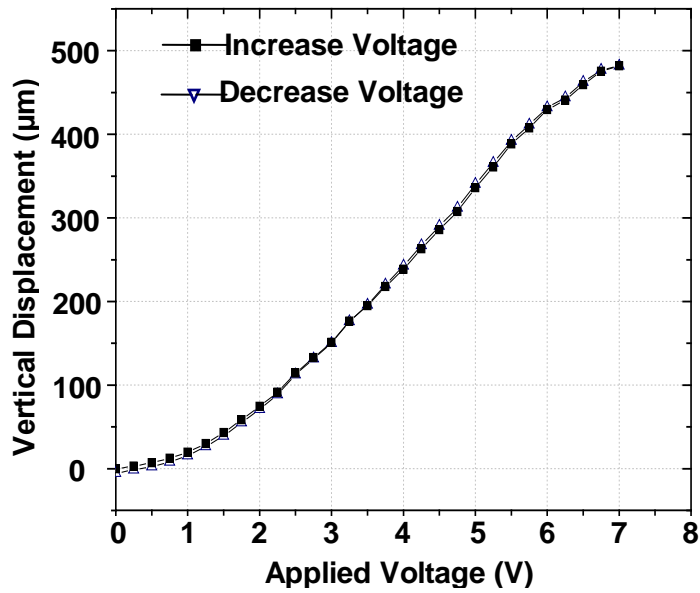


Figure 3-15. Static measurement result of piston mode actuation for the 2nd-generation FDS micromirror.

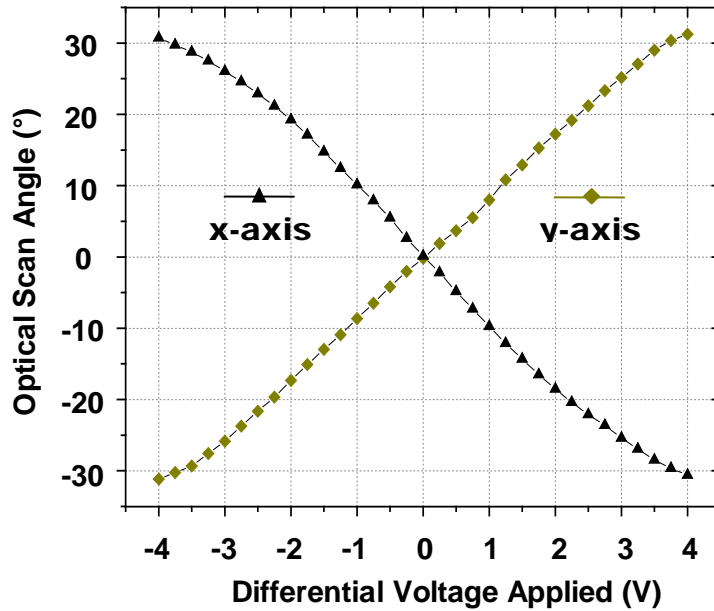


Figure 3-16. Static measurement result of rotation mode actuation for the 2nd-generation FDS micromirror. All actuators had a dc voltage of 4V.

The static testing procedures of the 2nd-generation FDS micromirror follow what has been done for the 1st-generation FDS device. Fig. 3-15 presents the static test result of piston actuation. A small lateral shift of 2 μ m was observed during the entire 480 μ m actuation range at 7V DC. The mirror plate showed similar initial tilting of $\sim 0.2^\circ$ but was increased to $\sim 0.5^\circ$ at the end of the actuation. This deterioration is mainly due to the variation in the resistances which were measured to be $550 \pm 20 \Omega$.

Tip-tilt actuation of the 2nd-generation FDS micromirror was also measured using a laser beam and a screen. Fig. 3-16 shows the static measurement result for the rotation actuation. An optical scan angle of $\pm 30^\circ$ was achieved for both x- and y-axis at a pair of 4V differential voltages.

Notice that the highest voltage applied in the above measurements was 8V dc. The maximum static power consumption for each actuator was estimated to be ~ 60 mW.

3.3.3.2 Dynamic test result

The electromechanical response time of the actuator was measured by monitoring the light spot reflected by the mirror plate with a photosensitive device (PSD). A 2 Hz square-wave voltage (0-3.5 V) was applied to a single actuator. The voltage output from the PSD shows that the 10% to 90% response time is less than 10 ms, as shown in Fig. 3-17.

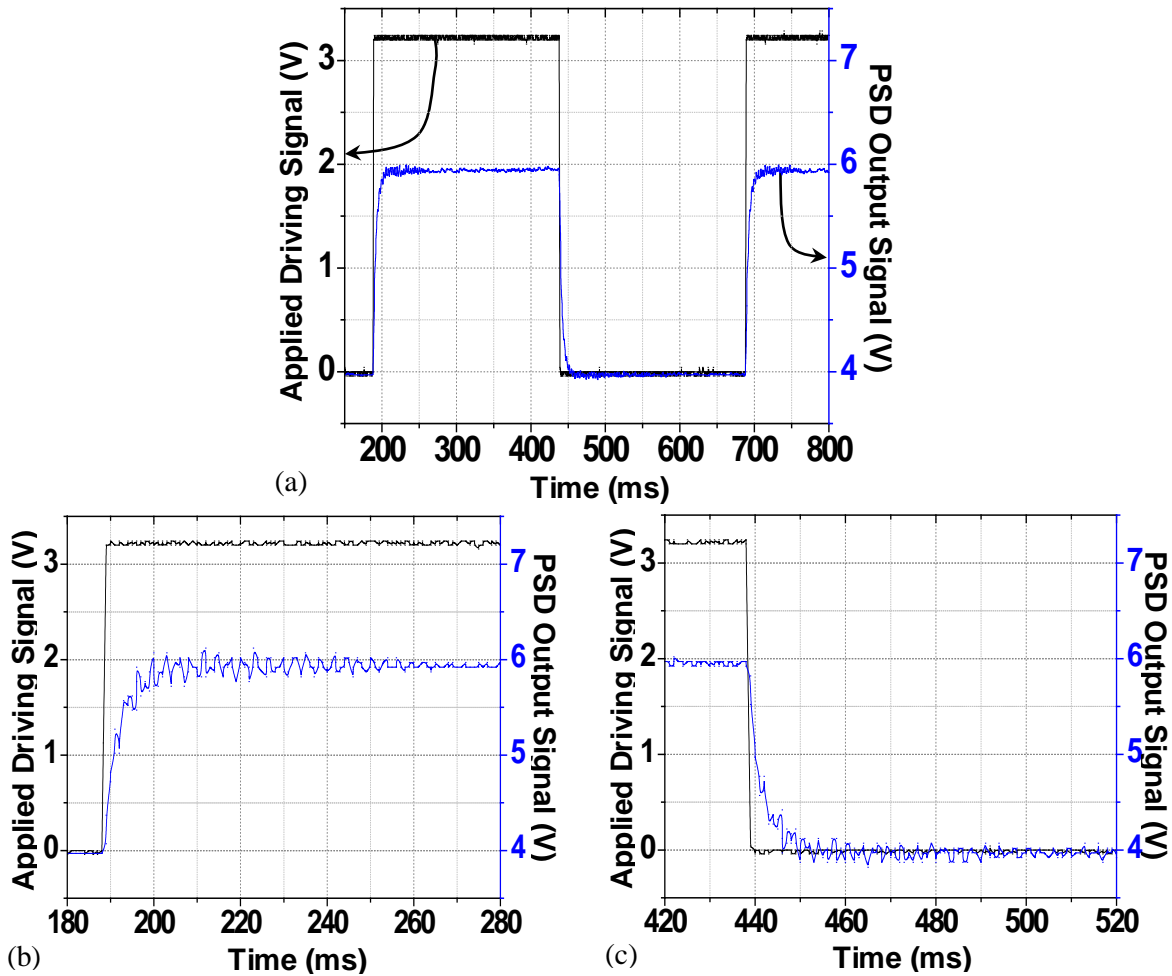


Figure 3-17. Transient response measurement. (a) Step response; (b) Rise edge; (c) Fall edge.

A Polytech Laser Vibrometer (LV) MSV 300 was used to obtain the frequency response of the piston mode. All four actuators were applied with a same driving signal from the LV to generate the piston actuation. The LV can calculate for the mirror plate vertical displacements

from the recorded interferogram data. The measured frequency response for the piston mode is shown in Fig. 3-18. The piston resonance frequency is 336 Hz with a Q-factor of 18.

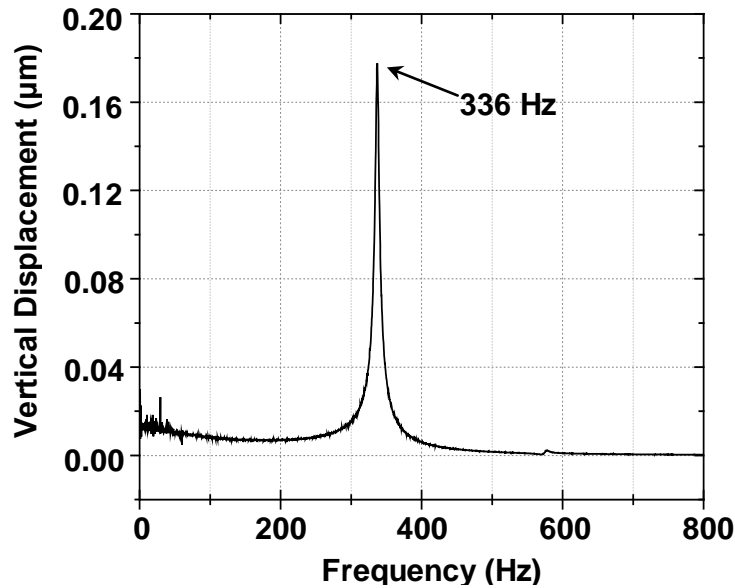


Figure 3-18. 2nd-generation FDS micromirror frequency response of piston actuation.

The frequency response of the tip-tilt mode was measured by applying a same DC voltage to all actuators and a pair of differential AC signals to one opposing actuator pair. Rotation angles at different frequencies of the AC signal were calculated using a laser and a screen. The frequency response for the rotation mode is shown in Fig. 3-19, indicating the resonance frequency of 488 Hz with a Q factor of 8. The small peak at 640 Hz corresponds to an unwanted resonance mode where the straight line-mode scanning deteriorates to an ecliptic scan pattern.

1-D and 2-D scans using this device were demonstrated by simultaneously exciting two pairs of the actuators. By varying the frequency and phase of the AC signals, different Lissajous patterns were generated and shown in Fig. 3-20 (a)-(d). It was noticed that when the device was driven at its resonance frequency of the rotation mode, the optical scan angle can go up to $\pm 60^\circ$ with 4V differential voltages.

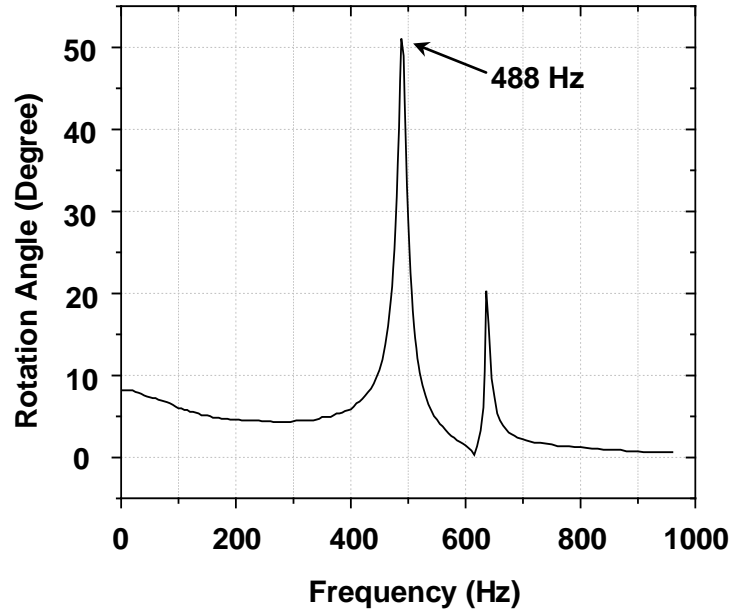


Figure 3-19. 2nd-generation FDS micromirror frequency response of rotation actuation.

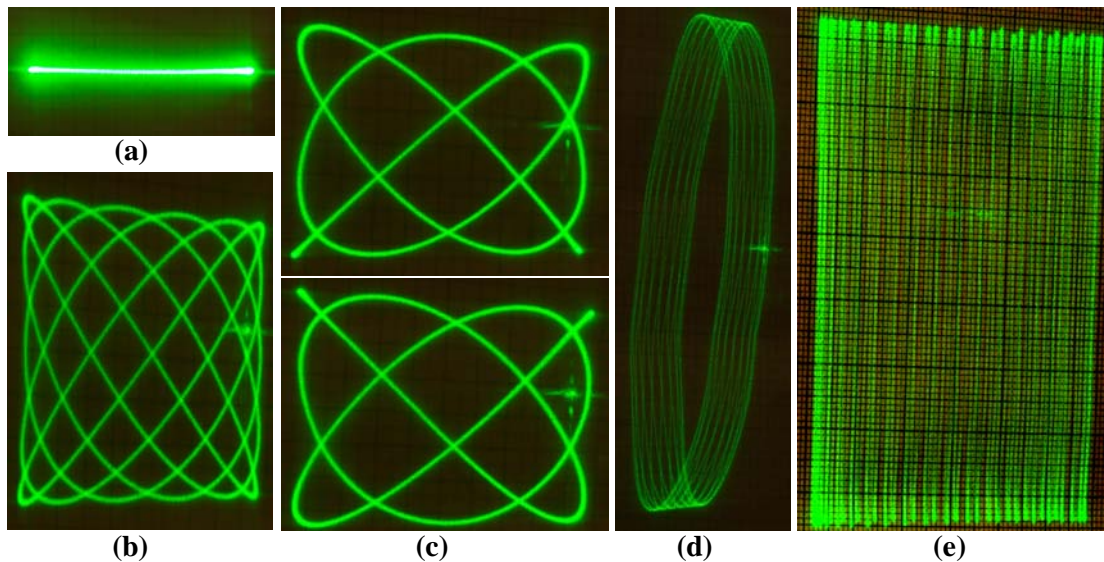


Figure 3-20. Various Lissajous patterns generated by varying AC signal frequency ratio and phase difference between the two orthogonal actuator pairs. (a) 1D scan; (b) Lissajous patterns with frequency ratio of 5:6; (c) Lissajous patterns with frequency ratio of 5:6 and a phase difference of 30 degrees; (d) Band pattern with one axis at resonance; (e) Raster scan with 40 lines (frequencies for two axes: 480Hz and 12Hz)

3.3.3.3 Test of device repeatability

A differential voltage pair swinging from 2 V to 6 V were applied to one opposing actuator pair of a fabricated device. The mirror scanned mechanically $\pm 10^\circ$ (equivalent optical scan

range: 40°) at 100 Hz for two weeks. The device initially experienced some scan range fluctuations, partially due to the self thermal annealing effect, but maintained stable scanning 12 hours later until the end of the test. Fig. 3-21 shows the reliability test result during the 336 hours. The device still operates normally after 120 million full-range scan cycles. More reliability study of similar devices has been reported in

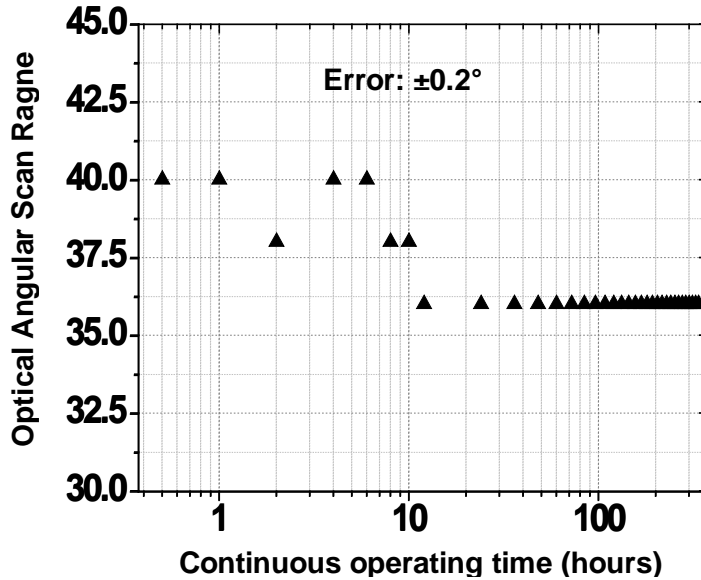


Figure 3-21. 2nd-generation FDS micromirror reliability test.

3.3.3.4 Quality of the mirror surface

The quality of the mirror plate was measured using a Wyko-Vision32 white light optical profilometer. Due to the 40 μm-thick bulk silicon mechanical support, the measured radius of curvature over the 1mm by 1mm mirror plate surface is about 0.5 m with the peak-to-valley deformation of 0.3 μm. The standard deviation surface roughness is about 30 nm. Fig. 3-22 shows the measured 2-D mirror surface contour plot and the surface profile along the center line. Surface reflection loss was estimated by measuring the optical power before and after reflected by the mirror, and a roughly 0.5 dB loss was measured.

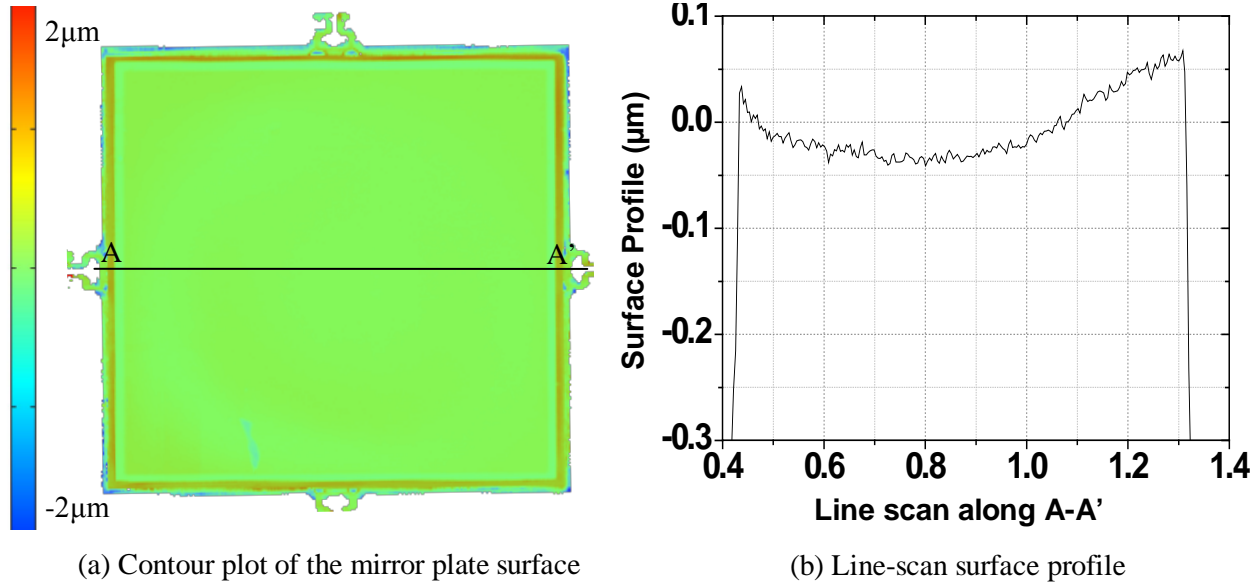


Figure 3-22. Mirror surface measurement result: (a) Contour plot of the 2-D surface; (b) Line scan mirror surface profile

3.4 Summary

From the experimental results summarized above, we see the performance of the 2nd-generation FDS micromirror device has been improved dramatically after being optimized from the 1st-generation FDS device. Compared with previously reported other electrothermal micromirrors, the 2nd-generation FDS micromirror has shown comparable operating range but much smaller lateral shift during piston actuation. The 2nd-generation FDS device also has structurally fixed rotation axes for both in-plane dimensions. The area fill factor has improved from 16% to 30%. The 30% area fill factor is among the highest ever reported and the device footprint of 2.0mm×2.0mm is also among the smallest. Biomedical imaging application based on the 2nd-generation FDS micromirror will be discussed in Chapter 5. Although the 2nd-generation FDS micromirror has achieved superior HFF and smaller footprint than other reported electrothermal micromirror, the design still need further improvement in order to achieve the projective of this work, which is a micromirror with ultra-high area fill factor and simple

packaging that would enable further miniaturization of the imaging probe. Micromirror device developed from the 2nd-generation FDS micromirror will be demonstrated to achieve ultra-high fill factor. An array of this design will also achieve HFF MMA. The development of the 3rd-generation FDS micromirror device and the HFF MMA device will be discussed in Chapter 4.

CHAPTER 4
DEVELOPMENT OF MICROMIRROR AND MICROMIRROR ARRAY DEVICES WITH
ULTRA-HIGH AREA FILL FACTOR

As mentioned in Chapter 2, in order to achieve high area fill factor, the actuator must be hidden under the mirror plate. The 1st- and 2nd-generation micromirror devices developed in Chapter 3 do not have the hidden actuator implemented and thus only achieve a fill factor of 30%. Moreover, if the 1st- and 2nd-generation micromirror devices were to be used in an imaging probe, they still need room for wire bonding and thus do not meet the objective of this work. In this chapter, based on the micromirror devices developed in Chapter 3, we will demonstrate the micromirror and MMA devices with ultra-high fill factor that meet the two objectives of this work as stated in Section 2.2 and Section 2.3.

4.1 Development of the 3rd-Generation FDS Micromirror Device

4.1.1 Design Concept of the 3rd-Generation FDS Micromirror

The area usage of 2nd-generation FDS micromirror is illustrated in Fig. 4-1. The outer area covered in dashed grey is the substrate silicon to support the actuator. The area in the middle covered in gradient yellow is taken by actuators. In the center is the mirror plate which is the effective optical aperture.

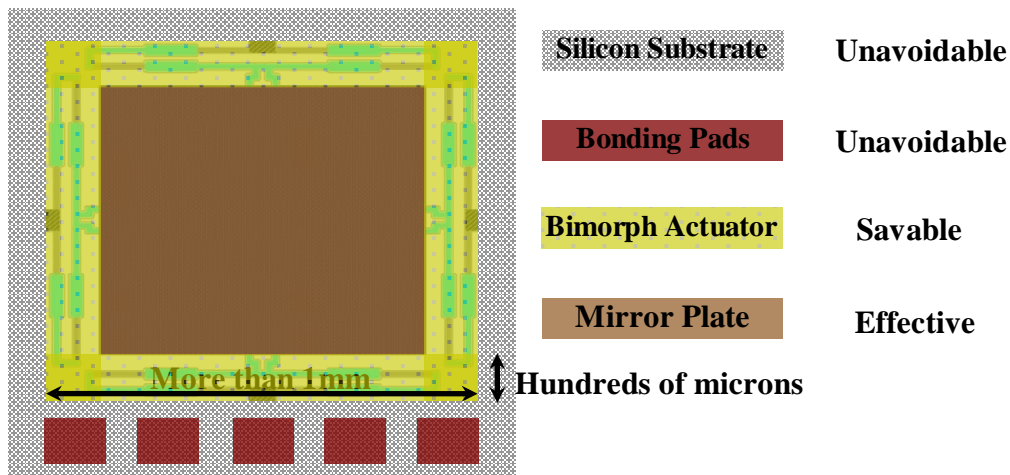


Figure 4-1. Area usage of 2nd-generation FDS micromirror

Calculated from the dimensions of the 1st- and 2nd- generations of the FDS micromirror, the area taken by the actuators is even more than the area of the mirror plate, which suggests that if the actuator area can be hidden, the fill factor could be doubled. We want to avoid the need of manually assembling or using a bonding-transfer technique to realize the hidden actuators. However, with the current designs in which the mirror plate rises above the substrate level, it is impossible to hide the actuators underneath the mirror plate based on this single wafer process. In Section 3.2 we have presented a FDS micromirror with mirror plate initial position below the substrate, as shown in Fig. 3-4. In Section 3.3 we also demonstrated a FDS micromirror based on SOI substrate with 480 μ m initial elevation. Combining the two designs provides a way to hide the FDS actuators underneath the mirror plate without extra bonding process. Fig. 4-2 illustrates the actuation concept of the hidden FDS actuators, *i.e.* the actuator of the 3rd-generation FDS micromirror. A 3-D model of the proposed 3rd-generation FDS micromirror is built and shown in Fig. 4-3 which can illustrate the device structure more clearly. For drawing conveniences, the bond pads and silicon support is not included in the model in Fig. 4-3.

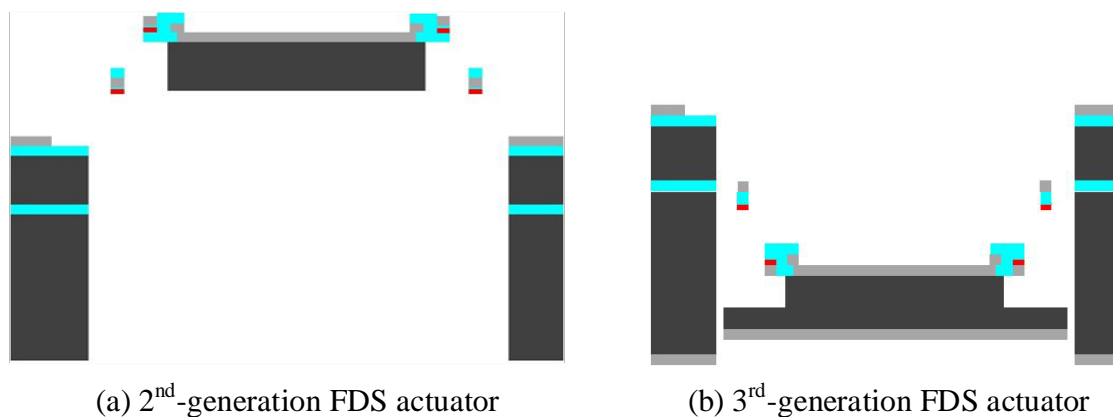


Figure 4-2. Structural demonstration of 2nd- and 3rd-generation FDS actuators

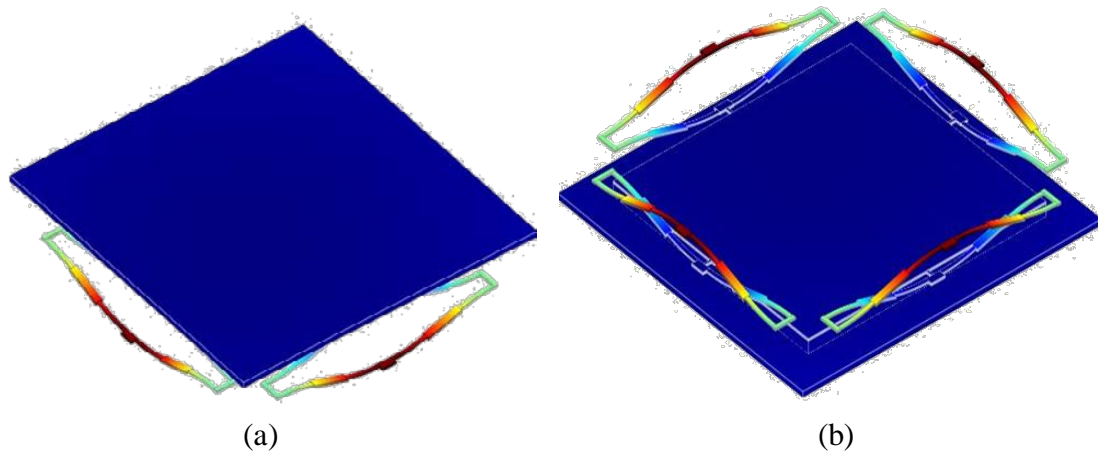


Figure 4-3. 3D illustration of the 3rd-generation FDS micromirror: (a) Bird view from mirror plate; (b) Bird view from the hidden actuators

This design can further increase the fill factor of the individual micromirror device. Meanwhile, because the bonding pads and the optical aperture are on opposite sides of the chip substrate, this design does not need wire bonding to realize the electrical connection. Instead, it can be implemented to an imaging probe by using surface mounting technique or flip-chip bonding technique, which can reduce the area consumption and further miniaturize the size of the imaging probe.

4.1.2 Fabrication Process of the 3rd-Generation FDS Micromirror

The fabrication process for the 3rd-generation FDS micromirror is illustrated in Fig. 4-4. The process steps on the actuator side is similar to the fabrication process of the 2nd-generation FDS micromirror, where SiO₂, Pt, SiO₂, Al, and SiO₂ thin films are sequentially deposited and patterned (Fig. 4-4a ~Fig. 4-4e). Then a front-side silicon etch is performed to define the mirror plates (Fig. 4-4f). Next, backside silicon etching and SiO₂ etching steps are performed to form the mirror plates, followed by Al deposition (0.2 μm) for reflective mirror surface (Fig. 4-4g). Finally, the silicon under the bimorph actuators is undercut to release the mirror plates (Fig. 4-4h). During the final release step, the isotropic Si etching will reduce the thickness of the

extended mirror plate where open gaps between the actuator beams are present. This requires the thickness of the device layer Si to be larger than what is required for previous designs. To maintain the flatness of the entire mirror plate, the device layer Si thickness is chosen to be 90~100 μm , which leaves $\sim 30 \mu\text{m}$ Si on the edge even after the final isotropic Si etching.

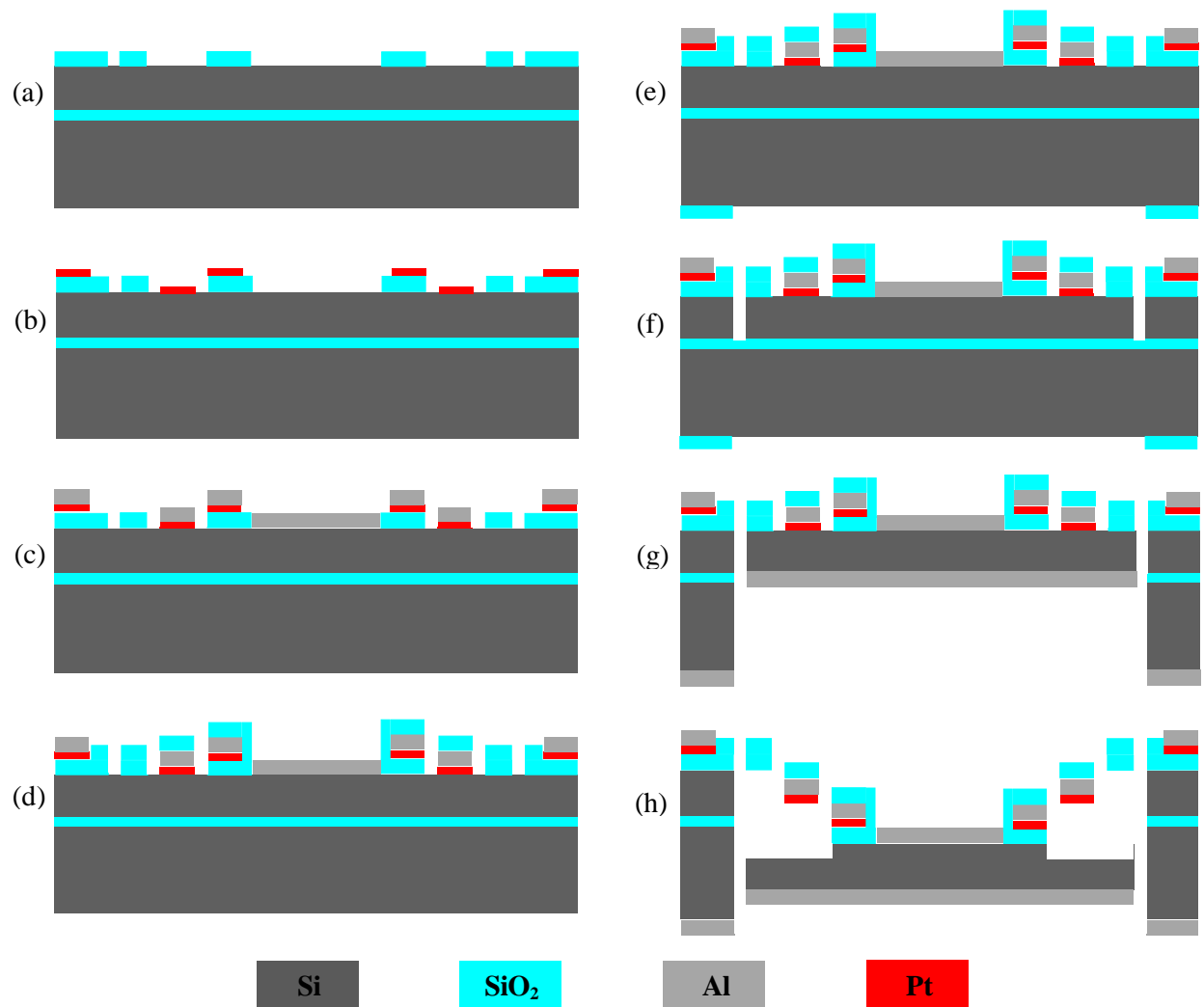


Figure 4-4. Cross-sectional view of the proposed process flow for 3rd generation FDS micromirror: (a) Start with SOI wafer; (b) Double side SiO₂ deposition and front side SiO₂ patterning; (c) Heater lift-off, insulation SiO₂ deposition and Al lift-off; (d) Top layer SiO₂ deposition and patterning; (e) Backside SiO₂ etch; (f) Front side Si etch; (g) Backside Si etch and buried SiO₂ etch; (h) Structure release and Al coating for reflective mirror surface.

From Fig. 4-2 and Fig. 4-4h, we can see that one challenge the proposed 3rd-generation FDS device will face is the structure release step in which the silicon underneath the actuator is removed while enough silicon should be kept un-etched underneath the mirror plate as mechanical support. This requires a time-controlled silicon etching. Meanwhile, the increase in Si thickness and mirror plate size will cause the 3rd-generation FDS device to have a heavier mirror plate than that of the 2nd-generation. Despite the fact that the weight of the mirror plate has negligible effect on the FDS actuator, the designs of the 3rd-generation FDS micromirror intentionally strengthen the actuator stiffness by either reducing bimorph length or connecting multiple bimorphs in parallel.

Other than the above addressed concerns, the 3rd-generation FDS actuator shares the same properties with the 2nd-generation FDS actuator. The optimization result presented in Section 3.3.1 can thus be used in the design of the 3rd-generation FDS actuator. The width and thickness of the bimorphs are chosen to be the same as the 2nd-generation devices. But due to the smaller footprint of the device, the lengths of the bimorph segments are shorter in the 3rd-generation device. The design parameters of the 3rd-generation FDS micromirror device are summarized in Table 4-1. The SEMs images of the fabricated device are shown in Fig. 4-5

Table 4-1. Summary of design parameters of the 3rd-generation FDS device

Structural Parameters	Value
Mirror plate size	1.0mm×1.0mm
Device footprint	1.45mm×1.55mm
Area fill factor	45%
Length of S-shaped bimorph actuator	320μm
Length of NI bimorph segment	75 μm
Length of IV bimorph segment	165 μm
Length of overlap region	80μm

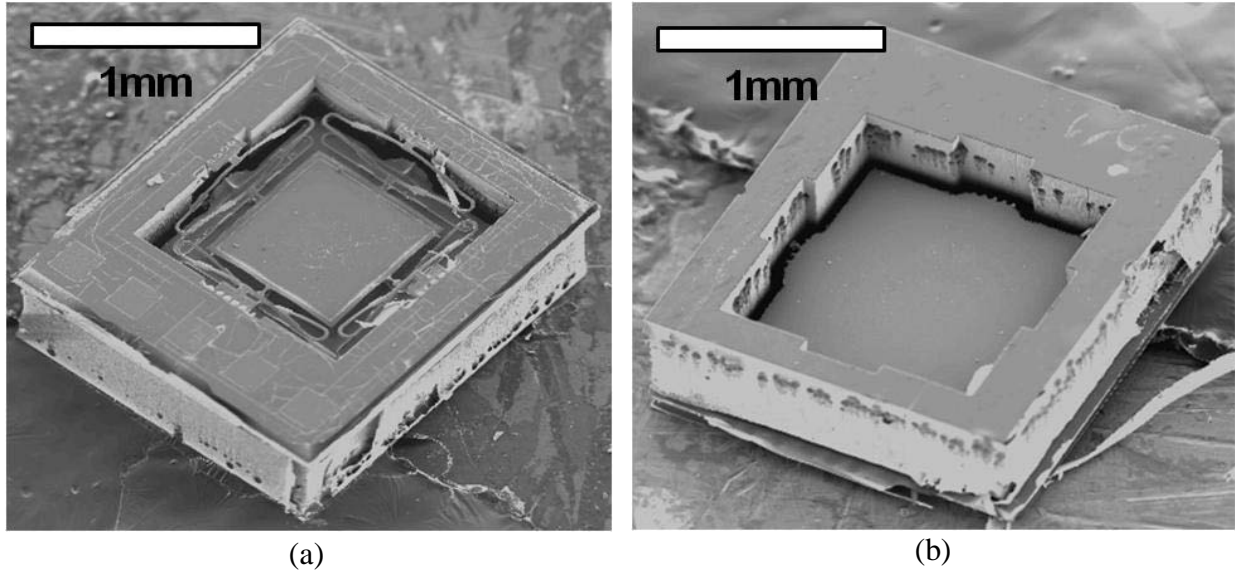


Figure 4-5. SEM images of the fabricated 3rd-generation FDS micromirror: (a) Bird view from the actuator side; (b) Bird view from the optical aperture side

4.1.3 Experimental Result of the 3rd-Generation FDS Micromirror

The characterization of the 3rd-generation FDS micromirror follows the testing procedures applied to the 2nd-generation devices. Due to the similar bimorph structure implemented, the device showed similar performance as the 2nd-generation FDS devices. The characterization result is summarized below.

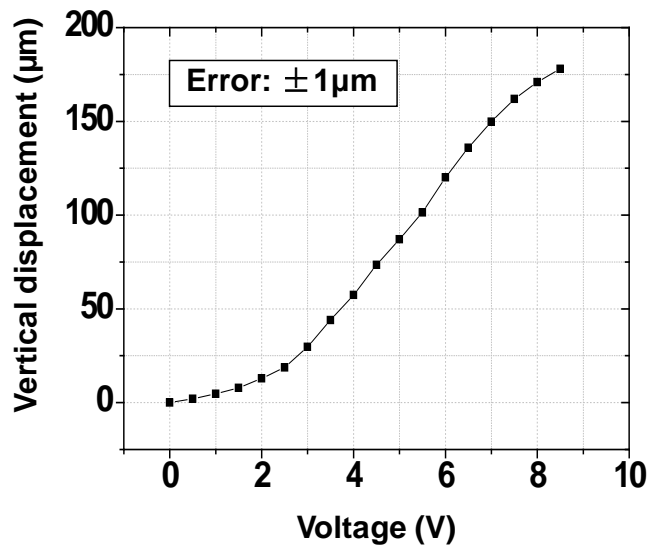


Figure 4-6. Static piston characterization of the 3rd-generation FDS micromirror

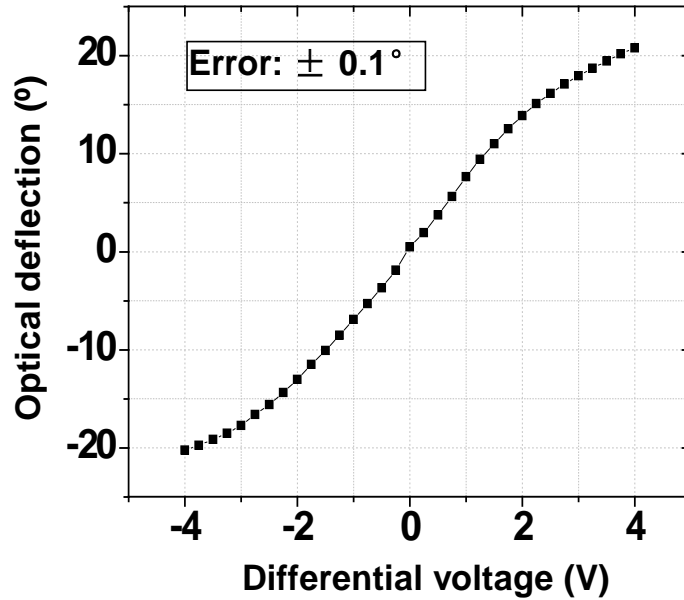


Figure 4-7. Static rotation characterization of the 3rd-generation FDS micromirror

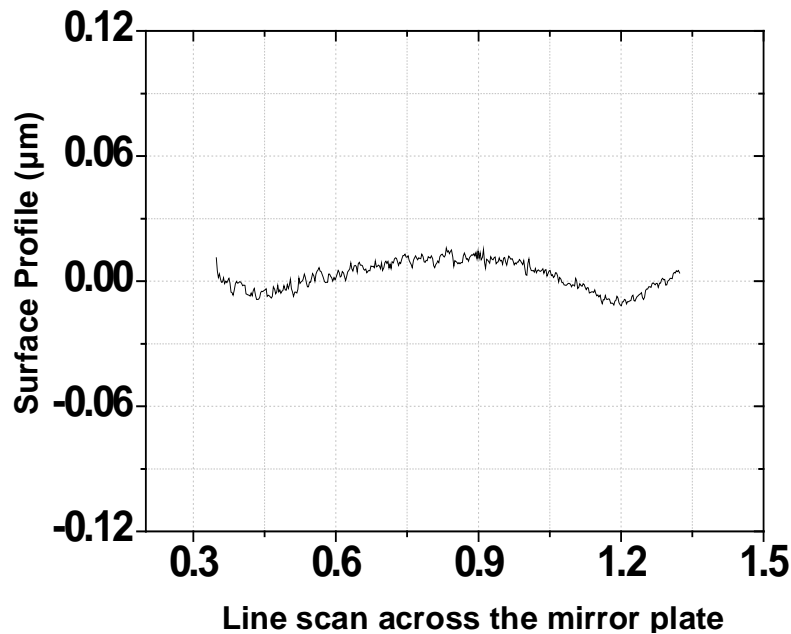


Figure 4-8. Surface quality characterization of the 3rd-generation FDS micromirror.

Static piston characterization of the 3rd-generation FDS micromirror is shown in Fig. 4-6. A vertical displacement of 178m is achieved at 8.5V dc. Static rotation characterization is shown in Fig. 4-7 where an optical deflection angle of $\pm 20^\circ$ is achieved at a pair of $\pm 4V$ dc differential driving voltage. Transient test indicates a $<10ms$ response time for the 3rd-generation FDS

micromirror. The resonance frequency of the rotation mode is found at 620Hz. Finally, the surface quality of the device is also characterized using a Wyko optical profilometer, as shown in Fig. 4-8, which indicates a radius of curvature of $\sim 11\text{m}$ with a surface roughness of 20nm. The large ROC of the device is the result of the thick device silicon layer in the chosen SOI substrate.

The $\pm 20^\circ$ of dual-axes optical scan capability of the 3rd-generation FDS micromirror is more than sufficient for biomedical imaging applications. The 45% of area fill factor of the 3rd-generation FDS micromirror is the highest among devices reported. The footprint of 1.45mm \times 1.55mm is also among the smallest. In fact, in order to increase the successful rate in the first round fabrication of the 3rd-generation FDS micromirror, the footprint chosen leaves approximately 200 μm wide silicon support for the three bimorph actuators away from the bonding pads. But it has been found from the first round fabrication that 100 μm wide silicon is already sufficient for providing the mechanical support for the actuators. Hence, we can further decrease the footprint to 1.25mm \times 1.35mm and boost the fill factor to even 60%. In this dissertation we only did one round of fabrication of the 3rd-generation FDS device, from which the concept of achieving individual micromirror with ultra-high fill factor without bonding-transfer technique is proved. In future work, we can further push the design parameters to achieve even higher fill factor. With the surface mounting capability of this device, even the first batch 3rd-generation device presented above is capable of achieving imaging probe smaller than 1.5mm. Hence, the first objective of this work has been met.

4.2 Development of the HFF MMA Devices

Section 4.1 presented the 3rd-generation FDS micromirror with hidden actuators that can achieve HFF. While single 3rd-generation FDS devices have great potential in endoscopic imaging applications, an array of such designs can form an HFF MMA that is suitable for OPA

applications. This section will present the development of the HFF MMAs based on the 3rd-generation FDS micromirrors.

4.2.1 Design Concept of the HFF MMA Devices

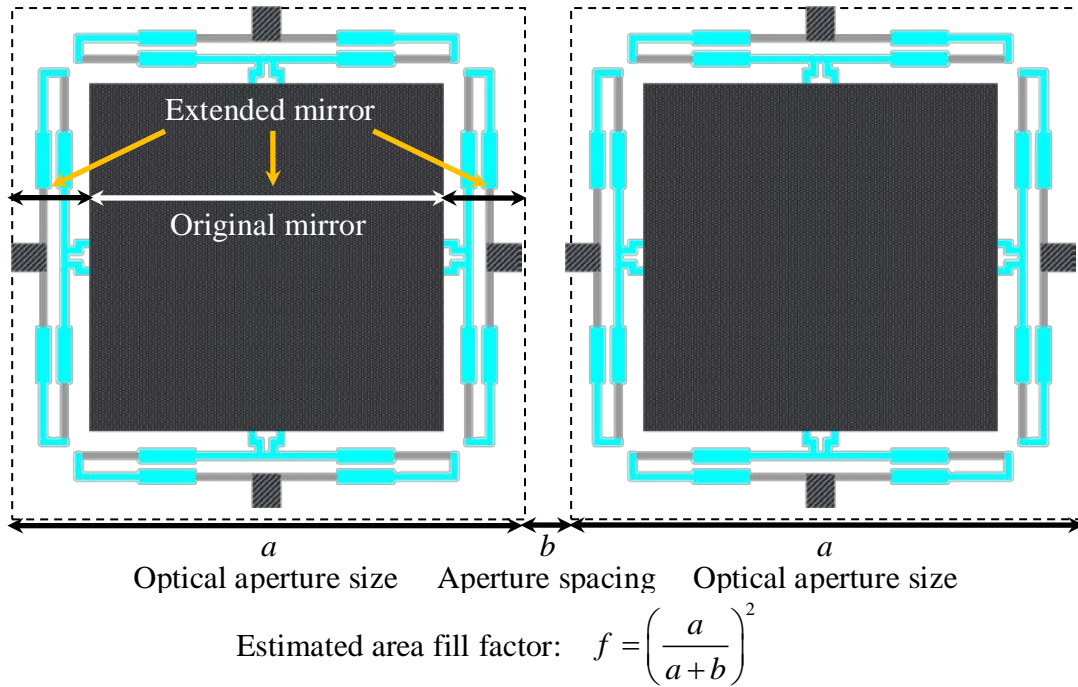


Figure 4-9. Portioned view of the proposed HFF MMA based on 3rd-generation FDS micromirror and its fill-factor estimation.

By placing two 3rd-generation FDS micromirrors adjacent to each other, a portion of the proposed HFF MMA can be schematically illustrated in Fig. 4-9. In this top view from the actuator side, the dashed lines represent the actual mirror plates, with a size a , that are being actuated toward the bottom of the substrate, as shown in Fig. 4-2b. The space between the two micromirrors, with a size b , is used for actuator mechanical support and sub-aperture separation. Electrical connections of each actuator also need to be wired out through the paths on this spacing. In order to provide strong enough mechanical support for the actuators, this spacing must be wide enough. Hence from geometry, we can calculate the fill factor at the MMA region to be $\left(\frac{a}{a+b}\right)^2$. From previous experience, we choose this spacing to be 100 μm . Assuming we

choose an optical aperture size of 1.5mm, the estimated fill factor on the MMA region is approximately 88%. Due to the larger mass of the extended mirror plate, the actuator of the MMA device need to be strengthened accordingly in order to maintain the mechanical performance of each sub-aperture. A 3D more realistic representation of the MMA design is shown in Fig. 4-9, in which the FDS bimorph actuator is doubly strengthened by parallel connecting two single-beam FDS actuators.

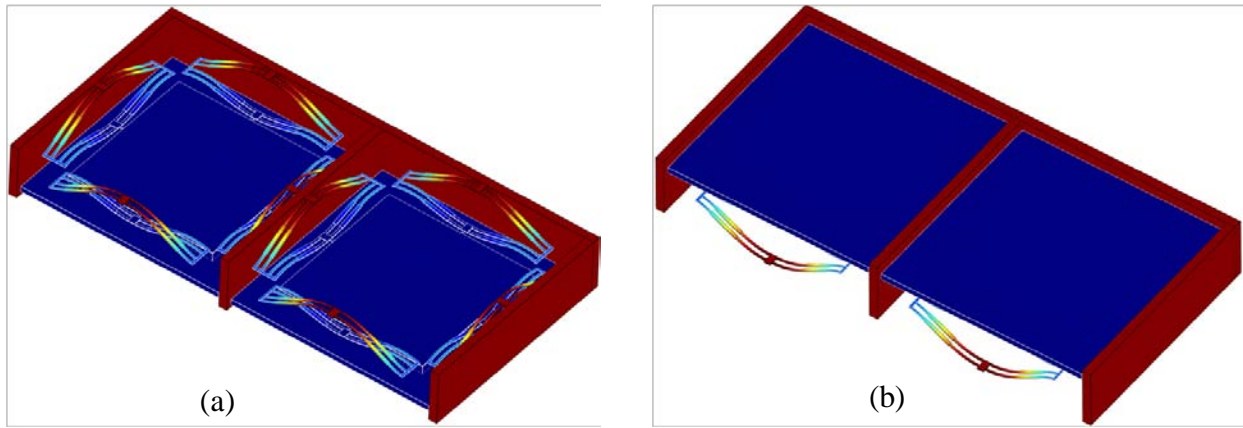


Figure 4-10. 3D realistic representation of the MMA device. (a) Actuator side; (b) Optical aperture side.

4.2.2 Structural Design of the HFF MMA Devices

The structural design of the HFF MMA is based on the combined consideration of the following factors. First of all, the mass of the mirror plate in the proposed MMA device is larger due to the increased aperture size and silicon thickness. Hence, the FDS actuator needs to be strengthened accordingly to maintain reasonable robustness of the device. The actuator design in this dissertation, as shown in Fig. 4-10a, employs parallel-doubled FDS structure. Secondly, as shown in Fig. 4-4h, we want the initial displacement of the mirror plate to be within the thickness of the SOI substrate layer to avoid possible collision between the mirror plate and the handling wafer during this step. It is also important to keep the mirror plate within the height of the surrounding Si walls in order to have full mechanical protection. However, we also hope that

the mirror plate to be as close to the surface as possible in order to maintain the large effective optical aperture. In the actual experiment, this issue can be eventually solved by choosing the right thickness of the SOI substrate for a specific design. But in the design phase, we assume a typical thickness of 400 μm . Considering and balancing all factors, the parameters of the proposed HFF MMA design are determined and summarized in Table 4-2. Compared with the design of the 2nd-generation FDS micromirror, it can be estimated from Table 4-2 that the mass of the whole mirror plate is increased by a factor of 3.3, while the stiffness of the FDS actuator is increased approximately by a factor of 2.6. The initial displacement of the mirror plate can also be extrapolated from previous experience to be $\sim 390 \mu\text{m}$.

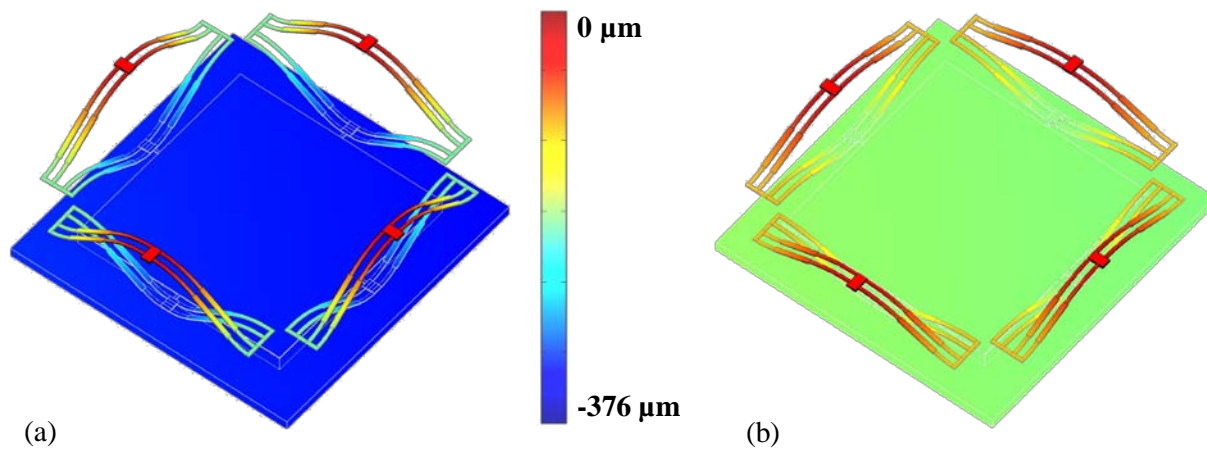


Figure 4-11. Static simulation result of an individual MMA pixel following the structural parameters in Table 4-2: (a) Initial downward displacement of the mirror plate due to the residual thermal stress; (b) Upward displacement of the mirror plate due to the same temperature rise on the four actuators.

An FEM model following the exact parameter settings in Table 4-2 has been built and shown in Fig. 4-11. Assuming all thin film layers are deposited at 600 K, the mirror plate is initially actuated downward by 376 μm due to the residual thermal stress, as shown in Fig. 4-11a. Increasing the temperature on the four actuators from 300 K to 450 K will give the mirror plate an upward displacement of 188 μm , as shown in Fig. 4-11b. The weight of the mirror plate will cause a vertical displacement of $\sim 3 \mu\text{m}$ when the device lies horizontally. Modal analysis of this

model shows that the first resonance mode is the piston resonance mode at 280Hz, while the rotation resonance mode occurs at 363Hz. The FEA simulation result is also listed in Table 4-2.

Table 4-2. Structural parameters of the HFF MMA

Structural Parameters	Value	Structural Parameters	Value
Mirror plate size	1.5mm×1.5mm	Length of Overlap	194μm
Mirror plate spacing	100μm	Width of NI bimorph	16μm
Area fill factor of MMA region	88%	Width of IV bimorph	16μm
Center mirror plate size	1.0mm×1.0mm	Width of Overlap	24μm
Outer mirror plate thickness	30μm	Width of Pt heater	6μm
Center mirror plate thickness	100μm	Thickness of bottom SiO ₂	1.3μm
Length of S-shape bimorph	506μm	Thickness of top SiO ₂	1.3μm
Length of IV bimorph	96μm	Thickness of Al	1.2μm
Length of IV bimorph	216μm	Thickness of Pt heater	0.3μm
Initial Displacement		Resonance Frequencies	
Extrapolated	Simulated	Piston	Rotation
390 μm	376 μm	280Hz	363Hz

Another concern in the MMA device design is the crosstalk between adjacent mirror pixels. The FEA model shown in Fig. 4-12 is the close resemblance of the two actuators of adjacent mirror pixels with the most physical proximity. The actuators are connected to the 60μm-wide, 400μm-deep Si separation wall by five SiO₂ beams. We set 300K as the initial temperature of all the structure and apply a power density of 3×10^{12} W/m³ to the embedded Pt heater, which equates to a 30mW power source for the given heater structure. We set 200W/m²-K convection coefficient to the bimorphs and the Si wall which is a common value for structures in the atmosphere. To imitate the worst case scenario, we also set the boundaries at the

end of the FDS actuators to be insulated which means that there is no power flowing into the mirror plate so that all the dissipated power is either into the ambient or into the adjacent inactive FDS actuator. The simulation result is shown in Fig. 4-12a, from which it can be seen that the Si separation wall also works as a heat dissipation plate and maintains the adjacent inactive actuator almost at room temperature. The extracted average temperature profile on the FDS actuator pair along x direction is shown in Fig. 4-12b in which we find that the average temperature rise on the active actuator is 214.2K and the average temperature rise on the inactive actuator is 4.4K, which can be translated to an equivalent displacement of $\sim 3.7\mu\text{m}$ at the free end of the inactive FDS actuator or an equivalent rotation angle of $\sim 0.15^\circ$ if connected to a mirror plate. This small influence is negligible compared with the large operating range of the actuators and can be easily compensated. The estimated crosstalk under this worst case scenario is -17dB. Considering other power dissipation factors, i.e. the mirror plate convection and radiation, in the actual case, this crosstalk could be reduced to below -20dB.

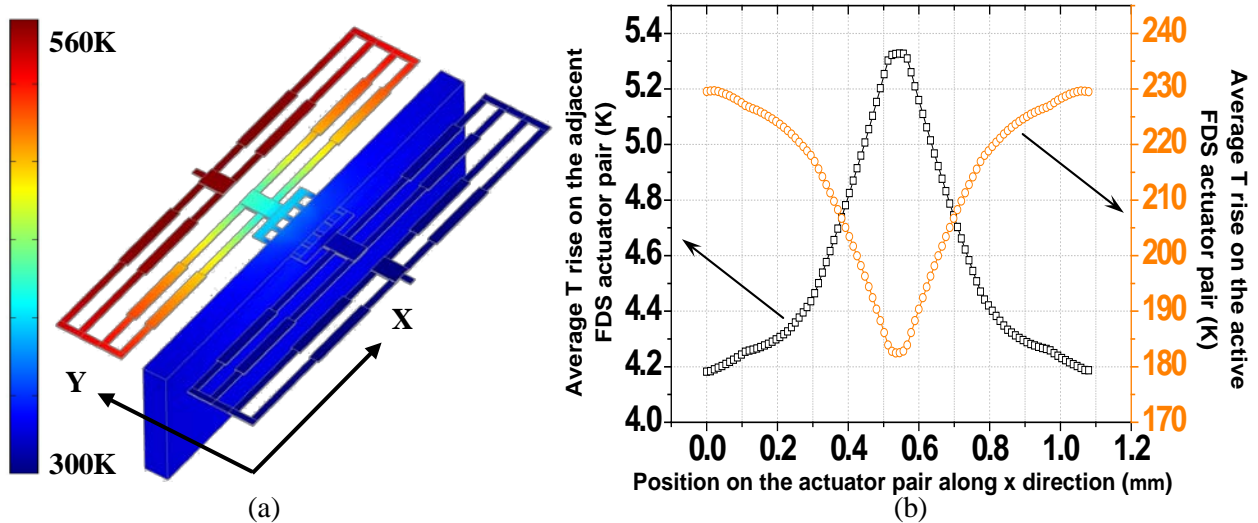


Figure 4-12. Worst case scenario simulation of the crosstalk between adjacent FDS actuators: (a) Static temperature distribution of two adjacent FDS actuator pairs; (b) Plots of averaged temperature rise on the active and inactive actuators.

4.2.3 Fabrication and Packaging of the HFF MMA Devices

The fabrication process flow of the single device described in Section 3.4 can be applied to the fabrication of the HFF MMA as well. For clear illustration, the cross sectional views of the fabrication process are redrawn to display the MMA device in Fig. 4-13.

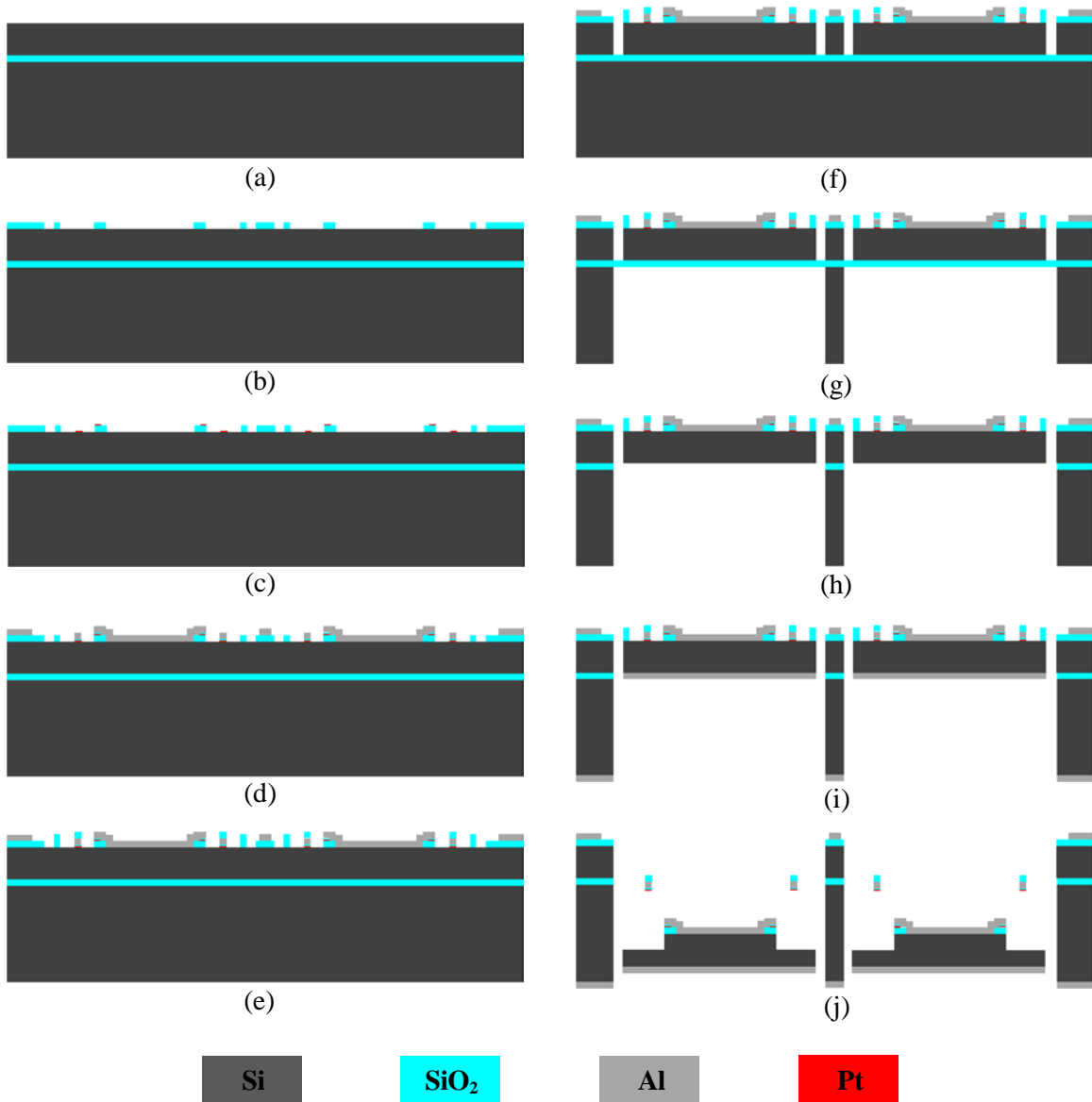


Figure 4-13. Cross-sectional view of the proposed process flow for HFF MMA: (a) Start with SOI wafer; (b) Front side SiO₂ patterning; (c) Pt lift-off and insulation SiO₂ deposition; (d) Al lift-off; (e) Second front side SiO₂ deposition and patterning; (f) Front side Si etch; (g)-(h) Backside Si etch and buried SiO₂ etch; (i) Al coating for reflective mirror surface; (j) Final structure release.

In OPA applications, sophisticated dynamic control of the MMA sub-apertures is of vital importance for the device functionality. Just like the 3rd-generation FDS micromirror devices, the HFF MMA developed also have the surface mounting capability to be integrated with IC or PCB driving electronics. This integration approach can be illustrated by Fig. 4-14.

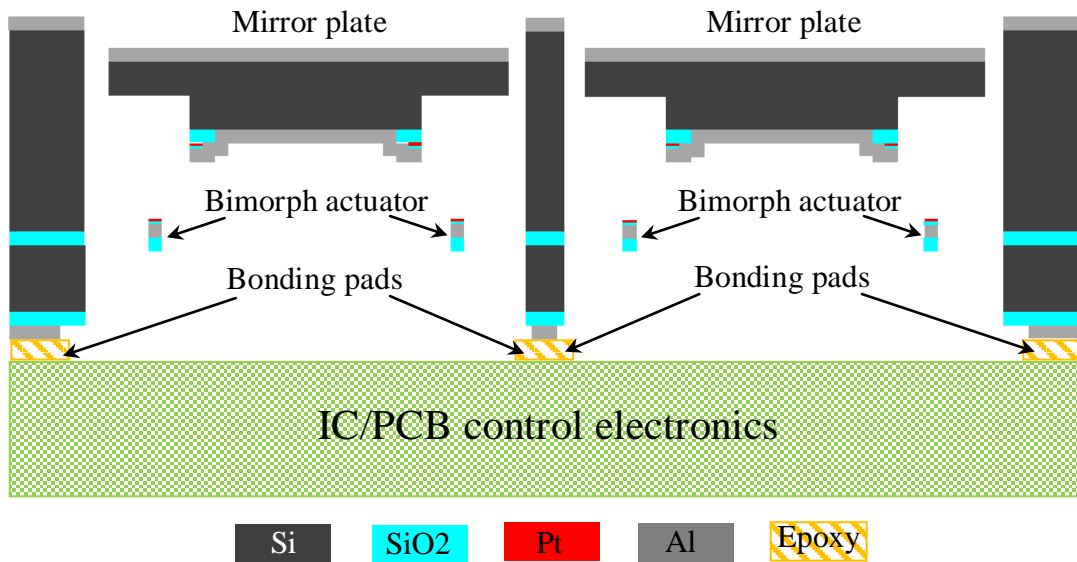


Figure 4-14. Surface mounting integration scheme of the HFF MMA devices with IC/PCB driving electronics.

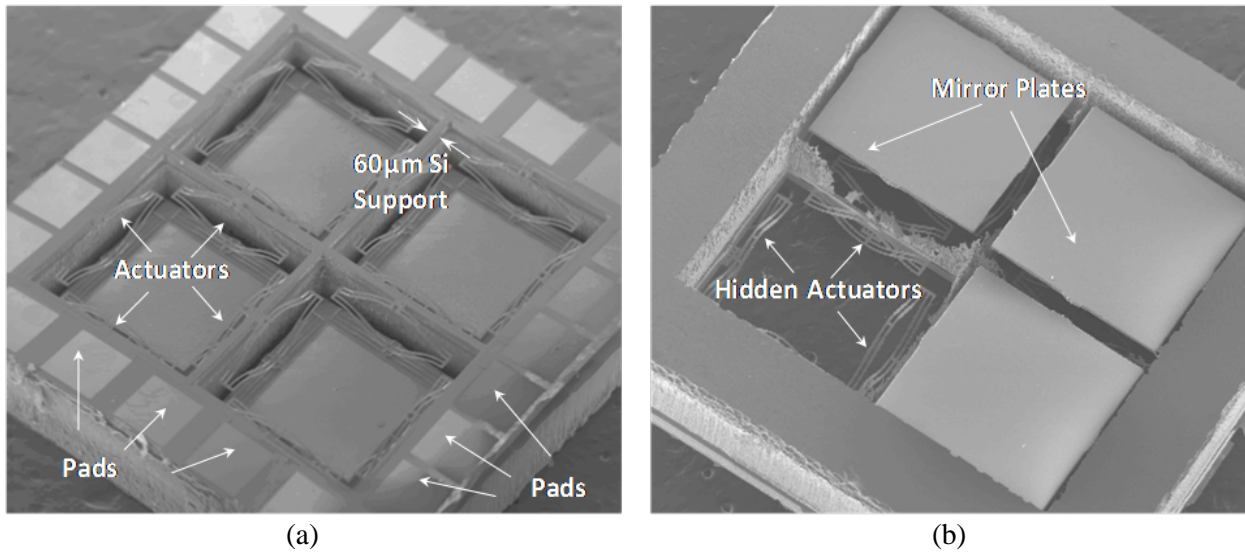


Figure 4-15. SEM images of the 2x2 HFF MMA devices from the 1st batch of fabrication: (a) Actuator side; (b) Optical aperture side.

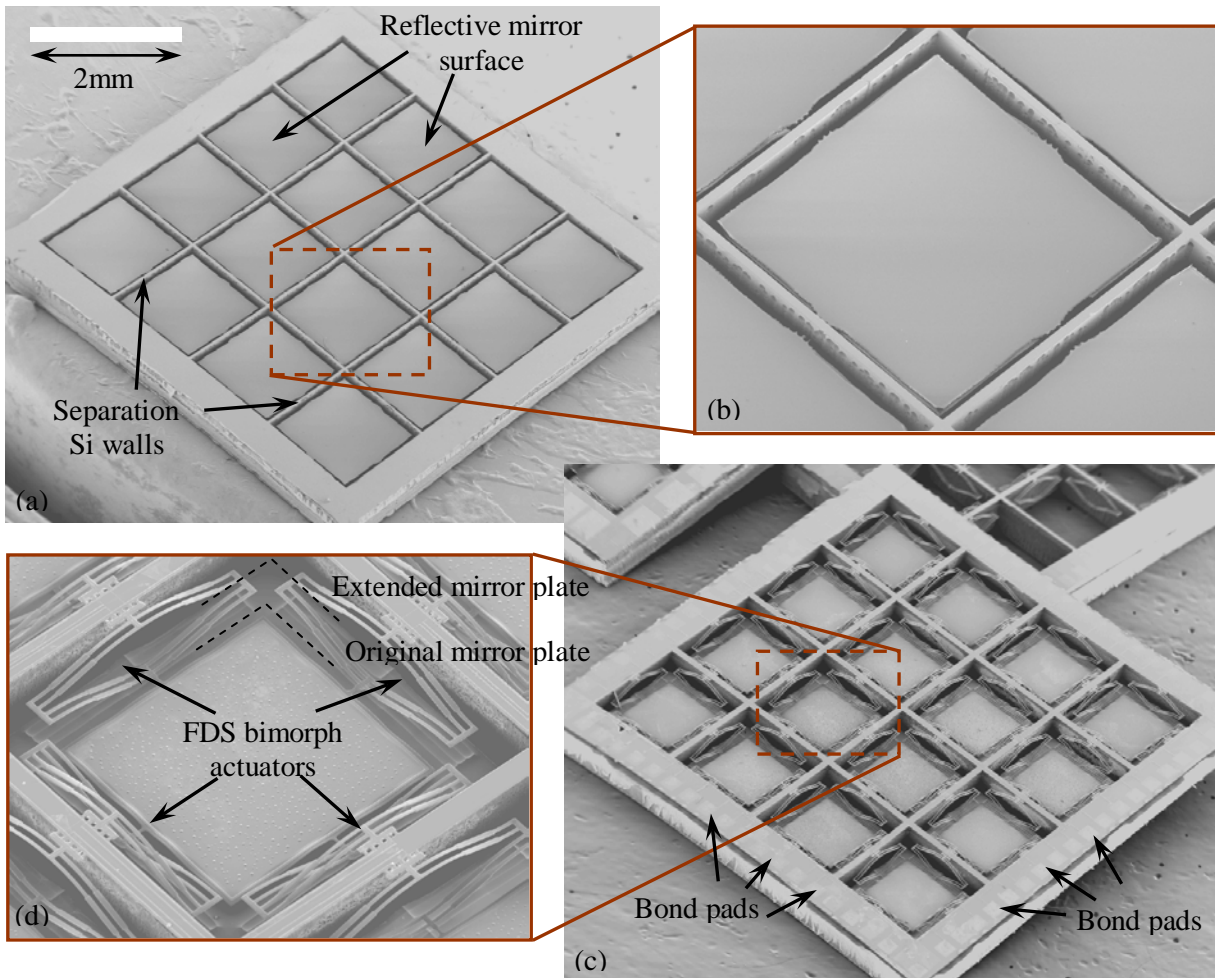


Figure 4-16. SEM images of the 4×4 HFF MMA devices from the 2nd batch of fabrication: (a) Top side of the MMA device showing mirror pixels and separation walls; (b) Close-up view of one mirror pixel; (c) Bottom side of the MMA device showing actuators and bond pads; (d) Close-up view of the FDS bimorph actuators of one mirror pixel.

The SEM images of the first batch 2×2 HFF MMA devices is shown in Fig. 4-15. The hidden bimorph actuator can be seen from Fig. 4-15b. It is also evident from Fig. 4-15 that the first batch HFF MMA devices suffer from poor process control and the separation/support walls are mostly gone due to the over etch on silicon. The devices from the second batch have much superior structure integrity. The SEM images of a 4×4 MMA device from the second batch fabrication are shown in Fig. 4-16. The aperture side of the MMA device is shown in Fig. 4-16a and Fig. 4-16b. Each mirror pixel is separated by 60 μm-thick SCS walls. The gap between the

mirror pixel and the SCS separation wall is $\sim 35\mu\text{m}$ which leaves enough room for the operation of the mirror plate. The actuator side of the MMA device is shown in Fig. 4-16c and Fig. 4-16d. Each mirror pixel is actuated by four FDS actuator pair with downward initial displacement. It can be seen from Fig. 4-16d that the present mirror plate has been extended under the actuators, in comparison with the original mirror plate of the 2nd-generation FDS micromirror. The optical images of the 8×8 HFF MMA device is shown in Fig. 4-17. With ultra- large sub-aperture size of 1.5mm×1.5mm, the 4×4 MMA and the 8×8 MMA achieve combined aperture size of 6.4mm×6.4mm and 1.34cm×1.34cm with only 16 and 64 sub-apertures, respectively. The second batch fabrication also achieved a high overall yield of 85%.

Following the packaging scheme in Fig. 4-14, the surface-mount packaging of the 4×4 MMA device and the PCB is done using the Semiconductor Equipment Corporation's Model 850 Flip Chip Placement System. We first dispense Epo-Tek-H20E silver epoxy on to the PCB which is designed to have rectangular Au-based pad correspond to the pads on the MMA device (Fig. 4-16c). Then, we use the Flip Chip Placement System to align and position the PCB onto the device and immediately cure the silver epoxy with a custom made thin film heater underneath. Fig. 4-18 shows the optical images of a surface mounted 4×4 MMA device wire-bonded on to a DIP ceramic package, with one pixel chosen to demonstrate the TTP capabilities. Due to the difference in the electrical wirings as well as the process variation, the electrical resistances of the heaters are measured to be $280\pm 90\Omega$ directly after device fabrication and $320\pm 120\Omega$ after surface mounting on to the PCB.

In our experiment, we only use a simple PCB to demonstrate the surface mounting and flip chip bonding capability of the MMA device. However, with the Al pads readily formed on the SOI substrate of the MMA device, as shown in Fig. 4-16c, it is conceivable that the direct

surface mounting or flip chip bonding integration of the device with more complex IC or board level driving electronics can be realized.

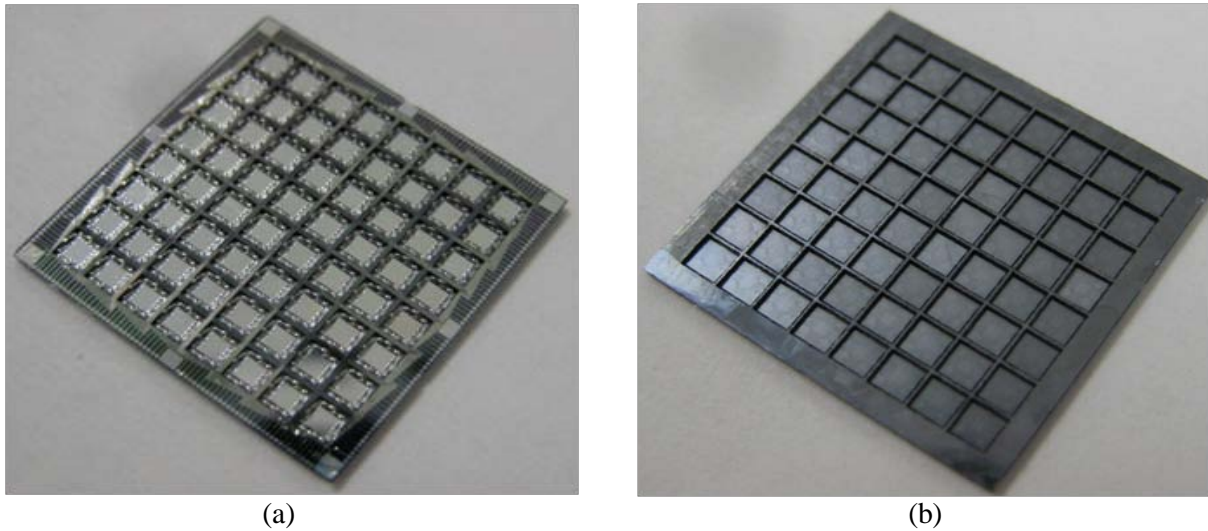


Figure 4-17. Optical images of the 8×8 HFF MMA devices from the second batch of fabrication: (a) Actuator side; (b) Optical aperture side.

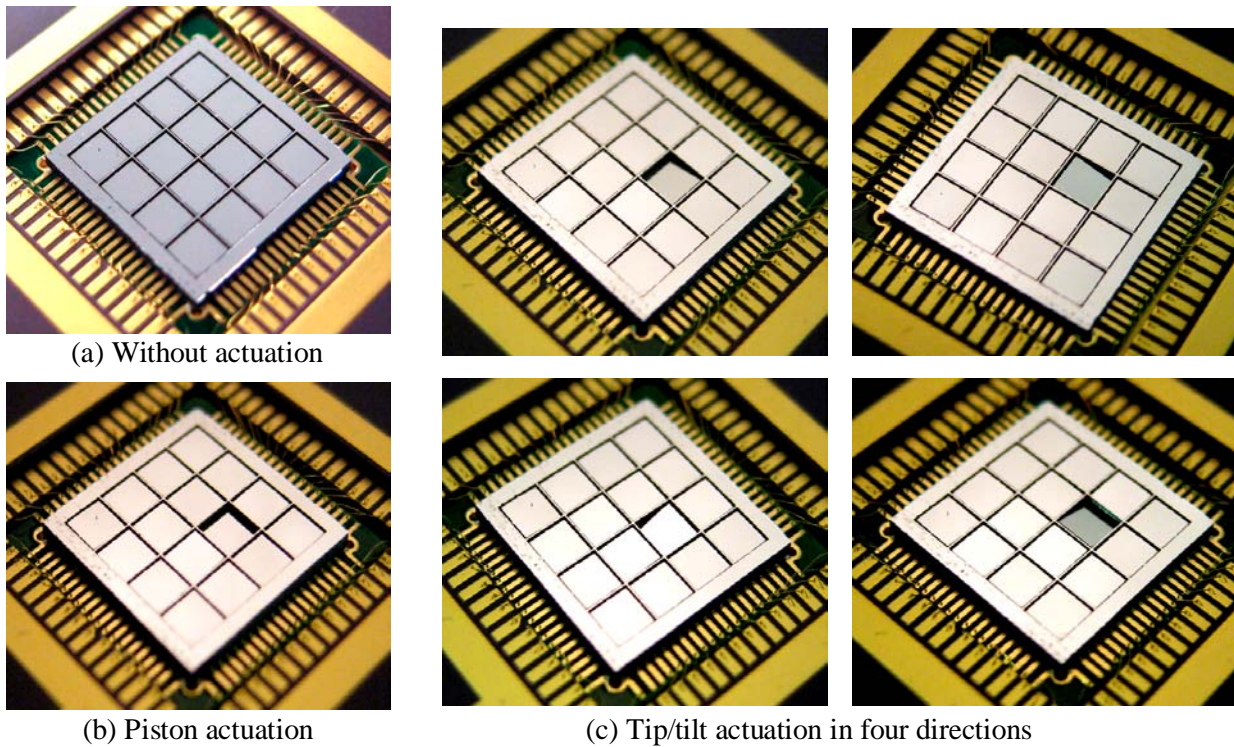


Figure 4-18. Optical images of a DIP-packaged surface-mounted 4×4 MMA device: (a) Without actuation; (b) Piston actuation of a single mirror pixel; (c) Rotation actuation of a single mirror pixel in four directions

4.2.4 Characterization of the HFF MMA Devices

A series of tests have been carried out to characterize the MMA device. Items of characterization include the initial position of the sub-apertures, static piston and rotation responses, the frequency responses of piston and rotation resonance modes, and finally the mirror surface quality.

4.2.4.1 Mirror plate initial position

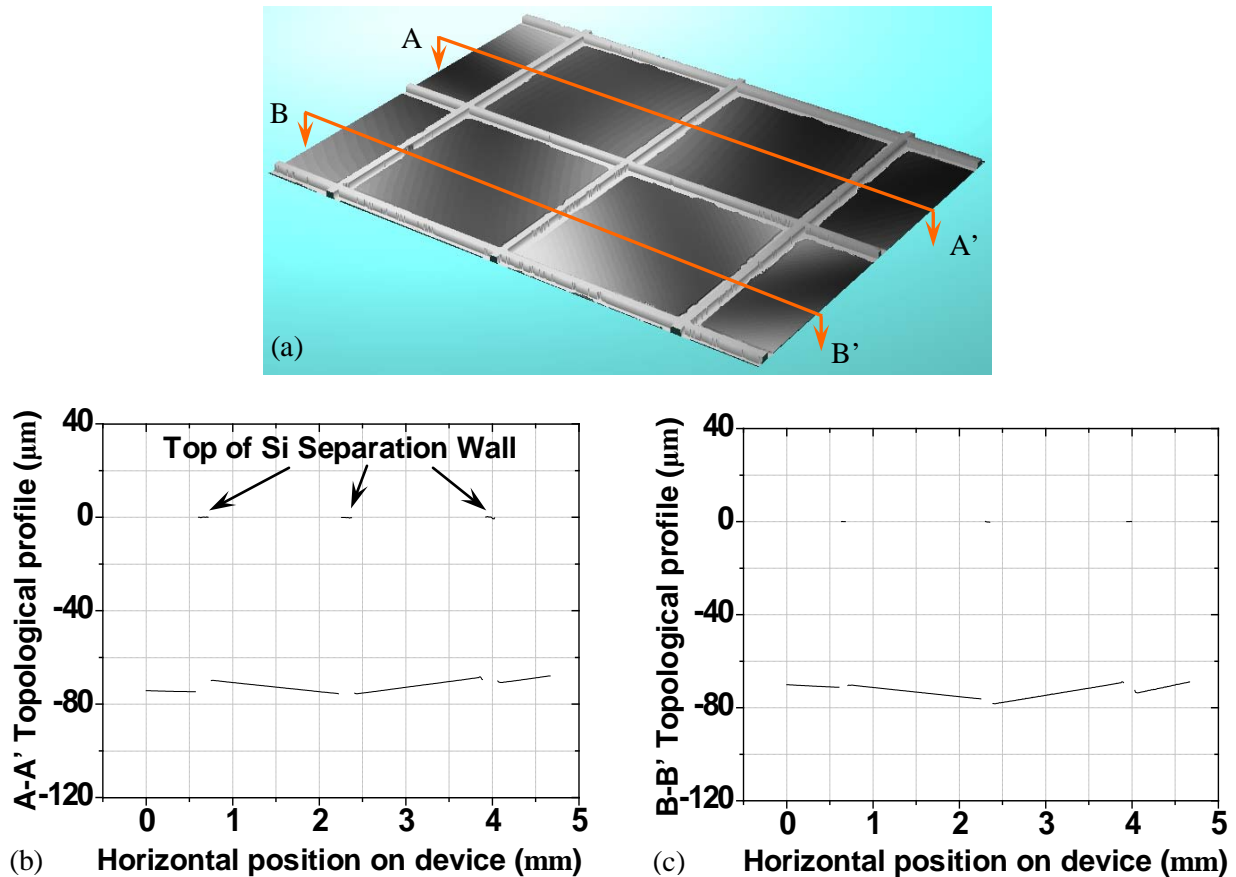


Figure 4-19. Device topological profiles measured by Wyko-Vision optical profilometer: (a) 3-D image of the measured device topological profile; (b) Topological profile data along A-A'; (c) Topological profile data along B-B'

The SOI wafer used in the experiment has a handle wafer thickness of $400 \pm 5 \mu\text{m}$. By measuring the positional differences of the reflective mirror apertures and the top surface of the Si separation walls in the vertical direction, the initial displacement of the mirror plate can be

determined. The topological profile of the 4×4 MMA device is characterized by a Wyko-Vision white light optical profilometer and is shown in Fig. 4-19. The extracted 2-D profile data shown in Fig. 4-19b and Fig. 4-19c indicates that the mirror plates are $75\pm 10\mu\text{m}$ below the top surface of the Si separation walls, which indicates the initial displacement of the mirror plates to be $325\pm 15\mu\text{m}$. It can also be estimated from Fig. 4-19b and Fig. 4-19c that the initial tilting of the mirror plates is $< 0.4^\circ$, resulting mainly from the process variation during the fabrication.

4.2.4.2 Static piston characterization

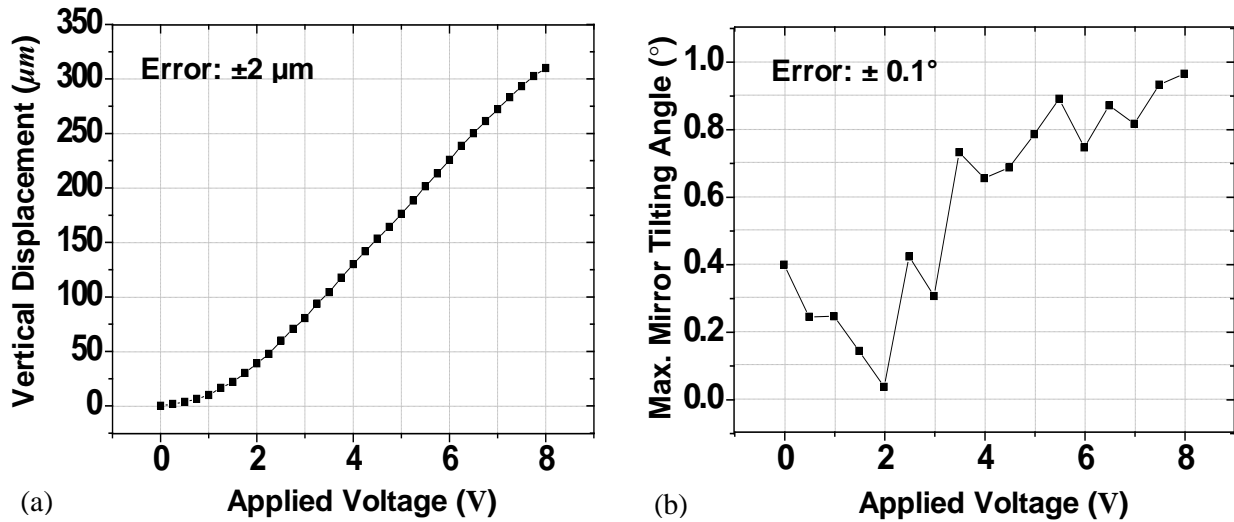


Figure 4-20. Characterization of static actuations: (a) Static piston actuation; (b) Change of mirror plate tilting angle during piston actuation.

The ideal piston displacement of each mirror pixel can be realized by driving the four actuators with the same electrical power input. In our experiment, we apply same dc voltage to the four actuators. As a result, piston displacement can be realized with some degree of degradation in the mirror plate tilting angle due to the difference in the electrical resistances of the four actuators. As the applied voltage increase, the mirror plate recedes towards the bottom of the ceramic package. We track the change of vertical position of the mirror plate under the microscope using a Quadra-Chek 200 micro-position recorder. Fig. 4-20a shows the static

measurement result of the piston actuation of one selected mirror pixel. The tilting angle of the mirror plate during the entire actuation range is shown in Fig. 4-20b. It is measured that a piston stroke of $\sim 310\mu\text{m}$ can be realized at 8V dc. Meanwhile, the tilting angle of the mirror plate is initially 0.4° and degrades to $<1.0^\circ$ at the end of the actuation. Due to the resistance variance among difference mirror pixels, the static measurement results shown in Fig. 4-20 apply only to the mirror pixel that is under test.

4.2.4.3 Static rotation characterization

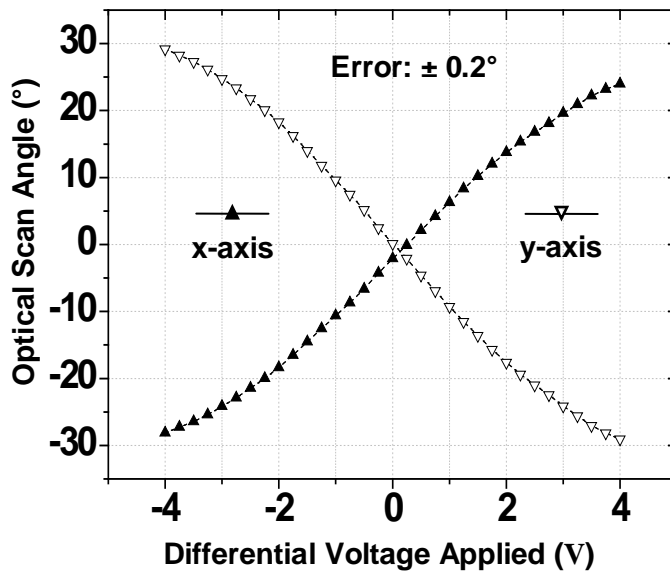


Figure 4-21. Characterization of static rotation actuation

The static rotation actuation of one mirror pixel is characterized using a laser beam and a screen. A same dc voltage of 4V is applied to all four actuators while one pair of differentially varying voltages is superimposed on one opposing actuator pair. As shown in Fig. 4-21, optical deflection angles of $\sim \pm 30^\circ$ are achieved for both axes at a pair of 4V differential voltages. The asymmetric performances between the two axes could be caused by several reasons including the relatively large difference in the electrical resistances and the difference in the thermal paths of each actuator.

4.2.4.4 Frequency responses measurement

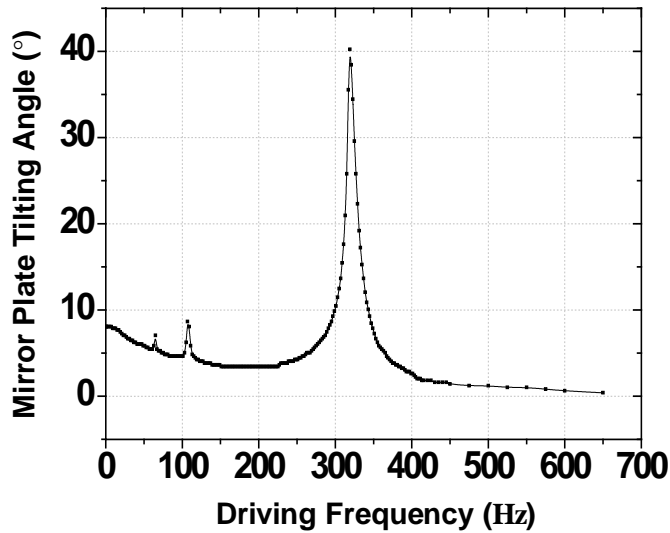
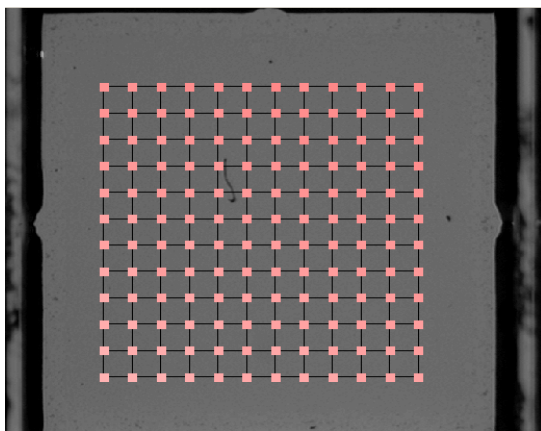


Figure 4-22. Frequency response of rotation resonance mode

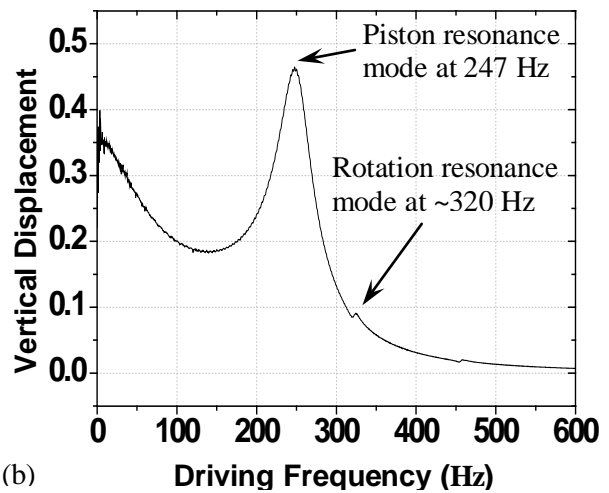
The frequency response of the rotation resonance mode is characterized also using a laser beam and a screen. 4V of dc bias voltages are applied to all actuators while a differential pair of ac triangular driving signals of 0.8V are applied to opposing actuator pair. The scanning angle as a function of the changing frequency is recorded and plotted in Fig. 4-22. At 319Hz the device exhibits a line mode resonance. During this measurement, some degree of mode coupling between the two axes is observed sporadically in the form of slightly curved or narrow elliptical scanning patterns due to the frameless structure design of the device.

The frequency response of the piston resonance mode is characterized using a Polytech Laser Vibrometer. In this experiment, in order to suppress other resonance modes (*e.g.*, rotation resonance mode) and excite mainly the piston resonance mode, one mirror pixel with closely matched resistance measurement is chosen. One opposing actuator pair of this mirror pixel has resistance measurement of 391 Ω and 392 Ω . We apply a periodic chirp driving signal of 6V dc + 0.2V ac simultaneously to this opposing actuator pair, while scanning a 12 \times 12 points array covering a square-shaped area of approximately 1mm \times 1mm at the center of the mirror

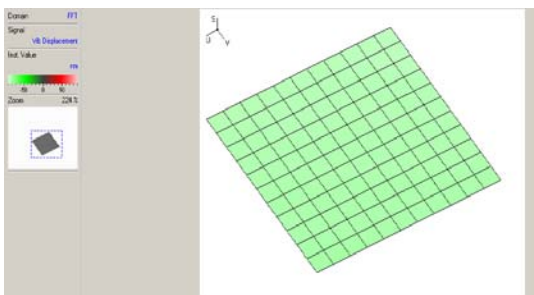
plate (Fig. 4-23a). The measured displacement data is shown in Fig. 4-23b, in which the peak at 247Hz represents the pure piston resonance mode. It is also noticed that a resonance mode at 324Hz is excited during this experiment, which matches closely with the rotation resonance mode observed in Fig. 4-22. To further verify the piston resonance mode at 247Hz, 3-D images of the scanned area in motion is obtained at different driving phases. Fig. 4-23c and Fig. 4-23d shows the images when the phase of the driving signal equals 80° and -80° , respectively. The uniform color distribution across the scanned area indicates uniform vertical displacement during the entire resonance. A correlative examination of the displacement data of the 144 scanned points shows near-zero non-uniformity.



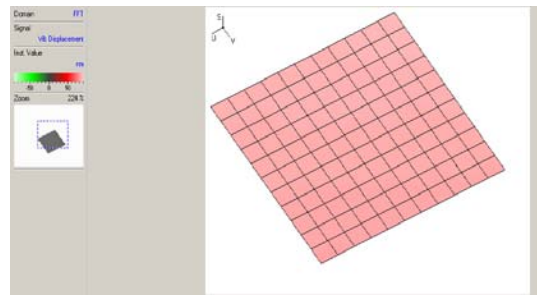
(a) Scan points array with respect to the mirror



(b)



(c) Displacement distribution across the scanned plane at 247 Hz: Phase = 80°

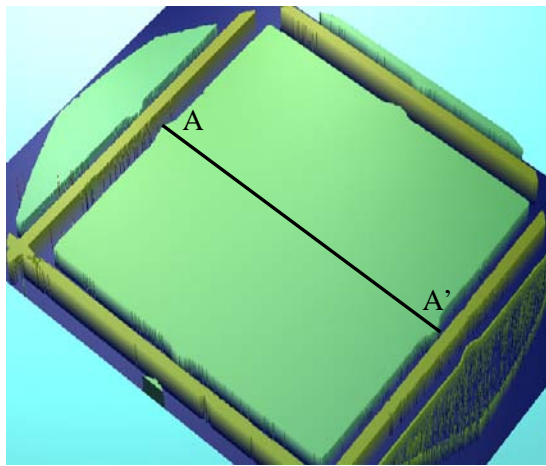


(d) Displacement distribution across the scanned plane at 247 Hz: Phase = -80°

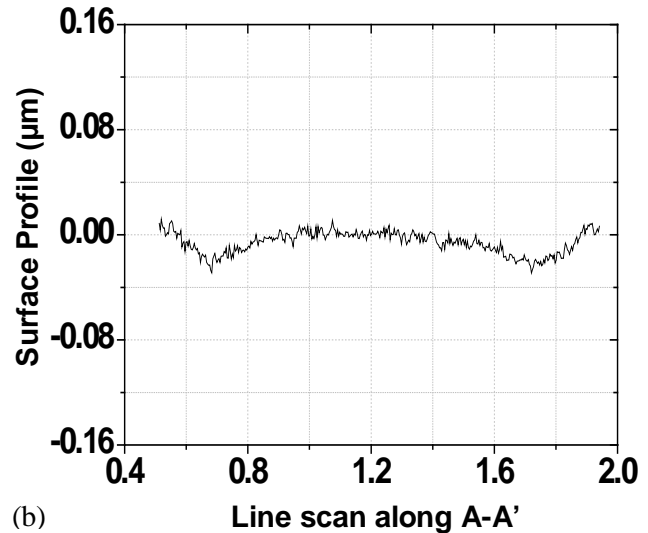
Figure 4-23. Piston resonance mode measurement result by Scanning Laser Vibrometer: (a) The array of scan points on mirror pixel surface; (b) Frequency response of piston excitation; (c), (d) In-motion images of the scanned mirror pixel at 247 Hz: (c) 80° , (d) -80° .

4.2.4.5 Mirror surface quality measurement

The mirror surface quality is characterized using Wyko Vision optical profilometer. Due to the 90 μm -thick device layer silicon, the mirror plate achieves a radius of curvature as large as -9 m (convex) at the center area. It is noticed that the radius of curvature deteriorates to about 0.6 m (concave) at ~ 0.2 mm to the edge, which is still sufficiently large for most applications. The maximum peak to valley deformation across the 1.5 mm mirror plate is 0.2 μm with a standard deviation surface roughness of < 10 nm. Fig. 4-24 shows the 3-D contour plot of the measurement result and the surface profile data extracted along the center line.



(a) 3-D Contour Measurement Result



(b)

Figure 4-24. Measurement results of mirror surface quality: (a) 3-D contour plot of mirror surface profile; (b) Surface profile data along A-A'.

4.3 Summary

This chapter presents the development of the 3rd-generation HFF FDS micromirror and the HFF MMA devices based on the same design concept. The individual 3rd-generation FDS micromirror has achieved a rare small footprint of 1.45mm \times 1.55mm with an unprecedented high area fill factor of 45%, which can be further enhanced to even 60%. This design also provides surface-mount integration capability that can avoid the use of wire bonding during image probe

assembling which can further miniaturize the design of the probe. The MMA design and fabrication method based on the 3rd-generation FDS micromirror is the only method capable of achieving HFF, SCS-backed mirror plate without any bonding transfer techniques. The fabrication process also achieved a high overall yield of 85%. With the superior actuation capability of the electrothermal bimorph actuator, large sub-aperture size of 1.5mm×1.5mm has been implemented to realize centimeter-scale combined optical aperture with less than 100 elements. With the simple and high yield fabrication process, further scale-up of the combined optical aperture can be realized simply by repeating more sub-apertures in the MMA design. The surface-mount packaging of the HFF MMA has been completed using a flip chip placement system. Tip-tilt-piston scan capability of the MMA sub-aperture has also been demonstrated.

The two primary objectives of this work have been summarized in Chapter 1: 1) To develop HFF individual micromirror devices with simple packaging method to enable further miniaturization of the imaging probe design; 2) To provide simple and scalable solution to design and fabricating MMA devices with HFF, SCS-backed sub-apertures and TTP scan capability. With the 3rd-generation FDS micromirror device and the HFF MMA devices demonstrated in this chapter, these two objectives have been met.

CHAPTER 5 APPLICATIONS OF DEVELOPED MEMS MICROMIRRORS AND MMAS

The initial goal of this work is to develop biomedical imaging probes based on MEMS micromirrors. Before working on the FDS micromirror (discussed in Chapter 3 and Chapter 4), the author was also involved in the design and fabrication of cantilever-bimorph based 1-D micromirror device. This device has been integrated to miniaturized probes for endoscopic OCT imaging by our collaborators in State University of New York at Stony Brook (SUNY-SB). With the collaboration with Lantis Laser, Inc., an imaging probe based on the 2nd-generation FDS micromirrors has been designed and integrated for dental OCT imaging application. Probe designs based on the 3rd-generation FDS micromirror has also started but not yet complete. Preliminary experiment to demonstrate the OPA applications potential of the developed HFF MMA devices has also been completed. In this chapter, the experimental result of these application attempts will be presented and discussed.

5.1 Endoscopic OCT Imaging Application Using 1-D Micromirror

Optical Coherence Tomography (OCT), first proposed by Prof. Fujimoto in 1990 [22], is a low coherence interferometry based imaging technique with micrometer to even sub-micrometer resolution and cross-sectional imaging capabilities. An OCT system collects the information-carried backscattered light beam from a sample the same way as ultrasonic imaging. This light beam is combined with a reference light beam so that only the light reflected from a certain depth at which the optical path difference is within the coherence length of the light source is detected. By axially scanning the reference light beam over a certain range, cross-sectional view of the corresponding range in the sample is obtained. Further implementing a 2-D transverse scanning mechanism on the sampling arm, a full 3-D image of the sample can be obtained. With its micron resolution, millimeter penetration depth, minimal invasiveness, instant imaging and

low cost, OCT is very suitable for early stage precancerous lesion detection. However, for the imaging of internal organs such as cardiovascular, gastrointestinal and pulmonary ducts, conventional transverse scanning units, usually based on galvanometric mirrors, are simply too big to be inserted in human body. Miniaturized imaging probes (several millimeters in diameter) with scanning units integrated with optic fibers and lenses need to be developed for this purpose. MEMS electrothermal micromirrors, with their small size, large-range and fast 2-D scanning capability, and safe driving voltage, fit naturally to the task.

Fig. 5-1 illustrates the schematic of the spectral-domain OCT imaging system built in SUNY-SB [135, 161, 162]. The endoscopic probe has a diameter of 5.6mm and is equipped with a rod lens, a fiber and an MEMS scanner. The schematic of the scanner unit and a SEM image of the 1-D micromirror are also shown in Fig. 5-1. The 1-D micromirror is glued on a half-circle shaped PCB board with ball-bonded signal wires conducted from the back of the PCB to the external control. The detailed design of this probe is not presented due to the non-disclosure agreement between University of Florida and SUNY-SB.

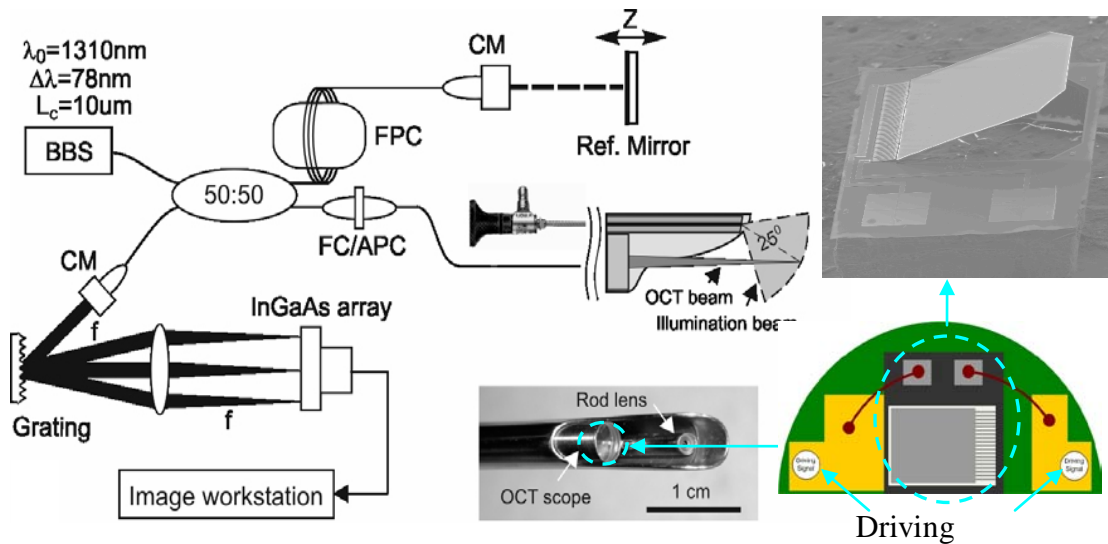


Figure 5-1. Schematic of the OCT imaging setup in SUNY-SB and the scan unit by UF. Courtesy to Hugang Ren of SUNY-SB for the images.

Using the system shown in Fig. 5-1, OCT images of precancerous (Fig. 5-2A) and cancerous (Fig. 5-2B) mouse bladder tissues were taken and further verified by histological images, as shown in Fig. 5-2.

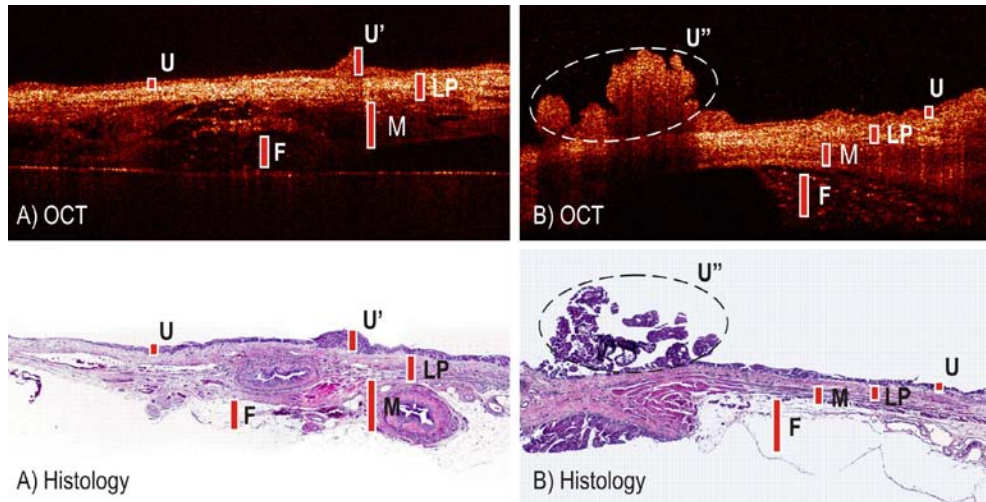


Figure 5-2. OCT images of precancerous and cancerous mouse bladder tissue compared with histology results. (U: Normal urothelia; U': Hyperplastic urothelia (precancerous); U'': Cancerous urothelia; F: Fat; M: Muscle; LP: Lamina Propria.). Courtesy to Hugang Ren of SUNY-SB for the image.

As mentioned early in Section 2.5, cantilevered bimorph actuators with a mirror plate connected at the free end will generate rotation axis shifting during actuation. When integrated in an OCT system, this shifting will bring extra path length difference between the sampling arm and reference arms. Therefore, for each transverse scan, instead of extracting information from the same depth in the tissue, the system actually collects images from a slanted or even curved axial layer, which will result in degraded image fidelity. With the improved micromirror and probe design, it is conceivable that the imaging capacity and fidelity could be enhanced.

5.2 Dental OCT Imaging Application Using the 2nd-Generation FDS Micromirror

The mainstream of the diagnostic imaging techniques used in dental practice today is X-ray. It has served dentistry so well that it remained the sole imaging method for 124 years since its first use in dental practice in 1885. Although its imaging capability has been gradually improved during the past century, it still has severe limitations in providing adequate information for dental diagnosis. Firstly, it provide on spatial reference of the tissue. Secondly, it can only image the hard tissue (teeth), but not the soft tissue (gums), with only limited resolution. Additionally, X-ray is potentially harmful for human body. Numerous dental literatures and researches show that dentistry needs a chair-side oral imaging system that can provide real-time qualitative and quantitative information of the dental microstructures for more accurate diagnosis of oral diseases including decay and periodontal disease.

OCT, however, provide precise spatial reference of the tissue, has 10 times better resolution than that of the x-ray and it is the only imaging modality that is able to image both soft and hard tissue. OCT uses a light source instead of harmful radiation. With up to several millimeters penetration depths and fast image processing, OCT can offer much more extensive, accurate and real-time information display on a chair-side monitor to provides higher level of professional service and patient care. Fig. 5-3 presents examples of OCT images showing dental microstructures that are not available through X-ray. Fig. 5-3a shows an OCT image of superimposed facial views of an incisor tooth compared with an X-ray image. The microstructures shown in this OCT image, namely, the dentin-enamel junction (DEJ), the cross striations of enamel (μm scale), the cross striation in dentin (μm scale), and the demineralization of the incisor edge, all pronounce clear advantages over conventional X-ray images. Fig. 5-3b shows an OCT cross sectional image of a molar tooth with a failing occlusal composite filling.

The voids and fractures are clearly shown in this OCT image, which usually would not be available through X-ray imaging.

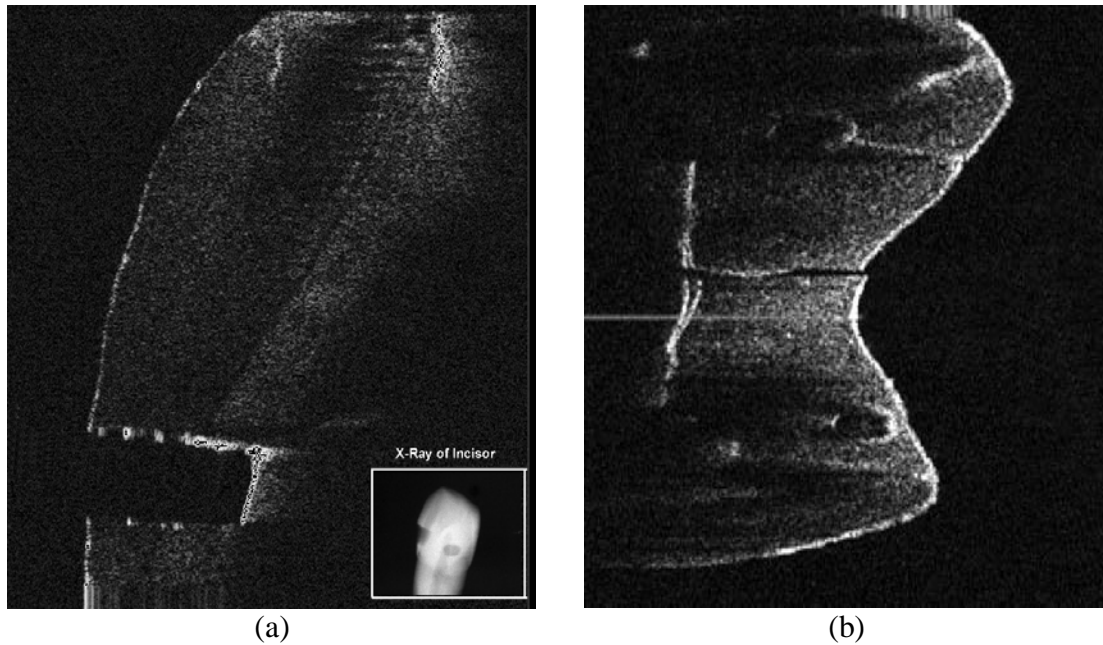


Figure 5-3. OCT images showing dental microstructures: (a) OCT cross sectional image of superimposed facial views of incisor tooth compared with X-ray image; (b) OCT cross sectional image of a molar tooth with failing occlusal composite filling. Image courtesy to Doug Hamilton of Lantis Laser, Inc.

University of Florida (UF) has been collaborating with Lantis Laser, Inc. for the development of the hand-held imaging probe for the OCT Dental Imaging SystemTM (OCT-DIS). In this project, the 2nd-generation FDS micromirror has been adopted as the scanning unit for the imaging probe. Fig. 5-4a schematically shows the imaging concept. Side-view instead of front view is chosen for the ease of manipulation and imaging flexibility. Lantis Laser, Inc. found that dentistry practitioners can handle the probe comfortably 1mm away from the tooth. Considering the size of the tooth, a $\pm 20^\circ$ optical scan angle is required, which can be easily achieved using the 2nd-generation FDS micromirror. The two-part probe design is shown in Fig. 5-4b. The MEMS micromirror is mounted on the MEMS based mount with a 45° slope, steering the light beam between the sample and the GRIN lens, while the fiber and GRIN lens are fixed on the

optics holder. The two parts are glued together and placed in stainless steel housing with a glass cover. A complementary mechanical seat in the two parts ensures proper optical alignment and mechanical integrity during assembly. The optical image of an assembled 2nd-generation FDS micromirror with the MEMS base-mount is shown in Fig. 5-5a.

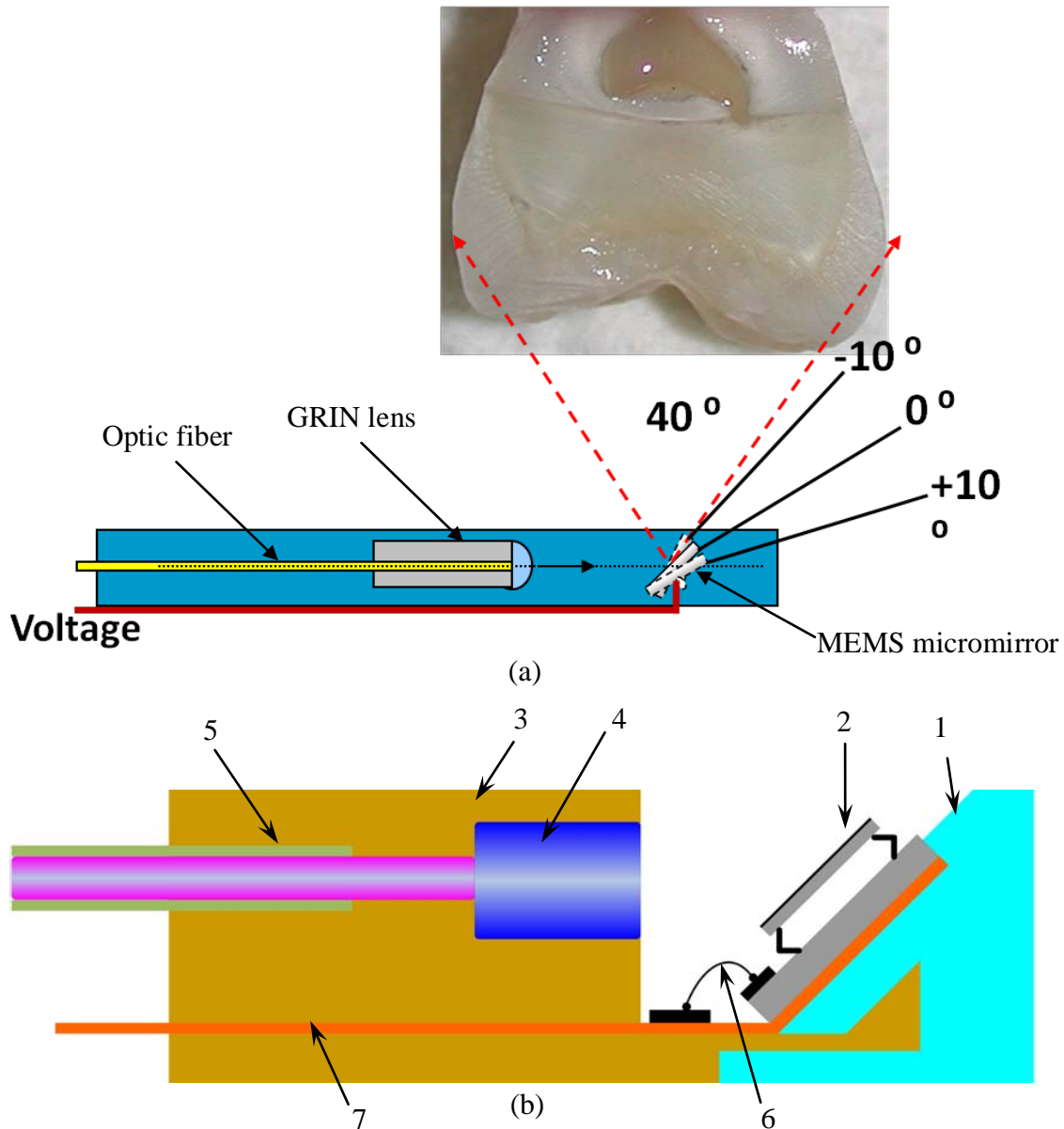


Figure 5-4. Concept and design schematic of the probe: (a) Imaging probe concept; (b) Schematic design of the probe. 1. MEMS base-mount; 2. MEMS device; 3. Optics holder; 4. GRIN lens; 5. Optic fiber; 6. Bond wire; 7. Driving signals.

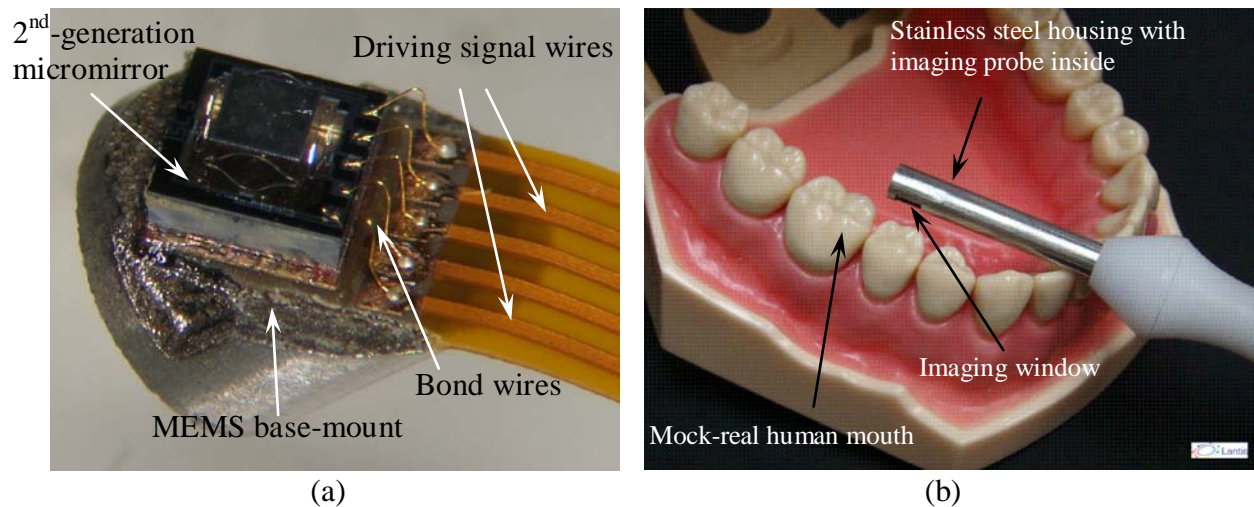


Figure 5-5. Prototype imaging probe developed based on 2nd-generation FDS micromirror: (a) An assembled 2nd-generation micromirror device on MEMS base-mount; (b) Optical image of the prototype image probe.

A prototype MEMS-based probe (Fig. 5-5b) has been developed for real-time dental OCT imaging at chair side. The probe, which is 4.2mm in diameter, consists of an optic fiber, a GRIN lens, and an electrothermally driven micromirror that can achieve dual-axis side-view optical transverse scanning of $\pm 20^\circ$ at less than 8V. The frequency domain OCT system uses a wavelength-swept laser source that scans over a 100nm bandwidth (1260nm ~1360nm) at 20kHz rate, providing an axial resolution of 10 μ m and 10 frame s⁻¹ for 2-D imaging with 1024 transverse pixels per image. The lateral resolution over the 6mm \times 6mm field of view is 35 μ m. Imaging result of human teeth sample shows evident microstructure details that are not available through traditional X-ray imaging technique.

Using the 2nd-generation FDS micromirror, human dental OCT images have been obtained, as shown in Fig. 5-6. Fig. 5-6a shows the OCT image of the cross sectional view of clear erosion to Enamel layer. Dentin Enamel Junction (DEJ), Ebner striations are clearly shown in this image. Fig. 5-6b shows the OCT image of an adult incisor. DEJ is also clearly shown in this image with Ebner striations. In the middle of this image, it is also clearly evident that the tooth surface has

eroded. The Cementium-Dentin boundary layer is also evident at the bottom part of this image. The bench top OCT imaging system setup is shown in Fig. 5-7a, which is now packaged into the chair side operation station shown in Fig. 5-7b.

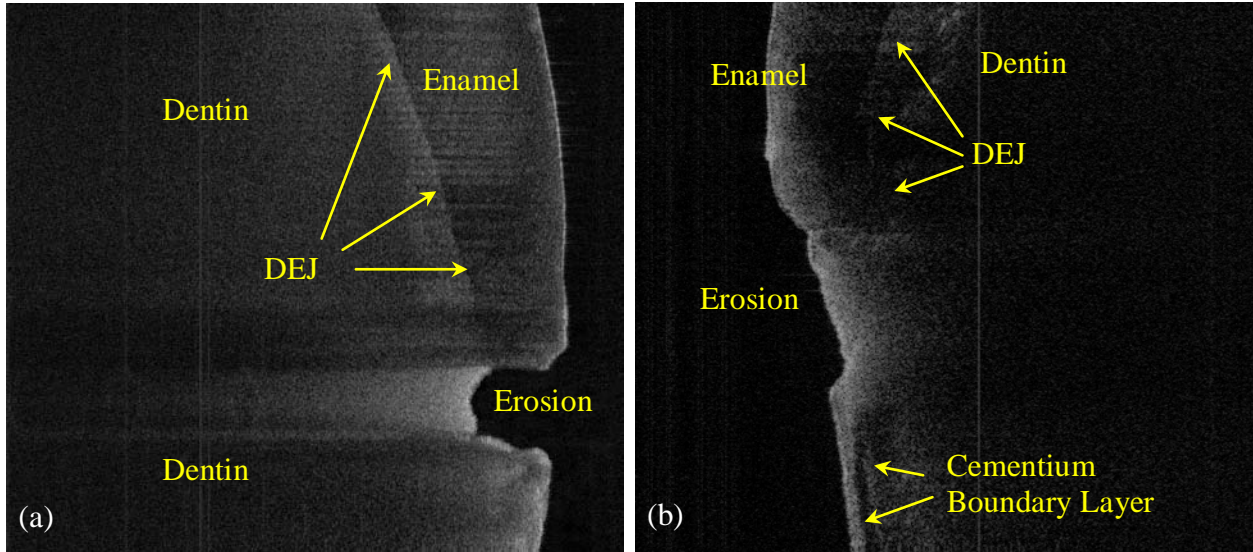


Figure 5-6. Dental OCT images taken by the 2nd-generation FDS micromirror: (a) Erosion of DEJ; (b) Adult incisor with erosion.

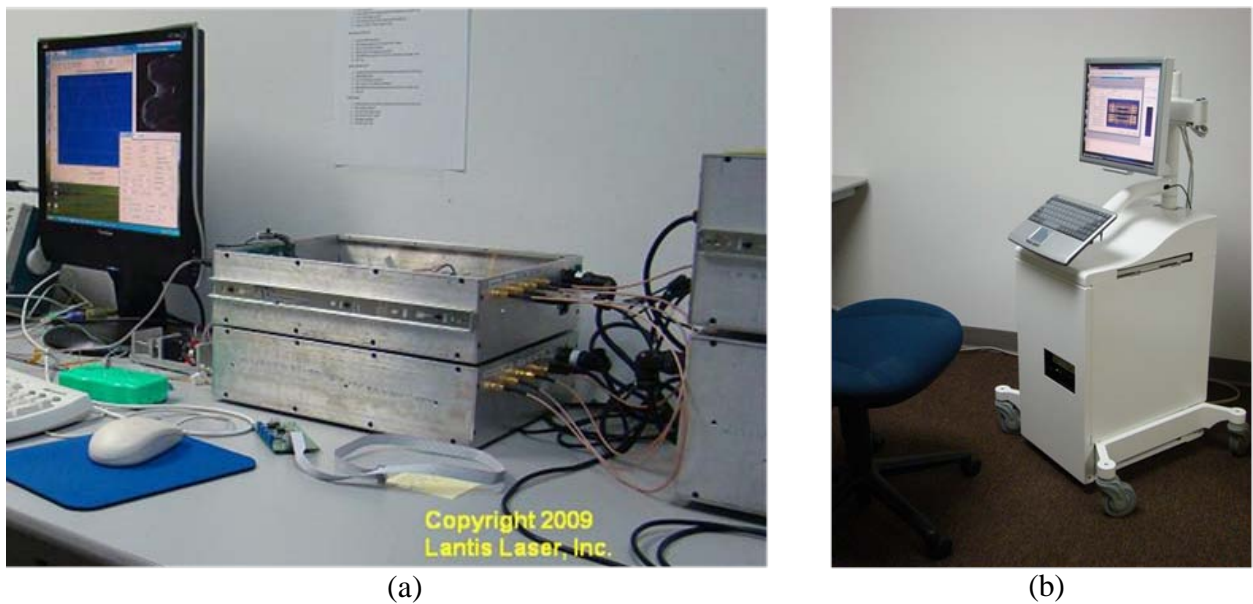


Figure 5-7. OCT imaging system setup: (a) Original bench top imaging system setup; (b) Packaged prototype imaging system product.

Hence, the prototype dental OCT imaging product has been demonstrated. Lantis Laser, Inc. has located a MEMS foundry for the second round mass production of the 2nd-generation FDS micromirror. Effort is being done to increase the device long term stability and resistance to shock vibration in order to be able to survive practical working environment.

5.3 Optical Phased Array Application Using the HFF MMA Devices

HFF MMA devices based on the 3rd-generation micromirror has been developed in Chapter 4. This device is particularly suitable for OPA application in that it can achieve large optical steering angle and SCS-backed large combined optical aperture with a small number of sub-apertures. A packaged MMA device showing the TTP scanning capability has been shown in Fig. 4-18. This section will focus on the experiment using the same device to demonstrate its capability for OPA applications.

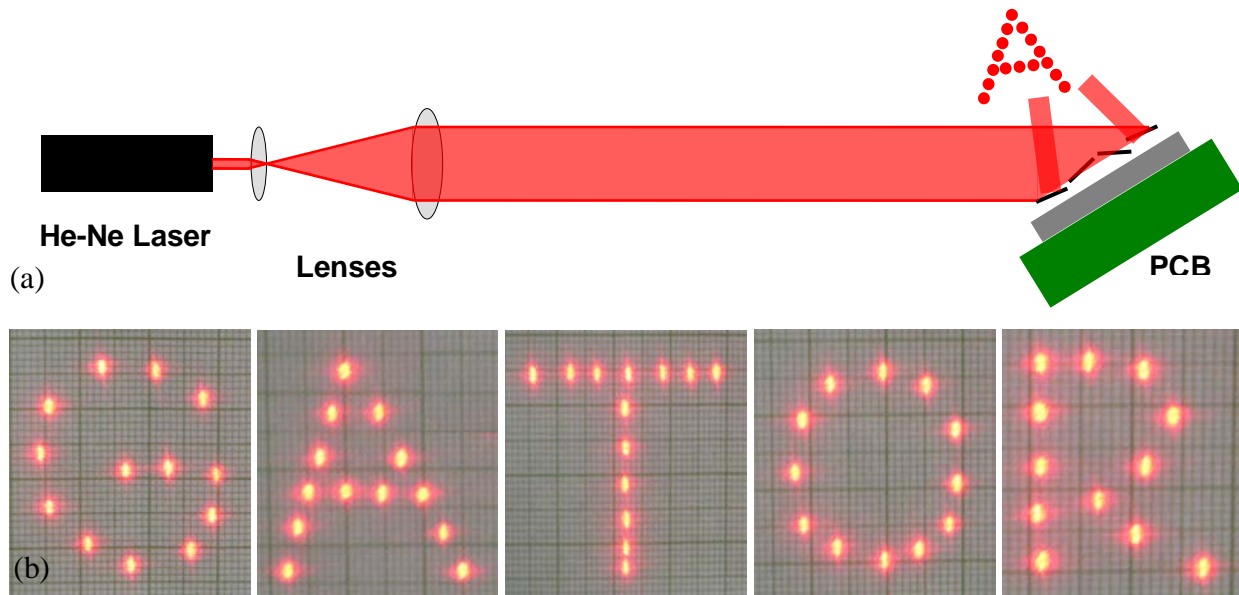


Figure 5-8. Demonstration of the motion capabilities of the mirror pixels: (a) Schematic of the experiment setup; (b) Letters achieved using the reflected light spots from the sub-apertures

To be implemented for OPA applications, the sub-apertures of the MMA device must have individual accessibility and provide accurate dual-axis steering angle. To demonstrate the individual accessibility of the sub-apertures of the surface-mounted 4×4 MMA device, a PCB driving circuit is built to avoid using multiple power supplies. We expand and collimate the beam of a He-Ne laser using two lenses and incident on the 4×4 MMA device. Using each reflected light spot as an image pixel, different letters are formed by controlling the actuators. Fig. 5-8 shows the schematic of this experiment setup and the achieved result.

The purpose of OPA is to use the array of sub-apertures to imitate a large combined optical aperture. This requires that the sub-apertures to have accurate angular steering capability such that as the laser beam is being steered, it should maintain continuous far field wave front as if it is reflected from an optical aperture in the same plane. Therefore, to demonstrate the accurate angle steering capability, we can study the far field pattern of adjacent sub-apertures. The far field Fraunhofer diffraction profile of the two adjacent sub-apertures can be expressed as:

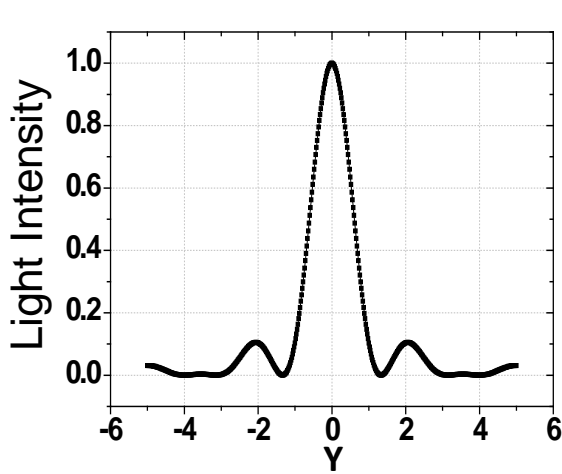
$$I = I_0 \cdot 4a^2 \cdot \frac{\sin^2 u}{u^2} \cdot \cos^2(v + \Phi) \quad (5-1)$$

in which I_0 is a constant, a is the size of each sub-aperture, u is the phase difference between the two edges of the same sub-aperture, and v is the phase difference between the centers of adjacent sub-apertures when they are in the same plane. Φ is the additional phase different between the adjacent sub-apertures when they are not in the same plane. u and v can be expressed as:

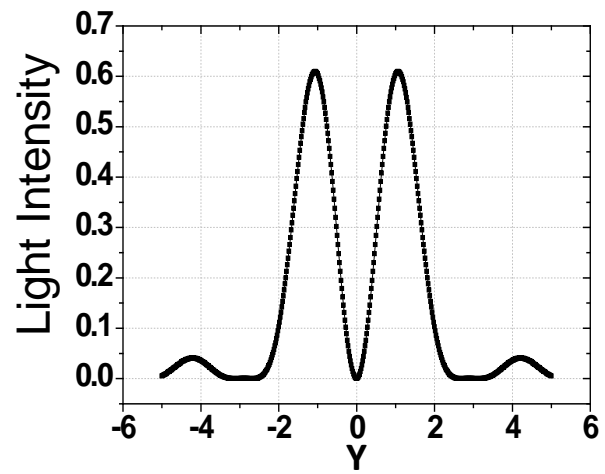
$$u = \frac{k \cdot a}{2} \sin\left(\frac{y}{L}\right) \quad (5-2)$$

$$v = \frac{k \cdot (a+b)}{2} \sin\left(\frac{y}{L}\right) \quad (5-3)$$

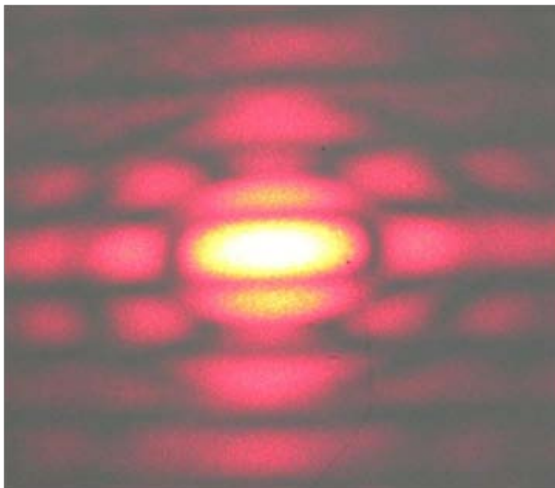
in which b is the spacing between the adjacent sub-apertures, $k=2\pi/\lambda$ is the wave number of the laser beam, y is the distance between the point on the screen to the point that correspond to the center of the two sub-apertures. L is the distance between the sub-apertures to the screen. In this experiment, $a=1.5\text{mm}$, $b=100\mu\text{m}$, $L=5\text{m}$, $\lambda=630\text{nm}$. When the two sub-apertures are in the same plane, $\Phi=0$. In fact, as long as the additional phase difference $\Phi=n\pi$, the far field wave front is the same as when $\Phi=0$. The calculated intensity profiles based on Eq. 5-1 are shown in Fig. 5-9a and Fig. 5-9b for different cases of Φ .



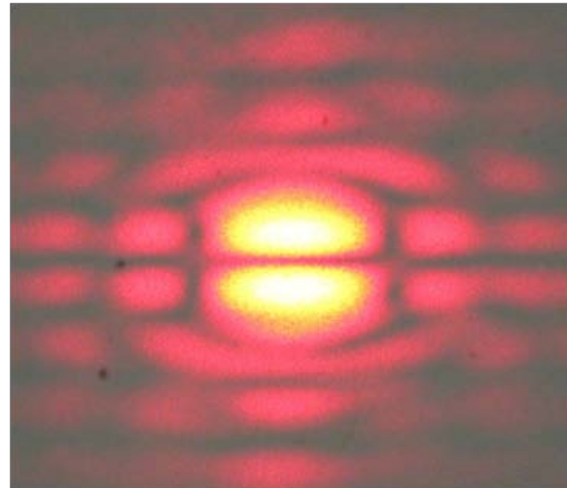
(a) Calculated intensity profile when $\Phi=n\pi$



(b) Calculated intensity profile when $\Phi=n\pi+\pi/2$



(a) $\Phi=n\pi$



(b) $\Phi=n\pi+\pi/2$

Figure 5-9. Theoretical and experimental far-field Fraunhofer diffraction profile of two adjacent sub-apertures: (a) When $\Phi=n\pi$; (b) When $\Phi=n\pi+\pi/2$

By adjusting the actuators of the adjacent sub-apertures, corresponding diffraction patterns to the calculated results shown in Fig. 5-9a and Fig. 5-9b have been achieved, as shown in Fig. 5-9c and Fig. 5-9d, which proves that the accurate control of the steering angle can be realized.

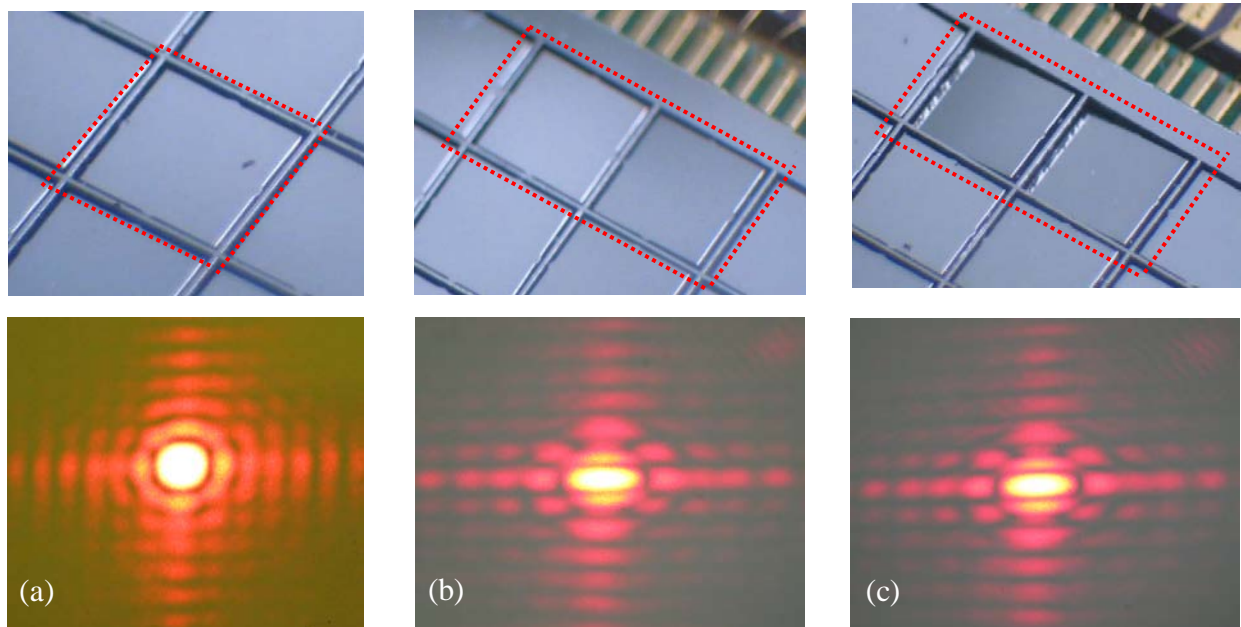


Figure 5-10. Comparative diffraction patterns of single and two adjacent sub-apertures: (a) Single mirror pixel. (b), (c) Two consecutive sub-apertures $n\pi$ -in-phase with 0° and 30° optical deflection angles.

The comparative diffraction patterns of a single sub-aperture and a rectangular aperture consisting of two consecutive sub-apertures are shown in Fig. 5-10a and Fig. 5-10b, respectively. It is clearly seen that the 2×1 rectangular aperture reduces the spot size in the longer-edge direction as the phase difference between the two sub-apertures was adjusted to be exactly $2n\pi$. If a 2×2 square aperture is used, the spot size will be reduced in both directions. The reduced spot can be steered to as much as 30° with little size change, as shown in Fig. 5-10c. Effort is being done to steer the laser beam with larger array sizes.

5.4 Summary

This chapter presented the application attempts using the electrothermal micromirrors and MMA developed. First, the 1-D micromirror has been integrated with the miniaturized catheter designed by SUNY-SB for endoscopic OCT imaging. Diagnostic images of precancerous and cancerous mouse bladder tissue have been obtained and verified by histology. Then, the 2nd-generation FDS micromirror has been implemented as the scan engine for the OCT Dental Imaging System of Lantis Lasers, Inc. Using the 2nd-generation FDS micromirror and the designed probe, DEJ erosion image of human tooth has been obtained which shows clear dental microstructures including DEJ, dentin and enamel striations that can not be offered by traditional X-ray imaging. Finally, experiments based on the HFF MMA device developed have been done to prove that the MMA devices have both individual accessibility as well as precise steering angle control, which demonstrates its potential and capability for OPA application.

CHAPTER 6 DEVELOPMENT OF THE PIEZOELECTRIC FDS MICROMIRROR

Piezoelectric actuation is another actuation mechanism that can potentially achieve large scanning range with relatively low driving voltage. Other advantages of piezoelectric actuation include wide operation bandwidth and extremely low power consumption. The deposition of thin film piezoelectric material has been a challenge. But with the recent development in various deposition techniques including sputtering [99, 100], Pulse Laser Deposition (PLD) [98], Metalorganic Chemical Vapor Deposition (MOCVD) [101-103], and Chemical Solution Deposition (Sol-gel, Aerogel) [105-109], mature preparation of high quality thin film piezoelectric material has become feasible. In this chapter, the theory of piezoelectric actuation will first be presented and compared with electrothermal actuation. Then, a piezoelectric actuator design, which has similar structure setting as the proposed FDS bimorph actuator in Chapter 3, will be presented and analyzed. This design demonstrates the same actuation concept and works as the piezoelectric counterpart of the electrothermal FDS bimorph actuator.

6.1 Principle of Piezoelectric Bimorph Actuation

Some materials experience mechanical deformation at the presence of an electric field. Conversely, mechanical deformation can also cause electric charge to gather on their surfaces. This phenomenon is known as the piezoelectric effect, first discovered by Pierre and Jacques Curie in 1880 [6]. While the later effect can be used for sensing, the former effect can be used for actuation. As sensors piezoelectric materials have been widely used in Micro-Ultrasonic-Transducers (MUTs) and microphones. As actuators, they are widely used in scanning micromirrors and deformable micromirror devices for beam steering and adaptive optics applications. Many of the piezoelectric materials need a poling process to activate their piezoelectric effect. For a well grown and activated piezoelectric layer under the presence of an

applied electric field, the strain-stress relationship that is used for describing the actuation can be modified as [163]:

$$\begin{pmatrix} \varepsilon_1 \\ \varepsilon_2 \\ \varepsilon_3 \\ \varepsilon_4 \\ \varepsilon_5 \\ \varepsilon_6 \end{pmatrix} = \begin{pmatrix} s_{11} & s_{12} & s_{13} & s_{14} & s_{15} & s_{16} \\ s_{21} & s_{22} & s_{23} & s_{24} & s_{25} & s_{26} \\ s_{31} & s_{32} & s_{33} & s_{34} & s_{35} & s_{36} \\ s_{41} & s_{42} & s_{43} & s_{44} & s_{45} & s_{46} \\ s_{51} & s_{52} & s_{53} & s_{54} & s_{55} & s_{56} \\ s_{61} & s_{62} & s_{63} & s_{64} & s_{65} & s_{66} \end{pmatrix} \begin{pmatrix} \sigma_1 \\ \sigma_2 \\ \sigma_3 \\ \sigma_4 \\ \sigma_5 \\ \sigma_6 \end{pmatrix} + \begin{pmatrix} d_{11} & d_{21} & d_{31} \\ d_{12} & d_{22} & d_{32} \\ d_{13} & d_{23} & d_{33} \\ d_{14} & d_{24} & d_{34} \\ d_{15} & d_{25} & d_{35} \\ d_{16} & d_{26} & d_{36} \end{pmatrix} \begin{pmatrix} E_1 \\ E_2 \\ E_3 \end{pmatrix} \quad (6-1)$$

in which ε_I, σ_J ($I, J=1, 2, 3, 4, 5, 6$) are strain and stress, respectively. Here 1, 2, 3, represents the x, y, z directions, respectively, while 4, 5, 6 represents y - z diagonal, x - z diagonal and x - y diagonal directions, respectively. E_i ($i=1, 2, 3$) is the applied electric field, i denotes the x, y, z directions, respectively. s_{IJ} is the elastic compliance of the material in different directions. d_{iI} is the piezoelectric constant. Under the condition that no other physical effect is involved in the analysis, the first item on the right side of Eq. (6-1) describes the residual or intrinsic stress induced strain, while the second item denotes the extrinsic strain induced by piezoelectric effect [163].

For hexagonal (Class 6) crystallized piezoelectric materials such as Lead-Zirconate-Titanate (PZT), Eq. (6-1) can be simplified to:

$$\begin{pmatrix} \varepsilon_1 \\ \varepsilon_2 \\ \varepsilon_3 \\ \varepsilon_4 \\ \varepsilon_5 \\ \varepsilon_6 \end{pmatrix} = \begin{pmatrix} s_{11} & s_{12} & s_{13} & 0 & 0 & 0 \\ s_{12} & s_{11} & s_{13} & 0 & 0 & 0 \\ s_{13} & s_{13} & s_{33} & 0 & 0 & 0 \\ 0 & 0 & 0 & s_{44} & 0 & 0 \\ 0 & 0 & 0 & 0 & s_{44} & 0 \\ 0 & 0 & 0 & 0 & 0 & s_{66} \end{pmatrix} \begin{pmatrix} \sigma_1 \\ \sigma_2 \\ \sigma_3 \\ \sigma_4 \\ \sigma_5 \\ \sigma_6 \end{pmatrix} + \begin{pmatrix} 0 & 0 & d_{31} \\ 0 & 0 & d_{31} \\ 0 & 0 & d_{33} \\ 0 & d_{15} & 0 \\ d_{15} & 0 & 0 \\ 0 & 0 & 0 \end{pmatrix} \begin{pmatrix} E_1 \\ E_2 \\ E_3 \end{pmatrix} \quad (6-2)$$

Two most commonly used piezoelectric multi-morphs-based actuator structures are shown in Fig. 6-1. Similar to electrothermal bimorph actuation, piezoelectric actuation also makes use

of the extrinsic stress/strain to realize the actuation. As shown in Fig. 6-1a, a single layer of a piezoelectric material with the top and bottom electrodes is supported by a layer of a dielectric material, usually SiO_2 . As an electric field is applied across the electrodes, piezoelectric effect causes the piezoelectric layer to generate a strain while the dielectric layer does not. This creates a one-sided strain mismatch. Whereas in Fig. 6-1b, two layers of a piezoelectric material are separated by three electrodes with the center one being the ground. As voltage signals with reversed polarity are applied to the top and bottom electrodes, the top and bottom piezoelectric layer undergo opposite strains. This creates a differential strain. Except for the difference in their strain mismatch, the analysis of the two structures shown in Fig. 6-1 is essentially the same. But due to the easier fabrication and poling process required for the structure in Fig. 6-1a, we will use it in the following analysis.

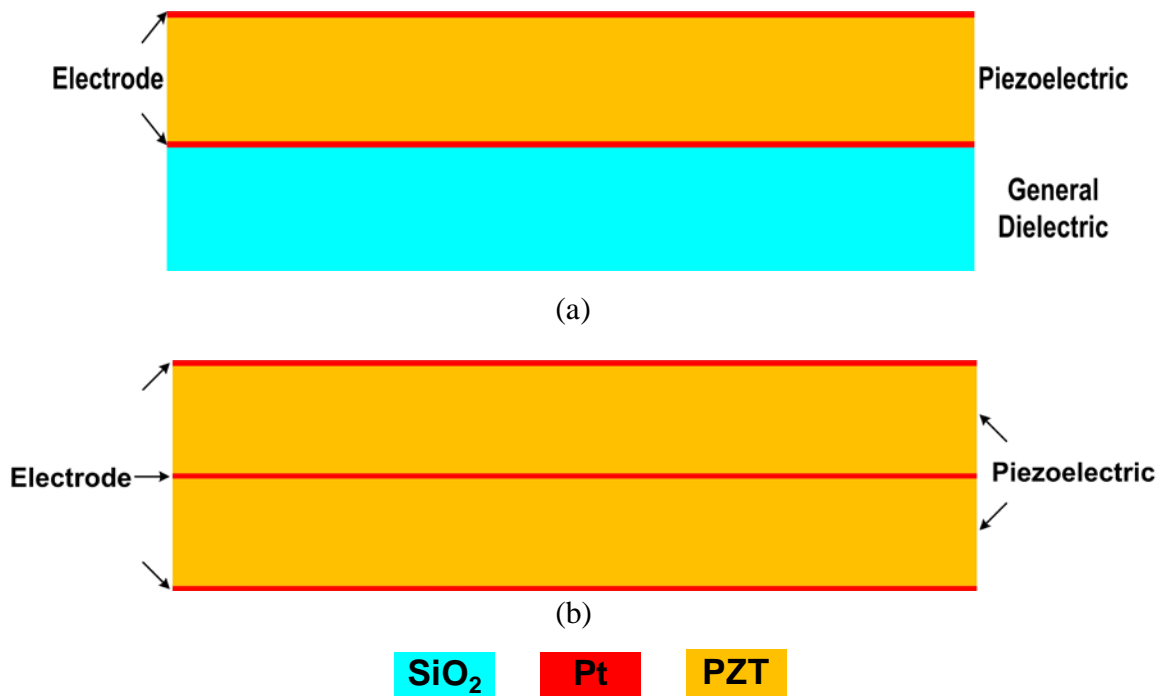


Figure 6-1. Common piezoelectric multi-morph actuator: (a) Single layer piezoelectric layer with general dielectric layer as support; (b) Double layer piezoelectric layers.

The difference between electrothermal and piezoelectric actuation methods is that electrothermal actuation uses Joule heating to generate the extrinsic stress/strain while piezoelectric actuation uses piezoelectric effect. If we assume that the electric field applied through the electrodes is uniformly distributed along the bimorph beam and therefore generates a constant radius of curvature along the bimorph beam, then the assumptions listed at the end of Section 2.1 are satisfied which means that the equations developed in Section 2.2 can be directly applied to piezoelectric actuation except for the strain mismatch $\Delta\varepsilon$ between the top piezoelectric layer and the bottom general dielectric layer.

Following the direction convention set in Fig 6-1, the length of the beam l_b is along x direction, the width w is along y direction and thicknesses, t_1 for piezoelectric layer and t_2 for general dielectric layer, is along z direction. Assume that w and t_1+t_2 are much smaller than l_b , and the mechanical impact of the electrodes is negligible, the strain-stress relationship described in Eq. (6-2) can be simplified to:

$$\varepsilon_1 = s_{11}\sigma_1 + s_{12}\sigma_2 + s_{13}\sigma_3 + d_{31}E_3 \quad (6-3)$$

The general dielectric layer at the bottom does not have strain change under the applied electric field; therefore we can obtain the piezoelectric effect induced strain mismatch $\Delta\varepsilon_{pz}$ as:

$$\Delta\varepsilon_{pz} = d_{31}E_3 \quad (6-4)$$

Inserting Eq. (6-4) into Eq. (2-7), we can express the tip-tilt angle caused by the piezoelectric actuation as:

$$\theta_{pz} = \frac{l_b}{\rho_{pz}} = \frac{\beta_b l_b}{t_1 + t_2} \Delta\varepsilon_{pz} = \frac{\beta_b l_b}{t_1 + t_2} d_{31} E_3 \quad (6-5)$$

in which β_b is the curvature coefficient of the bimorph as described in Eq. (2-4). t_1 and t_2 represent the thicknesses of the PZT and general dielectric layer, respectively. l_b is the length of the bimorph. With an input voltage of V , the electric field in the z direction can be expressed as:

$$E_3 = \frac{V}{t_1} \quad (6-6)$$

Inserting Eq. (5-6) into Eq. (5-5) renders the angular actuation capacity by piezoelectric effect, as shown in Eq. (5-7):

$$\theta_{pz} = \frac{l_b}{\rho_{pz}} = \frac{\beta_b l_b}{t_1 + t_2} \Delta \varepsilon_{pz} = \frac{\beta_b l_b}{t_1 (t_1 + t_2)} d_{31} V \quad (6-7)$$

Eq. (6-7) shows that the angle of the piezoelectric bimorph is linearly dependent on the driving voltage. This provides a better control of the actuation angle than electrothermal bimorph actuation because the later, as described in Eq. (2-9), is linearly dependent on the temperature, which has a square relation with the driving voltage. Moving V to the left side of Eq. (6-7) gives the responsivity of this bimorph actuator upon piezoelectric actuation as:

$$S_{pz} = \frac{\theta_{pz}}{V} = \frac{\beta_b l_b}{t_1 (t_1 + t_2)} d_{31} \quad (6-8)$$

Eq. (6-8) clearly states that in order to increase the actuation range of a piezoelectric bimorph actuator, we need longer beam l_b , thinner layer t_1 and t_2 , and higher piezoelectric coefficient d_{31} . The most direct and effective optimization of S_{pz} is to choose a large d_{31} . Some important properties of several piezoelectric materials are summarized in Table 6-1.

From Table 6-1 one can see that PZT has much superior performance in its high piezoelectric coefficient. Its d_{31} coefficient is hundreds to thousands of times higher than the other piezoelectric materials. This has made PZT a very popular material for piezoelectric actuator designs. We will also use PZT as the material of interest in the following analysis.

Table 6-1. Coefficients and mechanical properties of some piezoelectric materials [6, 163, 164]

Materials	d_{33} (Å/V)	d_{31} (Å/V)	d_{15} (Å/V)	Young's Modulus (GPa)	Density (g/cm ³)
PZT	152	-60.2	440	135 (c_{11})	7.6
PVdF	-0.35	0.28	-0.04	2×10^{-4}	1.78
Quartz	0.02	---	---	76-97	---
ZnO	0.12	-0.05	-0.08	---	---
LiNbO3	0.06	-0.01	0.68	---	---
LiTaO3	0.08	-0.02	0.26	---	---

Besides choosing a large d_{31} coefficient, S_{pz} can also be increased through the optimization of $\beta_b/t_1(t_1+t_2)$ by adjusting thickness ratio t_1/t_2 . Recall Eq. (2-18) we have:

$$\frac{\beta_b}{t_1(t_1+t_2)} = \frac{1}{t_1(t_1+t_2)} \cdot \frac{6(1+\zeta)^2}{\chi \cdot \zeta^3 + 4\zeta^2 + 6\zeta + 4 + \chi^{-1} \cdot \zeta^{-1}} \quad (6-9)$$

in which ζ is the thickness ratio between PZT and general dielectric layer $\zeta=t_1/t_2$, and χ is the ratio of their bi-axial Young's Modulus $\chi=E'_1/E'_2$.

In practical design, the thickness of PZT layer is always constrained by dielectric breakdown and process achievability. Therefore, it is more realistic and practical to choose a fixed thickness of the PZT layer and optimized the thickness of the general dielectric layer to achieve maximal S_{pz} . If we choose constant PZT thickness as $t_1=t_{pz}$, then Eq. (6-9) becomes:

$$\frac{\beta_b}{t_1(t_1+t_2)} = \frac{1}{t_{pz}^2} \cdot \frac{6\zeta(1+\zeta)}{\chi \cdot \zeta^3 + 4\zeta^2 + 6\zeta + 4 + \chi^{-1} \cdot \zeta^{-1}} \quad (6-10)$$

Assume the dielectric layer that supports the PZT layer is SiO₂, plugging in the mechanical properties of PZT and SiO₂ into Eq. (6-10), the optimal ratio ζ can be obtained numerically from the normalized plot of Eq. (6-10) and Eq. (6-8). As shown in Fig. 6-2, this optimal thickness ratio is found to be 1.55 for PZT and SiO₂.

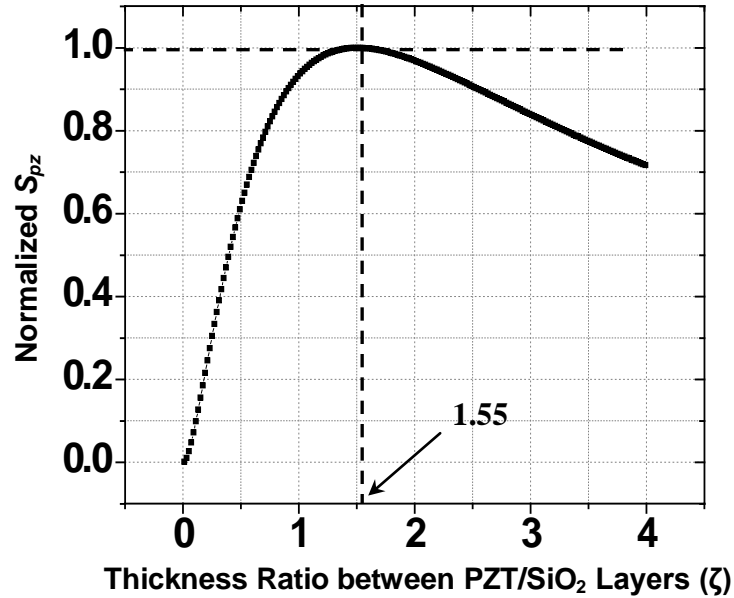


Figure 6-2. Numerical calculation of the optimal thickness ratio with fixed PZT thickness.

Hence, the actuation principle of single piezoelectric layer cantilevered bimorph actuator shown in Fig. 6-1a has been demonstrated. The voltage responsivity of this actuator has been obtained and optimized from material selection and structural parameters perspectives. In the next section, the analytical calculation shown in Section 6.1 will be examined and verified by FEM simulation result.

6.2 FEA Modeling of Single PZT Layer Cantilevered Bimorph Actuator

FEM model of single PZT layer cantilevered bimorph has been built and simulated to verify the analytical calculation result in Section 6.1. The general dielectric layer is SiO_2 . Table 6-2 lists the material properties and structural dimensions used in this simulation.

Table 6-2. Material properties and structural dimensions used in FEM simulation and theoretical calculation

Materials	Material Properties								
	Young's Modulus (GPa)					Poisson Ratio	Relative Permissivity	Piezo-Constants ($10^{12}C/N$)	
PZT	c_{11}	c_{12}	c_{13}	c_{33}	c_{44}	0.3	540	d_{31}	
	135	67	68	113	22			-60.2	
SiO ₂	70					0.17	3.9	---	
Materials	Structural Dimensions								
	Length (μm)			Width (μm)			Thickness (μm)		
PZT	120			12			1.2		
SiO ₂	120			12			0.3-9.6		

First, the bimorph tilting angle as a function of actuation voltage is simulated and compared to the analytical calculation result using Eq. (6-7) with same parameters. In this FEM simulation and theoretical calculation, the thickness of SiO₂ layer is set to 1.2 μm . The FEM simulation results provide the beam deflection which is used to calculate the bimorph tilting angle. The simulation and calculation result is presented in Fig. 6-3, which shows a clear linear relation between bimorph tilting angle and actuation voltage. The theoretical calculation result using Eq. (6-7) also shows close match to the FEM simulation result. Fig. 6-4a shows the 3-D image of the deformed bimorph beam upon piezoelectric actuation. Fig. 6-4b shows a plot of points on beam and the corresponding vertical displacement. As shown in Fig. 6-4, the 120 μm long, 2.4 μm thick (PZT: 1.2 μm ; SiO₂: 1.2 μm) bimorph beam showed $\sim 4\mu m$ tip vertical displacement with 20V actuation voltage.

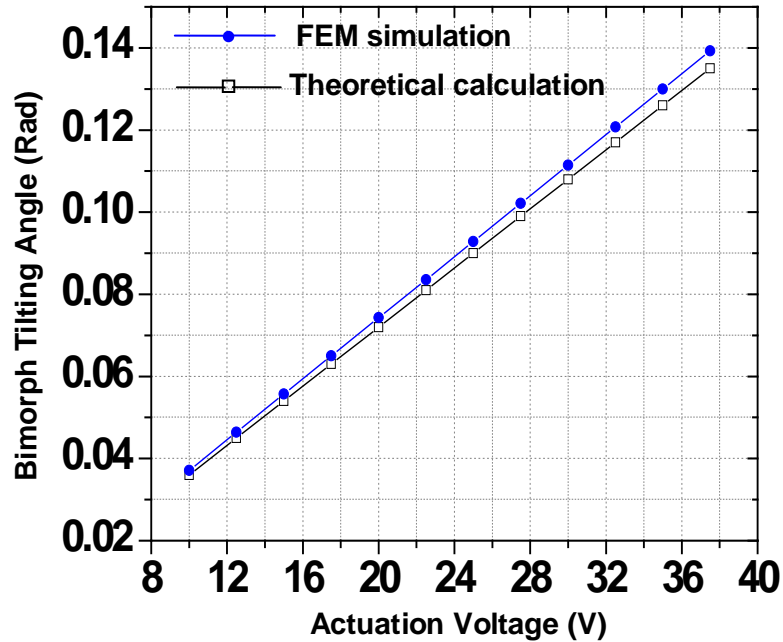


Figure 6-3. FEM simulation result showing close match to theoretical calculation result using Eq. (6-7). Linear relation between bimorph tilting angle and actuation voltage is verified.

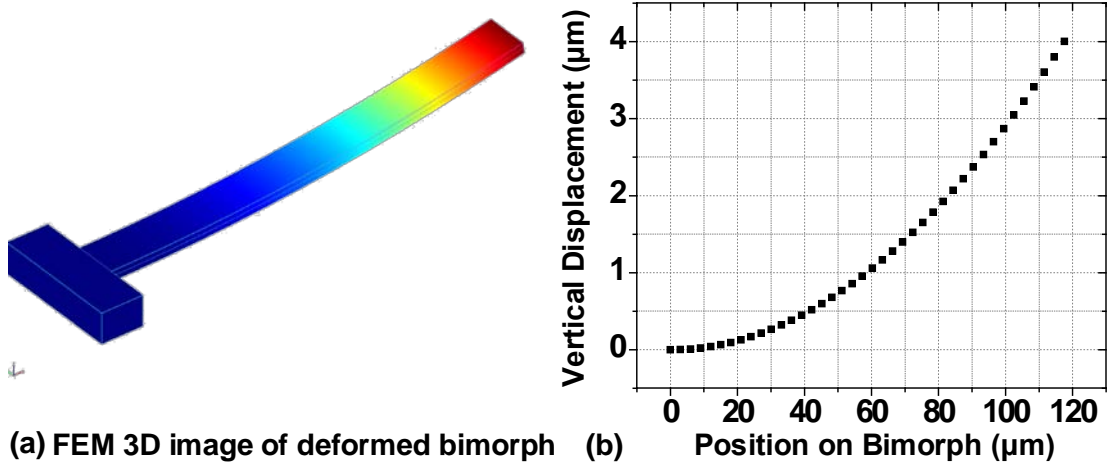


Figure 6-4. PZT-SiO₂ bimorph deflection upon voltage input: (a) 3D image of deformed bimorph; (b) Vertical displacement on bimorph beam.

A series of FEM simulations also has been conducted to find out the optimal thickness ratio. In these simulations, the thickness of the PZT layer is fixed to 1.2 μm , while the thickness of the SiO₂ layer changes from 0.3 μm to 9.6 μm . Actuation voltage is fixed to 30V. The

simulated bimorph tilting angles as a function of the layer thickness ratio is presented in Fig. 6-5. The corresponding calculated result is also shown in Fig. 6-5. Both results are normalized with reference to the simulation result. It is shown from Fig. 6-5 that the simulated optimal thickness ratio is a close match to what has been predicted in Fig. 6-2. The predicted optimal ratio is 1.55, while the simulated optimal ratio is 1.6.

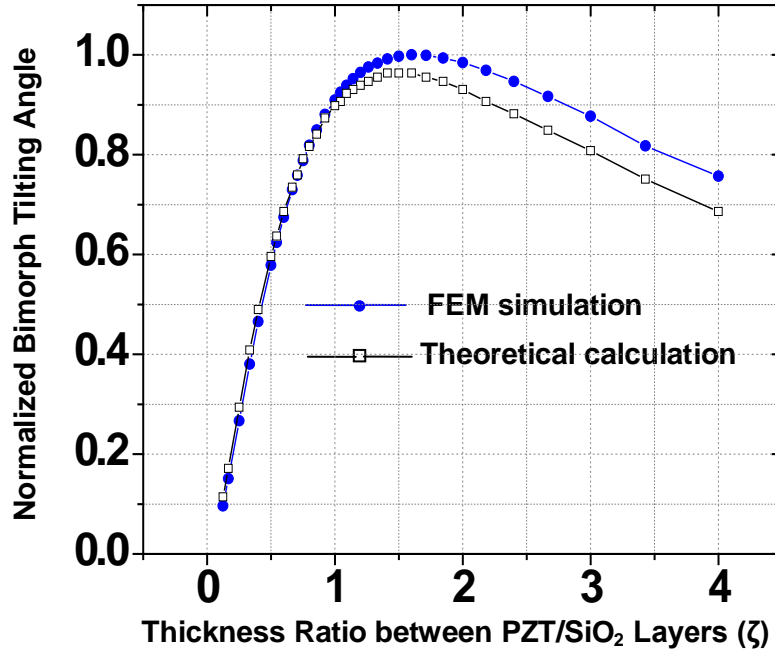


Figure 6-5. FEM simulations and theoretical calculations of optimal thickness ratio to achieve maximal bimorph deflection. Simulation: $\zeta=1.60$; Calculation: $\zeta=1.55$.

The discrepancy between the FEM simulation result and the theoretical calculation result shown in Fig. 6-3 and Fig. 6-4 is mainly caused by the discrepancy in the use of Young's Modulus. Eq. (6-7) assumes that the materials involved have isotropic mechanical properties, whereas PZT has slightly larger in-plane (135GPa for x and y axes) Young's modulus than out-of-plane (113GPa for z axis) Young's modulus. The function in Eq. (6-10) is also moderately influenced by $\chi=E'_{PZT}/E'_{SiO_2}$, therefore resulting in increased discrepancy as ζ increases in Fig. 6-4. However, the overall discrepancy in the target of analysis, *i.e.* the bimorph tilting angle

and optimal thickness ratio is very small (less than 3%). Hence, the theoretical calculation in Section 6.1 is solidified by the FEM simulation result shown in this section.

6.3 Folded Dual S-Shaped Bimorph Actuator based on Piezoelectric Actuation

From the analysis and calculation shown in the previous sections, we can have the conclusion that the deformed shape and deflection formula of a cantilevered piezoelectric bimorph actuator is analogous to that of the cantilevered electrothermal bimorph actuator. The only difference between the two actuators is the mechanisms that induce the strain mismatch, *i.e.* electrothermal bimorph actuator relies on Joule heating, while piezoelectric bimorph actuator uses piezoelectric effect. This analogy suggests that the Folded Dual S-Shaped (FDS) electrothermal bimorph actuation, presented in Chapter 3, can be realized in a piezoelectric way.

Fig. 6-6a shows the schematic of an S-shaped design that can realize the tilt-compensating piezoelectric actuation, analogous to that has been shown in Fig. 3-1b. The ground electrode and the piezoelectric layer are supported by a general dielectric layer, the same as in Fig. 6-1, but the top electrode layer is separated to two sections. Assume that the piezoelectric layer has been poled uniformly along its length, when voltages with reversed polarities are applied to the two top electrodes, the two bimorph segments will bend in opposite directions due to the opposite strain mismatches generated, as shown in Fig. 6-6b, resulting in compensated tilting angle at the tip of the bimorph. Ideally, if the two bimorph segments have the same length, complete tip tilting compensation, *i.e.*, zero tilting, can be achieved. In this design, the first bimorph segment acts as the non-inverted bimorph segment in electrothermal FDS bimorph actuator, while the second bimorph segment acts as the inverted segment. The piezoelectric S-shaped bimorph series do not need the overlap portion for increasing the robustness.

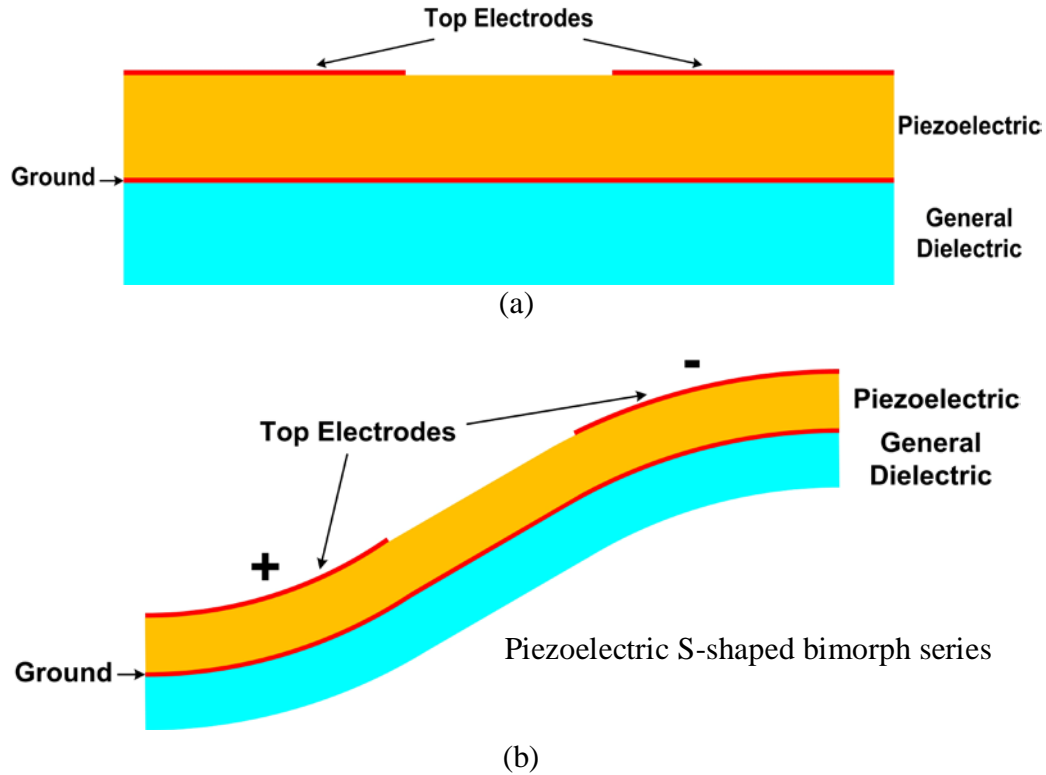


Figure 6-6. S-Shaped tilt-compensating piezoelectric bimorph actuator design. Voltages with reversed polarities are applied to two top electrodes: (a) Before actuation; (b) After actuation.

Hence, it is conceivable that by connecting two S-shaped piezoelectric bimorph actuators in series with the second one folded, a piezoelectric version of FDS bimorph actuator can be realized to achieve TTP actuation with zero lateral shift and fixed rotation axes. FEM models have been built to verify this actuation concept. First, the S-shaped bimorph actuator shown in Fig. 6-6b was built and simulated. The bimorph beam is 300 μm in length with the first segment 120 μm , 60 μm in the middle and the second segment also 120 μm . It was fixed at one end with reversed polarity voltages applied to the two top electrodes. The deformed S-shaped bimorph upon actuation is shown in Fig. 6-7a. A cross-section plot of the beam deflection along the bimorph was taken to verify the tilting compensation and is shown in Fig. 6-7c. It is clear that the

tilting angle at the tip of the bimorph has been compensated to be parallel to the substrate. With a pair of $\pm 30\text{V}$ actuation voltage, a tip vertical displacement of $12.5\mu\text{m}$ is achieved.

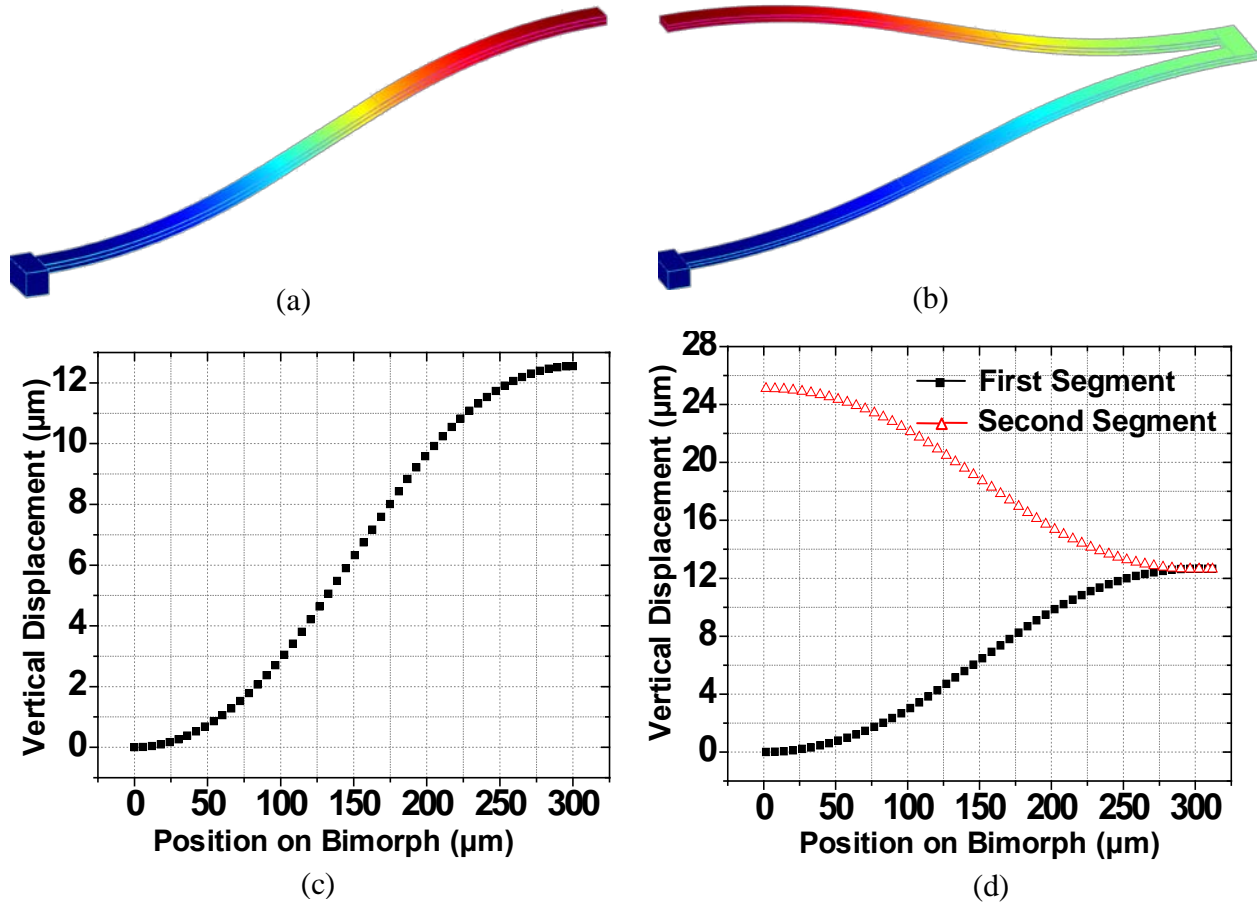


Figure 6-7. Deflection of piezoelectric FDS bimorph actuators. (a) FEM 3D image of one S-shaped bimorph actuator; (b) FEM 3D image of full FDS bimorph actuator; (c) Vertical deflection along single S-shaped bimorph beam showing compensated tilting; (d) Vertical deflection along whole FDS bimorph beam showing compensated tilting and zero lateral shift.

Then, two S-shaped bimorph beams were connected in series with the second one folded. Each S-shaped bimorph has the same structure and dimensions as the one shown in Fig. 6-7a. Again, one end of the bimorph is fixed and one pair of reversed polarity voltages is applied on the two top electrodes for both S-shaped bimorphs. The 3D image of this deformed FDS bimorph beam is shown in Fig. 6-7b. Cross section plot of the beam deflection along the bimorph was

also taken to verify the compensated tilting and lateral shift, as shown in Fig. 6-7d. With a pair of $\pm 30\text{V}$ actuation voltage, a tip vertical displacement of $25\mu\text{m}$ is achieved. It is also clear from the plot that the tip of the FDS bimorph beam has fully compensated tilting angle and near-zero lateral shift. The FDS bimorph actuator shown in Fig. 6-7c composes the piezoelectric version of half the actuator that has been shown in Fig. 3-2b.

6.4 Development of Piezoelectric FDS Micromirrors

From Section 6.3, it is conceivable that micromirror devices based on the piezoelectric version of the FDS bimorph actuator can be realized that is capable of achieving TTP scanning the same as the electrothermal FDS micromirrors proposed in Chapter 3. This section will focus on the development of this micromirror device.

6.4.1 Design of the Piezoelectric FDS Micromirror

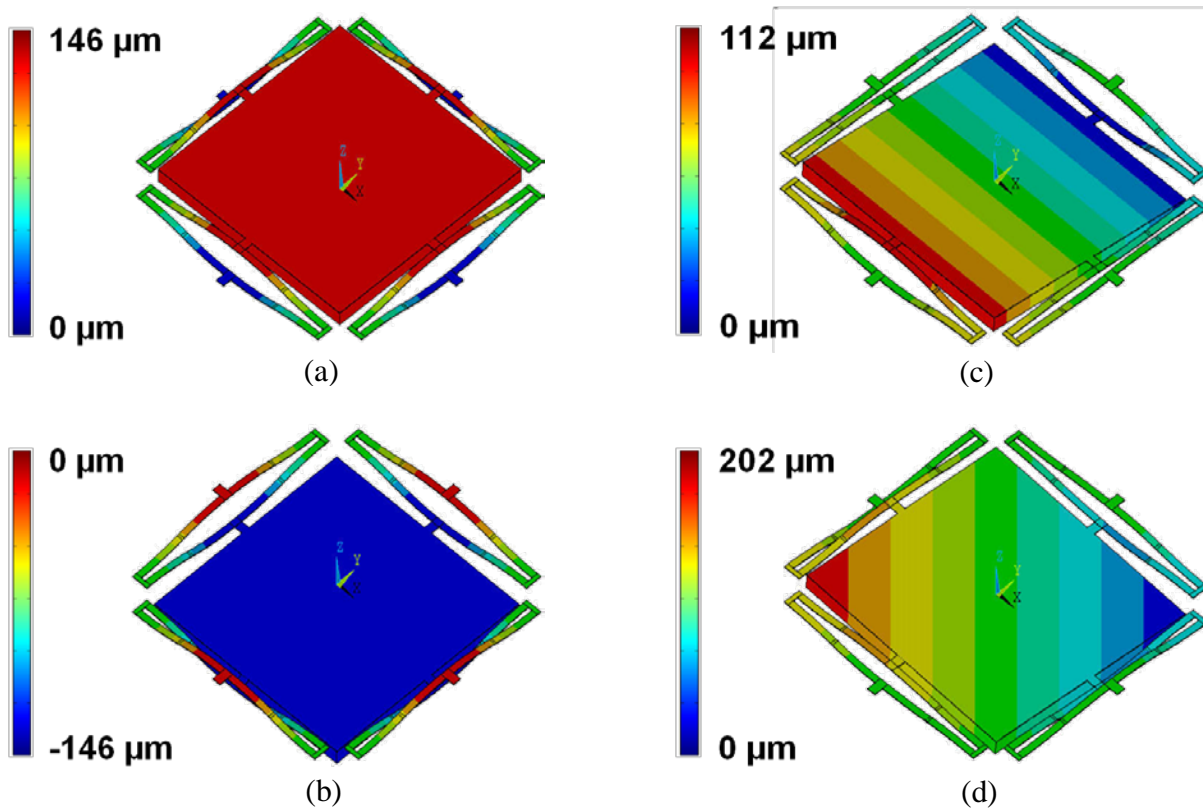


Figure 6-8. FEA simulation result of the piezoelectric FDS micromirror: (a) Piston upward; (b) Piston downward; (c) Orthogonal axis rotation; (d) Diagonal axis rotation.

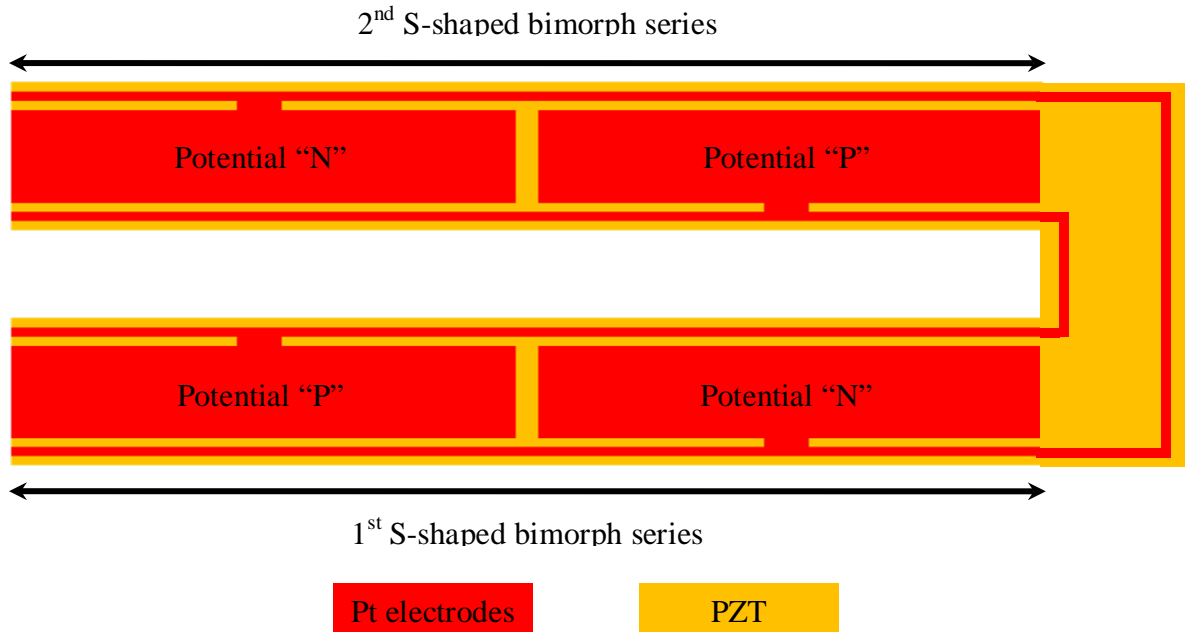


Figure 6-9. Electrical connections of the top electrodes on one FDS bimorph actuator.

FEA models have been built to verify the actuation of the piezoelectric FDS micromirror. Fig 6-8 shows the FEA simulation result of one such mirror. The mirror plate has a dimension of 1mm×1mm with 40μm of silicon as support. All FDS bimorph actuators share the same bottom electrode as the ground potential. Each FDS bimorph actuator has four patterned top electrodes, two for each S-shaped bimorph series. The length and width of each S-shaped bimorph series is 500μm and 60μm, respectively. Each electrode is 36μm wide and 240μm in length. The separation between the two electrodes on the same S-shaped bimorph series is 20μm. Electrodes that ought to have the same electrical potentials are interconnected within the actuator by a 6μm wide serial bus. The electrical connections of the top electrodes of each FDS actuator are shown in Fig. 6-9. When all the "P" top electrodes are applied +30V and all the "N" electrodes are applied -30V, the mirror plate pistons upward by 146μm, as shown in Fig. 6-8a. In reverse, when all the "N" top electrodes are applied +30V and all the "P" electrodes are applied -30V, the mirror plate pistons downward by 146μm, as shown in Fig. 6-8b. When voltages of ±30V are

applied to “N”/“P” and “P”/“N” top electrodes of one opposing actuator pair, the mirror plate performs a rotation of 6.5° along the direction orthogonal to the edge of the mirror plate, as shown in Fig. 6-8c. Similarly, when adjacent actuator pairs are applied the same voltage arrangement, while the other adjacent actuator pairs are applied reversed voltage arrangement, the mirror plate performs a rotation of 8.2° along the diagonal direction of the mirror plate, as shown in Fig. 6-8d.

Compared with the electrothermal FDS bimorph actuators, the piezoelectric FDS bimorph actuator is simpler in structure. The width of the piezoelectric bimorph is much larger than that of the electrothermal bimorph due to the need of electrical wirings. FEA simulations of the piezoelectric version of the FDS micromirror show similar behavior as the electrothermal FDS micromirror but with smaller displacement and deflection per unit voltage.

6.4.2 Fabrication of the Piezoelectric FDS Micromirror

The cross sectional view of the fabrication process of the piezoelectric FDS micromirror is shown in Fig. 6-10. The process starts with a SOI wafer with $1\mu\text{m}$ thermal SiO_2 already grown on the top device side (Fig. 6-10a). The good quality of the thermal SiO_2 is essential to the successful growth of the PZT layers. Then, 200nm of Ti (20nm) / Pt (180nm) layer is deposited using sputtering to form the bottom electrode (Fig. 6-10b). Next step is the sol-gel growth of the PZT layer (Fig. 6-10c). The detailed steps of the PZT solution preparation and the film growth can be found in [163]. Then, the top electrode is deposited and pattern using a lift-off process (Fig. 6-10d) followed by an Al lift-off process (Fig. 6-10e) to form the mirror plate and bonding pads. Next, the PZT layer, the bottom electrode layer and the thermal SiO_2 layer is sequentially etched to expose the Si (Fig. 6-10f~g). Then, the backside Si/ SiO_2 is etched to form the mirror plate (Fig. 6-10h). Finally, the structure is released from the front side by anisotropic (Fig. 6-10i) and isotropic (Fig. 6-10j) Si etching.

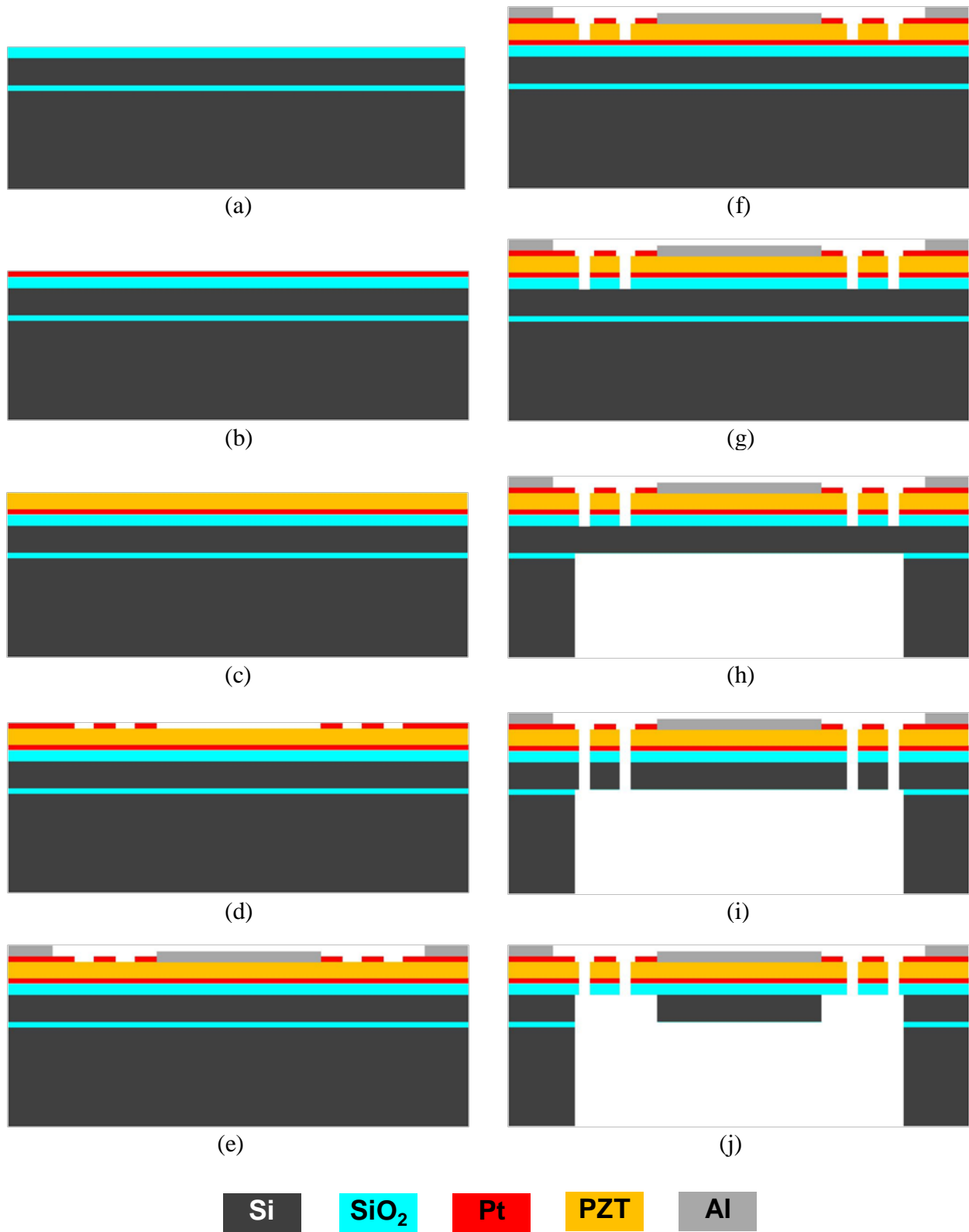


Figure 6-10. Cross sectional view of the fabrication process of the piezoelectric FDS micromirror.

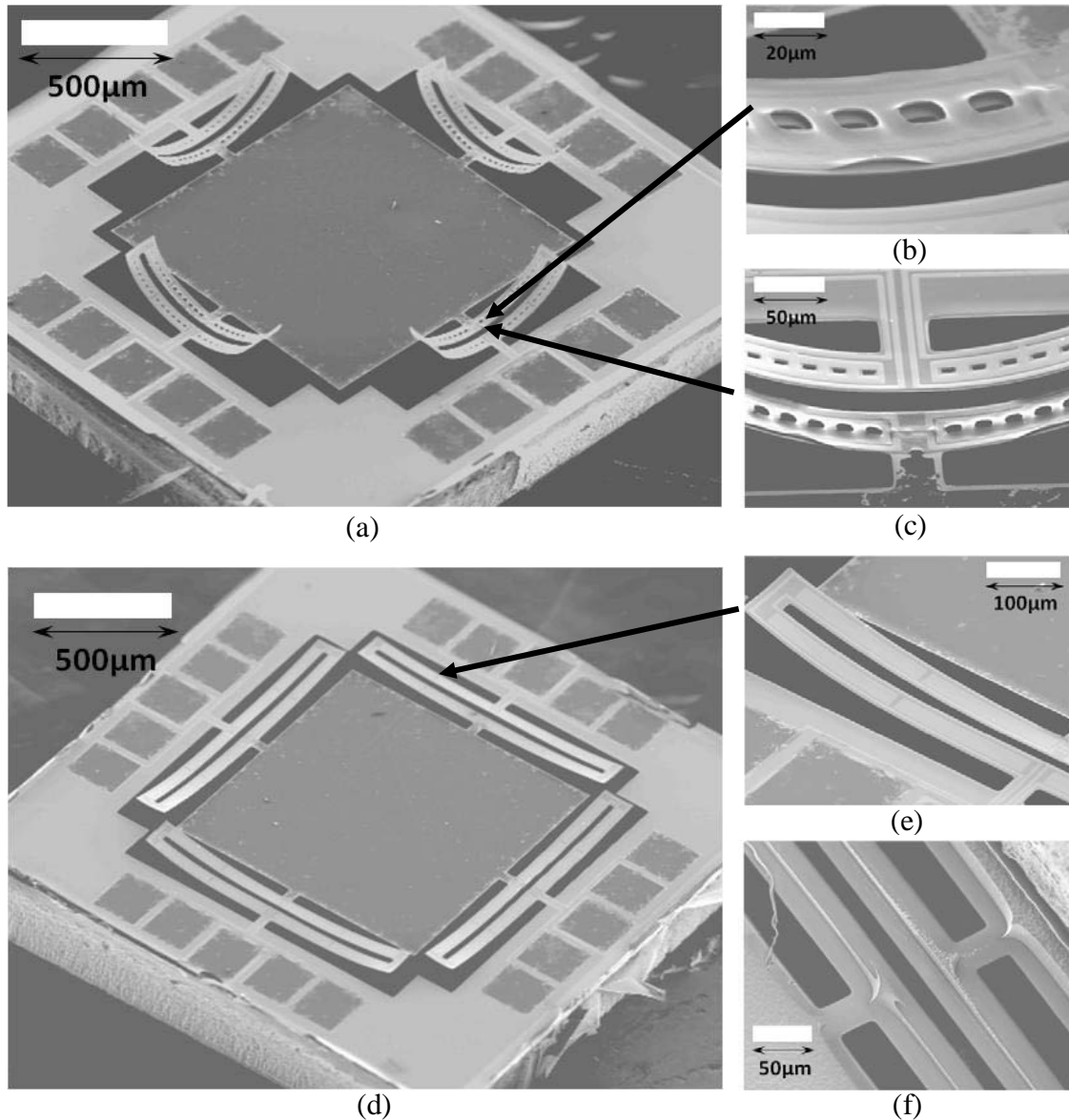


Figure 6-11. SEM images of the fabricated piezoelectric FDS micromirrors: (a) The design with square-shaped holes on the bimorph; (b) and (c) PZT peeling off at the end of the actuators; (d) The design without the holes on the bimorph; (e) Close up image of the FDS actuator; (f) Remaining Si on the back of the bimorph actuator.

The SEM images of the fabricated PZT mirror are shown in Fig. 6-11. Square-shaped holes are applied to some of the devices to facilitate the final release step of the micromirror, shown in Fig. 6-11a. But this has caused the PZT layer at the bimorph of the FDS actuator to peel off from the SiO₂ layer, as shown in Fig. 6-11b and Fig. 6-11c. Hence, only the designs without the holes on the bimorphs, as shown in Fig. 6-11d, remain functional after fabrication.

The large thermal stress of the PZT layer caused the SiO₂/PZT bimorph to have an initial curling after the structure release (step Fig. 6-10j), as shown in Fig. 6-11a. The designs with the square holes on the bimorph have larger initial curling than the designs that without the holes. This is because the large width of the bimorph without the holes provides better protection to the Si underneath and the actuator after release still has a thin line of silicon remaining on the back, as shown in Fig 6-11f. This behavior was not anticipated in our previous projection, shown in Fig. 6-6a, of the piezoelectric FDS bimorph without actuation. This initial curling prevents the successful formation of the S-shaped bimorph series and hence the actuation of the micromirror can not be executed as efficient as anticipated. However, by actuating one set of either “P” or “N” electrodes, the mirror plate can still generate detectable displacement and tilting. The testing result shown in the next section is from the design without the holes on the bimorph.

6.4.3 Characterization of the Piezoelectric FDS Micromirror

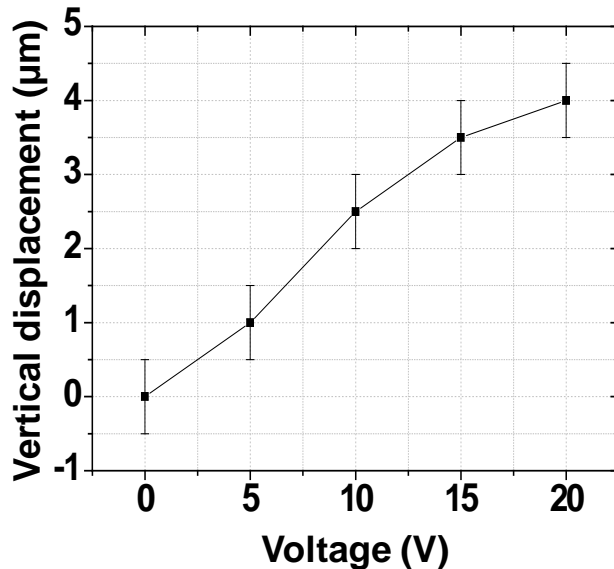


Figure 6-12. Static piston characterization of the piezoelectric FDS micromirror.

The piezoelectric FDS micromirror developed has been characterized following the testing procedures taken by the electrothermal FDS micromirrors. The static piston characterization

result is shown in Fig. 6-12, where only $\sim 4\mu\text{m}$ vertical displacement was observed when 20V dc voltage is applied to one set of “N” electrodes on all FDS actuator. Static rotation characterization is unavailable due to the unperceivable static deflection. However, the rotation angle became detectable when the micromirror was driven at its resonance frequency. It has been found that the resonance frequencies for both orthogonal rotation modes are around 1.58k Hz. When driven at resonance, the rotation angle as a function of the driving voltage on the set of “N” electrodes on one FDS actuator has been recorded and plotted in Fig. 6-13.

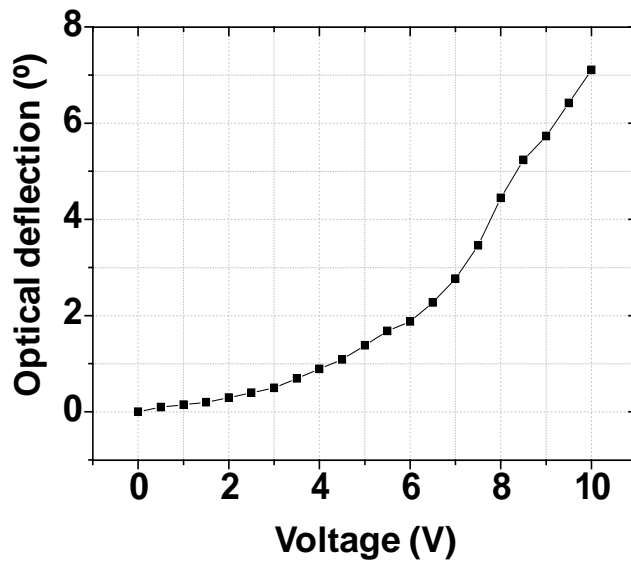


Figure 6-13. Rotation characterization of the piezoelectric FDS micromirror at resonance. Voltages are applied to the “N” electrodes on one FDS actuator.

Some Lissajous patterns achieved by the piezoelectric FDS micromirror at resonance are shown in Fig. 6-14, which demonstrate the dual axis scanning capability of the device. However, the testing result shown in Fig. 6-12, Fig. 6-13 and Fig. 6-14 do not prove that the actuation is the result of the piezoelectric effect. In fact, it is highly possible that the actuation is the result of the electrothermal effect induced by the leakage current. Currently, further testing is being conducted to determine which effect is responsible for the actuation.

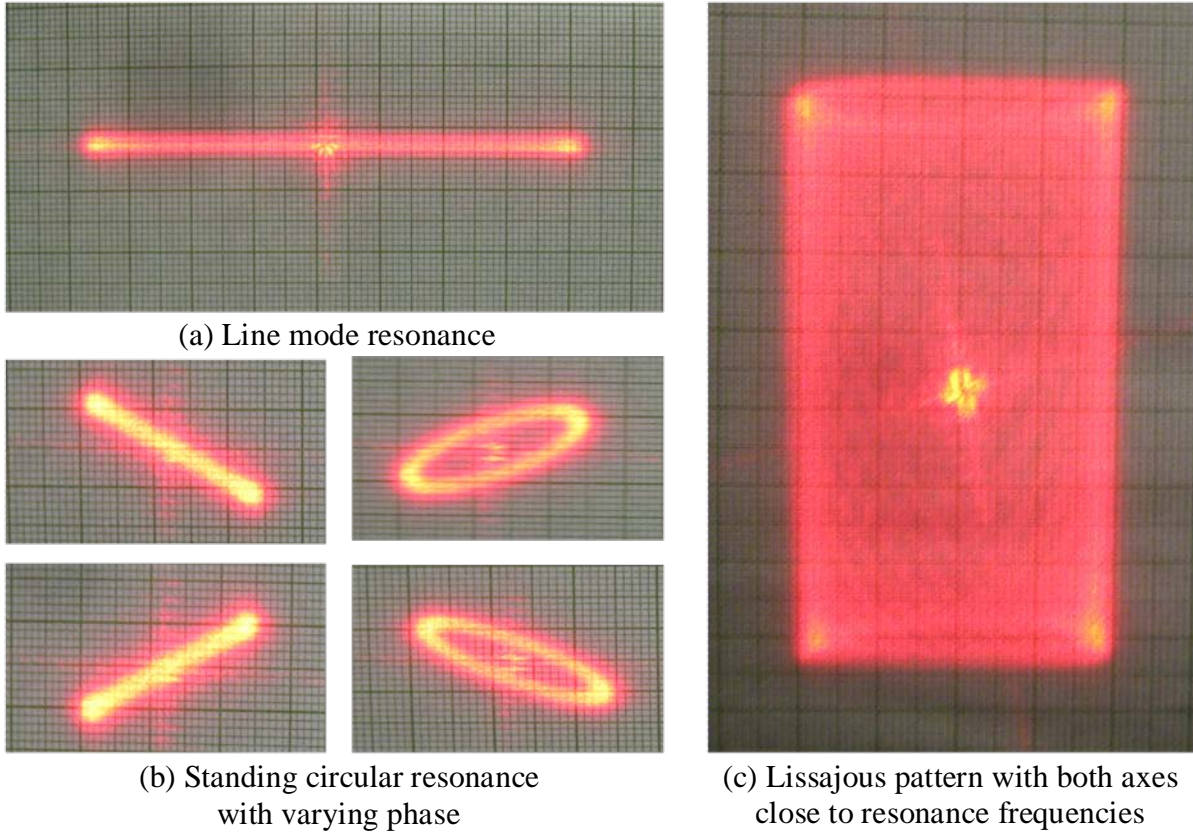


Figure 6-14. Lissajous scanning patterns achieved by the piezoelectric FDS micromirror at resonance frequency.

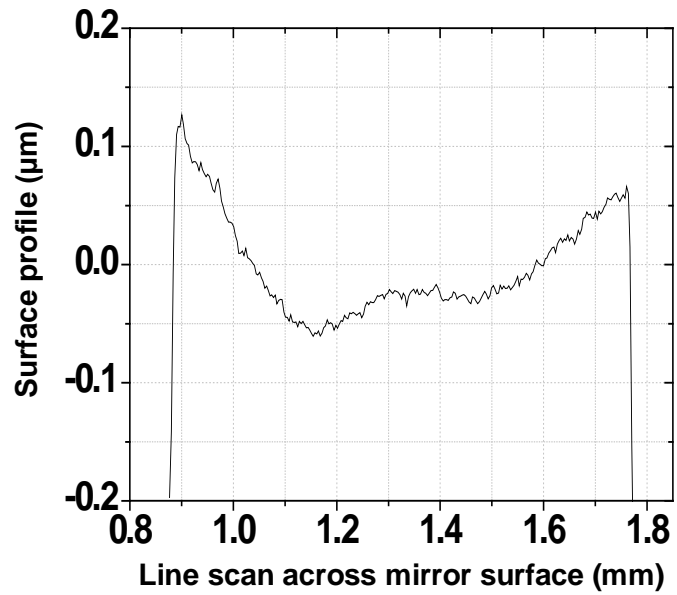


Figure 6-15. Surface quality characterization using Wyko optical profilometer.

Finally, the mirror surface quality of the device was characterized by Wyko optical profilometer with the result shown in Fig. 6-15. The device shows a radius of curvature of $\sim 0.5\text{m}$ with a surface roughness of $\sim 30\text{nm}$.

6.5 Summary

This chapter first discussed the principle of piezoelectric actuation. Two designs of piezoelectric bimorph actuators were revealed in Section 6.1. The theoretical calculation of the first piezoelectric bimorph design has been carried out to understand the actuation capability including beam deflection angle and actuator responsivity. Based on the calculation results, optimizations in terms of material selection and structural dimensions were discussed to maximize the actuator responsivity. FEM modeling of the discussed actuator has been done to verify the theoretical calculation result in Section 6.2. FEM simulation result of the beam deflection angle matched closely with the theoretical calculation result. The calculation of the optimal thickness ratio with a fixed piezoelectric layer thickness has resulted in close match with the FEM simulation result. A piezoelectric version of FDS bimorph actuator, as proposed in Section 3.1, was proposed in Section 6.3. FEM modeling of half and full FDS actuator has been performed to verify the actuation concept. It can be concluded from the theoretical analysis and FEM simulation that the piezoelectric FDS bimorph actuator has the potential to achieve the same TTP actuation capability just as the electrothermal FDS bimorph actuator proposed in Chapter 3. Section 6.4 presents the design, fabrication and characterization of the piezoelectric FDS micromirror. The large thermal stress of the PZT layer caused the bimorph beam to curl initially after release, which limits the actuation efficiency of the actuator. Although static piston actuation and rotation actuation at resonance have been realized, it is inconclusive that the actuations are the result of the piezoelectric effect. It is suspected that the actuations are caused by the bimorph structure due to the leakage current. Currently, more testing is being conducted.

Piezoelectric bimorph actuator has linear transduction between actuation voltage and deflection angle, offering easier dynamic device control. It has comparatively large operation range and low driving voltage. It also has extremely low power consumption and wide operation bandwidth. This gives piezoelectric FDS micromirrors advantages over electrothermal FDS micromirrors especially MMA devices in applications such as OPAs where a large number of devices are required and low power consumption is desired.

CHAPTER 7 CONCLUSION AND FUTURE PLAN

This research work has developed the folded dual S-shaped (FDS) bimorph actuator which can achieve piston displacement without any lateral shifting and rotation scanning with stationary rotation axis. Based on this actuator design, a novel design and fabrication method for high fill-factor, small footprint, and tip-tilt-piston micromirrors and MMAs with SCS-supported mirror plate have been developed. The 2nd-generation FDS micromirror achieves a fill factor of 30% with a footprint of 2mm×2mm and dual-axis optical scanning range of $\pm 30^\circ$ at less than 8V. The 2nd-generation FDS micromirror has been successfully implemented as the scan engine for prototype commercial Dental OCT imaging applications. The 3rd-generation FDS micromirror achieves a record high fill factor of 45%, a record small footprint of 1.45mm×1.55mm and $\pm 20^\circ$ dual-axis optical scanning range. The MMAs developed achieve a fill factor of 88% in the mirror array region. The fabrication method of the HFF MMAs is the only design with SCS-backed mirror plate while does not need any bonding-transfer techniques. The MMAs achieve a record high sub-aperture size of 1.5mm×1.5mm and centimeter-scale combined optical aperture size with less than 100 elements. Each sub-aperture has a radius of curvature of several meters and is capable of 320 μ m vertical piston and 30° optical tip/tilting at less than 8V. The MMAs developed has also demonstrated the capability for optical phased array applications. The high fill factor micromirrors and MMAs also have surface-mount integration capability that can further reduce the space consumption in imaging probe and OPA systems.

Based on the same design concept, a piezoelectric version of the FDS micromirror has been proposed and experimentally demonstrated. Although the initial curling of the bimorph actuator caused by the thermal stress of the PZT layer limits the actuation efficiency of the actuator, detectable static piston actuation and rotation scanning at resonance have been realized.

7.1 Research Accomplishment

The following tasks have been accomplished for this work:

1. A 1-D micromirror has been designed, fabricated and implemented for the application of endoscopic OCT imaging to detect early cancer. The device is capable of achieving 30° of 1-D optical deflection with a dimension of $1.9\text{mm}\times 2.4\text{mm}$. Clinical result using the implemented imaging probe has been obtained and verified by histology result.
2. A novel FDS electrothermal bimorph actuator design has been proposed and designed that solves the lateral shifting problem and the mirror plate initial tilting problem in previous electrothermal micromirror devices.
3. Two generations of micromirror devices have been designed and developed based on this FDS electrothermal bimorph actuator. The devices can achieve a piston stroke of up to $480\mu\text{m}$ with near-zero lateral shifting and $\pm 30^\circ$ dual axis rotation scanning with fixed rotation axes at small driving voltage of less than 8V. The device shows 10ms response time and a 3dB cut-off frequency of up to 200Hz.
4. A prototype imaging probe has been designed and implemented using the 2nd-generation FDS micromirror as the scanning engine. Dental OCT imaging using this probe has been successfully demonstrated. The team is currently working on the technology transfer for the commercial mass production of this probe.
5. A novel design and fabrication method of micromirror with ultra-high fill factor and ultra-small footprint has been proposed and implemented for the 3rd-generation FDS micromirror. The device has a unprecedented small footprint of $1.45\text{mm}\times 1.55\text{mm}$ with a fill factor of 45% and is capable of achieving piston stroke of up to $180\mu\text{m}$ and $\pm 30^\circ$ dual axis optical deflection at small driving voltage of less than 8V.
6. High fill factor micromirror array devices have been developed based on the 3rd-generation FDS micromirror. The obtained 4×4 and 8×8 micromirror array device achieve a fill factor of 88% and combined optical aperture of $6.4\text{mm}\times 6.4\text{mm}$ and $1.34\text{cm}\times 1.34\text{cm}$, respectively. Each sub-aperture is capable of piston stroke of $320\mu\text{m}$ and $\pm 30^\circ$ dual axis optical deflection all at less than 8V. Preliminary optical phased array capability has been demonstrated using the 4×4 micromirror array device.
7. The Sol-gel PZT growth and fabrication process has been co-developed. A PZT version of the FDS micromirror has been designed, fabricated and characterized. The device shows $\sim 4\mu\text{m}$ static piston stroke and $\sim 7^\circ$ optical deflection at the resonance frequency of 1.58K Hz. However, whether the actuation is based on piezoelectric effect of electrothermal effect is still under investigation.

7.2 Future Work

The micromirror and MMA devices developed in this work have shown great potential in the applications of biomedical imaging and optical phased array. However, to realize the end goals, additional work need to be done.

For biomedical imaging applications, although the 2nd-generation FDS micromirror has been implemented for prototype dental OCT imaging application, it has been found during the prototype probe assembling process that the current micromirror devices are susceptible to improper handling. The long term reliability and the resistance to shock vibration need to be improved in order to survive the practical working environment.

To achieve ultra-small imaging probe with less than 2mm diameter, the 3rd-generation FDS micromirror need to be implemented. Currently, the design of the probe based on the 3rd-generation FDS micromirror is on going. One drawback with the 3rd-generation FDS micromirror is the recessed mirror plate, as shown in Fig. 4-5b, which limit the effective optical aperture size. This can be solved by either choosing a SOI with thinner substrate, or increase the length of the bimorph actuator to enlarge the initial vertical displacement. At this point it is very promising that we would be able to achieve the smallest imaging probe ever.

For OPA applications of the HFF MMA devices, although optical experiment has demonstrate its capability of arbitrary and precise angular steering of the sub-apertures, more work need to be done to demonstrate its full OPA capability. In order to develop MMA devices with larger combined optical aperture, flip chip integration of the MMA device and the electronics is eventually needed. Dedicated driving electronics also need to be developed to drive all the actuators simultaneously. Dynamic laser beam steering experiment need to be carried out using larger MMAs. The design and fabrication concept of the HFF MMA can be applied to

other designs, *e.g.* the lateral shift free (LSF) micromirrors developed by L.Wu and other driving method, *e.g.* piezoelectric bimorph actuation.

The development of the piezoelectric FDS micromirror is not accomplished as well as anticipated. Further improvement on both design and fabrication process are needed. Eventually, a large MMA array based on piezoelectric bimorph actuation could be realized.

LIST OF REFERENCE

- [1] "Microelectromechanical Systems (MEMS) Technology: Current And Future Markets," *Electronics.ca Research Network*, 2006.
- [2] P. Rai-Choudhury, "MEMS and MOEMS: Technology and Applications," *SPIE Press*, 2000.
- [3] M. E. Motamedi, "MOEMS: history, current status and future trends," *MEMS Investor Journal*, 2007.
- [4] Y. B. Gianchandani, O. Tabata, and H. Zappe, "Comprehensive Microsystems," *Published by Elsevier Science & Technology, ISBN 0444521941, 9780444521941*, vol. 3, 2007.
- [5] J. Ford, "Optical MEMS: A Brief History and Future Trends," *MEMS Investor Journal*, 2005.
- [6] M. E. Motamedi, "MOEMS: Micro-opto-electro-mechanical Systems," *Published by SPIE Press, ISBN 0819450219, 9780819450210*, 2005.
- [7] G. A. Feather and D. W. Monk, "The digital micromirror device for projection display," *Wafer Scale Integration, Proceedings., Seventh Annual IEEE International Conference on*, pp. 43-51, 1995.
- [8] R. Gale, "Principles and applications of the digital micromirror device in projection displays," *Lasers and Electro-Optics Society 12th Annual Meeting*, vol. 1, pp. 212-213, 1999.
- [9] L. J. Hornbeck, "Current status of the digital micromirror device (DMD) for projection television applications," *Electron Devices Meeting, Technical Digest., International*, pp. 381-384, 1993.
- [10] L. J. Hornbeck, "Digital Light Processing and MEMS: an overview," *Advanced Applications of Lasers in Materials Processing*, pp. 7-8, 1996.
- [11] D. W. Monk, "Digital light processing: a new image technology for the television of the future," *International Broadcasting Convention*, vol. 581-586, 1997.
- [12] S. A. Khan and N. A. Riza, "Demonstration of the MEMS Digital Micromirror Device-Based Broadband Reconfigurable Optical Add-Drop Filter for Dense Wavelength-Division-Multiplexing Systems," *Lightwave Technology, Journal of*, vol. 25, pp. 520-526, 2007.
- [13] N. A. Riza and F. N. Ghauri, "Super resolution hybrid analog-digital optical beam profiler using digital micromirror device," *Photonics Technology Letters*, vol. 17, pp. 1492-1494, 2005.

- [14] N. A. Riza and S. A. Reza, "Broadband All-Digital Variable Fiber-Optic Attenuator Using Digital Micromirror Device," *Photonics Technology Letters*, vol. 19, pp. 1705-1707, 2007.
- [15] B.-A. Yu, W. Shin, Y. L. Lee, T. J. Eom, Y.-C. Noh, D.-K. Ko, and J. Lee, "Multiwavelength Switchable Erbium-Doped Fiber Ring Laser using Digital Micromirror Device," *CLEO/Pacific Rim. Conference on*, vol. 1-2, 2007.
- [16] W. M. Duncan, T. Barlett, E. M. Koontz, B. Lee, D. Powell, P. Rancuret, and B. Sawyers, "Dynamic optical filtering in DWDM systems using the DMD," *International Semiconductor Device Research Symposium*, vol. 430, 2001.
- [17] S. J. Shellhammer, D. P. Goren, and T. Palidis, "Novel signal-processing techniques in barcode scanning," *Robotics & Automation Magazine*, vol. 6, pp. 57-65, 1999.
- [18] T. M. Lippert, "Virtual retinal display, a scanned photon delivery system," *LEOS Annual Meeting*, vol. 1, pp. 283-284, 1999.
- [19] Microvision, "Virtual retinal display technology," *Digital Avionics Systems Conference, 17th DASC*, vol. 1, pp. D35/1 - D35/6, 1998.
- [20] Davis, W. O, Sprague, Randy, Miller, and Josh, "MEMS-based pico projector display," *Optical MEMs and Nanophotonics, IEEE/LEOS International Conference on*, pp. 31-32, 2008.
- [21] W. Drexler, U. Morgner, F. X. Kartner, C. Pitris, S. A. Boppart, X. D. Li, E. P. Ippen, and J. G. Fujimoto, "In vivo ultrahigh-resolution optical coherence tomography," *OPTICS LETTERS*, vol. 24, pp. 1221-1223, 1999.
- [22] D. Huang, E. A. Swanson, C. P. Lin, J. S. Schuman, W. G. Stinson, W. Chang, M. R. Hee, T. Flotte, K. Gregory, and C. A. Puliafito, "Optical coherence tomography," *Science*, vol. 254, pp. 1178-1181, 1991.
- [23] D. T. McCormick, J. Woonggyu, Z. Chen, and N. C. Tien, "3D MEMS based minimally invasive optical coherence tomography," *Solid-State Sensors, Actuators and Microsystems. Digest of Technical Papers.*, vol. 2, pp. 1644-1648, 2005.
- [24] J. M. Schmitt, "Optical Coherence Tomography (OCT): A Review," *IEEE JOURNAL OF SELECTED TOPICS IN QUANTUM ELECTRONICS*, vol. 5, pp. 1205-1215, 1999.
- [25] C. R. Chu, D. Lin, J. L. Geisler, C. T. Chu, F. H. Fu, and Y. Pan, "Arthroscopic Microscopy of Articular Cartilage Using Optical Coherence Tomography," *American Journal of Sports Medicine*, vol. 32, pp. 1-11, 2004.

- [26] Y. Pan, R. Birngruber, J. Rosperich, and R. Engelhardt, "Low-coherence optical tomography in turbid tissue: theoretical analysis," *Applied Optics*, vol. 34, pp. 6564-6574, 1995.
- [27] T. Xie, Z. Wang, and Y. Pan, "High-speed optical coherence tomography using fiberoptic acousto-optic phase modulation," *Optics Express*, vol. 11, pp. 3210-3219, 2003.
- [28] J. T. W. Yeow, V. X. D. Yang, A. Chahwana, M. L. Gordon, B. Qi, I. A. Vitkin, B. C. Wilson, and A. A. Goldenberg, "Micromachined 2-D scanner for 3-D optical coherence tomography," *Sensors and Actuators A*, vol. 117, pp. 331-340, 2005.
- [29] W. Denk, J. H. Strickler, and W. W. Webb, "Two-photon laser scanning fluorescence microscopy," *Science*, vol. 248, pp. 73-76, 1990.
- [30] L. FU and M. GU, "Fibre-optic nonlinear optical microscopy and endoscopy," *Journal of Microscopy*, vol. 22, pp. 195-206, 2007.
- [31] L. Fu, A. Jain, C. Cranfield, H. Xie, and M. Gu, "Three-dimensional nonlinear optical endoscopy," *J. Biomed. Opt.*, vol. 12, pp. 040501, 2007.
- [32] W. Piyawattanametha, R. P. Barretto, T. H. Ko, B. A. Flusberg, E. D. Cocker, H. Ra, D. Lee, O. Solgaard, and M. J. Schnitzer, "Fast-scanning two-photon fluorescence imaging based on a microelectromechanical systems two-dimensional scanning mirror," *OPTICS LETTERS*, vol. 21, pp. 2018-2020, 2006.
- [33] R. M. Williams, W. R. Zipfel, and W. W. Webb, "Multiphoton microscopy in biological research," *Curr Opin Chem Biol*, vol. 5, pp. 603-608, 2001.
- [34] M. Gu and C. J. R. Sheppard, "Three-dimensional Imaging in Confocal Fluorescent Microscopy with Annular Lenses," *Journal of Modern Optics*, vol. 38, pp. 2247-2263 1991.
- [35] J. B. Pawley, "Handbook of Biological Confocal Microscopy," *New York: Plenum Press*, 1995.
- [36] C. J. R. Sheppard and D. M. Shotton, "Confocal Laser Scanning Microscopy," *Oxford, United Kingdom: BIOS Scientific Publishers*, 1997.
- [37] S. Claxton, T. J. Fellers, and M. W. Davidson, "LASER SCANNING CONFOCAL MICROSCOPY," 2006.
- [38] H. Miyajima, N. Asaoka, T. Isokawa, M. Ogata, Y. Aoki, M. Imai, O. Fujimori, M. Katashiro, and K. Matsumoto, "A MEMS Electromagnetic Optical Scanner for a Commercial Confocal Laser Scanning Microscope," *JOURNAL OF MICROELECTROMECHANICAL SYSTEMS*, vol. 12, pp. 243-251, 2003.

- [39] H. Ra, W. Piyawattanametha, Y. Taguchi, D. Lee, M. J. Mandella, and O. Solgaard, "Two-Dimensional MEMS Scanner for Dual-Axes Confocal Microscopy," *JMEMS*, vol. 16, pp. 969, 2007.
- [40] A. Jain and H. Xie, "Microendoscopic Confocal Imaging Probe Based on an LVD Microlens Scanner," *IEEE JOURNAL OF SELECTED TOPICS IN QUANTUM ELECTRONICS*, vol. 13, pp. 228-234, 2007.
- [41] J. J. Bernstein, M. R. Dokmeci, Gregory Kirkos, A. B. Osenar, J. Peanasky, and A. Pareek, "MEMS Tilt-Mirror Spatial Light Modulator for a Dynamic Spectral Equalizer," *JOURNAL OF MICROELECTROMECHANICAL SYSTEMS*, vol. 13, pp. 272-278, 2004.
- [42] I. W. Jung, B. Wang, and O. Solgaard, "Optical Pattern Generation Using a Spatial Light Modulator for Maskless Lithography," *Selected Topics in Quantum Electronics, IEEE Journal of*, vol. 13, pp. 147-154, 2007.
- [43] J. Suzuki, A. Komai, Y. Ohuchi, Y. Tezuka, H. Konishi, M. Nishiyama, Y. Suzuki, and S. Owa, "Micro-mirror On Ribbon-actuator (MOR) for high speed spatial light modulator," *MEMS 2008*, pp. 762-765, 2008.
- [44] J. Tsai, S. Huang, and M. C. Wu, "High fill-factor two-axis analog micromirror array for $1/\text{spl times N/sup 2/}$ wavelength-selective switches," *Micro Electro Mechanical Systems, 17th IEEE International Conference on. (MEMS)*, pp. 101-104, 2004.
- [45] J. Tsai, T. H. Sophia, D. Hah, and M. C. Wu, " $1/\text{spl times N/sup 2/}$ wavelength-selective switch with two cross-scanning one-axis analog micromirror arrays in a 4-f optical system," *Lightwave Technology, Journal of*, vol. 24, pp. 897-903, 2006.
- [46] J. Tsai and M. C. Wu, "A high port-count wavelength-selective switch using a large scan-angle, high fill-factor, two-axis MEMS scanner array," *Photonics Technology Letters, IEEE*, vol. 18, pp. 1439-1441, 2006.
- [47] N. Clark and P. Furth, "Silicon Eye: Using MEMs Micro-Mirrors," *Optics and Photonics News*, pp. 34-38, 2000.
- [48] S. He and R. B. Mrad, "Large-Stroke Microelectrostatic Actuators for Vertical Translation of Micromirrors Used in Adaptive Optics," *JMEMS*, vol. 52, pp. 974-983, 2005.
- [49] D. S. Greywall, "High-fill-factor adaptive optics mirrors with independent piston, tip and tilt controls," *JOURNAL OF MICROMECHANICS AND MICROENGINEERING*, vol. 16, pp. N1-N7, 2006.
- [50] J. B. Stewart, T. G. Bifano, S. Cornelissen, P. Bierden, B. M. Levine, and T. Cook, "Design and development of a 331-segment tip-tilt-piston mirror array for space-based adaptive optics," *Sensors and Actuators A*, vol. 138, pp. 230-238, 2007.

- [51] J. P. Siepmann, "Fusion of current technologies with real-time 3D MEMS ladar for novel security & defense applications," *Proceedings of SPIE*, vol. 6214, 2006.
- [52] S. Serati and J. Stockley, "Phased Array of Phased Arrays for Free Space Optical Communications," *Aerospace Conference, 2003. Proceedings. IEEE*, vol. 4, pp. 1809-1816, 2003.
- [53] U. Krishnamoorthy, K. Li, K. Yu, D. Lee, J. P. Heritage, and O. Solgaard, "Dual-mode Micromirrors for Optical Phased Array Applications," *Sensors and Actuators A*, vol. 97-98, pp. 21-26, 2002.
- [54] J. R. BRONSON, "MODELING AND CONTROL OF MEMS MICROMIRROR ARRAYS WITH NONLINEARITIES AND PARAMETRIC UNCERTAINTIES," *Ph.D. Dissertation*, 2007.
- [55] P. F. MCMANAMON, T. A. DORSCHNER, D. L. CORKUM, L. J. FRIEDMAN, DOUGLAS S. HOBBS, M. HOLZ, S. LIBERMAN, H. Q. NGUYEN, DANIEL P. RESLER, R. C. SHARP, and E. A. WATSON, "Optical Phased Array Technology," *Proceeding of the IEEE*, vol. 84, pp. 268-298, 1996.
- [56] P. F. McManamon, P. J. Bos, M. J. Escuti, J. Heikenfeld, S. Serati, H. Xie, and E. A. Watson, "A Review of Phased Array Steering for Narrow-Band Electrooptical Systems," *Proceedings of IEEE*, vol. 97, 2009.
- [57] W. Piyawattanmetha, L. Fan, S. Hsu, M. Fujino, and M. C. Wu, "Two-Dimensional Endoscopic MEMS Scanner for High Resolution Optical Coherence Tomography," *Conference on Lasers and Electro-Optics, CLEO*, vol. 1, pp. 3, 2004.
- [58] Z. Jason, I. Joseph, O. Bruce, and S. Stephen, "Endoscopic optical coherence tomography imaging probe using a MEMS actuator," *SPIE Proceedings*, vol. 5389, pp. 324-332, 2004.
- [59] T. Mitsui, Y. Takahashi, and Y. Watanabe, "A 2-axis optical scanner driven nonresonantly by electromagnetic force for OCT imaging," *JOURNAL OF MICROMECHANICS AND MICROENGINEERING*, vol. 16, pp. 2482-2487, 2006.
- [60] L. Kebin, U. Krishnamoorthy, J. P. Heritage, and O. Solgaard, "Phased arrays of micromirrors for programmable shaping of ultrashort pulses," *Technical Digest. Summaries of papers presented at the Conference on Lasers and Electro-Optics*, pp. 339-340, 2001.
- [61] L. Wu, S. B. Maley, S. R. Dooley, T. R. Nelson, P. F. McManamon, and H. Xie, "A LARGE-APERTURE, PISTON-TIP-TILT MICROMIRROR FOR OPTICAL PHASE ARRAY APPLICATIONS," *Micro Electro Mechanical Systems, 2008. MEMS 2008. IEEE 21st International Conference on*, pp. 754-757, 2008.

- [62] F. Pardo, R. A. Cirelli, E. J. Ferry, W. Y.-C. Lai, F. P. Klemens, J. F. Miner, C. S. Pai, J. E. Bower, W. M. Mansfield, A. Kornblit, T. W. Sorsch, J. A. Taylor, M. R. Baker, R. Fullowan, M. E. Simon, V. A. Aksyuk, R. Ryf, H. Dyson, and S. Arney, "Flexible fabrication of large pixel count piston-tip-tilt mirror arrays for fast spatial light modulators," *Microelectronic Engineering*, vol. 84, pp. 1157-1161, 2007.
- [63] K. E. Petersen, "Silicon Torsional Scanning Mirror," *IBM J. RES. DEVELOP.*, vol. 24, pp. 631-637, 1980.
- [64] G.-D. J. Su, H. Toshiyoshi, and M. C. Wu, "Surface-Micromachined 2-D Optical Scanners with High-Performance Single-Crystalline Silicon Micromirrors," *PHOTONICS TECHNOLOGY LETTERS*, vol. 13, pp. 606-608, 2001.
- [65] M. R. Dokmeci, A. Pareek, S. Bakshi, M. Waelti, C. D. Fung, K. H. Heng, and C. H. Mastrangelo, "Two-Axis Single-Crystal Silicon Micromirror Arrays," *JMEMS*, vol. 13, pp. 1006-1017, 2004.
- [66] D. S. Greywall, C.-S. Pai, S.-H. Oh, C.-P. Chang, D. M. Marom, P. A. Busch, R. A. Cirelli, J. A. Taylor, F. P. Klemens, T. W. Sorsch, J. E. Bower, W. Y.-C. Lai, and H. T. Soh, "Monolithic Fringe-Field-Activated Crystalline Silicon Tilting-Mirror Devices," *JMEMS*, vol. 12, pp. 702-707, 2003.
- [67] K. Joudrey, G. G. Adams, and N. E. McGruer, "Design, modeling, fabrication and testing of a high aspect ratio electrostatic torsional MEMS micromirror," *JOURNAL OF MICROMECHANICS AND MICROENGINEERING*, vol. 16, pp. 2147-2156, 2006.
- [68] D. S. GREYWALL, P. A. BUSCH, F. PARDO, D. W. CARR, G. BOGART, and H. T. SOH, "Crystalline silicon tilting mirrors for optical cross-connect switches," *JMEMS*, vol. 12, pp. 708-712, 2003.
- [69] L. Fan and M. C. Wu, "Two-Dimensional Optical Scanner with Large Angular Rotation Realized by Self-Assembled Micro-Elevator," *IEEE/LEOS Summer Topical Meetings*, pp. 107-108, 1999.
- [70] Z. HAO, W. Brian, W. Michael, B. Justin, and H. J. A, "A design methodology for a bulk-micromachined two-dimensional electrostatic torsion micromirror," *Journal of microelectromechanical systems*, vol. 12, pp. 692-701, 2003.
- [71] J.-C. Chiou and Y.-C. Lin, "A Multiple Electrostatic Electrodes Torsion Micromirror Device With Linear Stepping Angle Effect," *JMEMS*, vol. 12, pp. 913-920, 2003.
- [72] I. W. Jung, U. Krishnamoorthy, and O. Solgaard, "High Fill-Factor Two-Axis Gimbaled Tip-Tilt-Piston Micromirror Array Actuated by Self-Aligned Vertical Electrostatic Combdrives," *JMEMS*, vol. 15, pp. 563-571, 2006.

- [73] S. Kwon, V. Milanovic, and L. P. Lee, "A high aspect ratio 2D gimbaled microscanner with large static rotation," *Proc. IEEE/LEOS Int. Conf. Optical MEMS*, pp. 149-150, 2002.
- [74] T. Fujita, K. Maenaka, and Y. Takayama, "Dual-axis MEMS mirror for large deflection-angle using SU-8 soft torsion beam," *Sensors and Actuators A*, vol. 121, pp. 16-21, 2005.
- [75] S. Kwon, V. Milanovic, and L. P. Lee, "Vertical Combdrive Based 2-D Gimbaled Micromirrors with large Static Rotation by Backside Island Isolation," *IEEE JOURNAL OF SELECTED TOPICS IN QUANTUM ELECTRONICS*, vol. 10, pp. 498-504, 2004.
- [76] D. Lee and O. Solgaard, "Two-axis gimbaled microscanner in double SOI layers actuated by self-aligned vertical electrostatic combdrive," *Proc. Technical Digest Solid-State Sensor, Actuator and Microsystems Workshop, Hilton Head Island*, pp. 352-355, 2004.
- [77] H. Schenk, P. Durr, D. Kunze, H. Lakner, and H. Kuck, "A resonantly excited 2D-micro-scanning-mirror with large deflection," *Sensors and Actuators A*, vol. 89, pp. 104-111, 2001.
- [78] H. Xie, Y. Pan, and G. K. Fedder., "A CMOS-MEMS Mirror With Curled-Hinge Comb Drives," *JMEMS*, vol. 12, pp. 450-457, 2003.
- [79] P. R. Patterson, D. Hah, H. Nguyen, H. Toshiyoshi, R.-m. Chao, and M. C. Wu, "A SCANNING MICROMIRROR WITH ANGULAR COMB DRIVE ACTUATION," *Proceedings, IEEE micro electro mechanical systems*, pp. 544-547, 2002.
- [80] W. Piyawattanametha, P. R. Patterson, D. Hah, H. Toshiyoshi, and M. C. Wu, "Surface- and Bulk- Micromachined Two-Dimensional Scanner Driven by Angular Vertical Comb Actuators," *JMEMS*, vol. 14, pp. 1329-1338, 2005.
- [81] J. Kim, D. Christensen, and L. Lin, "Monolithic 2-D Scanning Mirror Using Self-Aligned Angular Vertical Comb Drives," *PHOTONICS TECHNOLOGY LETTERS*, vol. 17, pp. 2307-2309, 2005.
- [82] V. Milanovic, G. A. Matus, and D. T. McCormick, "Gimbal-Less Monolithic Silicon Actuators for Tip-Tilt-Piston Micromirror Applications," *JOURNAL OF SELECTED TOPICS IN QUANTUM ELECTRONICS*, vol. 10, pp. 462-471, 2004.
- [83] J.-c. Tsai and M. C. Wu, "Gimbal-Less MEMS Two-Axis Optical Scanner Array With High Fill-Factor," *JMEMS*, vol. 14, pp. 1323-1328, 2005.
- [84] H. Tien-liang, C. Yao-tien, C. Sheng-jie, T. Jui-che, H. Dooyoung, and M. C. Wu, "Performance improvement of a two-axis radial-vertical-combdrive scanner by using a symmetric spring design," *IEEE/LEOS International Conference on Optical MEMS and Nanophotonics*, pp. 108-109, 2008.

- [85] H. Schenk, P. Durr, T. Haase, D. Kunze, U. Sobe, H. Lakner, and H. Kuck, "Large deflection micromechanical scanning mirrors for linear scans and pattern generation," *JOURNAL OF SELECTED TOPICS IN QUANTUM ELECTRONICS*, vol. 6, pp. 715-722, 2000.
- [86] H. Toshiyoshi, W. Piyawattanametha, C.-T. Chan, and M. C. Wu, "Linearization of Electrostatically Actuated Surface Micromachined 2-D Optical Scanner," *JOURNAL OF MICROELECTROMECHANICAL SYSTEMS*, vol. 10, pp. 205-214, 2001.
- [87] D. Elata, V. Leus, A. Hirshberg, O. Salomon, and M. Naftali, "A NOVEL TILTING MICROMIRROR WITH A TRIANGULAR WAVEFORM RESONANCE RESPONSE AND AN ADJUSTABLE RESONANCE FREQUENCY FOR RASTER SCANNING APPLICATIONS," *TRANSDUCERS 2007*, pp. 1509-1512, 2007.
- [88] H. Ra, W. Piyawattanametha, M. J. Mandella, P.-L. Hsiung, J. Hardy, T. D. Wang, C. H. Contag, G. S. Kino, and O. Solgaard, "Three-dimensional in vivo imaging by a handheld dual-axes confocal microscope," *Optics Express*, vol. 16, pp. 7224-7232, 2008.
- [89] D. T. McCormick, W. Jung, Y.-C. Ahn, Z. Chen, and N. C. Tien, "ATHREE DIMENSIONALREAL-TIMEMEMS BASED OPTICALBIOPSY SYSTEM FOR IN-VIVO CLINICALIMAGING," *TRANSDUCERS 2007*, pp. 203-208.
- [90] W. Jung, D. T. McCormick, J. Zhang, L. Wang, N. C. Tien, and Z. Chen, "Three-dimensional endoscopic optical coherence tomography by use of a two-axis microelectromechanical scanning mirror," *Applied Physics Letters*, vol. 88-163901, pp. 1-3, 2006.
- [91] A. D. Yalcinkaya, H. Urey, and S. Holmstrom, "NiFe Plated Biaxial MEMS Scanner for 2-D Imaging," *IEEE PHOTONICS TECHNOLOGY LETTERS*, vol. 19, pp. 330-332, 2007.
- [92] H.-A. Yang, T.-L. Tang, S. T. Lee, and W. Fang, "A Novel Coilless Scanning Mirror Using Eddy Current Lorentz Force and Magnetostatic Force," *JOURNAL OF MICROELECTROMECHANICAL SYSTEMS*, vol. 16, pp. 511-520, 2007.
- [93] S.-H. Ahn and Y.-K. Kim, "Silicon scanning mirror of two DOF with compensation current routing," *JOURNAL OF MICROMECHANICS AND MICROENGINEERING*, vol. 14, pp. 1455-1461, 2004.
- [94] J. J. Bernstein, W. P. Taylor, J. D. Brazzle, C. J. Corcoran, G. Kirkos, J. E. Odhner, A. Pareek, M. Waelti, and M. Zai, "Electromagnetically Actuated Mirror Arrays for Use in 3-D Optical Switching Applications," *JOURNAL OF MICROELECTROMECHANICAL SYSTEMS*, vol. 13, pp. 526-535, 2004.

- [95] A. D. Yalcinkaya, H. Urey, D. Brown, T. Montague, and R. Sprague, "Two-Axis Electromagnetic Microscanner for High Resolution Displays," *JOURNAL OF MICROELECTROMECHANICAL SYSTEMS*, vol. 15, pp. 786-794, 2006.
- [96] C.-H. Ji, M. Choi, S.-C. Kim, K.-C. Song, J.-U. Bu, and H.-J. Nam, "Electromagnetic Two-Dimensional Scanner Using Radial Magnetic Field," *JOURNAL OF MICROELECTROMECHANICAL SYSTEMS*, vol. 16, pp. 989-996, 2007.
- [97] K. H. Kim, B. H. Park, G. N. Maguluri, T. W. Lee, F. J. Rogomentich, M. G. Bancu, B. E. Bouma, J. F. d. Boer, and J. J. Bernstein, "Two-axis magnetically-driven MEMS scanning catheter for endoscopic high-speed optical coherence tomography," *Optics Express*, vol. 15, pp. 18130-18140, 2007.
- [98] P. Verardi, F. Craciun, and M. Dinescu, "Characterization of PZT thin film transducers obtained by pulsed laser deposition," *Proceedings of Ultrasonics Symposium*, vol. 1, pp. 569-572, 1997.
- [99] D. X. Lu, E. Y. B. Pun, and Y. L. Zhang, "PZT thin film preparation on Pt/Ti by RF magnetron sputtering," *Proceedings of International Symposium on Applications of Ferroelectrics*, vol. 1, pp. 451-454, 1996.
- [100] K. Yamakawa, O. Arisumi, K. Okuwada, K. Tsutsumi, and T. Katata, "Development of stable PZT sputtering process using ex-situ crystallization and PZT/Pt interface control technique," *IEEE International Symposium on Applications of Ferroelectrics*, vol. 159-162, 1998.
- [101] T. Shiosaki, H. Fujisawa, and M. Shimizu, "MOCVD growth and characterization of Pb-based ferroelectric thin films," *IEEE International Symposium on Applications of Ferroelectrics*, vol. 1, pp. 45-50, 1996.
- [102] H. Funakubo and K. Nagashima, "Ferroelectric property improvement of Pb(Zr_xTi_{1-x})O₃ films by source gas pulse-introduced MOCVD," *IEEE International Symposium on Applications of Ferroelectrics*, vol. 1, pp. 67-70, 2000.
- [103] M. Shimizu, M. Yoshida, H. Fujisawa, and H. Niu, "Refinement of Pb(Zr,Ti)O₃ thin films grown by MOCVD," *IEEE International Symposium on Applications of Ferroelectrics*, pp. 139-142, 1998.
- [104] K. Kubo, M. Echizen, T. Nishida, T. Takeda, K. Uchiyama, and T. Shiosaki, "Synthesis and Characterization of PZT Ferroelectric Nanocrystals Current Measurement," *IEEE International Symposium on Applications of Ferroelectrics*, pp. 291-292, 2007.
- [105] S. K. Dey, K. D. Budd, and D. A. Payne, "Thin films of ferroelectrics PZT by Sol-Gel processing," *IEEE Transactions on Ultrasonic, Ferroelectrics and Frequency Control*, vol. 35, 1988.

- [106] Z. J. Wang, J. Tsaur, R. Maeda, and H. Kokawa, "Deposition of PZT thin films by hybrid process comprising sol-gel method and laser ablation for microscanners," *IEEE Symposium on Applications of Ferroelectrics*, pp. 169-172, 2004.
- [107] S.-G. Lee, S.-M. Park, C.-J. Kim, and Y.-H. Lee, "Characterization of PZT composite thick films fabricated using a modified Sol-Gel based process," *IEEE Conference on Nanotechnology Materials and Devices*, vol. 1, pp. 500-501, 2006.
- [108] G. Pang, M. Sayer, G. R. Lockwood, and M. Watt, "Fabrication of PZT sol gel composite ultrasonic transducers using batch fabrication micromolding," *IEEE Transactions on Ultrasonic, Ferroelectrics and Frequency Control*, vol. 53, pp. 1679-1684, 2006.
- [109] Y.-C. Hsu, K.-C. Kuo, and L.-S. Jang, "Development of characterization of PZT thick films fabricated by an improved sol-gel method," *IEEE International Conference on Robotics and Biomimetics*, vol. 778-782, 2005.
- [110] L. Zhang, M. Ichiki, Z. J. Wang, and R. Maeda, "Pulsed laser deposited lead zirconate titanate thin films for micro actuators," *Conference on Microprocesses and Nanotechnology*, pp. 135-140, 2002.
- [111] J.-H. Park, Y. Park, and J. Akedo, "Temperature Properties of PZT Actuated High-Speed Metal-Based Optical Resonant Scanners," *Applications of Ferroelectrics, ISAF. 16th IEEE International Symposium on*, pp. 711-713, 2007.
- [112] F. Filhol, E. Defay, C. Divoux, C. Zinck, and M.-T. Delaye, "Resonant micro-mirror excited by a thin-film piezoelectric actuator for fast optical beam scanning," *Sensors and Actuators A*, vol. 123-124, pp. 483-489, 2005.
- [113] H. Kueppers, T. Leuerer, U. Schnakenberg, W. Mokwa, M. Hoffmann, T. Schneller, and U. Boettger, "PZT thin films for piezoelectric microactuator applications," *Sensors and Actuators A*, vol. 97-98, pp. 680-684, 2002.
- [114] C. L. Pan, Y. T. Ma, Y. B. Liu, Q. Zhang, and Z. H. Feng, "Torsional displacement of piezoelectric fiber actuators with helical electrodes," *Sensors and Actuators A*, 2008.
- [115] J.-H. Park, J. Akedo, and H. Sato, "High-speed metal-based optical microscanners using stainless-steel substrate and piezoelectric thick films prepared by aerosol deposition method," *Sensors and Actuators A*, vol. 135, pp. 85-91, 2007.
- [116] J. G. Smits, K. Fujimoto, and V. F. Kleptsyn, "Microelectromechanical flexure PZT actuated optical scanner: static and resonance behavior," *JOURNAL OF MICROMECHANICS AND MICROENGINEERING*, vol. 15, pp. 1285-1293, 2005.
- [117] M. Tani, M. Akamatsu, Y. Yasuda, and H. Toshiyoshi, "A Two-Axis Piezoelectric Tilting Micromirror with a Newly Developed PZT-Meandering Actuator," *MEMS 2007*, pp. 699-702, 2007.

- [118] B. Barua, M. H. Nayim, and M. M. Bhuiyan, "A 2x2 MEMS Optical Switch Based on Piezoelectric Actuation," *International Conference on Electrical and Computer Engineering*, vol. 52-55, 2006.
- [119] H.-J. Nam, Y.-S. Kim, S.-M. Cho, Y. Yee, and J.-U. Bu, "Low voltage PZT actuated tilting micromirror with hinge structure," *IEEE/LEOS International Conference on Optical MEMS*, pp. 89-90, 2002.
- [120] Y. Yee, H.-J. Nam, S.-H. Lee, J. U. Bu, Y.-S. Jeon, and S.-M. Cho, "PZT actuated micromirror for nano-tracking of laser beam for high-density optical data storage," *MEMS 2000*, pp. 435-440, 2000.
- [121] J.-H. Park and J. Akedo, "Fabrication and Scanning-Angle Temperature Dependence of Metal-Based, Optical Resonant Scanners with PZT Actuation," *IEEE Transactions on Ultrasonic, Ferroelectrics and Frequency Control*, vol. 55, pp. 942-945 2008.
- [122] A. Jain, H. Qu, S. Todd, and H. Xie, "A thermal bimorph micromirror with large bi-directional and vertical actuation," *Sensors and Actuators A*, vol. 122, pp. 9-15, 2005.
- [123] A. Jain and H. Xie, "A single-crystal silicon micromirror for large bi-directional 2D scanning applications," *Sensors and Actuators A*, vol. 130-131, pp. 454-460, 2006.
- [124] L. Wu and H. Xie, "124 Degree Rotation Angle Electrothermal Micromirror With Integrated Platinum Heater," *IEEE JOURNAL OF SELECTED TOPICS IN QUANTUM ELECTRONICS*, vol. 13, pp. 316-321, 2007.
- [125] H. Xie, Y. Pan, and G. K. Fedder, "A SCS CMOS micromirror for optical coherence tomographic imaging," *MEMS 2002*, pp. 495-498, 2002.
- [126] A. Jain, A. Kopa, Y. Pan, G. K. Fedder, and H. Xie, "A Two-Axis Electrothermal Micromirror for Endoscopic Optical Coherence Tomography," *IEEE JOURNAL OF SELECTED TOPICS IN QUANTUM ELECTRONICS*, vol. 10, pp. 636-642, 2004.
- [127] J. Singh, J. H. S. Teo, Y. Xu, C. S. Premachandran, N. Chen, R. Kotlanka, M. Olivo, and C. J. R. Sheppard, "A two axes scanning SOI MEMS micromirror for endoscopic bioimaging," *JOURNAL OF MICROMECHANICS AND MICROENGINEERING*, vol. 18, 2008.
- [128] L. Wu and H. Xie, "A large vertical displacement electrothermal bimorph microactuator with very small lateral shift," *Sensors and Actuators A*, 2007.
- [129] J. P. Yang, X. C. Deng, and T. C. Chong, "An electro-thermal bimorph-based microactuator for precise track-positioning of optical disk drives," *JOURNAL OF MICROMECHANICS AND MICROENGINEERING*, vol. 15, pp. 958-965, 2005.

- [130] K. Jia and H. Xie, "Multi-Axis Electrothermal Scanning Micromirror with Low Driving Voltage," *Conference on Lasers and Electro-Optics, CLEO*, pp. 1-2, 2007.
- [131] K. Jia and H. Xie, "A Low-Voltage, Multi-Axis Scanning Electrothermal Micromirror," *Optics in the Southeast, Session 2: Optical Imaging and Sensing*, pp. 75, 2006.
- [132] K. Jia, S. Pal, and H. Xie, "An Agile Tip-Tilt-Piston Micromirror With Large Aperture, Large Scanning Range and Low Driving Voltage," *Solid-State Sensors, Actuators, and Microsystems Workshop, Hilton Head Island*, 2008.
- [133] M. Ataka, A. Omodaka, N. Takeshima, and H. Fujita, "Fabrication and operation of polyimide bimorph actuators for a ciliary motion system," *JMEMS*, vol. 2, pp. 146-150, 1993.
- [134] J. Buhler, J. Funk, O. Paul, E.-P. Steiner, and H. Baltes, "Thermally actuated CMOS micro mirrors," *Sensors and Actuators A*, vol. 47, pp. 572-575, 1995.
- [135] Y. T. Pan, Z. G. Wang, Z. L. Wu, A. Jain, and H. K. Xie, "DIAGNOSIS OF BIOLOGICAL TISSUE MORPHOLOGY AND FUNCTION WITH ENDOSCOPIC OPTICAL COHERENCE TOMOGRAPHY," *Proceedings of IEEE Annual Conference on Engineering in Medicine and Biology*, pp. 7217-7220, 2005.
- [136] Y. Xu, J. Singh, C. S. Premachandran, A. Khairyanto, K. W. S. Chen, N. Chen, C. J. R. Sheppard, and M. Olivo, "Design and development of a 3D scanning MEMS OCT probe using a novel SiOB package assembly," *JOURNAL OF MICROMECHANICS AND MICROENGINEERING*, vol. 18, 2008.
- [137] D. Morrish, L. Wu, H. Xie, J. Reynolds, A. Boussioutas, and M. Gu, "Nonlinear Imaging by an Endoscope Probe Incorporating a Tip-Tilt-Piston Microelectromechanical System Mirror," *OSA Spring Optics & Photonics Congress*, 2009.
- [138] X.-H. Xu, B.-Q. Li, Y. Feng, and J.-R. Chu, "Design, fabrication and characterization of a bulk-PZT-actuated MEMS deformable mirror," *JOURNAL OF MICROMECHANICS AND MICROENGINEERING*, vol. 17, pp. 2439-2446, 2007.
- [139] W. D. Cowan, M. K. Lee, B. M. Welsh, V. M. Bright, and M. C. Roggemann, "Surface micromachined segmented mirrors for adaptive optics," *Selected Topics in Quantum Electronics, IEEE Journal of*, vol. 5, pp. 90-101, 1999.
- [140] A. Tuantranont and V. M. Bright, "Segmented silicon-micromachined microelectromechanical deformable mirrors for adaptive optics," *Selected Topics in Quantum Electronics, IEEE Journal of*, vol. 8, pp. 33-45, 2002.
- [141] D. J. Dagel, W. D. Cowan, O. B. Spahn, G. D. Grossetete, A. J. Griñe, M. J. Shaw, P. J. Resnick, and J. Bernhard Jokiel, "Large-Stroke MEMS Deformable Mirrors for Adaptive Optics," *JMEMS*, vol. 15, pp. 572-583, 2006.

- [142] D. P. Resler, D. S. Hobbs, R. C. Sharp, L. J. Friedman, and T. A. Dorschner, "High-efficiency liquid-crystal optical phased-array beam steering," *OPTICS LETTERS*, vol. 21, pp. 689-691, 1996.
- [143] X. Wang, B. Wang, and P. J. Bas, "2-D Liquid Crystal Optical Phased Array," *IEEE Aerospace Conference Proceedings*, pp. 905-913, 2004.
- [144] P. F. McManamon and E. A. Watson, "Design of optical phased array beam steering with limited dispersion," *IEEE Proceedings of Aerospace Conference*, vol. 2, pp. 1583-1591, 2001.
- [145] P. J. Gilgunn and G. K. Fedder, "FLIP-CHIP INTEGRATED SOI-CMOS-MEMS FABRICATION TECHNOLOGY," *Solid-State Sensors, Actuators, and Microsystems Workshop, Hilton Head Island*, pp. 10-13, 2008.
- [146] M. Kim, J.-H. Park, J.-A. Jeon, B.-W. Yoo, I. H. Park, and Y.-K. Kim, "High fill-factor micromirror array using a self-aligned vertical comb drive actuator with two rotational axes," *Journal of Micromechanics and Microengineering*, vol. 19, pp. 035014, 2009.
- [147] M. Ohring, "Materials Science of Thin Films: Deposition and Structure," *2nd Edition*, Academic Press, 2002.
- [148] L. B. Freund and S. Suresh, "Thin Film Material: Stress, Defect Formation and Surface Evolution," *Cambridge University Press*, vol. ISBN 0521822815, 2003.
- [149] W. Peng, Z. Xiao, and K. R. Farmer, "Optimization of Thermally Actuated Bimorph Cantilevers for Maximum Deflection," *Nanotech*, vol. 1, pp. 376-379, 2003.
- [150] S. T. Todd, "ELECTROTHERMOMECHANICAL MODELING OF A 1-D ELECTROTHERMAL MEMS MICROMIRROR," *Master Thesis*, 2005.
- [151] *Wiki Online Encyclopedia*.
- [152] A. Govindaraju, A. Chakraborty, and C. Luo, "Reinforcement of PDMS masters using SU-8 truss structures," *J. Micromech. Microeng.*, vol. 15, pp. 1303-1309, 2005.
- [153] C. Livermore and J. Voldman, "Material Property Database," <http://web.mit.edu/6.777/www/matprops/matprops.htm>, 2004.
- [154] W. N. Sharpe, B. Yuan, and R. Vaidyanathan, "MEASUREMENTS OF YOUNG'S MODULUS, POISSON'S RATIO, AND TENSILE STRENGTH OF POLYSILICON," pp. 424-429, 1997.

- [155] A. A. Geisberger, N. Sarkar, M. Ellis, and G. D. Skidmore, "Electrothermal Properties and Modeling of Polysilicon Microthermal Actuators," *JOURNAL OF MICROELECTROMECHANICAL SYSTEMS*, vol. 12, pp. 513-523, 2003.
- [156] S. T. Todd and H. Xie, "Steady-state 1D electrothermal modeling of an electrothermal transducer," *JOURNAL OF MICROMECHANICS AND MICROENGINEERING*, vol. 15, pp. 2264-2276, 2005.
- [157] S. T. Todd and H. Xie, "An Electrothermomechanical Lumped Element Model of an Electrothermal Bimorph Actuator," *JOURNAL OF MICROELECTROMECHANICAL SYSTEMS*, vol. 17, pp. 213-225, 2008.
- [158] S. T. Todd and H. Xie, "Steady-state 1D electrothermal modeling of an electrothermal transducer," *J. Micromech. Microeng.*, vol. 15, 2005.
- [159] J. Singh, T. Gan, A. Agarwal, Mohanraj, and S. Liw, "3D free space thermally actuated micromirror device," *Sensors and Actuators A*, vol. 123-124, pp. 468-475, 2005.
- [160] S. T. Todd, A. Jain, H. Qu, and H. Xie, "A multi-degree-of-freedom micromirror utilizing inverted-series-connected bimorph actuators," *JOURNAL OF OPTICS A: PURE AND APPLIED OPTICS*, vol. 8, pp. S1-S8, 2006.
- [161] Z. Wang, C. S. D. Lee, W. C. Waltzer, J. Liu, H. Xie, Z. Yuan, and Y. Pan, "In vivo bladder imaging with microelectromechanicalsystems-based endoscopic spectral domain optical coherence tomography," *Journal of Biomedical Optics*, vol. 12, pp. 034009-1--034009-7, 2007.
- [162] Z. WANG, C. S. D. LEE, W. C. WALTZER, Z. YUAN, and Y. PAN, "INTERPIXEL-SHIFTED ENDOSCOPIC OPTICAL COHERENCE TOMOGRAPHY FOR IN VIVO BLADDER CANCER DIAGNOSIS," *International Journal of Image and Graphics*, vol. 7, pp. 105-117, 2006.
- [163] Y. Zhu, "Study on Silicon-Based Ferroelectric Micromachined Ultrasonic Transducers," *PH. D. Dissertation*, 2007.
- [164] MEMSnet.org, *Online Material Database*.

BIOGRAPHICAL SKETCH

Kemiao Jia was born in Shenyang, Liaoning province, P. R. China in January of 1982. He enrolled in the Zhejiang University (ZJU), Hangzhou, Zhejiang province, P. R. China in the fall of 1998. He received his B. S. degree in electrical and computer engineering in June 2002. He continued his master study in the same department and participated in the joint master program by the ZJU and the Shanghai Institute of Microsystems and Information Technology (SIMIT), Chinese Academy of Sciences, Shanghai, P. R. China. During the one year M. S. study at ZJU and two years of M.S. study at SIMIT, Kemiao was introduced to the fields of integrated optics and Micro-electro-mechanical Systems (MEMS). His main research focus was on the SOI-based arrayed waveguide ratings for wavelength division multiplexing applications. He also worked on the project of MEMS electrostatic optical switch. His research work in this period has been published on key IEEE journals and letters. In June 2005, Kemiao received his M.S. degree in Microelectronics and Solid- State Electronics.

Kemiao joined the Biophotonics and Microsystems Lab, Interdisciplinary Microsystems Group at the University of Florida in August of 2005 to pursue his Ph.D. degree. His main research focus which also composed his dissertation is the development of high fill-factor, small footprint MEMS micromirror scanners and micromirror array devices for biomedical imaging applications and optical phased array applications, respectively. He also worked on Post-CMOS MEMS inertial sensors. His research interests include MEMS actuators, MEMS optical scanners, biomedical imaging, photonics, optical phased array, free-space optical communications and MEMS inertial measurement unit (IMU). Upon the completion of his dissertation, he has contributed more than 10 peer reviewed research publications on prestigious conference and journals and 3 provisional patents from his doctoral research.

Kemiao is a member of the Institute of Electrical and Electronics Engineers and the Optical Society of America. He received his Ph.D. degree in December 2009. He will pursue a career in the field of MEMS and photonics.